ACCRETING X–RAY PULSARS.
THE HIGH ENERGY PICTURE

PhD Thesis presented by
Ascensión Camero Arranz

September 2007

Deparment of Astronomy & Astrophysics
University of Valencia

Dr. Victor Reglero Velasco,
catedrático de la Universidad de Valencia,

CERTIFICA:

Que la presente memoria, "ACCRETING X-RAY PULSARS. THE HIGH ENERGY PICTURE", ha sido realizada bajo su dirección, por Ascensión Camero Arranz, y que constituye su tesis doctoral para optar al grado de Doctor en Físicas.

Y para que quede constancia y tenga los efectos que corresponda, firma el presente certificado en Valencia, a 17 de Septiembre de 2007.

Firmado: Victor Reglero Velasco

Dr. Colleen A. Wilson-Hodge,
investigadora del National Space Science and Technology Center (NASA),

CERTIFICA:

Que la presente memoria, "ACCRETING X-RAY PULSARS. THE HIGH ENERGY PICTURE", ha sido realizada bajo su dirección, por Ascensión Camero Arranz, y que constituye su tesis doctoral para optar al grado de Doctora en Físicas.

Y para que quede constancia y tenga los efectos que corresponda, firma el presente certificado en Valencia, a 17 de Septiembre de 2007.

Firmado: Colleen A. Wilson-Hodge

Dr. Mark H. Finger,
investigador del National Space Science and Technology Center (NASA),

CERTIFICA:

Que la presente memoria, "ACCRETING X-RAY PULSARS. THE HIGH ENERGY PICTURE", ha sido realizada bajo su dirección, por Ascensión Camero Arranz, y que constituye su tesis doctoral para optar al grado de Doctor en Físicas.

Y para que quede constancia y tenga los efectos que corresponda, firma el presente certificado en Valencia, a 17 de Septiembre de 2007.

Firmado: Mark H. Finger

Contents

Chapter 1

INTRODUCTION

Cosmic X–ray sources were a challenging issue at the moment of their discovery in the 1960s. No physical process was known at the time which was capable of generating the enormous X–ray luminosities observed. On the other hand, the optical stars associated with these extremely powerful X–ray sources were rather faint and would not be obviously picked out on optical photographs or surveys. A major understanding of the nature of bright X–ray sources has been provided by the intermittent launch of a series of spacecrafts.

High energy photons in the X and γ-ray bands come from a great variety of sources, from our Sun to Supernovae and Supernova remnants and the compact objects left, black holes and neutron stars. At larger scales, galaxies especially those with active nuclei, and hot gas between galaxies can emit X–rays, as well as the interstellar medium (see Fig. 1.1).

The first X–ray sources discovered were naturally the brightest, the accretion-powered binaries within our galaxy. High Mass X–ray binaries (the targets of our study) are composed of an early-type massive star and accreting compact object (neutron star or black hole). When the compact object is a neutron star they are called X–ray pulsars.

High Mass X–ray binaries are objects of the highest astrophysical interest. Their study help us to address fundamental questions, from the masses of neutron stars to the structure of stellar winds. They represent

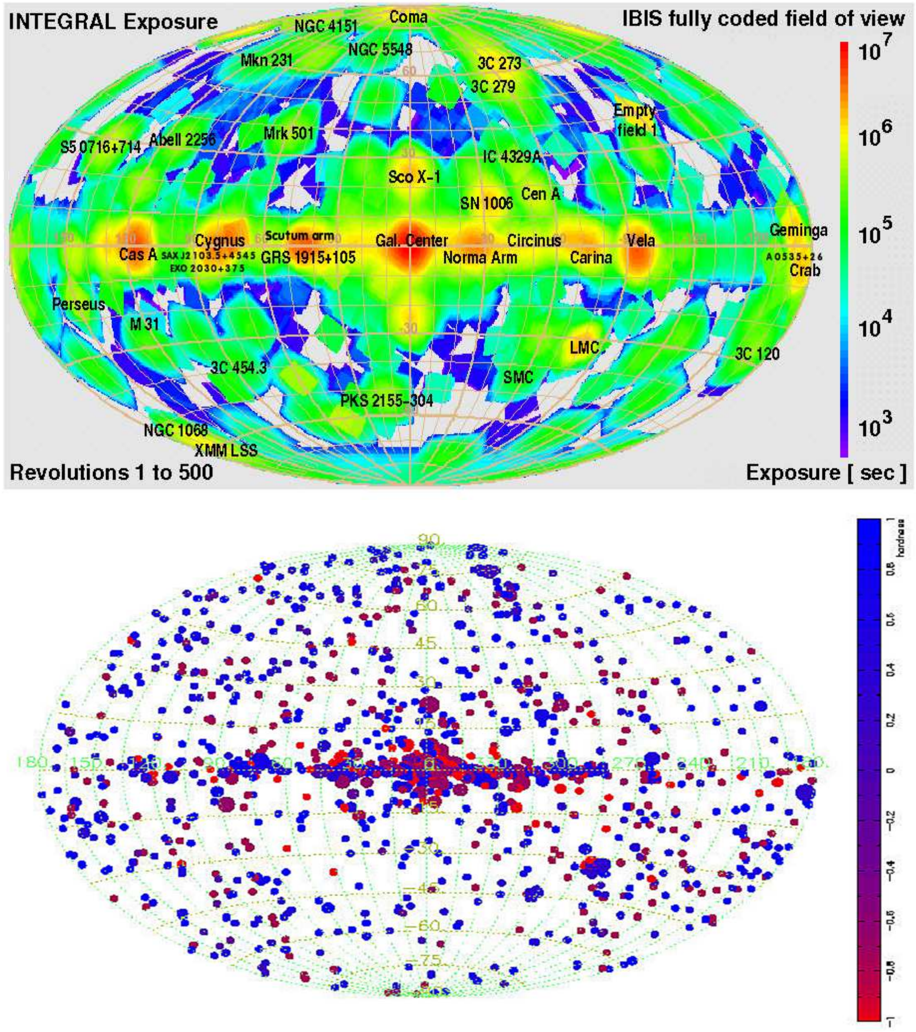

Figure 1.1: Top. *INTEGRAL* exposure map (IBIS) of the whole sky in galactic coordinates for the 500 first revolutions. The main targets are labeled. Bottom: The galactic distribution of the latest 1652 sources of the 27th catalog. The size and color of the symbols indicate approximate brightness and hardness. The (20–200 keV) ISGRI counting rate is the hard-band, and the soft-band is the (3–10 keV) JEM–X counting rate. Credits: ISDC (2007).

an important phase of massive binary evolution and the mechanisms for the formation of neutron stars and black holes. In general, X–ray studies are of interest as a probe of fundamental physics issues in unusual environments, which are in the majority of the cases extremely difficult to obtain in a laboratory.

Despite more than three decades of studies, however, many details of their formation and evolution, and the physical mechanisms involved remain not very well understood. It seems that as more and more systems are identified, the picture grows in complexity (Negueruela 2004, and references therein).

The Be/X-ray binaries are worth studying in several aspects. The presence of an X–ray pulsar has also allowed the determination of orbital parameters for a large number of binary systems via analysis of Doppler shifts in the pulse arrival times. Here we point out some conclusions by A. Okazaki [1] (Hokkai-Gakuen University, Sapporo, Japan) which describe the current situation

- The mechanisms that cause the transient X-ray activity (i.e., Type I and Type II outbursts) are not clearly known. The conventional model for the Type I outbursts, which assumes a big disk around the Be star, is outdated.
- The Be disk in Be/X-ray binaries cannot be steady (due to the resonant truncation). It grows, and then at some point it decays (disappears). The mechanism for the disk decay, which is related to the origin of the Type II outburst (Negueruela et al. 2001), is not known.
- Be/X-ray binaries are interacting binaries. Usually, studies of interacting binaries are related to the interaction between an accretion disk around a compact star and a companion in an circular orbit. Few study has been done on the interaction between a viscous (decretion) disk and a (compact) star in an eccentric orbit.

After all these open questions, the main goal of this thesis is to study the transient behavior of several X–ray pulsars during outburst. We expect to find similar temporal and spectral properties in the X–ray regimen, since they belong to the same class of objects (Be/X–ray binaries). This will

---

[1] http://www.elsa.hokkai-s-u.ac.jp/%7Eokazaki/index-e.html

lead to a better understanding of their nature and the physical mechanisms operating in this scenario.

Basically, this dissertation consists in the data reduction and analysis of the observations of a selection of accreting X-ray pulsars, obtained with the **INTE**rnational **G**amma-**R**ay **A**strophysics **L**aboratory (*INTEGRAL*) and **R**ossi **X**–ray **T**iming **E**xplorer (*RXTE*) missions.

In addition, during the last couple of years, the γ-ray observatory *INTEGRAL* has been conducting a continuous monitoring of the Galactic Plane revealing large numbers of new X-ray sources. A substantial fraction of these sources are believed to be high mass X-ray binaries (HMXRBs), in many cases, this has been proved by the identification of their counterparts (Negueruela and Schurch 2007, and references therein).

The Scutum region has been proposed to be the site of vigorous formation of X–ray pulsars. Our second aim is to search for new HMXRB candidates most likely situated in this region of strong absorption, which still remain undetected. Spectral and temporal studies of those sources in X-rays would be a next step in the future.

In chapters 2 and 3 we find some topics about X–ray accreting pulsars, and a description of all the instruments on board *INTEGRAL* and *RXTE* .

Chapter 4 includes a general explanation of the imaging, spectral and timing techniques used in this dissertation.

Chapter 5 focuses in the study of the high energy emission of the binary system EX0 2030+375. In the first part of this chapter we present timing and spectral analysis of this binary system. Two unusual features were found in the light curve of an outburst which took place in December 2002, with an initial peak before the main outburst and another possible spike after the maximum. *RXTE* observations confirm only the existence of the initial spike. The second part of this chapter abords a giant outburst of EXO 2030+375 observed with *RXTE* in 2006 June-October. It has been approximately 21 years since its last giant outburst in 1985. We present a study of the evolution of the spectral parameters during this giant outburst. We found correlations of some of these parameters with the luminosity of the system.

Chapter 6 presents the long-term pulse profile analysis of the Be/X-ray binary system SAX J2103.5+4545. The main goal was to study the pulse shape correlation with luminosity, time and energy using mainly 6 years of *RXTE* observations. The pulse shape obtained was complex and highly variable with both time or luminosity, and with a pulsed fraction that increases almost always with increasing luminosity. The long-term spectral variability, flux, frequency and spin-up rate histories were obtained, as well as a new set of orbital parameters.

Chapter 7 shows the evolution of the pulse profile of the accreting X-ray pulsar A 0535+26, from *RXTE* pointed observations made on the tail of the May-June 2005 giant outburst, and during two consecutive normal outbursts after the giant one. Simultaneous *INTEGRAL* observations from a shorter period of the first normal outburst were also analyzed. Luminosity and energy correlation patterns were found. The pre–spike present in the 2005 normal outburst shows a different pulse shape, and there might be changes in the profile at energies around the 45 keV cyclotron line.

Chapter 8 contains the imaging results of the Scutum survey performed by *INTEGRAL*. This is the first step of an on going project. Therefore, these results are preliminary, and will be pursued in the future. Data from the Galactic Plane Scan (GPS) and Galactic Center Deep Exposure (GCDE) surveys of the same region have also been used in order to increase the signal to noise. The analysis of the data might suggest the presence of a few possible new sources, although our results are not conclusive. The identification and follow up studies of the counterparts will be done in the IR bands, as well as spectral and timing studies in the X–ray band of those possible new X–ray source candidates.

Bibliography

Negueruela, I.: 2004, *ArXiv Astrophysics e-prints*

Negueruela, I., Okazaki, A. T., Fabregat, J., Coe, M. J., Munari, U., and Tomov, T.: 2001, *A&A* **369**, 117

Negueruela, I. and Schurch, M. P. E.: 2007, *A&A* **461**, 631

Chapter 2

X–RAY MISSIONS

2.1 THE *INTEGRAL* MISSION

INTEGRAL (Winkler et al. 2003) payload consists of three coded mask telescopes: the spectrometer SPI (20 keV–8 MeV), the imager IBIS (15 keV–10 MeV), and the X-ray monitor JEM-X (4–35 keV), as well as the optical monitoring camera OMC (V, 500–600nm).

The scientific goals that *INTEGRAL* address are the fine spectroscopy and the accurate location of γ-ray sources. The γ-sky has already been observed with previous missions, but *INTEGRAL* provides us with a new view of this fundamental region of the electromagnetic spectrum, since it is the observatory with the highest spectral and angular resolution so far. Its capabilities are aimed to study the following topics: compact objects, extragalactic astronomy, stellar nucleosynthesis, galactic plane and centre structure, particle processes acceleration, identification of high-energy sources and unexpected discoveries.

2.2 The instruments

Fig. 2.1 shows an overall view of the *INTEGRAL* spacecraft. It consists of two main structures: the service module (hosting the thermal, attitude, orbit and electrical control systems) and the payload module (accommodating the detector assemblies and an empty box supporting at about 3.4 m of height the coded masks). Table 2.1 shows the scientific capabilities of all the instruments.

The spectrometer, the imager and the X-ray monitor use the coded-mask technique to separate and locate the γ and X-ray sources. Coded Mask Imagers consist of a coded mask, i.e, an array of opaque and transparent elements which are arranged in a regular pattern, places between the sources and a position sensitive detector plane. There are several possible patterns. In the case of *INTEGRAL* , a HURA (**H**exagonal **U**niform **R**edundant **A**rray) pattern was chosen for SPI and JEM-X and a MURA (**M**odified **U**niform **R**edundant **A**rray) for IBIS.

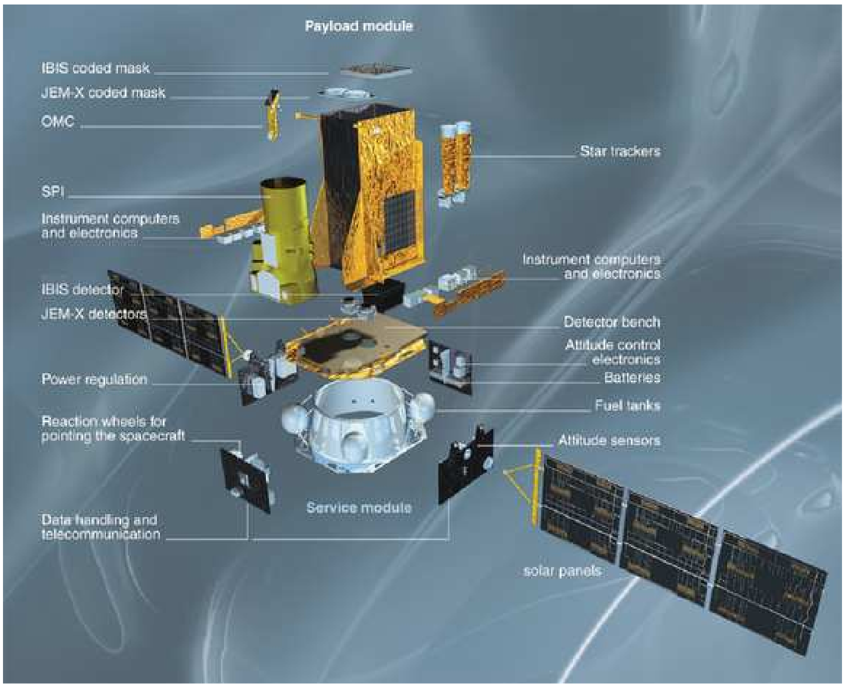

Figure 2.1: Exploded view of the *INTEGRAL* spacecraft. Credits: ESA 2002.

Table 2.1: *INTEGRAL* key instrumental parameters. Credits: ESA 2002.

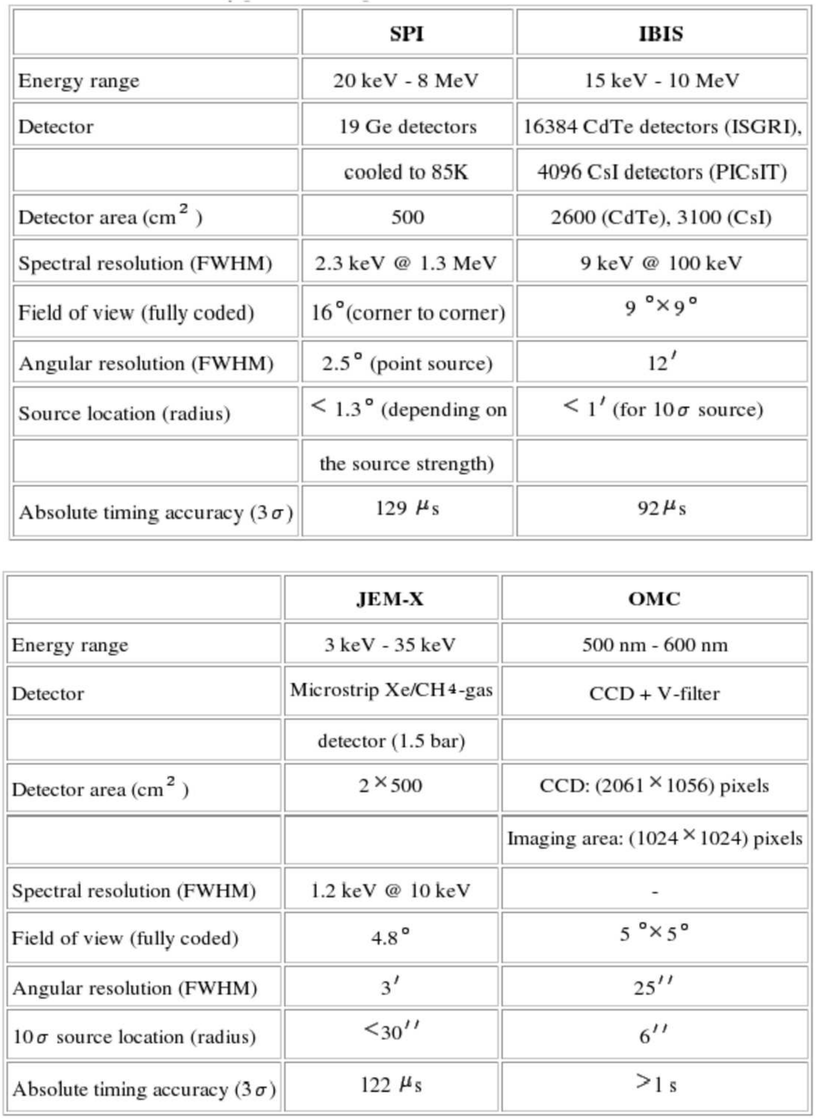

	SPI	**IBIS**
Energy range	20 keV - 8 MeV	15 keV - 10 MeV
Detector	19 Ge detectors	16384 CdTe detectors (ISGRI),
	cooled to 85K	4096 CsI detectors (PICsIT)
Detector area (cm^2)	500	2600 (CdTe), 3100 (CsI)
Spectral resolution (FWHM)	2.3 keV @ 1.3 MeV	9 keV @ 100 keV
Field of view (fully coded)	16°(corner to corner)	$9^\circ \times 9^\circ$
Angular resolution (FWHM)	2.5° (point source)	$12'$
Source location (radius)	$< 1.3^\circ$ (depending on	$< 1'$ (for 10σ source)
	the source strength)	
Absolute timing accuracy (3σ)	129 μs	92μs

	JEM-X	**OMC**
Energy range	3 keV - 35 keV	500 nm - 600 nm
Detector	Microstrip Xe/CH$_4$-gas	CCD + V-filter
	detector (1.5 bar)	
Detector area (cm^2)	2×500	CCD: (2061×1056) pixels
		Imaging area: (1024×1024) pixels
Spectral resolution (FWHM)	1.2 keV @ 10 keV	-
Field of view (fully coded)	4.8°	$5^\circ \times 5^\circ$
Angular resolution (FWHM)	$3'$	$25''$
10σ source location (radius)	$<30''$	$6''$
Absolute timing accuracy (3σ)	122 μs	>1 s

2.2.1 The SPectrometer on-board INTEGRAL satellite

SPI (Vedrenne et al. 2003) is a spectrometer devoted to study the γ-ray sky in the energy range 18 keV – 8 MeV with an energy resolution of 2.5 keV at 1.1 MeV. The γ camera is formed by 19 high purity Germanium (GeDs) detectors with a geometric area of 508 cm^2 (see Fig. 2.2). An active cryogenic system is used to maintain the Ge detectors at their low working temperatures (85 – 90 K). The imaging capabilities of the instrument are obtained using a tungsten coded mask located 1.7 m from the Ge detectors with an angular resolution of 2.5°.

The background due to cosmic ray interactions with the Ge detectors and all the materials around them is reduced using an **A**ctive **A**nti-coincidence **S**ystem of BGO crystals. The field of view of the instrument is defined by the detector size, the mask size and their distance. The FC-FOV is 16° on diameter. However, the instrumental background exceeds the pre-launch simulations by 30%–40%, dominating the overall signal.

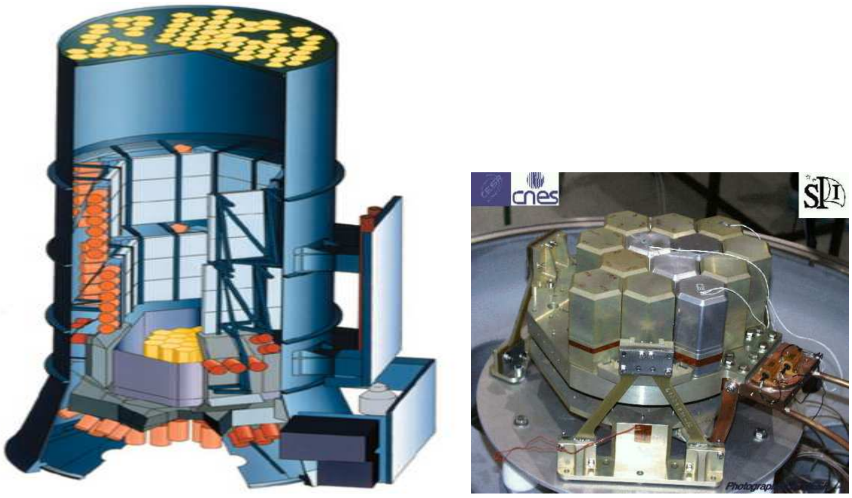

Figure 2.2: Left. The SPI instrument. Right. View of its 19 hexagonal germanium detectors. Photo by J.P Roques, CESR, 2001.

2.2.2 The Imager on-Board INTEGRAL Satellite

IBIS (Ubertini et al. 2003) is devoted to obtain γ-ray images with high angular resolution ($12'$) in the energy range 15 keV–10 MeV. The imager consists of two independent solid state detector arrays: ISGRI – the lower layer– and PICsIT, plus a tungsten coded mask located at 3.4 m from ISGRI (see Fig 2.3).

The **I**NTEGRAL **S**oft **G**amma-**R**ay **I**mager (ISGRI) (Lebrun et al. 2003), is formed by 16384 CdTe detectors with a total geometric area of 2621 cm^2. It is optimized to work in the energy range 15 keV-1 MeV with an energy resolution of $\sim$ 8% at 60 keV.

The **P**ixellated **I**maging **C**aesium **I**odide **T**elescope (PICsIT) (Labanti et al. 2003), consists of 4096 CsI(Tl) scintillator detectors with an active area of 2890 cm^2. It is optimized to work in the energy range 0.17-10 MeV with an energy resolution of 18.4% at 511 keV.

Like SPI, an active anti-coincidence system is used to minimize the induced background by the cosmic ray interactions with the detectors. The field of view of the instruments are respectively, (FCFOV) 9° and 19°.

In this work, we have only analyzed ISGRI data, since our sources are well below of PCIsIT sensitivity, which was badly affected by a high background count rate ($\sim$3500 c/s) after launch[1]. An on-board processing of the data from integration events into histograms is performed because of the limited telemetry available.

2.2.3 The Joint European X-Ray Monitor

The JEM-X (Lund et al. 2003) provides X-ray imaging with arcmin angular resolution ($3.35'$) and spectra with an energy resolution of 2 keV at 22 keV in the energy range 4 – 35 keV. It consists of two co-aligned coded mask telescopes. Each of the telescope comprises two major subsystems:

---

[1] http://www.iasfbo.inaf.it/ foschini/

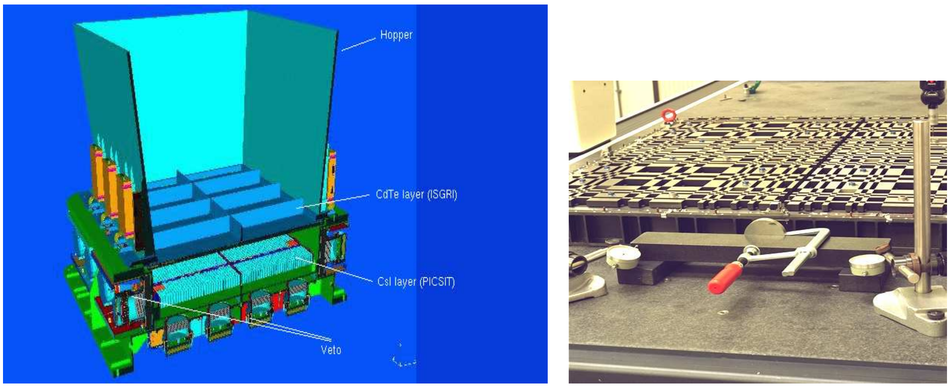

Figure 2.3: Left. Overall IBIS design. Cut-away view of detector assembly and shield (hopper). The mask at 3.2 m above focal plane is shown on the right panel.

the coded mask and the detector unit (see Fig. 2.4). The two telescopes are identical, except that the coded masks are inverted with respect to each other.

The photon detection system is a **M**icro**S**trip **G**as **C**hamber (MSGS) with a sensitive geometric area of ~ 500 cm^2 per unit. The detector unit is formed by: the detector vessel, the X-ray entrance window, the collimator and the Microstrip sensor package with the associated electronics. The gas inside the detector vessel is a mixture of Xenon (90%) and Methane at 1.5 bar pressure.

The collimator plays a dual role, it supports the X-ray entrance window against the internal pressure and defines the field of view of the instrument (FCFOV 4.8°). The collimator reduces the count rate of the diffuse X-ray background but also the count rate of sources located in the edges of the field of view. This vignetting effect has to be taking into account in the data reduction.

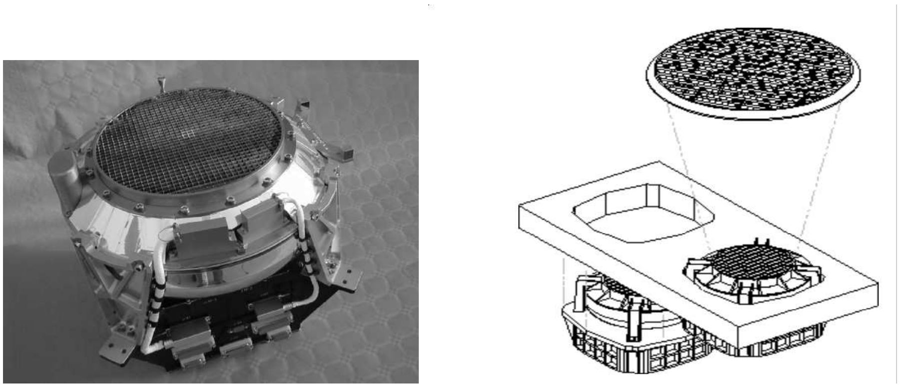

Figure 2.4: Left. View of a detector unit. Right: JEM-X instrument schematic representation.

2.2.4 The Optical Monitoring Camera

The OMC (Mas-Hesse et al. 2003) provides photometry observations of long duration in the optical band simultaneously with the X and γ-rays. The camera is based in refractive optics with an aperture of 50 mm focused onto a large format CCD with a V sensitivity of 18. The main scientific objectives are: to monitor the optical emission from the sources observed by the high-energy instruments, producing light curves in the optical band for comparison with the high-energy ones. And to provide the brightness and the position of the optical counterpart of any γ or X-ray transient within its field of view ($\sim 5^\circ \times 5^\circ$). Due to a strong optical extinction in our sources, this instrument has not been used for the present work.

2.3 The Observing Programme

The *INTEGRAL* observing programme is divided in two main categories: the general programme and the core programme (CP). The general programme is devoted to open proposals of the scientific community, thus *INTEGRAL* works as an observatory mission. The core programme is guaranteed time to those scientific collaborations and individual scientists

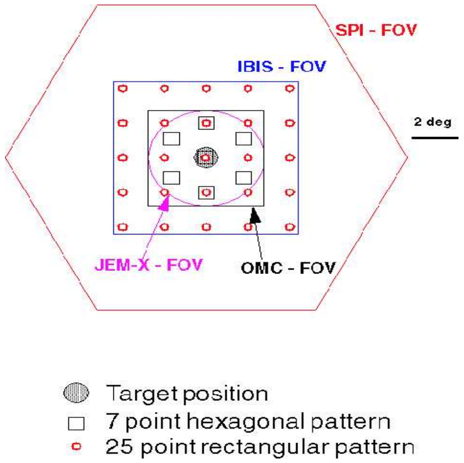

Figure 2.5: Dithering *INTEGRAL* patterns and Fully Coded Field Of View of the instruments. Credits: ESA 2002.

who contributed to the development, design and procurement of *INTEGRAL* . Most of the total observing time is devoted to the general programme. In the core programme the observing strategy consisted up to middle 2006 of three elements, which are in priority: a Deep exposure of the Galactic Central Radian, regular scans of the Galactic Plane and pointed observations of selected sources.

There are three possible ways to perform an observation: staring mode (constantly pointing at a target in the centre of the FOV of the instruments) or two dithering modes (performing at scan around the targets). The two dithering modes are the 7–pointing hexagonal pattern and the 25 rectangular pattern (see Fig. 2.5). Each pointing usually lasts 1800–3600 s.

2.4 THE *RXTE* MISSION

The Rossi X–ray Timing Explorer (*RXTE*) was launched on December 30, 1995 from NASA's Kennedy Space Center. A Delta II rocket put *RXTE* into its intended low-earth circular orbit at an altitude of 580 km, corresponding to an orbital period of about 90 minutes, with an inclination of 23 degrees. *RXTE* features unprecedented time resolution in combination with moderate spectral resolution to explore the variability of X-ray sources. Time scales from microseconds to months are covered in an instantaneous spectral range from 2 to 250 keV. Originally designed for a required lifetime of two years with a goal of five, *RXTE* has substantially exceeded that goal.

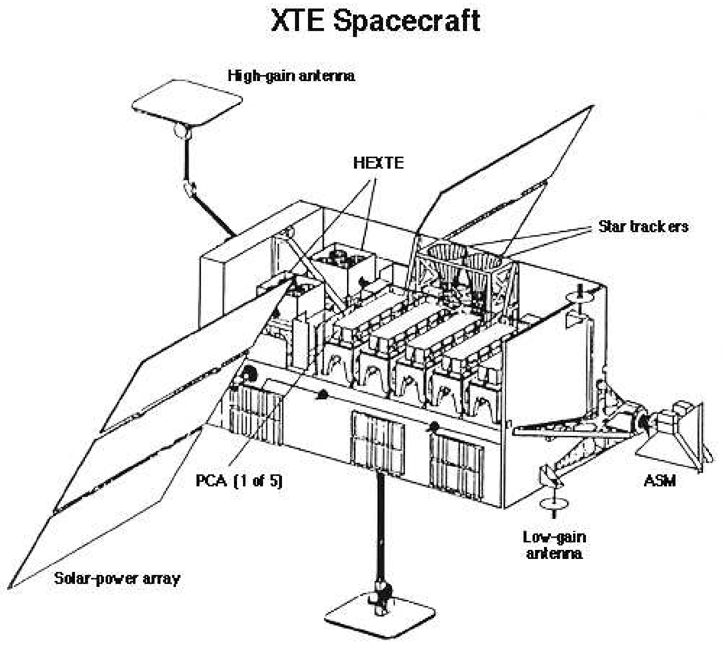

Figure 2.6: Diagram of the XTE spacecraft, with the instruments labeled. Credits: NASA 1996.

2.5 The instruments

RXTE (Bradt et al. 1993) carries 3 instruments on board (Fig. 2.6). The Proportional Counter Array (PCA; Jahoda et al. 1996), sensitive from 2–60 keV, was designed to perform observations of bright X-ray sources with high timing and modest spectral resolution. The High Energy X-ray Timing Experiment (HEXTE Gruber et al. 1996) extends the X-ray sensitivity up to 200 keV. Monitoring the long-term behavior of some of the brightest X-ray sources, the All Sky Monitor (ASM Levine et al. 1996) scans most of the sky every 1.5 hours at 2–10 keV. The properties of all the instruments are listed in Table 2.2.

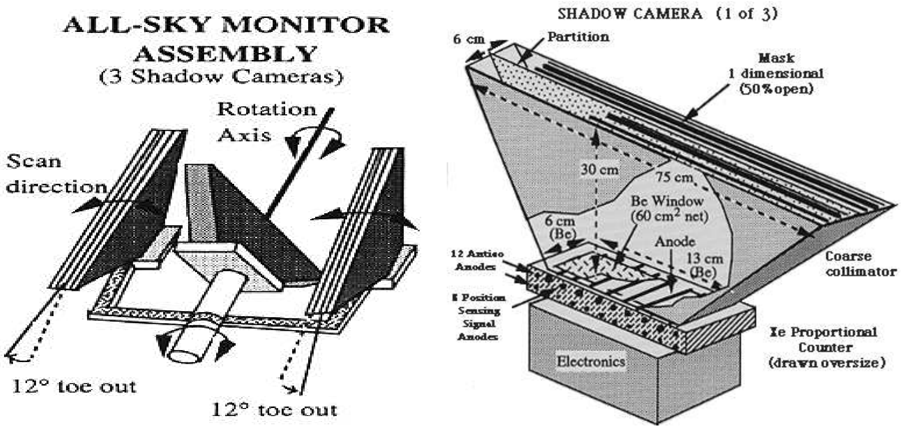

Figure 2.7: Left: Diagram of the ASM assembly. Right: Diagram of one of the ASM shadow cameras. Credit: NASA.

2.5.1 The All-Sky Monitor

The ASM consists of three Scanning Shadow Cameras (SSCs) mounted on a motorized rotation drive (Fig. 2.7, left). Each SSC contains a position-sensitive proportional counter (PSPC) that views the sky through a slit mask (Fig. 2.7, right). The mask is a thin aluminum sheet that is subdivided into 6×2 subsections, each comprised of a pseudo-random pattern of open and closed elements.

A partition between the mask and the PSPC causes to view the sky only through half of the mask. This yields a FOV of 6° by 90° FWHM. Each PSPC is shielded with 8 μm of aluminized plastic and a 50 μm beryllium. Within each PSPC are 8 resistive carbon-coated quartz fiber anodes, each end of which is connected to a dedicated electronics.

Table 2.2: The instrumental properties of the 3 instruments on board *RXTE* .

	ASM	PCA	HEXTE
Energy range	2 - 10 keV	2 - 60 keV	15 - 250 keV
Energy resolution		$< 18\%$ at 6 keV	15% at 60 keV
Time resolution	80% of the sky every 90 min	1 μsec	7.6 μsec
Spatial resolution	3' x 15'	collimator with 1 ° FWHM	
Field of view			1° FWHM
Detectors	Xenon proport. count. position-sensitive	5 proportion. counters	two 4 NaI/CsI clusters scintillation counters
Number of shadow cameras	3 (6×90 deg FOV, each)		
Collecting area	90 cm^2	6500 cm^2	2×890 cm^2
Layers		1 Propane veto; 3 Xenon, each split into 2; 1 Xenon veto layer	
Sensitivity	30 mCrab	0.1 mCrab	1 Crab=360 c s^{-1}cluster^{-1}
Background		2 mCrab	50 c s^{-1}cluster^{-1}

The volume around the anodes is filled with a 95% Xenon,5% CO_2 gas mixture (total pressure 1.2 atm) (Levine et al. 1996).

Event data are normally compressed within the two ASM Event Analyzers (EAs) in the Experiment Data System (see section 1.5.4), before insertion into the telemetry stream. One ASM EA accumulates histograms of counts binned as a function of position for each of the resistive anodes and for each of three energy bands roughly corresponding to 1.5–3, 3–5, and 5–12 keV. These position histograms are accumulated in series of $\sim$90 s "dwells". The other ASM EA produces count rates for both X–ray ($\frac{1}{8}$ s time bins) and background (1 s time bins) events and pulse-height spectra (64 s time resolution, 64 channels for 0–20 keV).

The light curves included in this thesis work were obtained from the *RXTE* Guest Observer facility[2] and from the ASM team[3].

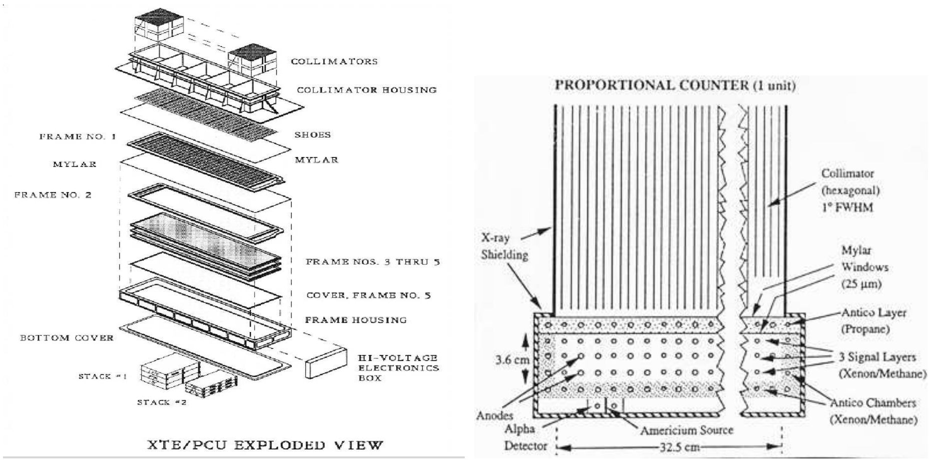

Figure 2.8: Left: Assembly of one PCA detector (Jahoda et al. 2006). Right: Diagram of a proportional-counter unit. Credit: NASA.

---

[2] http://heasarc.gsfc.nasa.gov/0/docs/xte/xte_1st.html

[3] http://xte.mit.edu/XTE/XTE.html

2.5.2 The Proportional Counter Array

The PCA consists of five large-area proportional counter units (PCUs). Each has a net geometric collecting area of $\sim$1600 cm^2. The essential features are visible in the detector cross section (Fig. 2.8, right) and assembly view (Fig. 2.8, left). The detectors consist of a mechanical collimator with FWHM $\sim 1^\circ$, an aluminized Mylar window, a propane-filled "veto" volume, a second Mylar window, and a xenon-filled main counter. The xenon volume is divided into cells of $\sim$1.3 cm$\times$1.3 cm$\times$1 m by wire walls. The detector bodies are constructed of aluminum and surrounded by a graded shield consisting of a layer of tin followed by a layer of tantalum (Jahoda et al. 2006).

There are three layers of xenon cells, and each layer is divided in half by connecting alternate cells to either the "right" or "left" amplifier chain. The division of each layer is significant for data screening and background modeling. The overall PCA instrument is operating nominally. However, the five individual PCU detectors have their own individual details, which are listed in Fig. 2.9.

Events detected by the PCA will be processed on board by the EDS before insertion into the telemetry stream. They can be packaged as several different guest investigator specified data types. Four PCA data types were used in the present work. Standard1 data (0.125 s time resolution, no energy resolution) for the light curves. Standard2 data (16 s

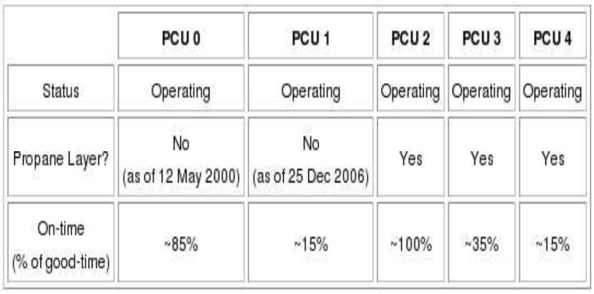

	PCU 0	PCU 1	PCU 2	PCU 3	PCU 4
Status	Operating	Operating	Operating	Operating	Operating
Propane Layer?	No (as of 12 May 2000)	No (as of 25 Dec 2006)	Yes	Yes	Yes
On-time (% of good-time)	~85%	~15%	~100%	~35%	~15%

Figure 2.9: Status of the five individual PCU detectors.

time resolution, 129 channel energy resolution) for spectral analysis using Ftools V6.0.5. In addition, GoodXenon (256-channel resolution and time stamped with μs time resolution) and Event mode data (125μs time resolution in 64 PHA channel bands, 0 keV low energy cuttoff and read out one per second) were selected for the pulse profile study.

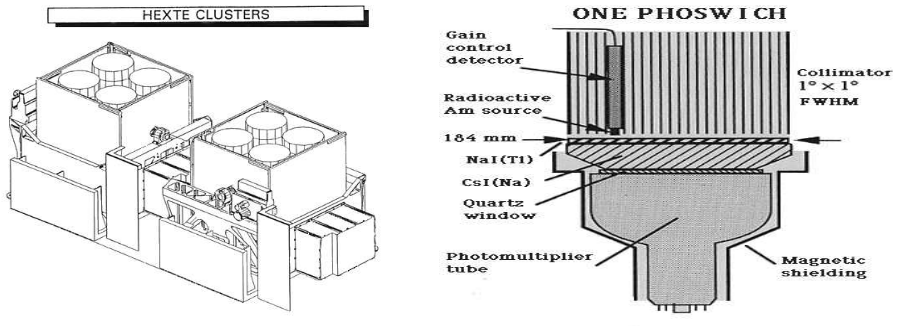

Figure 2.10: Left: Diagram of the HEXTE Clusters. Courtesy of UCSD HEXTE team. Right: A depiction of a Phoswich Camera. Adapted from a diagram provided by Hale Bradt. M. Halverson, and students.

2.5.3 The High Energy X-ray Timing Experiment

The HEXTE consists of two clusters each containing four phoswich scintillation detectors (see Fig. 2.10). The two clusters can "rock" (beamswitch) along mutually orthogonal directions to provide background measurements 1.5 or 3° away from the source every 16 to 128 s. Automatic gain control is provided by using a ^{241}Am radioactive source mounted in each detector's field of view (Gruber et al. 1996).

The primary function of the instrument (to measure high energy cosmic X-rays) is accomplished via thallium-doped sodium iodide (NaI(Tl)) scintillation crystals viewed by photomultiplier tubes. In addition, particle detectors are used to reject contaminating events from cosmic ray interactions, and to provide a signal from the calibration source which is used for automatic gain control.

Events detected by HEXTE will be processed on board by its own data system before insertion into the telemetry stream at an average data rate of 5 kbit/s. In the present work HEXTE binned mode data from clusters A and B have been used for the spectral analysis, and event mode data for timing analysis. On 1996 March 6, detector 2 in cluster B lost its ability to provide spectral information. Therefore, only data from detectors 0,1, and 3 were taken for this cluster. On the other hand, since 2006 July, cluster A is permanently fixed on source, i.e., there are no quasi-simultaneous background measurements for cluster A anymore due to rocking mechanism problems. Nevertheless, Pottschmidt et al. (2006) have developed a Ftool (`hextebackest`) for estimating the HEXTE A background spectrum.

2.5.4 The Experiment Data System

The EDS consists of eight Event Analyzers (EA), of which six are dedicated to the PCA and two to the ASM. Each EA contains an Intel 80286 processor and associated memory. The EAs can be programmed independently to process incoming events from the instruments in any of the following modes: Transparent (using 1, 2, or 3 EAs), Event (using 1 or 2 EAs), Binned (time and/or energy), Burst catcher, Fourier transform, Pulsar fold, Autocorrelation and Arrival time differences histogram mode.

Bibliography

Bradt, H. V., Rothschild, R. E., and Swank, J. H.: 1993, *A&AS* **97**, 355

Gruber, D. E., Blanco, P. R., Heindl, W. A., Pelling, M. R., Rothschild, R. E., and Hink, P. L.: 1996, *A&AS* **120**, C641+

Jahoda, K., Markwardt, C. B., Radeva, Y., Rots, A. H., Stark, M. J., Swank, J. H., Strohmayer, T. E., and Zhang, W.: 2006, *ApJS* **163**, 401

Labanti, C., Di Cocco, G., Ferro, G., Gianotti, F., Mauri, A., Rossi, E., Stephen, J. B., Traci, A., and Trifoglio, M.: 2003, *A&A* **411**, L149

Lebrun, F., Leray, J. P., Lavocat, P., Crétolle, J., Arquès, M., Blondel, C., Bonnin, C., Bouère, A., Cara, C., Chaleil, T., Daly, F., Desages, F., Dzitko, H., Horeau, B., Laurent, P., Limousin, O., Mathy, F., Mauguen, V., Meignier, F., Molinié, F., Poindron, E., Rouger, M., Sauvageon, A., and Tourrette, T.: 2003, *A&A* **411**, L141

Levine, A. M., Bradt, H., Cui, W., Jernigan, J. G., Morgan, E. H., Remillard, R., Shirey, R. E., and Smith, D. A.: 1996, *ApJ Lett.* **469**, L33+

Lund, N., Budtz-Jørgensen, C., Westergaard, N. J., Brandt, S., Rasmussen, I. L., Hornstrup, A., Oxborrow, C. A., Chenevez, J., Jensen, P. A., Laursen, S., Andersen, K. H., Mogensen, P. B., Rasmussen, I., Omø, K., Pedersen, S. M., Polny, J., Andersson, H., Andersson, T., Kämäräinen, V., Vilhu, O., Huovelin, J., Maisala, S., Morawski, M., Juchnikowski, G., Costa, E., Feroci, M., Rubini, A., Rapisarda, M., Morelli, E., Carassiti, V., Frontera, F., Pelliciari, C., Loffredo, G., Martínez Núñez, S., Reglero, V., Velasco, T., Larsson, S., Svensson, R., Zdziarski, A. A., Castro-Tirado, A., Attina, P., Goria, M., Giulianelli, G., Cordero, F., Rezazad, M., Schmidt, M., Carli, R., Gomez, C., Jensen, P. L., Sarri, G., Tiemon, A., Orr, A., Much, R., Kretschmar, P., and Schnopper, H. W.: 2003, *A&A* **411**, L231

Mas-Hesse, J. M., Giménez, A., Culhane, J. L., Jamar, C., McBreen, B., Torra, J., Hudec, R., Fabregat, J., Meurs, E., Swings, J. P., Alcacera, M. A., Balado, A., Beiztegui, R., Belenguer, T., Bradley, L., Caballero, M. D., Cabo, P., Defise, J. M., Díaz, E., Domingo, A., Figueras, F., Figueroa, I., Hanlon, L., Hroch, F., Hudcova, V., García, T., Jordan, B., Jordi, C., Kretschmar, P., Laviada, C., March, M., Martín, E., Mazy, E., Menéndez, M., Mi, J. M., de Miguel, E., Muñoz, T., Nolan, K., Olmedo, R., Plesseria, J. Y., Polcar, J., Reina, M., Renotte, E., Rochus, P., Sánchez, A., San Martín, J. C., Smith, A., Soldan, J., Thomas, P., Timón, V., and Walton, D.: 2003, *A&A* **411**, L261

Pottschmidt, K., Rothschild, R. E., Gasaway, T., Suchy, S., and Coburn, W.: 2006, in *AAS High Energy Astrophysics Division*, Vol. 9 of *AAS High Energy Astrophysics Division*, p. 18.21

Ubertini, P., Lebrun, F., Di Cocco, G., Bazzano, A., Bird, A. J., Broenstad, K., Goldwurm, A., La Rosa, G., Labanti, C., Laurent, P., Mirabel, I. F., Quadrini, E. M., Ramsey, B., Reglero, V., Sabau, L., Sacco, B., Staubert, R., Vigroux, L., Weisskopf, M. C., and Zdziarski, A. A.: 2003, *A&A* **411**, L131

Vedrenne, G., Roques, J.-P., Schönfelder, V., Mandrou, P., Lichti, G. G., von Kienlin, A., Cordier, B., Schanne, S., Knödlseder, J., Skinner, G., Jean, P., Sanchez, F., Caraveo, P., Teegarden, B., von Ballmoos, P., Bouchet, L., Paul, P., Matteson, J., Boggs, S., Wunderer, C., Leleux, P., Weidenspointner, G., Durouchoux, P., Diehl, R., Strong, A., Cassé, M., Clair, M. A., and André, Y.: 2003, *A&A* **411**, L63

Winkler, C., Courvoisier, T. J.-L., Di Cocco, G., Gehrels, N., Giménez, A., Grebenev, S., Hermsen, W., Mas-Hesse, J. M., Lebrun, F., Lund, N., Palumbo, G. G. C., Paul, J., Roques, J.-P., Schnopper, H., Schönfelder, V., Sunyaev, R., Teegarden, B., Ubertini, P., Vedrenne, G., and Dean, A. J.: 2003, *A&A* **411**, L1

Chapter 3

ACCRETING X-RAY PULSARS

3.1 THE FINAL STAGE OF STELLAR EVOLUTION

Compact objects (white dwarfs, neutron stars, and black holes) are born when normal stars die, that is, when most of their nuclear fuel has been consumed. Therefore, they cannot support themselves against gravitational collapse by generating thermal pressure. Instead, white dwarfs are supported by the pressure of degenerated electrons, while neutron stars are supported largely by the pressure of degenerate neutrons. Black Holes, on the other hand, are completely collapsed stars that could not hold back the pull of gravity and therefore collapsed to singularities.

Another characteristic distinguishing compact objects is their exceedingly small size, compared to normal stars of similar mass. Their smaller radii and much stronger surface gravitational fields define these enormous dense objects. The primary factor determining whether a star ends up as a white dwarf, neutron star or black hole is likely to be the star's mass. Neutron stars and black holes are believed to originate from massive stars larger than 4 $M\odot$ (Shapiro and Teukolsky 1983).

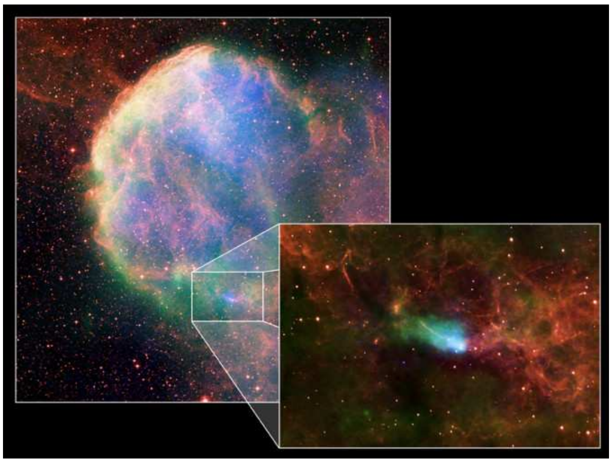

Figure 3.1: An image after a supernova explosion (IC 443). The box at the the bottom right-hand side shows the remnant, i.e. the neutron star. Credits: NASA (2006).

Neutron stars take this name due to the predominance of neutrons within them, following the mutual elimination of electrons and protons by inverse β-decay. They can be observed directly as pulsating radio sources (pulsars) and indirectly as gas-accreting, periodic X–ray sources (X–ray pulsars).

3.2 ACCRETING X–RAY PULSARS

Initially, X–ray binaries were classified depending on the nature of the optical companion (see Corbet 1986; Nagase 1989) as (a) Low Mass X-Ray Binary systems (LMXRBs) and (b) High Mass X-Ray Binary systems (HMXRBs).

The optical companion in the LMXRBs is a late low-mass star (later than type A), e.g. Her X-1 (Crampton and Hutchings 1972). In HMXRBs the optical companion could be either a massive early type supergiant (Supergiant systems (b1)) or a O,B main sequence star (BeX systems (b2)).

According to observational evidence, the Supergiant systems (b1) were also divided in two subgroups: (b1.1) systems with high luminosity and short pulse period, as Cen X-3 (Peterson 1972; Shklovsky et al. 1972), and (b1.2) systems with moderate luminosity and long pulse periods, as GX 301-2 (Pakull 1982).

The new edition of the HMXRBs catalog by Liu et al. (2006) provides information for 114 of this type objects in our galaxy. Up to now, the number of LMXRBs cataloged are 150 (Liu et al. 2001). Raguzova and Popov (2005) compiled 130 Be/X-ray systems within our galaxy, the LMC & SMC. Many of the X-ray pulsars, especially those in class (b2) are of transient nature.

3.2.1 Accretion processes

As stated before, X–ray pulsars are rotating and strongly magnetized ($B \gtrsim 10^{11}$ G) neutron stars which accrete gas from a stellar companion. As the accreting material approaches the neutron star, the plasma is channeled to the magnetic polar caps, where it releases its gravitational energy as X–ray and γ-radiation. The magnetic and spin axes are not aligned, so an observer sees variations of the X-ray flux at the rotation period (pulsations) of the hot spots move around (Bildsten et al. 1997, and references therein).

If the amount of matter falling onto the polar caps is high enough that an X-ray luminosity greater than about 10^{37} erg/s is reached, then a radiation-dominated (collisionless) shock will form at some distance above the neutron star surface, creating the accretion column. For luminosities lower than 10^{37} erg/s radiation pressure is not sufficient to stop the infalling matter, which therefore can impact directly onto the neutron star. In this case the source of X–rays is an accretion slab and emission occurs in a direction parallel to the magnetic field (pencil beam), while in the case of emission from an accretion column X–rays are emitted from the sides of the column (fan bean) because the column is optically thick to X–rays. Recently, the effect of bulk or dynamical Comptonization in the accretion column has been introduced opening new insight in the comprehension of this quite complicate issue (Orlandini 2006, and references therein)(see Fig. 3.2 for a schematic view).

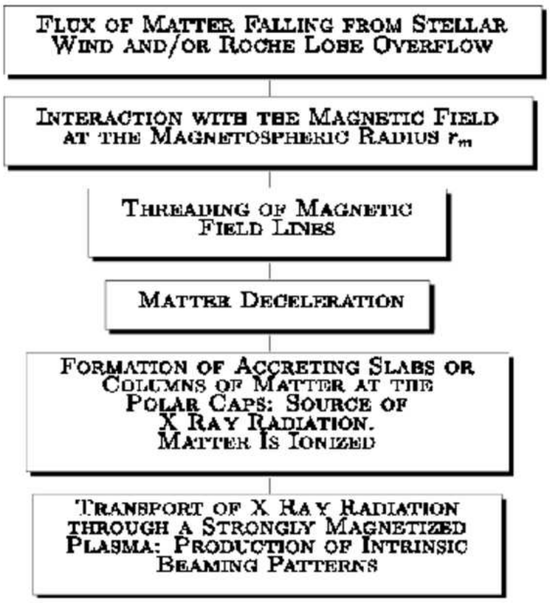

Figure 3.2: Schematic block diagram of the physical processes occurring in a X-ray binary pulsar accreting from its companion. For a detailed discussion on the physics involved in each block see Orlandini (2004). (Orlandini 2006) .

The luminosity, temporal and spectral behavior of the X-ray binary pulsars depend mainly on the mass of the optical counterpart, the accretion rate, the strength and geometry of the magnetic field and the geometry of the accretion flow from the companion.

The accretion process, i.e, the transfer of mass from the companion star to the neutron star can be due basically to three mechanisms:

• Roche Lobe overflow accretion: during the evolutionary process of the donor star, its size can change several times, achieving and exceeding the size its Roche Lobe and starting an overflow of matter to the companion (see Fig. 3.3, top panel).

• Stellar wind accretion: the strong stellar wind of the normal star is caught in the gravitational potential of the compact object. These systems are called wind-fed systems (see Fig. 3.3, middle panel).

• Equatorial mass flow, for instance, accretion from the circumstellar disk surrounding a Be star: when the neutron passes through the circumstellar stellar disk of a Be star, mass is transferred from the donor star to the compact object (see Fig. 3.3, bottom panel).

X-ray pulsars in LMXRBs and Supergiant systems with high luminosity and short pulse period are mostly powered by mass accretion via Roche-lobe overflow (so-called "disk-fed" pulsars), whereas those in BeX and Supergiant systems with moderate luminosity and long pulse periods are considered to be powered by mass accretion via stellar wind capture (so-called "wind-fed" systems Nagase 1989).

3.2.2 Elementary accretion theory

Simple accretion theory assumes that the material from the companion star is flowing onto a rotating neutron star with a strong magnetic field (B $\sim 10^{12}$ G). The accretion luminosity when the gravitational energy releases as X-ray and γ-radiation is given by

$$L_X = \frac{GM\dot{M}}{R} \tag{3.1}$$

where G is the gravitational constant, M is the mass of the neutron star, $\dot{M}$ is the mass accretion rate, and R is the radius of the neutron star when the gravitational energy releases as X-ray and γ-radiation.

The magnetic field determines the motion of material in a region of space called the magnetosphere. The size of this region is denoted by the magnetospheric radius r$_m$ (it also depends on the mass accretion rate) and is given by (Pringle and Rees 1972; Lamb et al. 1973):

$$r_m \simeq k(GM)^{-1/7}\mu^{4/7}\dot{M}^{-2/7} \tag{3.2}$$

where G is again the gravitational constant, k is a constant factor of order 1, $\dot{M} = 4\pi d^2 FR/GM$ (R is the radius of the neutron star and d is the distance to the pulsar).

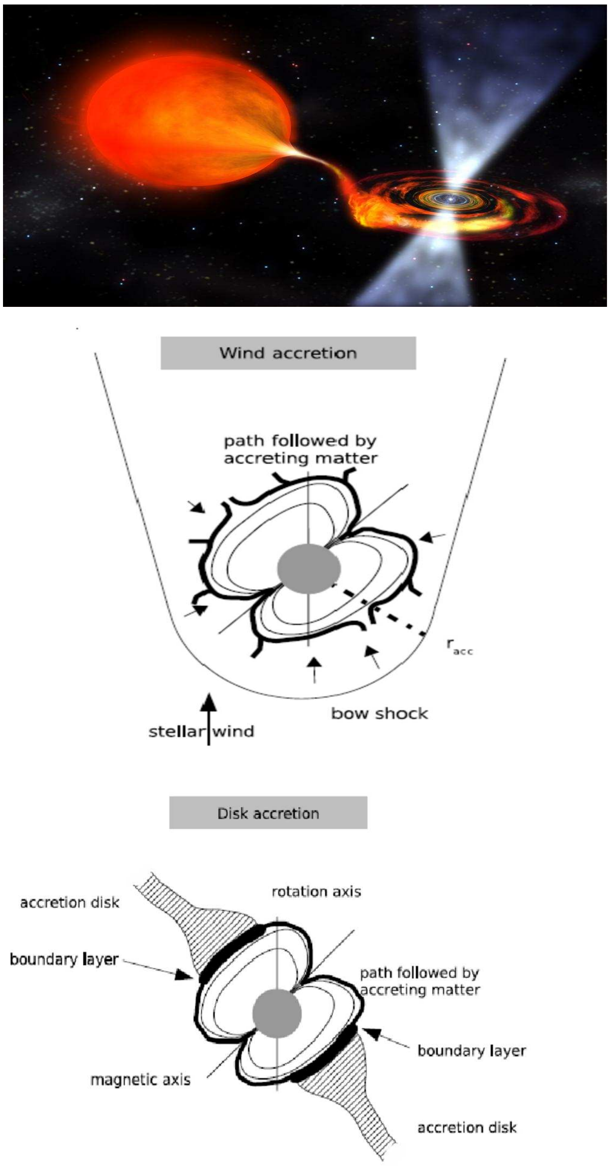

Figure 3.3: Top. Artist representation of a Roche-lobe overflow accretion mechanism in a LMXRB system. Middle. Wind accretion process representation. Bottom. Disk accretion geometry. Both pictures courtesy of Pere Blay (University of Valencia).

Equation 3.2 with $k \simeq 0.91$ gives the Alfvén radius for spherical accretion, or the distance at which the pressure exerted by infalling matter onto the magnetic field lines (called ram pressure) equals the outwards pressure exerted by the magnetic field itself. With $k \simeq 0.47$ it gives the magnetospheric radius derived by Ghosh and Lamb (1979), for a magnetic neutron star accreting from a keplerian disk.

It is important to note that we only may concentrate on conditions needed for disk formation, since up to now there is not an accurate description of how an accretion disk forms.

The magnetic field is in co-rotation with the compact object. Infalling matter at a certain distance from the compact object will also be corotating. The distance at which the pulsar corotation velocity equals the Keplerian velocity is called the co-rotation radius (r_{co})

$$r_{co} = (GM)^{1/3}(2\pi\nu)^{-2/3} \tag{3.3}$$

where ν is the spin frequency of the pulsar.

The neutron star will capture all material from the wind within a cylinder of radius r_{acc}, called the accretion cylinder. The accretion radius, r_{acc}, can be estimated as the distance when the magnitude of the gravitational potential energy of the matter balances the kinetic energy (Hoyle and Lyttleton 1939; Bondi and Hoyle 1944; Davidson and Ostriker 1973; Lamb et al. 1973; Longair 1994):

$$r_{acc} = \frac{2GM}{v_{rel}^2 + c_s^2} \tag{3.4}$$

where v_{rel} is the relative velocity of the material and c_s is the local sound speed, in the pulsar's reference frame.

Whether or not accretion occurs depends upon, the relationship between the accretion radius, r_{acc}, the magnetospheric radius, r_m, and the corotation radius, r_{co}, (Stella et al. 1986). Three regimes, direct wind accretion, centrifugal inhibition of accretion, and magnetic inhibition of accretion, will be described here (Wilson 1999):

- When $r_{acc} > r_m$ and $r_{co} > r_m$, captured wind material flows from the accretion radius onto the magnetosphere where it flows along magnetic field lines to be accreted onto the surface of the pulsar. This scenario is called direct wind accretion and may produce X-ray outbursts or persistent emission.

• If $\mathrm{r}_{co} < \mathrm{r}_m < \mathrm{r}_{acc}$, captured wind material flows from the accretion radius to the magnetosphere where it cannot penetrate. This scenario is called centrifugal inhibition of accretion. Because $\mathrm{r}_{co} < \mathrm{r}_m$, the magnetic forces accelerate the material to super-Keplerian velocities, which may eject material via the propeller effect (Illarionov and Sunyaev 1975) and cause the pulsar to spin down.

• Lastly, if $\mathrm{r}_m > \mathrm{r}_{acc}$, the stellar wind will flow around the magnetosphere and very little material will be accreted (Illarionov & Sunyaev 1975). This scenario is called magnetic inhibition of accretion and may occur in Be/X-ray binaries near apastron if the wind velocity is large compared to the orbital velocity.

Setting Equation 3.1 equal Equation 3.2 and solving for L_X gives the X-ray luminosity at which transition from accretion to centrifugal inhibition occurs ($\mathrm{r}_{co} = \mathrm{r}_m$)

$$L_X^{min} = 2^{-3/2}\mu^2(GM)^{-2/3}R^{-1}\Omega^{7/3} \tag{3.5}$$

where Ω is the pulsar's angular velocity ($2\pi\nu$). X-ray minimum luminosity values for periods of 10-100 s respectively and for typical neutron star parameters, have been obtained between $L_X^{min} \sim 10^{35}$– 10^{33}.

The torque applied by accretion of matter onto a neutron star, assuming torques due to matter leaving the system are negligible, is given by (Lamb, Pethick & Pines 1973)

$$\frac{d}{dt}(2\pi I\nu) = \dot{M}\ell \tag{3.6}$$

where I is the moment of inertia of the neutron star and ℓ is the specific angular momentum of the material. If I is assumed constant, then ℓ is given by

$$\ell = 2\pi I\dot{\nu}\dot{M}^{-1} \tag{3.7}$$

where $\dot{\nu}$ is the spin-up rate.

If only radial density gradients and a spherical wind are assumed, then the specific angular momentum of the captured material with respect to the neutron star is given by (Shapiro and Lightman 1976; Henrichs 1983)

$$l = \frac{1}{2}\Omega_{orb} r_{acc}^2 \eta \tag{3.8}$$

where Ω_{orb} is the orbital angular velocity, and $\eta = 1$ is an estimate of non-spherical accretion effects. The fraction of the captured angular momentum actually transferred to the neutron star is not well known. An accretion disk will form if the specific angular momentum of the material accreted from the Be star's disk is comparable to the Keplerian specific angular momentum at the magnetospheric radius, i.e.

$$\ell \simeq \ell_m = (GMr_m)^{1/2} \tag{3.9}$$

Combining 3.2 and 3.1, and solving for the spin-up rate yields

$$\dot{\nu} = 2^{-3/14}(2\pi I)^{-1}\mu^{2/7}(GM)^{-3/7}R^{6/7}L_X^{6/7} \tag{3.10}$$

For disk accretion, $\dot{\nu} \propto L_X^{6/7}$. For direct wind accretion $\dot{\nu} \propto L_X$ (substituting Eqs. 3.8, 3.4 and 3.1 into 3.6).

Disk formation is more likely in the case of a giant outburst when $\dot{M}$ is expected to increase and $\eta > 1$. In normal outbursts no disk is expected to form around the neutron star and accretion is directly from the disk-like outflow from the Be star, so significant spin-up is not expected because direct wind accretion is not likely to be very efficient at transferring angular momentum (Wilson et al. 2002, and references therein). However, evidence for spin-up during normal outbursts has been observed in GS 0834-430 (Wilson et al. 1997), 2S 1417-624 (Finger et al. 1996), 2S 1845-024 (Finger et al. 1999), and in EXO 2030+375 (Stollberg et al. 1999; Wilson et al. 2002, 2005).

3.3 RADIATION PROCESSES IN X–RAY BINARIES

More than 30 years after their discovery, there is not yet a satisfactory theoretical model for the spectral emission in X–ray binary pulsars which is able to explain the observed spectra. The apparent spectrum always is the superposition of several spectral components which originate in different emission regions of the binary system. In this section we will summarize the radiation emission processes in X-ray binaries (Longair 1981; Schönfelder 2001):

- Thermal emission. Hot gas can produce thermal emission in the form of a black body radiation whose maximum can be in the X-ray regime. This situation is common e.g. in very hot plasma-like shocks in hot star winds, stellar coronae, or accretion disks.

- Compton scattering. This is the interaction of photons with stationary electrons, in such a way that the high energy photon looses energy which is gained by the electron.

- Inverse Compton scattering. In this interaction interaction photon gains energy which is lost by the very energetic particle. In those environments we say that the high energy spectrum is comptonized. This is the case of the corona surrounding black holes or neutron stars in X-ray binary systems (hot plasma highly ionized, i.e., with a large amount of very energetic free electrons).

- Synchrotron radiation. Charged particles accelerate when interacting with a magnetic field. The trajectory of these particles is modified, loosing energy, which is emitted in the form of synchrotron radiation. Charged particles will follow trajectories bound to the magnetic field lines. The energy components perpendicular to the magnetic field are quantized. Thus, photons can be emitted or absorbed in frequencies corresponding to the energy difference between such levels, and Cyclotron emission or absorption can be produced.

- Bremsstrahlung. Charged particles can also interact with electrostatic fields, as is, for example, the case of an electron passing by an ionized atom. In this case the charged particle is 'braked' and the energy lost is emitted in the form of bremsstrahlung emission.

- Photoelectric Absorption. The atomic electrons are removed from their nuclei by the X-ray and γ-ray photons, thus the incident photon is absorbed by an electron whose binding energy was equals to the photon's energy.

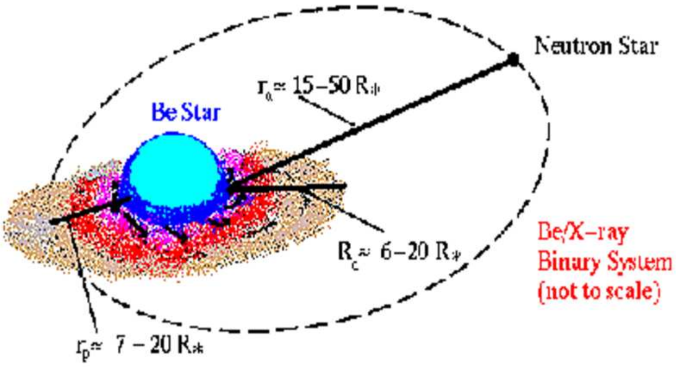

Figure 3.4: Typical Be/X–ray binary system representation, not to scale (http://www.disc.ua.es/∼ignacio/bex_research.html).

- De-excitation of Atomic Nuclei. Atomic nuclei in excited states are produced in energetic collisions in interstellar space and in the vicinity of compact objects. The de-excitation of atomic nuclei produces a photon of energy equal to the binding energy between the two nuclei atomic states, creating fluorescence lines in the photon spectrum.

3.4 Be/X–RAY BINARIES

Be stars are rapidly rotating objects with a quasi-Keplerian disk around their equator. The ultimate cause of the formation of the disk is still under heavy debate, but the high rotation velocities of these types of stars must play an important role (Townsend et al. 2004). The optical and infrared emission is dominated by the donor star and characterized by spectral lines in emission (particularly those of the Balmer series) and IR excess. Figure 3.4 shows a common Be/X–ray system representation.

The evolutionary history of Be stars in Be/X–ray systems is somewhat different to that of their isolated colleagues. Figure 3.5 shows the widely accepted evolutionary path based upon conservative mass transfer that

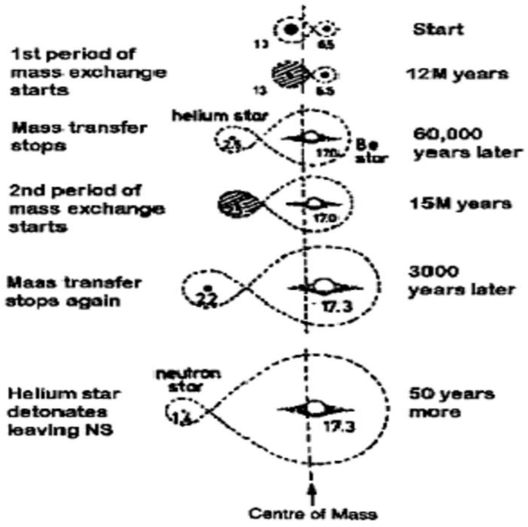

Figure 3.5: Evolution of a Be/X–ray binary system after van den Heuvel (1983) and others (Coe 2000).

has been developed by van den Heuvel (1983) and Verbunt & van den Heuvel (1995). The important consequence of the scenario is that wide binary orbits (200-600d) are produced before the final supernova explosion. Hence, any small asymmetries in that explosion will then produce the frequently observed eccentric orbits (Coe 2000).

Most Be/X–ray binaries are transient systems. Persistent BeX display much less X-ray variability and lower flux ($L_X < 10^{35}$ erg s^{-1}) and contain slowly rotating neutron stars ($P_{spin} \geq 100$ s).

The variability time scales in Be/X–ray binaries range from seconds to years. Pulse periods cover the range 3.6–1412 s. On longer time scales (months to years), the variability is also apparent in the optical and IR bands and it is attributed to structural changes of the circumstellar disk. Sometimes, the Be star loses its disk. When this occurs the H_α line shows an absorption profile and the X-ray activity ceases.

The long-term X-ray variability of the transient BeX is characterized by two type of outbursting activity (Reig 2007, and references therein):

- Type I outbursts. These are regular and (quasi)periodic outbursts, normally peaking at or close to periastron passage of the neutron star. They are short-lived, i.e., tend to cover a relatively small fraction of the orbital period (typically 0.2-0.3 P_{orb}). The X-ray flux increases by up to two orders of magnitude with respect to the pre-outburst state, reaching peak luminosities $L_X \leq 10^{37}$ erg s^{-1}.

- Type II outbursts represent major increases of the X-ray flux, 10^3 - 10^4 times that at quiescence. They reach the Eddington luminosity for a neutron star (i.e., when the gravitational attraction balances the outward radiation force on the accreting material; $L_X \sim 10^{38}$ erg s^{-1}) (Frank et al. 2002) and become the brightest objects of the X-ray sky. They do not show any preferred orbital phase and last for a large fraction of an orbital period or even for several orbital periods. The formation of an accretion disk during Type II outbursts may occur. The discovery of quasi-periodic oscillations in some systems would support this scenario. The presence of an accretion disk also helps explain the large and steady spin-up rates seen during the giant outbursts, which are difficult to account for by means of direct accretion.

We cannot conclude this summary without noting very interesting recent works on Be disk modeling. The viscous decretion disk model proposed by Lee et al. (1991) seems promising (Porter 1999). In this model, the matter supplied from the equatorial surface of the star drifts outward by viscosity and forms the disk (Okazaki and Negueruela 2001). Figure 3.6 shows very nice simulations of the Be disk-neutron star interaction by Okazaki's team. We invite to visit his web page[1] to find out more about latest developments on this topic, and to play around with their Be/X simulations.

---

[1] http://www.elsa.hokkai-s-u.ac.jp/ okazaki/index-e.html

Figure 3.6: Recent Be/X–ray binary simulations of the neutron star-Be interaction process by A. Okazaki, for a coplanar system with moderate eccentricity (Hokkai-Gakuen University, Sapporo, Japan). The interaction starts at the top left and conclude at the bottom right.

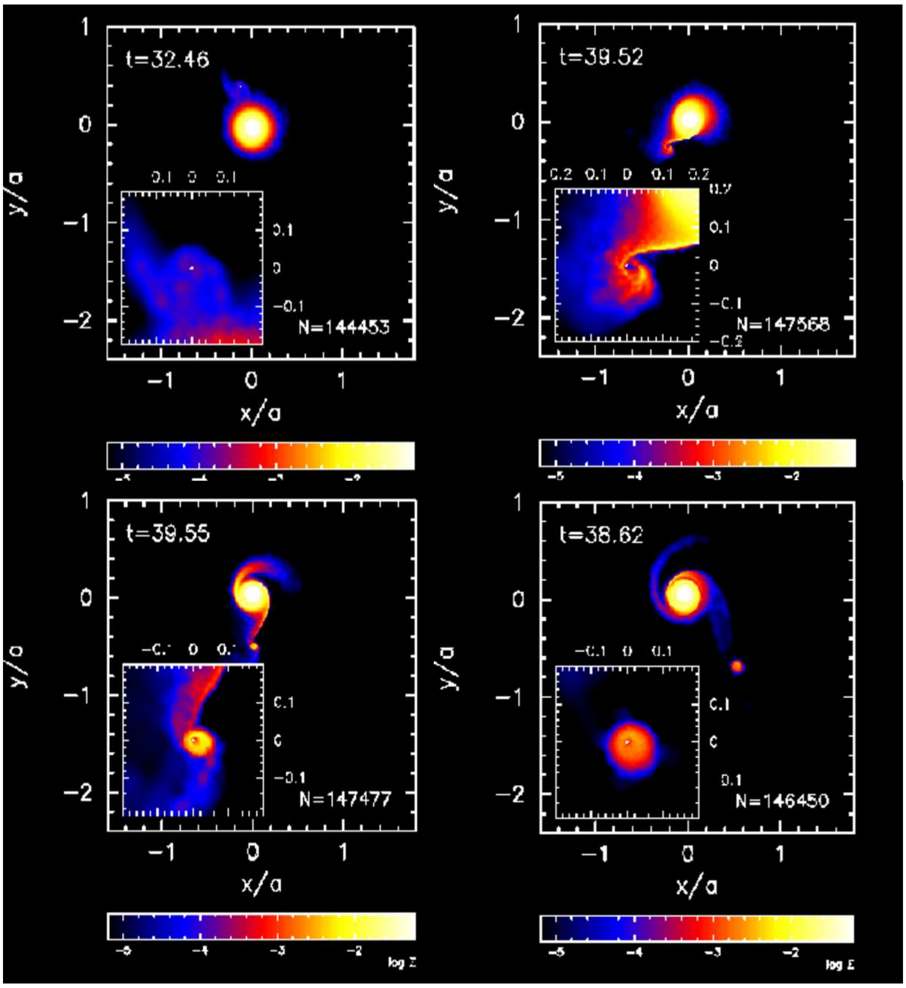

Bibliography

Bildsten, L., Chakrabarty, D., Chiu, J., Finger, M. H., Koh, D. T., Nelson, R. W., Prince, T. A., Rubin, B. C., Scott, D. M., Stollberg, M., Vaughan, B. A., Wilson, C. A., and Wilson, R. B.: 1997, *ApJS* **113**, 367

Bondi, H. and Hoyle, F.: 1944, *MNRAS* **104**, 273

Coe, M. J.: 2000, in M. A. Smith, H. F. Henrichs, and J. Fabregat (eds.), *IAU Colloq. 175: The Be Phenomenon in Early-Type Stars*, Vol. 214 of *Astronomical Society of the Pacific Conference Series*, p. 656

Corbet, R. H. D.: 1986, *MNRAS* **220**, 1047

Crampton, D. and Hutchings, J. B.: 1972, *ApJ Lett.* **178**, L65+

Davidson, K. and Ostriker, J. P.: 1973, *ApJ* **179**, 585

Finger, M. H., Bildsten, L., Chakrabarty, D., Prince, T. A., Scott, D. M., Wilson, C. A., Wilson, R. B., and Zhang, S. N.: 1999, *ApJ* **517**, 449

Finger, M. H., Wilson, R. B., and Chakrabarty, D.: 1996, *A&AS* **120**, C209+

Frank, J., King, A., and Raine, D. J.: 2002, *Accretion Power in Astrophysics: Third Edition*, Accretion Power in Astrophysics, by Juhan Frank and Andrew King and Derek Raine, pp. 398. ISBN 0521620538. Cambridge, UK: Cambridge University Press, February 2002.

Ghosh, P. and Lamb, F. K.: 1979, *ApJ* **234**, 296

Henrichs, H. F.: 1983, in W. H. G. Lewin and E. P. J. van den Heuvel (eds.), *Accretion-Driven Stellar X-ray Sources*, pp 393–429

Hoyle, F. and Lyttleton, R. A.: 1939, in *Proceedings of the Cambridge Philisophical Society*, Vol. 34 of *Proceedings of the Cambridge Philisophical Society*, p. 405

Illarionov, A. F. and Sunyaev, R. A.: 1975, *A&A* **39**, 185

Lamb, F. K., Pethick, C. J., and Pines, D.: 1973, *ApJ* **184**, 271

Lee, U., Osaki, Y., and Saio, H.: 1991, *MNRAS* **250**, 432

Liu, Q. Z., van Paradijs, J., and van den Heuvel, E. P. J.: 2001, *VizieR Online Data Catalog* **5106**, 0

Liu, Q. Z., van Paradijs, J., and van den Heuvel, E. P. J.: 2006, *A&A* **455**, 1165

Longair, M. S.: 1981, in R. Giacconi (ed.), *Astrophysics and Space Science Library*, Vol. 87 of *Astrophysics and Space Science Library*, pp 241–259

Longair, M. S.: 1994, *High energy astrophysics. Vol.2: Stars, the galaxy and the interstellar medium*, Cambridge: Cambridge University Press, —c1994, 2nd ed.

Nagase, F.: 1989, *PASJ* **41**, 1

Okazaki, A. T. and Negueruela, I.: 2001, *X-ray Astronomy: Stellar Endpoints, AGN, and the Diffuse X-ray Background* **599**, 810

Orlandini, M.: 2006, *Advances in Space Research* **38**, 2742

Pakull, M.: 1982, in W. Brinkmann and J. Truemper (eds.), *Accreting Neutron Stars*, pp 53–56

Peterson, B. A.: 1972, *Nat* **237**, 508

Porter, J. M.: 1999, *A&A* **348**, 512

Pringle, J. E. and Rees, M. J.: 1972, *A&A* **21**, 1

Raguzova, N. V. and Popov, S. B.: 2005, *Astronomical and Astrophysical Transactions* **24**, 151

Reig, P.: 2007, *MNRAS* **377**, 867

Schönfelder, V.: 2001, *The Universe in Gamma Rays*, The Universe in Gamma Rays

Shapiro, S. L. and Lightman, A. P.: 1976, *ApJ* **204**, 555

Shapiro, S. L. and Teukolsky, S. A.: 1983, *Black Holes, White Dwarfs, and Neutron Stars. The physics of compact objects. Ed: John Wiley and Sons. Cornell University, Ithaca, New York.*

Shklovsky, J. S., Cherepashchuk, A. M., and Efremov, Y. N.: 1972, *Nat* **236**, 448

Stella, L., White, N. E., and Rosner, R.: 1986, *ApJ* **308**, 669

Stollberg, M. T., Finger, M. H., Wilson, R. B., Scott, D. M., Crary, D. J., and Paciesas, W. S.: 1999, *ApJ* **512**, 313

Townsend, R. H. D., Owocki, S. P., and Howarth, I. D.: 2004, *MNRAS* **350**, 189

Wilson, C. A.: 1999, *PhD thesis University of Alabama in Hunstville*

Wilson, C. A., Fabregat, J., and Coburn, W.: 2005, *ApJ Lett.* **620**, L99

Wilson, C. A., Finger, M. H., Coe, M. J., Laycock, S., and Fabregat, J.: 2002, *ApJ* **570**, 287

Wilson, C. A., Finger, M. H., Harmon, B. A., Scott, D. M., Wilson, R. B., Bildsten, L., Chakrabarty, D., and Prince, T. A.: 1997, *ApJ* **479**, 388

Chapter 4

ANALYSIS TECHNIQUES

To achieve our goals it was necessary to apply a series of reduction tools and specific software to the *INTEGRAL* and *RXTE* data, developed by different teams. In this Chapter we will expose the techniques we will use throughout this work.

4.1 *INTEGRAL* SCIENTIFIC DATA ANALYSIS

The INTEGRAL data are received at the rate of 120 kbits/s at a ground station. The technical and scientific data are then sent in real time to the **I**ntegral **S**cience **D**ata **C**enter (ISDC) which is located in Versoix near Geneva. The data arrive at the ISDC with a delay of typically few seconds.

The INTEGRAL data are divided in a (often large) number of data sets, each associated with a single pointing or slew. Single pointings and slews are called science windows. They are the most important unit in the data processing and analysis, and are processed at the ISDC (Courvoisier et al. 2003).

To perform analysis interactively it has been created a set of programs called the **O**ffline **S**cience **A**nalysis (OSA) distributed to the community by the ISDC [1]. High level products like deconvolved images, light curves and spectra are derived by the users for each instrument, using a **G**raphical **U**ser **I**nterface (GUI).

The ISDC identifies a set of tasks/levels common to all the instruments and designates them with unique labels. In Table 4.1 the different **Analysis Levels** are listed. A detailed information about data repository and analysis can be found in each instrument data analysis manual or at *Introduction to the INTEGRAL Data Analysis* (Chernyakova 2005).

Table 4.1: Overview of the Analysis levels.

Level	Description
COR IBIS, SPI, JEM-X, OMC	Corrects science data for instrumental effects.
POIN SPI	Defines a number of time periods with constant spacecraft attitude.
GTI IBIS, SPI, JEM-X, OMC	Generates, selects, and merges Good Time Intervals to produce a single table.
DEAD IBIS,SPI, JEM-X	Computes dead time, i.e., the time during which the instrument was not capable to register the incoming photons.
BIN_I IBIS, SPI, JEM-X	Defines the energy bins to be used for imaging, selects good events within the GTI, and creates event arrays.
BKG, BKG_I, BKG_S IBIS, SPI, JEM-X	Background Model Generation and Correction.
CAT, CAT_I, CAT_S IBIS, SPI, JEM-X	Selects a list of known sources from the ISDC reference catalog.
IMA IBIS, SPI, JEM-X, OMC	Generates sky images and searches for significant sources.
IMA2 JEM-X	The mosaic image of JEM-X observations along with the summary list of all found sources are created.
BIN_S IBIS, SPI, JEM-X	Defines the energy bins to be used for spectral analysis, selects good events within the GTI, and creates detector spectra.
SPE IBIS, JEM-X	Extracts spectra for individual sources, and produces the specific response files.
BIN_T JEM-X	Defines the energy bins to be used for light curves analysis.
LCR BIS,JEM-X	Extracts light curves for individual sources.

---

[1] http://isdc.unige.ch

This software has been continuously improved since the *INTEGRAL* launch. However, it is to be noted that there are still some restrictions which will explained in the next sections.

4.1.1 Software limitations

ISGRI software limitations: In the image reconstruction, secondary lobes of strong very-of-axis sources are sometimes not fully corrected/cleaned in reconstructed images. Addition of many spectra of a weak source obtained for the different science windows with `ii_spectra_extract` (standard ISGRI spectral extraction package) may give a bad total spectrum, because spectral reconstruction is very sensitive to the background correction. In certain cases, running the imaging procedure on several (large) energy bands can provide a better spectrum. It must also be noted that bellow 20 keV the spectrum is not properly corrected.

SPI software limitations: The background subtraction is one of the critical points on the SPI analysis. In the analysis done in this work, we have used `spiros` software with a **M**ean **C**ount **M**odulation (MCM) background handling. This method assumes that for each source the background is the sum of the contribution to the shadowgram of the other sources in the field of view plus the induced background from the cosmic rays. This method works iteratively modeling the background for each source as a function of energy and time.

Another unexpected problem showed up when the SPI detectors 2 and 17 failure. The background modulation pattern changed again according to 3 periods: when no detector was dead, one was dead, and 2 were dead. To solve this problem 2 steps were taken: (a) `spiros` was run separately in each interval to obtain the different background pattern per detector. (b) A new global **I**nstrument **R**esponse **F**unction (IRF) was built from the individual IRFs of each period, taking into account the overall background modulation pattern. After these corrections `spiros` can be rerun in the long data set as usual.

JEMX software limitations: Vignetting modeling still needs further development. Sources at the edge of the field of view must be treated very carefully, since the systematics introduced by the incomplete vignetting correction can be of the order of 30%.

4.2 *RXTE* SCIENTIFIC DATA ANALYSIS

All science operations are performed in the RXTE **S**cience **O**perations **C**enter (SOC), located at Goddard Space Flight Center. It comprises the **S**cience **O**perations **F**acility (SOF), which runs the satellite observatory and the **G**uest **O**bserver **F**acility (GOF) which provides scientific services to astronomers who use RXTE. Before sending the data to Guest Observers, the RXTE data processing pipeline converts the data to FITS format, arranges the FITS files into a hierarchical set of directories, and performs a set of standard calibrations.

RXTE data reduction involves: (1) Navigate into the directory structure with the GUI-driven program XDF (XTE Data Finder) to identify the files which contain the data you want to reduce; (2) Manipulate these FITS files by a set of tasks, called "**F**ITS file manipulation **tools**" (Ftools). The Ftools may also be used to produce a filter file that contains the time-histories of various parameters, in reference to which good data can be identified and screened.

Using a filter file for the observation, one can produce a list of good time intervals based on various selection criteria. At this stage, one can also specify filters to single out parts of the good data. The final step is to apply the good time intervals and extract data products (light curves or spectra) through the filters. These products can be read into the appropriate data analysis programs (e.g. `xronos`, `xspec` or any others equipped to handle the formats).

The PCA WWW page[2] collects links to published and unpublished material relevant to the calibration and operation of the PCA. For further HEXTE-specific information we can refer to the HEXTE Calibration News WWW page (at UCSD)[3]. HEASARC software (HEAsoft)[4] has been widely adopted as a standard for high energy data manipulation.

---

[2] http://astrophysics.gsfc.nasa.gov/xrays/programs/rxte/pca

[3] http://mamacass.ucsd.edu/hexte/hexte_calib.html

[4] http://heasarc.gsfc.nasa.gov/

4.3 ANALYSIS TOOLS

4.3.1 IMAGING

An important achievement with *INTEGRAL* mission is the possibility to combine high accuracy in imaging and spectroscopy at the same time. Imaging with ISGRI and JEM-X will allow us to determine with high precision the coordinates of high energy sources. The source location accuracy will depend on the signal to noise ratio. ISGRI can locate a source detected with a signal to noise ratio of 20 with a <1 arcmin error (Gros et al. 2003).

On the other hand, for ISGRI the OSA5.1 pipeline has no option for a right background correction implemented yet (only available in OSA6.0). To correct this issue, we have used preliminary software by P. Connell (University of Valencia). The output maps from this procedure are derived from mosaic maps output from OSA5.1 coded mask image reconstruction software. These reconstruction methods used are those of mask-detector correlation or back projection, which introduce an implicit non statistical background component into the maps (Goldwurm et al. 2003).

This background was removed by scanning the maps and fitting a local B-spline (a truncated gaussian) source of 12' FWHM, plus a flat background component covering a radius of 30'. The output of this fitting procedure was a source flux map and its (robust) variance map. In this kind of map the residue is not background, but statistical noise (mean = -0.2, standard deviation = 1.1), and the map can then be searched for new sources above some sigma significance level (usually 5 sigma).

Although SPI is not expected to perform very accurate imaging specially for point sources, we discovered that the imaging capabilities of this spectrometer were sometimes complementary, since it has the largest field of view. From the analysis of many SPI images it is found that the source identification sigma threshold is about 5 sigma rather than the usual value of 3.0 expected. This is due to systematic errors inherent in an imager having a coded-mask with only 127 elements, combined with long sequences of exposures (required to obtain any sort of significant image) and variations in an uncertain background rate which can find their way into the image. SPI is not an imager with a large complicated mask pattern like ISGRI but a spectrometer with an imaging capability and ∼3.0° FWHM resolution.

JEM–X can locate a bright source with an error of the order of ∼30 arcsec (for a 10σ source, see Lund et al. (2003)). Apart from the source location, imaging will provide count rates integrated over the typical *INTEGRAL* pointing time scales (i.e. of the order of 2 ks). Furthermore, the possibility of computing mosaics can increase the instruments sensitivities allowing us to detect very weak sources.

The imaging software (`j_ima_iros`) reconstructs the sky image by back projection of the shadowgram. j ima iros includes an IROS loop (**I**terative **R**emoval **O**f **S**ources) where a model shadowgram corresponding to each identified source is constructed and a fit to the original shadogram is made with all the source model shadowgrams plus two background model shadowgrams. In this way a large part of the systematic features associated with the strong sources are removed and a repeated backprojection will have increased sensitivity for weak sources. The JEM-X imaging software considers that a source is reliable in a given science window if it is detected in two cases: (1) when the source is detected in several energy bands regardless its strength, and (2) when the source is detected in a single energy band with a strength exceeding a given limit (we consider a reasonable limit 7)[5].

To obtain a list of detected sources from the JEM–X mosaicking images, we have used a new tool called `j_ima_src_locator` developed by the JEM-X team. The tool is still under validation and therefore these results are preliminary. The sigma values reported are obtained from the Gaussian fit performed by the source finding software around the source position (3×3 pixels) to determinate the source position, flux and peak size of the detection. (JEM-X team, priv. commun.).

Another limitation of the ISGRI standard software is that it is highly unstable. The more pointing observations you have, the more trouble you will find in finishing the reduction process. This has been a great obstacle to achieving our goals.

---

[5] http://isdc.unige.ch/doc/rep/sci_val/JEM-X/jemx_svr_5_0.pdf

To increase our success in the search process another package was used, the source extractor package (SExtractor v2.4.4), which determines the background and whether pixels belong to background or objects. Then it splits up the area that does not belong to the background into separate objects and determines the properties of each object, writing all the pixel positions. Finally, we translated the source pixels coordinates to the World Coordinate System by using `xy2sky` tool from the WCStools package.

SExtractor[6] estimates the background of the image as well as the RMS noise in that background, mapping both. Then this software subtracts the estimated background from the photometry and uses the RMS to estimate errors. In an given area, the mean and the standard deviation of the distribution of pixel values are computed. After a rejecting process of the most deviant values, the remaining pixel values are within a mean $\pm 3\sigma$. The value for the background in the area is (a) the mean in a non-crowed case, or (b) 2.5×median - 1.5×mean (crowded case), both values computed in the last iteration. The background map is a bi-cubic-spline interpolation over all the area's of a given size (see SExtractor manual[7] for more details).

In addition, Segreto and Ferrigno[8] have developed a method to analyze ISGRI data in a more straightforward way than it is done by the standard pipeline. Up to now, this software was focused only on spectral and timing analysis. However, in this work we have used preliminary imaging ISGRI software recently developed by Alberto Segreto, still under validation. Therefore, the OSA5.1 analysis will be complemented by the use of this software, with the results still preliminary.

4.3.2 SPECTRAL ANALYSIS

RXTE spectral extraction

In order to perform the *RXTE* PCA spectral extraction of Standard 2 data, we generally followed the standard recipe from the cookbook[9].

---

[6] http://terapix.iap.fr/soft/sextractor/

[7] http://terapix.iap.fr/soft/sextractor/

[8] http://www.pa.iasf.cnr.it/ferrigno/INTEGRALsoftware.html

[9] http://heasarc.gsfc.nasa.gov/docs/xte/abc/extracting.html

We first found the good PCU combinations per observation (using the corresponding filter files created with `xtefilt`). The good time intervals were then created with `maketime` and also files with different layers combinations. We took the top layer, because it is the best choice for background purposes. The background was obtained , applying either faint or bright background model when it was necessary, using `pcabackest`. We finally extracted background and source spectra with `saextract`. The response files were produced with the `pcarsp` tool.

HEXTE spectra were obtained after a series of steps following the *RXTE* cookbook recipe. We separated background from source in raw fits data with `hxtback`. After this, it is important to check how many background and/or source files were missing. Background and source spectra were finally created with `seextrct`.

Spectral fit

The most widely used software package for spectral analysis of high energy sources is `xspec`, provided by HEASARC. This package does not only allow to display and visually inspect our spectra, but it lets the user fit a great variety of models to the data. One of the most powerful aspects of `xspec` is the possibility to introduce the users' own models to fit the data. Therefore, we will use `xspec` for fitting the *INTEGRAL* and *RXTE* spectra.

Broad-band spectra of accreting X–ray binary pulsars can be fitted by a composition of phenomenological models, e.g. a power law with a high energy rolloff above 10 keV, plus a blackbody component with a temperature of few hundred eV. Qualitatively, the hard tail may be explained in terms of (inverse) Compton scattering, but the origin of the soft component cannot find a unique explanation. Recently, the effect of bulk Comptonization in the accretion column has been studied. After a review of these recent theoretical developments, it was found that different modeling of the continuum may affect broad features (Orlandini 2006, and references therein).

In the present work we have chosen different phenomenological models to obtain an acceptable fit to the spectral continuum. They will not give us information about the physical processes operating on them, but they will give us important information about the source variability (e.g. changes in the slope of the continuum). We will describe schematically the following models, since a very detailed description is out of the scope of this work:

- phabs(gaussian+powerlow) highecut
- phabs (gaussian+cutoffpl)
- phabs (gaussian+powerlaw) highecut*gabs

Compton scattering from free electrons may alter the observable spectrum. A simple photon power law model takes the form:

$\mathrm{F(E)} = \mathrm{KE}^{\Gamma}$

where F(E) is the flux at a given energy, E, measured in photons cm^{-2} keV^{-1}, K is a normalization factor, and Γ is called the photon index that will give us information about the slope of the continuum.

When the slope of the continuum changes at certain energy (called the cut-off energy), the power law model is then modified and the model will be:

$\mathrm{F(E)} = \mathrm{KE}^{\Gamma} e^{((E_{cut}-E)/E_{fold})}$ for E $> E_{cut}$
$\mathrm{F(E)} = \mathrm{KE}^{\Gamma}$ for E $< E_{cut}$

where F(E), K, and Γ stand as above, E_{cut} is the energy at which the cut-off is produced, and E_{fold} is the factor which quantifies changes on the slope (called the folding energy).

Sometimes, another phenomenological model can give us a better fit. When a cutoffpl model is used, the power model is modified with the following high energy exponential rolloff:

$\mathrm{A(E)} = \mathrm{K(E/1keV)}^{-\Gamma}\ e^{(-E/E_{fold})}$

To account for photoelectric absorption by cold or partially ionized material, as present in the outer and cooler parts of the accretion disk, we can multiply by the phabs model:

$\mathrm{N(E)} = e^{-n_H \sigma(E)}$

where n_H is the equivalent hydrogen column (in units of $10^{22} atoms/cm^2$).

If a fluorescent line is emitted then a simple gaussian line profile can be added:

$C(E) = K(1./\sigma\sqrt{2\pi})e^{-0.5((E-E_{line})/\sigma)^2}$

where the σ is the width in keV, and E_{line} is the line energy in keV, and K is the normalization factor or the total $photons/cm^2/s$ in the line.

Cyclotron resonant scattering in the present of a strong magnetic field can be reproduced by the multiplicative gabs model:

$M(E) = e^{(-(\tau/(\sqrt{2\pi}\sigma))e(-0.5((E-E_{line})/\sigma)^2))}$

where the E_{line} is the line energy in keV, σ is the line width in keV, and τ is called the optical depth parameter.

The thermal blackbody radiation from an accretion disk is approximated by multiple blackbody components (diskbb model) (Mitsuda et al. 1984; Makishima et al. 1986), where the main parameter kT_{BB} is the temperature at inner disk radius (keV). The compTT model describes the comptonization of soft X–ray photons in a hot plasma including relativistic effects. It was developed by Titarchuk (1994). In order to allow us some comparison we have combined the diskbb+pow and diskbb+compTT additive models for the study of some of our sources.

4.3.3 TIMING ANALYSIS

To investigate the presence of variability a preliminary visual inspection of the light curves will give us hints about the kind of variability expected. However, in some cases the noise in the data will hide variability from visual inspection.

We will first introduce the standard process for extracting *RXTE* light curves, and then we will explain the specific and non-standard software, in order to confirm any variability. In Section 4.3.3 we will focus on the ISGRI timing analysis procedure.

For the study of pulse profile dependence on luminosity, time or orbital phase we extracted *RXTE* PCA Standard1 light curves in a certain energy range (e.g. 2–60 keV). Again, we followed the standard recipe and extracted light curves with `saextrct`. The rates were corrected so they are normalized for 1 average PCU with `correctlc`, and the lightcurves were barycentered using `faxbary`. The background was not subtracted in this first step.

For the energy dependence analysis we proceeded to extract science event data. Science event files contain irregularly spaced time-stamped event which, in the case of the PCA, are interspersed at regular time intervals with various flags (also known as clock events). This means that extracting light curves from an event file involves removing the clock events, and, if desired, picking a subset of the valid events, e.g. data from PCU 0 only. In practice, this entails defining a bitmask: a binary string (or set of strings) which the event words in the file must match in order pass through extraction.

The ftool to create bitmask-filtered light curves `seextrct` applies but does not define bitmask selections, so another program must be run before the extraction. This caveat applies to (a) all PCA and HEXTE data if you want to apply a particular bitmask (e.g. to pick out events from a single PCU or HEXTE detector) and (b) all PCA event mode configurations except Good Xenon regardless of whether you want to apply a particular bitmask.

Therefore, by using `fselect` we created single bitmask-filtered event files and with `seextrct` we extracted the light curves. In this step background light curves were obtained using again `pcabakest`. The source light curves were barycentered with `faxbary`, and background subtracted for this energy study.

Making *RXTE* pulse profiles

After obtaining the corresponding light curves using the standard software for each instrument, a visual inspection was crucial to eliminate bad data that could interfere with later results. Then, we corrected the times for the orbital motion using the binary orbital parameters by previous works (e.g. Baykal et al. (2002) for the Be/X–ray binary system SAX J2103.5+4545).

We constructed pulse profiles by fitting the data with a harmonic expansion in pulse phase (6 or 12 harmonics were usually used)

$$m(t_j) = a_0 + \sum_{h=1}^{N}(a_h cos2\pi h\phi(t_j) + b_h sin2\pi h\phi(t_j)) \tag{4.1}$$

where $m(t_j)$ is the model count rate, h is the harmonic number of the N selected, and $\phi(t_j)$ is the phase model.

Typically we use data within a 4000 s interval segment. This segment duration was chosen because it contains several pulse periods and yet is short enough that a quadratic model provides a good fit to the detector background. Initially we used a simple phase model

$$\phi(t_j) = \phi_o + (f_o \times (t_j - t_o)) \tag{4.2}$$

where f_o is the pulse frequency at time t_o and ϕ_o is the phase at time t_o. The pulse frequency $f(t_j)$ is the first derivative of the phase model, i.e., $f(t_j) = f_o$, which is a constant frequency. This is a very simple model and our goal is to determine it as accurately as possible. As a reminder, a pulse phase model would take the following form when it is represented by a quadratic expansion

$$\phi(t_j) = \phi_o + (f \times (t_j - t_o)) + \frac{1}{2}(\dot{f} \times (t_j - t_o)^2) \tag{4.3}$$

To obtain the harmonic coefficients a_h and b_h from Eq. 4.1, we performed a fit to the short stretch of data by minimizing

$$\chi^2(a_h, b_h) = \sum_{j=1}^{W} \frac{(c(t_j) - m(t_j))^2}{\sigma^2_{c_j}} \tag{4.4}$$

where $c(t_j)$ and $\sigma^2_{c_j}$ are the measured count rates and errors, and W is the number of data points. At its minimum, derivatives of $\chi^2(a_h, b_h)$ with respect to a_h and b_h vanish

$$0 = \frac{\partial \chi^2}{\partial a_h} \qquad and \qquad 0 = \frac{\partial \chi^2}{\partial b_h} \tag{4.5}$$

After all this process, we will obtain the harmonic coefficients a_h and b_h by solving a 2h×2h dimension matrix.

The errors were corrected for the non-Poisson noise found in the power spectra (Wilson et al. 2002). This is due to the fact that errors on the Fourier coefficients are rarely Poisson, since many pulsars have additional aperiodic noise.

Next section will show how a more precise quadratic-spline phase model is created, which will be used to make again the profiles. This process will be used as well for obtaining changes in the pulse frequency within a given period, and in some cases, an improved orbit solution.

Phasing

The initial profiles were grouped into few day intervals (4 or 5 days), or periods determined by the orbital period of the system (e.g. 12.69 d for SAX J2103.5+4545). We will call "boxes" to those intervals in which we are keeping our fitted profiles. For SAX J2103.5+4545 in each 12.69 days box we have approximately 274 profiles, each one made of 4000 s segment of data.

Then we obtained the most significant average pulse profile per box after a series of steps. First, we estimated an average phase offset $\delta\phi_{\mathrm{k}}$ which will be applied to the profile number k (fitted in the k-th 4000s segment within the ∼12 days box). For each frequency offset $(\delta f_p, \dot{f}_q)$ we then computed the mean phase offset in segment k,

$$\delta\phi_{\mathrm{k}}(\delta f_p, \dot{f}_q) = \delta f_p \times (\bar{\mathrm{t}}_{\mathrm{k}} - \tau) + \frac{1}{2}\dot{f}_q \times (\bar{\mathrm{t}}_{\mathrm{k}} - \tau)^2 \tag{4.6}$$

where $\bar{t}_k$ is the time at the midpoint of the segment k, τ is an epoch near the center of our box time interval (by definition at the epoch τ, $\delta\phi_{\mathrm{k}}=0$), and δf_p is the offset in pulse frequency from f_0. It is easier to search only in pulse frequency at first, and then add a search in frequency derivatives $(\dot{f}_q)$ to refine measurements.

The shifted k profile may be written for only the harmonic number h this way (we are using now complex numbers to simplify the notation)

$$\alpha_{kh}(\delta f_p, \dot{f}_q) = (a_{kh} - ib_{kh})exp(-i2\pi h\delta\phi_k(\delta f_p, \dot{f}_q)) \tag{4.7}$$

Then we computed each of the new harmonic coefficients of the best-fit average pulse profile per box, at each grid point, by minimizing (Finger et al. 1999)

$$\chi^2(\mu_h) = \sum_{h=1}^{N} J_h(\mu_h) \tag{4.8}$$

with

$$J_h(\mu_h) = \sum_{k=1}^{M} \frac{(\alpha_{kh} - \mu_h)^2}{\sigma_{kh}^2} \tag{4.9}$$

where σ_{kh} are the Poisson errors on α_{kh} , μ_h are the harmonic complex coefficients for the mean profile and M is the number of profiles in a box.

Then we repeated the process for other frequency offsets. Initially, the frequency offset can be estimated from past measurements, or select a trial range of $\sim \pm 0.01 f_0$. A initial value for the frequency derivative ($\dot{f}_q$) may be estimated from accretion theory (see Eq. 3.10, Chap. 3, Sec. 3.2.2).

Using the Y_n statistic (Finger et al. 1999), which is derived from the Z_n^2 statistic (Buccheri et al. 1983), we attained the most significant frequency offset per box. This was done, since the Z_n^2 statistic may be expressed as

$$Z_n^2 = \sum_{h=1}^{N} \frac{|\widehat{\mu}_h|^2}{\sigma_{\mu_h}^2} \tag{4.10}$$

where $\widehat{\mu}_h$ is the estimate that optimizes the Fourier coefficient for harmonic h from all the profiles in a box (i.e., the best fit Fourier coefficient for harmonic h found after Eq. 4.8), and σ_{μ_h} is the Poisson error on $\widehat{\mu}_h$.

We accounted for aperiodic noise as in Finger et al. (1999). If not aperiodic noise is present the reduced χ^2 of the fit of Eq. 4.9 for each harmonic (given by $J_h(\widehat{\mu}_h)/2M - 2$) would be equal to unity. When such a noise is present that reduced $\chi^2 > 1$. By multiplying the statistical variance $\sigma_{\mu_h}^2$ by this reduced χ^2 in Eq. 4.10 we accounted for this noise.

Before using the frequency search results for further analysis, any non-detections (extremely large or small values) must be removed. The good measured frequencies were then fitted with a piecewise-linear model (or spline model), and new profiles were obtained using the integral of the fitted frequency model as a phase model.

If this new phase model was good enough then all the profiles should be phase aligned. To check this out we created a scaled and shifted template profile in which we compared the K individual profiles. This template is represented by a complex Fourier coefficient T_h and an estimate pulse intensity A_K. We then estimated the offsets in pulse phase ($\Delta\phi_K$) and the intensity A_K from our template model by minimizing

$$\chi^2_K(\Delta\phi_K, A_K) = \sum_{h=1}^{N} \frac{|\omega_{Kh} - A_K T_h exp(-i2\pi h\Delta\phi_K)|^2}{\sigma^2_{Kh}} \tag{4.11}$$

where $\omega_{Kh} = a_{Kh} - b_{Kh}$ is the complex Fourier coefficient for harmonic h and profile K, and σ_{Kh} is the error on its real or imaginary component.

Then the resulting phase offsets were examined, and since they were not consistent with a constant value, we tried a global fit using a new polynomial spline model (composed of the initial improved spline phase model plus the previously computed offset).

The PCA spin rates were computed by fitting a quadratic function to the phases, which were divided in a certain number of time intervals depending on the amount of available initial observations.

If variations of the offsets are found to be modulating with the orbital period, then we can try to improve the pulsar orbit. The pulsar emission time t_j^{em} is related to the barycenter corrected observation time t_j by (Deeter et al. 1981)

$$t = t^{em} + a_x sini[sin\omega(cosE - e) + \sqrt{1-e^2}cos\omega sinE]/c \tag{4.12}$$

where the eccentric anomaly E is related to time through Kepler's equation (Roy 1988),

$$E - esinE = \frac{2\pi}{P_{orbit}} \times (t^{em} - \tau_{periastron}) \tag{4.13}$$

with the orbit's projected semimajor axis $a_x sini$, argument of periastron ω, eccentricity e, orbital period P$_{orb}$, and periastron epoch $\tau_{periastron}$ all being adjusted in the fit performed by minimizing

$$\chi^2(\phi_{model}) = \sum_{k=1}^{M} \frac{(\phi(t_j^{em}) - \phi_{model}(t_j^{em}))^2}{\sigma^2_{\phi_j}} \tag{4.14}$$

where $\phi(t_j^{em})$ and $\sigma^2_{\phi_j}$ are the total measured pulse phase and the error on that phase, and $\phi_{model}(t_j^{em})$ is the best phase model we can finally determine. All the process was then repeated. Figure 4.1 displays a diagram representing the complete timing process.

INTEGRAL **ISGRI timing analysis**

For the *INTEGRAL* IBIS/ISGRI data the approach was different, due to the non continuous observational pattern and the sensitivity of the ISGRI detector. For each science window, our software selected good events in the 20–60 keV band using the **P**ixel **I**nformation **F**unction (PIF). The events were then epoch folded using initially a simple pulse phase model based on spin-frequency measurements from *RXTE.*

To remove effects of binning, we then fit each folded profile with a Fourier series of harmonic coefficients. A template profile was then created from the average profile obtained for each science window. For each harmonic coefficient, we computed a reduced χ^2

$$\frac{\chi^2_h}{\text{d.o.f}} = \sum_{i=1}^{N} \frac{1}{(2N-2)} \left\{ \frac{(a_{ih} - \bar{a}_h)^2}{\sigma^2_{a_{ih}}} + \frac{(b_{ih} - \bar{b}_h)^2}{\sigma^2_{b_{ih}}} \right\} \tag{4.15}$$

where a_{ih} and b_{ih} are the cosine and sine coefficients for science window i and harmonic h, $\sigma_{a_{ih}}$ and $\sigma_{b_{ih}}$ are the errors on those coefficients, $\bar{a}_h$ and $\bar{b}_h$ are the cosine and sine coefficients for the mean profile, and N is the number of science windows.

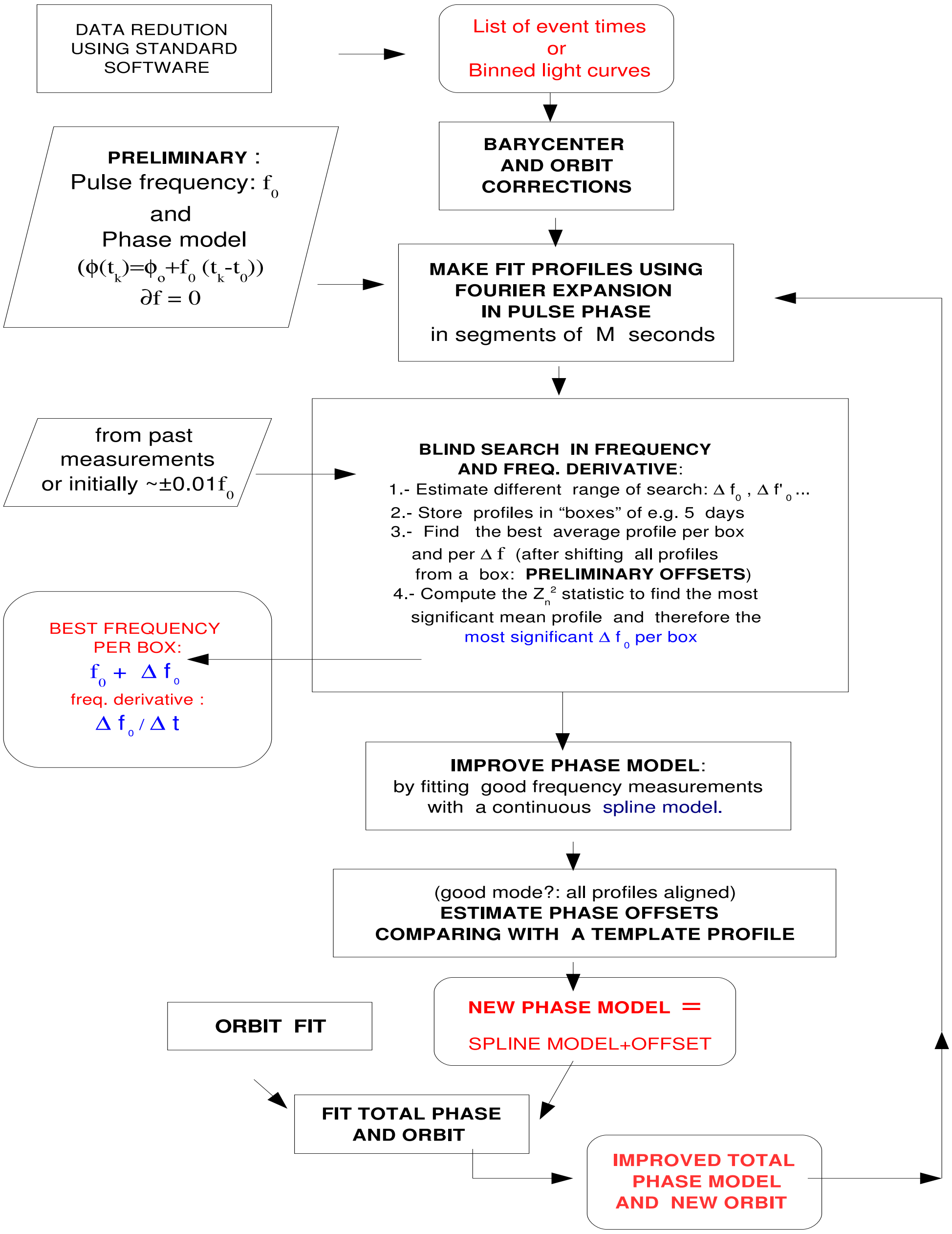

Figure 4.1: Schematic chronological view of the timing process.

To account for excess aperiodic noise from Cygnus X-1, since it cannot be completely removed from the data, the errors on the harmonic coefficients for the individual science windows were multiplied by $(\chi_h^2/\mathrm{d.o.f})^{1/2}$. A similar technique was also applied to account for excess aperiodic noise in BATSE data (Wilson et al. (2002), Finger et al. (1999)).

To generate phase offsets from the model, we then cross-correlated the individual *INTEGRAL* ISGRI and *RXTE* PCA profiles with the corresponding template profiles. The new phases (model + offset) were then fitted with a linear or quadratic phase model, and the process was repeated, creating new folded profiles, new harmonic coefficients, and new phase offsets. The pulse profiles were then combined over time using the phase model to improve statistics and allow the phase measurements to constrain spin-up during outburst.

For ISGRI the spin rates were computed by differencing adjacent frequency measurements and dividing by the corresponding time difference.

Orbit fitting

Errors in the orbital parameters caused by coupling between the intrinsic spin variations of the pulsar with orbital effects, can scatter the detected pulse frequencies. To take into account the phase noise caused for pulse profiles variations we split the results into a number of intervals and fit an orbit to the phases in each interval (the orbital Period was fixed).

The fitting model for each interval consisted of a quadratic phase model combined with an orbital model elaborated by Mark H. Finger, and parametrized by the elements $a_x \sin i$, $g = e\sin(\omega)$, $h = e\cos(\omega)$, and $T_{\pi/2}$, with the orbital period P_{orb} fixed, and $T_{\pi/2}$ (the epoch when the mean orbital longitude is equal to 90 deg) placed near the middle of the interval, $\mathrm{a}_x\mathrm{sin}i/\mathrm{c}$ is the light-travel time for the projected semi-major axis (i is the inclination angle), e is the eccentricity and ω is the longitude of periastron.

The final orbital parameters were obtained from a unweighted average of the best fit parameters from only those not highly dispersed fit intervals (e.g., finally only 28). This method of averaging local orbits was introduced by Boynton et al. (1986) so that the errors in the orbital elements introduced by random torque variations could be empirically accounted for. The eccentricity e and argument of periastron ω were also obtained from the average values of g and h.

Bibliography

Bird, A. J., Barlow, E. J., Bassani, L., Bazzano, A., Bélanger, G., Bodaghee, A., Capitanio, F., Dean, A. J., Fiocchi, M., Hill, A. B., Lebrun, F., Malizia, A., Mas-Hesse, J. M., Molina, M., Moran, L., Renaud, M., Sguera, V., Shaw, S. E., Stephen, J. B., Terrier, R., Ubertini, P., Walter, R., Willis, D. R., and Winkler, C.: 2006, *ApJ* **636**, 765

Bird, A. J., Barlow, E. J., Bassani, L., Bazzano, A., Bodaghee, A., Capitanio, F., Cocchi, M., Del Santo, M., Dean, A. J., Hill, A. B., Lebrun, F., Malaguti, G., Malizia, A., Much, R., Shaw, S. E., Stephen, J. B., Terrier, R., Ubertini, P., and Walter, R.: 2004, *ApJ Lett.* **607**, L33

Boynton, P. E., Deeter, J. E., Lamb, F. K., and Zylstra, G.: 1986, *ApJ* **307**, 545

Buccheri, R., Bennett, K., Bignami, G. F., Bloemen, J. B. G. M., Boriakoff, V., Caraveo, P. A., Hermsen, W., Kanbach, G., Manchester, R. N., Masnou, J. L., Mayer-Hasselwander, H. A., Ozel, M. E., Paul, J. A., Sacco, B., Scarsi, L., and Strong, A. W.: 1983, *A&A* **128**, 245

Chernyakova, M.: 2005, *ISDC/OSA–INTRO*

Courvoisier, T. J.-L., Walter, R., Beckmann, V., Dean, A. J., Dubath, P., Hudec, R., Kretschmar, P., Mereghetti, S., Montmerle, T., Mowlavi, N., Paltani, S., Preite Martinez, A., Produit, N., Staubert, R., Strong, A. W., Swings, J.-P., Westergaard, N. J., White, N., Winkler, C., and Zdziarski, A. A.: 2003, *A&A* **411**, L53

Deeter, J. E., Boynton, P. E., and Pravdo, S. H.: 1981, *ApJ* **247**, 1003

Finger, M. H., Bildsten, L., Chakrabarty, D., Prince, T. A., Scott, D. M., Wilson, C. A., Wilson, R. B., and Zhang, S. N.: 1999, *ApJ* **517**, 449

Goldwurm, A., David, P., Foschini, L., Gros, A., Laurent, P., Sauvageon, A., Bird, A. J., Lerusse, L., and Produit, N.: 2003, *A&A* **411**, L223

Gros, A., Goldwurm, A., Cadolle-Bel, M., Goldoni, P., Rodriguez, J., Foschini, L., Del Santo, M., and Blay, P.: 2003, *A&A* **411**, L179

Lund, N., Budtz-Jørgensen, C., Westergaard, N. J., Brandt, S., Rasmussen, I. L., Hornstrup, A., Oxborrow, C. A., Chenevez, J., Jensen, P. A., Laursen, S., Andersen, K. H., Mogensen, P. B., Rasmussen, I., Omø, K., Pedersen, S. M., Polny, J., Andersson, H., Andersson, T., Kämäräinen, V., Vilhu, O., Huovelin, J., Maisala, S., Morawski, M., Juchnikowski, G., Costa, E., Feroci, M., Rubini, A., Rapisarda, M., Morelli, E., Carassiti, V., Frontera, F., Pelliciari, C., Loffredo, G., Martínez Núñez, S., Reglero, V., Velasco, T., Larsson, S., Svensson, R., Zdziarski, A. A., Castro-Tirado, A., Attina, P., Goria, M., Giulianelli, G., Cordero, F., Rezazad, M., Schmidt, M., Carli, R., Gomez, C., Jensen, P. L., Sarri, G., Tiemon, A., Orr, A., Much, R., Kretschmar, P., and Schnopper, H. W.: 2003, *A&A* **411**, L231

Makishima, K., Maejima, Y., Mitsuda, K., Bradt, H. V., Remillard, R. A., Tuohy, I. R., Hoshi, R., and Nakagawa, M.: 1986, *ApJ* **308**, 635

Mitsuda, K., Inoue, H., Koyama, K., Makishima, K., Matsuoka, M., Ogawara, Y., Suzuki, K., Tanaka, Y., Shibazaki, N., and Hirano, T.: 1984, *PASJ* **36**, 741

Orlandini, M.: 2006, *Advances in Space Research* **38**, 2742

Roy, A. E.: 1988, *Orbital motion*, Bristol, England ; Philadelphia : A. Hilger, 1988. 3rd ed.

Titarchuk, L.: 1994, *ApJ* **434**, 570

Wilson, C. A., Finger, M. H., Coe, M. J., Laycock, S., and Fabregat, J.: 2002, *ApJ* **570**, 287

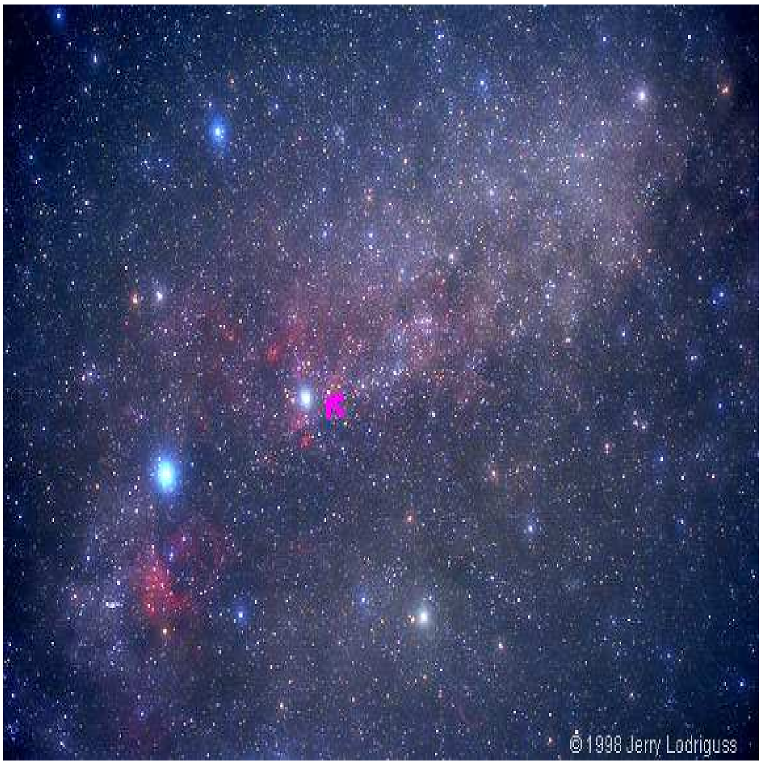

Figure 4.2: The Cygnus constellation. The arrow mark on magenta denotes approximately our region of study. Credits: Jerry Lodriguss (1998).

Chapter 5

EXO 2030+375

The HMXRB EXO 2030+375 is a Be/X-ray binary discovered by *EXOSAT* in 1985 during a giant X-ray outburst (Parmar et al. 1989). The X-ray luminosity in the 1-20 keV energy range reached a value of $L_x \sim 10^{38}$erg s^{-1}, and a large intrinsic spin-up rate (Reynolds et al. 1993) along with a 0.2 Hz QPO (Angelini et al. 1989) were observed. With an orbital period of $P_{\rm orb}$=46.0214±0.0005 d and an eccentricity of e=0.419±0.002 (Wilson et al. 2002), EXO 2030+375 exhibits variability on all time scales. Its optical counterpart is a Be ($V = 20\,$mag) main-sequence star (Motch and Janot-Pacheco 1987; Coe et al. 1988). The optical/IR emission seems to be related to the activity of the Be star's disk (Reig and Coe 1998).

In the X-ray band the neutron star shows 41.7-s pulsations (Parmar et al. 1989; Reynolds et al. 1993; Reig and Coe 1998; Wilson et al. 2002, 2005), and active/inactive periods are mainly related to the periastron passage (46 d). The spectral shape of EXO 2030+375 in the 2-20 keV energy range has been modeled by an exponential cut-off ($\Gamma = 1.00 \pm 0.06$) plus absorption and an iron emission line at $\sim$ 6.5 keV (Reig and Coe 1999). In the 20-150 keV energy band Stollberg et al. (1999) found a thermal bremsstrahlung model to be the best fit ($kT = 20.2 \pm 0.3\,$keV).

After EXO 2030+375's discovery only normal outbursts have been detected up to middle 2006: *EXOSAT* (28 October - 3 November 1985, Parmar et al. 1989), *Ginga* (29-31 October 1989 and 24 October 1991, Sun et al. 1992), *ROSAT*(November 1990, Mavromatakis 1994), *CGRO* BATSE and *RXTE* satellites (since April 1991 outbursts were detected at most periastron passages and continue to be detected with the ASM, Wilson et al. (2002, 2005), and *INTEGRAL* (6-18 December 2002, and continue to be detected during GPS and pointed observations). These type I outbursts have $L_x < 10^{37}$ erg s^{-1}, are modulated with the orbital period and display low spin-up rate episodes. For these normal outbursts, the intensity and the global spin-up rate appeared to be tied to the K-band intensity of the Be star (Wilson et al. 2005).

From 1992-1993, EXO 2030+375 showed spin-up at an average rate of 1.91×10^{-13} Hz/s. Then from 1993-2000, it spun down at an average rate of -5.3×10^{-14} Hz/s (Wilson et al. 2002), and the outbursts were fainter (see top panel of Fig. 5.1). In 2002-2004, the outbursts again brightened and a spin-up rate of 1.2×10^{-13} Hz/s was observed (Wilson et al. 2005). The outbursts continued to brighten and showed spin-up rate increased up to 2.6×10^{-13} Hz/s until 2006 June, when EXO 2030+375 underwent its second giant outburst since its discovery in 1985 (Corbet and Levine 2006; Krimm et al. 2006; McCollough et al. 2006; Wilson and Finger 2006; Wilson et al. 2006).

Figure 5.1 (bottom) displays the long-term flux behavior of EXO 2030+375 by *RXTE* /ASM and the three high-energy instruments on board *INTEGRAL* , as well as *INTEGRAL* & *Swift* observation times of a Target of Opportunity (TOO) during 2006 giant outburst (Klochkov et al. 2007). For the first time, Wilson and Finger (2006) discovered evidences for a cyclotron line at ∼10 keV during the 2006 giant outburst. Klochkov et al. (2007) found that either a broad emission line at ∼13-15 keV (a “bump”) or a two absorption lines at ∼10 and ∼20 keV could model some features appeared between 10 and 20 keV in the spectrum. Previously a tentative cyclotron at 36 keV feature was reported in a 1996 normal outburst (Reig and Coe 1999); however, this feature has not been seen in any other observations.

In the first part of this chapter we present timing and spectral analysis of the high-mass X–ray binary EXO 2030+375, detected during normal outbursts by *INTEGRAL* and *RXTE. INTEGRAL* preliminary results of EXO 2030+375 have been reported by Martínez Núñez et al. (2003);

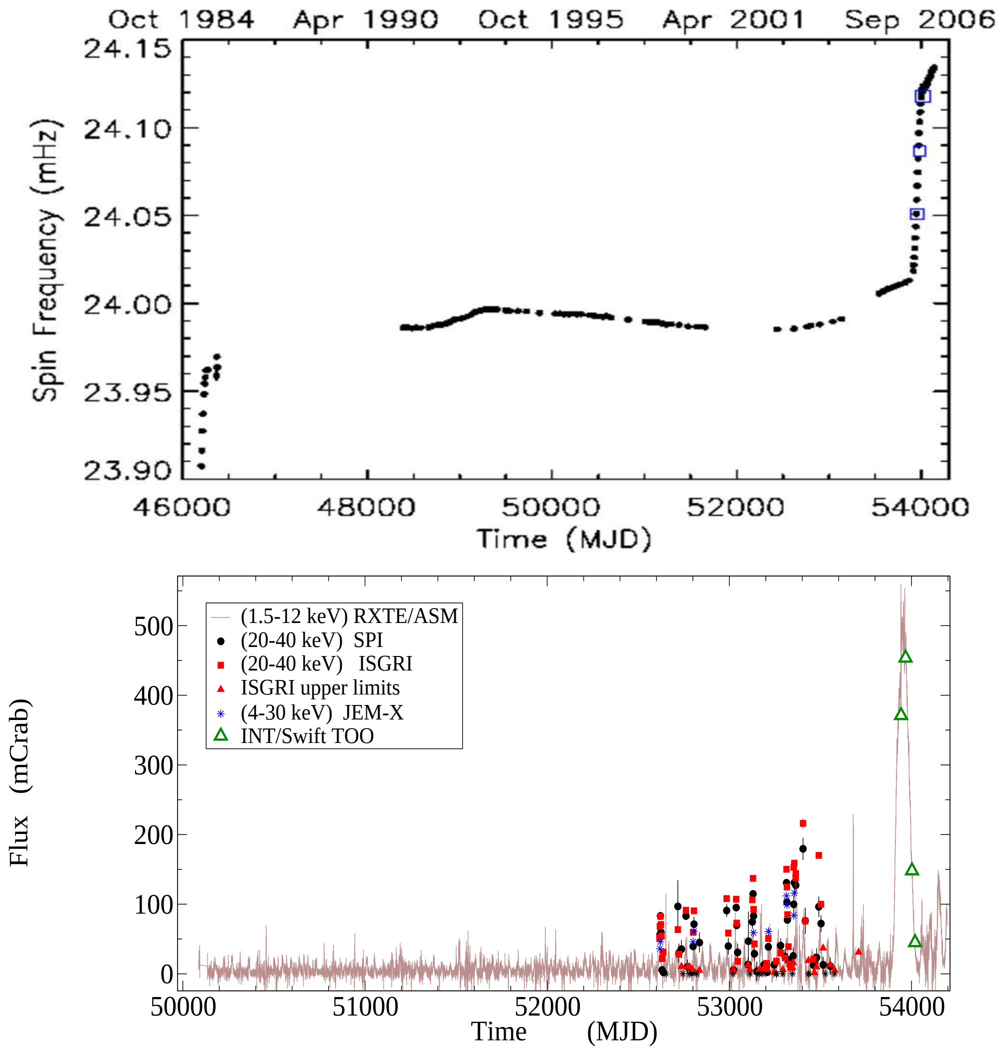

Figure 5.1: Top: Barycentered, orbit corrected, spin-frequency measurements for EXO 2030+375 measured with *EXOSAT*, *BATSE*, *RXTE* PCA and *INTEGRAL* by Wilson et al. (2006). Blue rectangles are measurements by Klochkov et al. (2007) during the last *INTEGRAL* /*Swift* TOO. Bottom: Long-term flux history of EXO 2030+375 by *RXTE* ASM and *INTEGRAL*. Green triangles denote the times of *INTEGRAL* and *Swift* observation times.

Kuznetsov et al. (2003, 2004); Bouchet et al. (2003); Camero Arranz et al. (2005). The second part of this chapter reports the giant outburst of EXO 2030+375 observed with *RXTE* in 2006 June–October. We present a study of the evolution of the spectral parameters during this giant outburst using *RXTE* data. Previous works on the 2006 giant outburst have been performed by Wilson and Finger (2006), Wilson et al. (2006) and Klochkov et al. (2007).

5.1 THE NORMAL OUTBURSTS

5.1.1 Observations and data reduction

During the *INTEGRAL* PV phase (from launch on October 17, 2002 to the end of December 2002), an outburst of EXO 2030+375 was observed. This has been the one and only outburst completely covered from the beginning to the end, lasting approximately 12 days. In the study presented here we have analyzed SPI, ISGRI and JEM-X data from revolutions 18 to 23 (3-18 December 2002) around the Cygnus region, where this source is located.

IBIS/ISGRI detected EXO 2020+375 in almost 285 pointing exposures. However, only those pointings giving a detection level above 7σ have been taken into account ($\sim$ 170 pointings). SPI data almost cover the duration of the outburst ($\sim$ 450 pointings). However, SPI data from revolution 18 was excluded since it was a staring observation (see Chapter 4.3.3). Due to the pattern of observation exposures made by *INTEGRAL*, EXO 2030+375 was outside the JEM-X field of view during the second part of the outburst, being detected in 10 pointings. Only in 5 of them the detection level was above 7σ.

In addition, sixteen more outbursts have been partially detected during *INTEGRAL*/GPS surveys and pointing observations in the Cygnus region. The period analyzed includes revolutions 25 to 384 (MJD 52630-MJD 53709). We have obtained positive detections with SPI in 52 revolutions, with a total observing time of $\sim$2660 ks. ISGRI has detected it in 30 revolutions with a detection level above 7σ, and upper limits detections

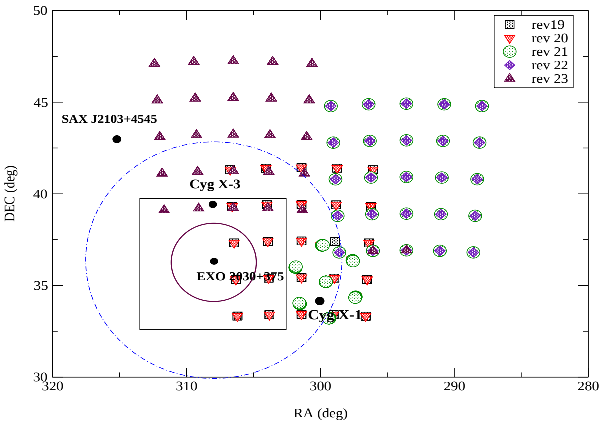

Figure 5.2: Dithering pattern (5x5) during December 2002 normal outburst around the Cygnus region. From inside to outside, overplotted are the fully coded fields of view of JEM-X, ISGRI and SPI instruments.

in other 38 revolutions (∼1600 ks). JEM-X has detected EXO 2030+375 with a detection level above 7σ in 8 revolutions (∼41 ks) (see Table A.1).

INTEGRAL data reduction was carried out with ISDC's (Courvoisier et al. 2003) Offline Scientific Analysis software, release 5.1. A software description can be found in Goldwurm et al. (2003), Diehl et al. (2003), Westergaard et al. (2003).

In 1996 July (MJD 50265-50275), 2002 June (MJD 52425-52446), and 2003 September (MJD 52894-52899), EXO 2030+375 was observed with the *RXTE* Proportional Counter Array (PCA) and the High Energy Timing Experiment (HEXTE). For each observation, we analyzed PCA Standard1 data for light curves and Standard2 data for hardness ratio and spectral analysis, using Ftools v5.3.1.

5.1.2 The PV Phase Normal outburst

Imaging

Fig. 5.2 shows the 5×5 and hexagonal dithering patterns carried out by *INTEGRAL* during the PV phase in the Cygnus region, together with the fully coded field of view of the three high-energy instruments. We observed that the 450 pointings can be grouped into a subset of 75 ($5 \times 5 \times 3$) which are independent, due to repetitions of the observation pattern at the same location.

Table A.1 shows the observations per instrument, and the mean flux in different energy ranges per revolution. PV phase fluxes in the 20-40 keV energy range obtained by ISGRI and SPI increase from MJD 52618 (revolution 19), peaking at around MJD 52622 (revolution 20), and finally decreasing to the end of the outburst at MJD 52630 (revolution 23).

Using PV phase data for a total observing time of 306 ks and covering revolutions 18 to 22, ISGRI located EXO 2030+375 at R.A.=308.09° and DEC=37.65°, with a 0.03° error radius. SPI detected this source with a statistical significance of 35σ, averaging over revolutions 19 to 23 (730 ks), at R.A.=308.12±0.07° and DEC=37.47±0.05°. Only in 10 pointings of revolutions 19 and 20 (18 ks) could JEM-X detect EXO 2030+375, because it has the smallest fully coded field of view. Its best location was at R.A.=308.06° and DEC=37.64° with an error radius of 0.03°.

Timing

X-ray pulsations have been detected by JEM-X and IBIS/ISGRI. A standard epoch-folding analysis on JEM-X data gives a value of 41.601±0.005 s for the period. In addition, we have analyzed ISGRI data using the technique described in Chapter 4.3.3 (Sec. 4.3.3). The best-fit period is 41.691798 ± 0.000016 s (epoch MJD 52621.6913), using data spanning revolutions 18 to 22 (MJD 52614.41–52628.96), including barycenter (Walter et al. 2003) and orbit corrections. This result is in very good agreement with previous results (Parmar et al. 1989; Reynolds et al. 1993; Reig and Coe 1998; Kuznetsov et al. 2004; Wilson et al. 2002, 2005).

Figure 5.4 shows 0.5 day phase residuals for our best fit model with a constant period, indicating that no significant spin-up (or spin-down) was detected during the outburst. All of the individual pulse profiles were then combined using our phase model to produce the mean 20-60 keV profile shown in the bottom panel of Figure 5.4.

During brighter EXO 2030+375 outbursts observed with BATSE, Wil-

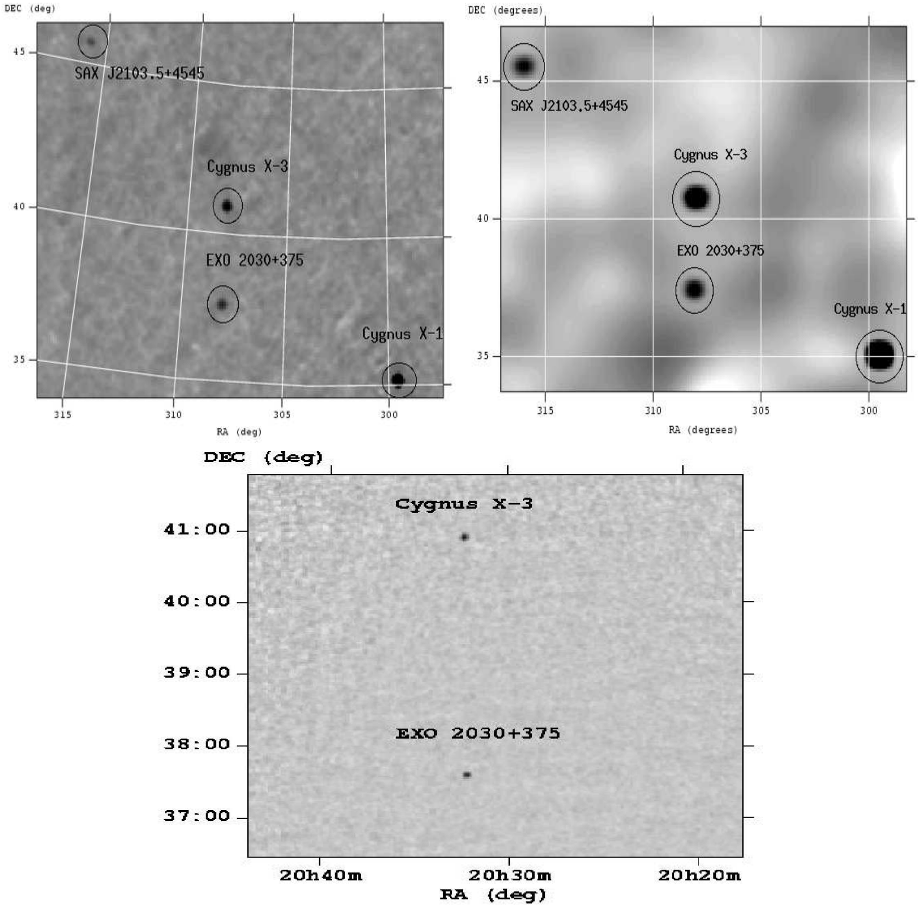

Figure 5.3: A mosaic of the Cygnus region by ISGRI (revolution 20, 20-40 keV) (top left); from revolutions 19 to 23 by SPI (20-40 keV) (top right), and by JEM-X (Dec. 2002 data, 5-30 keV) (bottom).

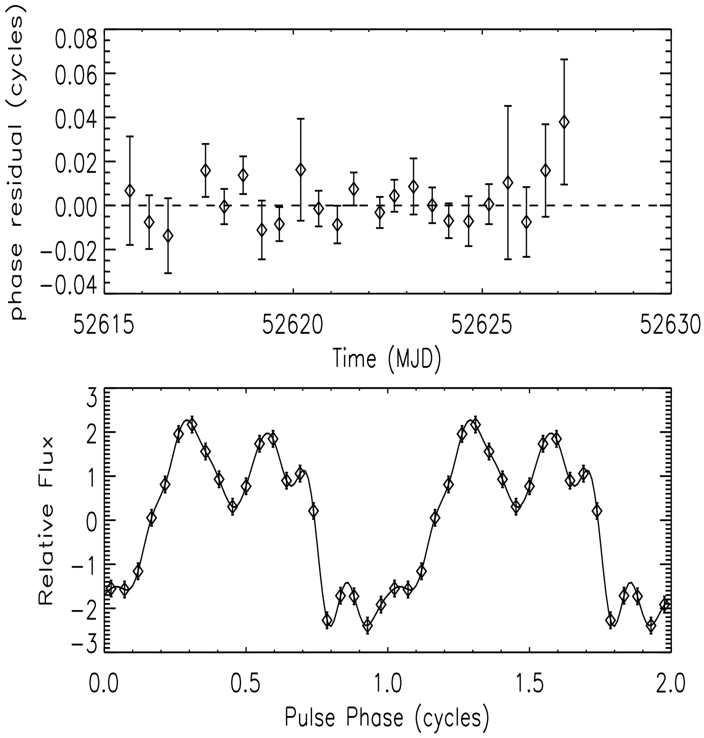

Figure 5.4: Top: Pulse phase residuals for EXO 2030+375 ISGRI 20-60 keV data from revolutions 18-22 from a fit to a linear phase model. Bottom: Mean pulse profile from revolutions 18-22 (Dec. 2002 outburst) generated by combining profiles from individual science windows using our linear pulse phase model.

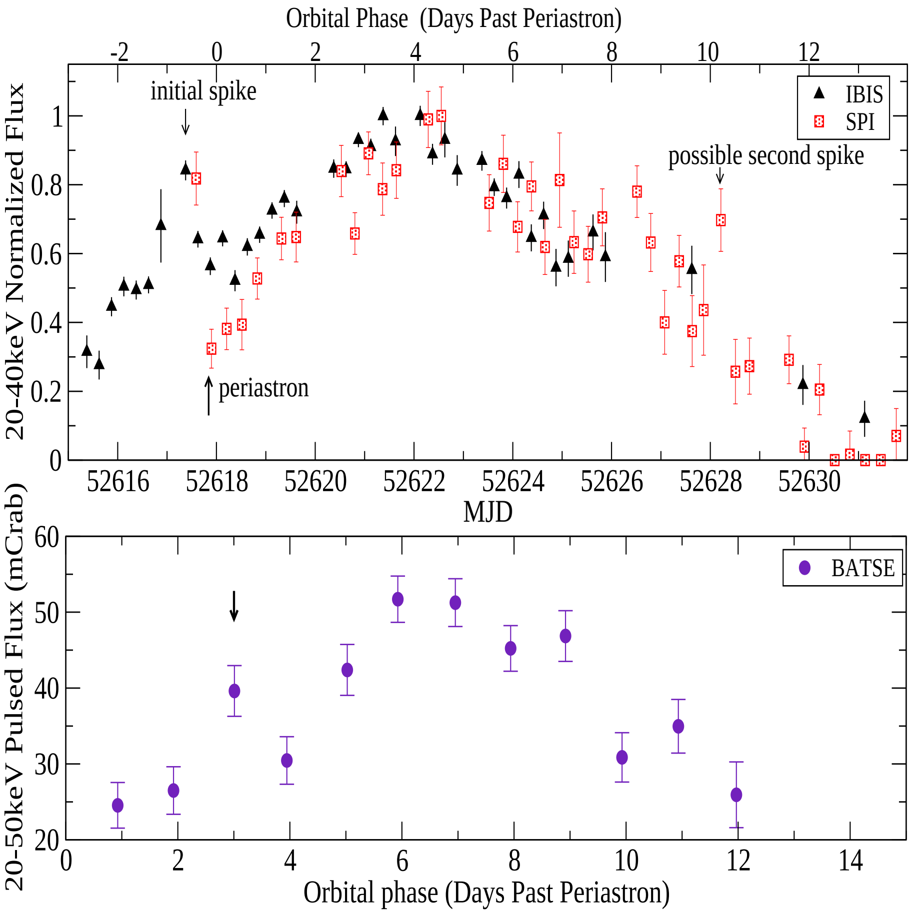

Figure 5.5: Top Panel: *INTEGRAL* (ISGRI-SPI, 20-40 keV) light curves of EXO 2030+375 outburst seen in Dec. 2002. The unusual features are marked in both light curves. Bottom Panel: BATSE 1-day average pulsed flux light curve (20-50 keV) from an outburst seen in 1993 May. Fluxes were generated as described in Wilson et al. (2002). Only a marginal detection of the initial spike is observed.

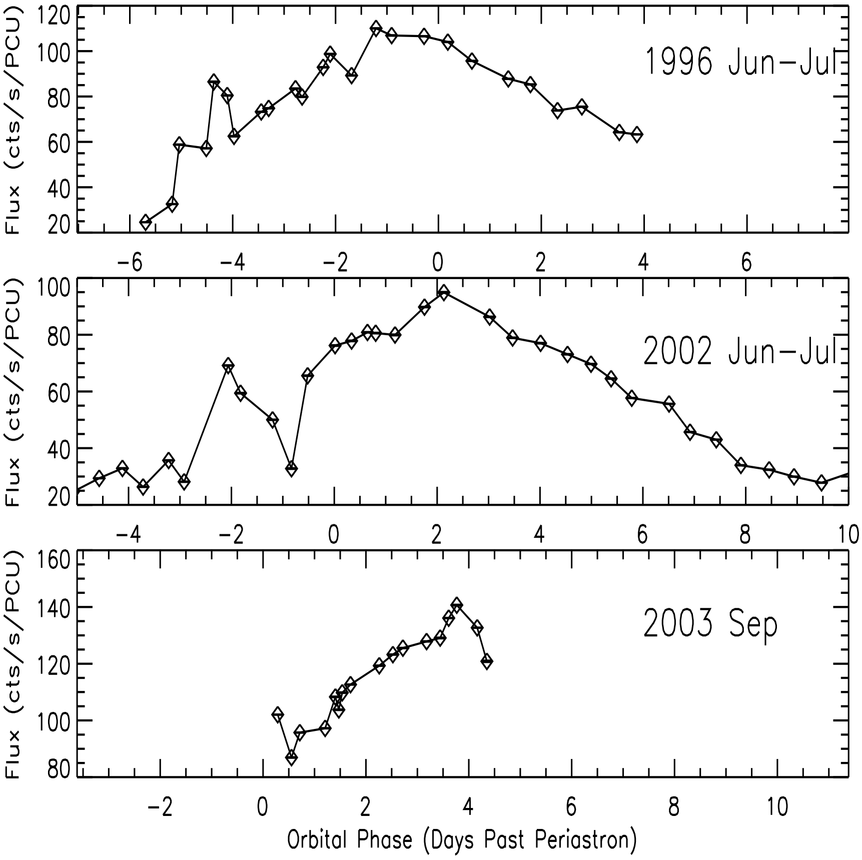

Figure 5.6: *RXTE* PCA light curves (2-60 keV) from 3 outbursts of EXO 2030+375. Evidence for an initial peak preceding the main outburst is present in all 3 outbursts, although coverage for the third outburst is incomplete. No secondary peak was seen. *RXTE* ASM data are not shown due to their large uncertainties.

son et al. (2002) found a correlation between spin-up rate and pulse flux, suggesting that an accretion disk was likely to be present. The behavior during the December 2002 outburst can be seen in Fig. 5.5, where a comparison of the (20-40 keV) ISGRI and SPI light curves with that of an earlier outburst detected by BATSE (20-50 keV) is shown.

The shape and amplitude of variability in both cases are analogous, as well as the duration of the phenomenon (about 12 days). However, it is to be noted that in the same figure the *INTEGRAL* light curves show a 4 day delay of the maximum of luminosity after the periastron passage of the neutron star, while the earlier outburst detected by BATSE peaked 6 days after periastron.

Furthermore, Fig. 5.5 shows very clearly an initial spike in both *INTEGRAL* light curves, and another possible spike after the outburst maximum. BATSE data shows marginal evidence for only an initial spike about 3-4 days before the maximum. *RXTE*/PCA light curves from June-July 1996, June-July 2002, and September 2003 all show evidence for an initial peak preceding the maximum, but no evidence for a second spike (see Fig. 5.6).

In these 3 outbursts, the initial spike, dip, and maximum each appear to occur at approximately the same relative orbital phase, despite the fact that the orbital phase of the maximum shifts dramatically from about 1 day before periastron in June-July 1996 to about 2 days after periastron in June-July 2002 and then to about 4 days after periastron as of September 2003.

Hardness Ratios

In order to study the spectral variability of EXO 2030+375 we have carried out a hardness ratio (*HR*) analysis, since the quality the data prevent us from performing a detailed spectral analysis. Table 5.1 lists the energy bands used. The HR is defined as:

$$HR = \frac{H-S}{H+S} \tag{5.1}$$

with H and S being the hard and soft band fluxes, respectively.

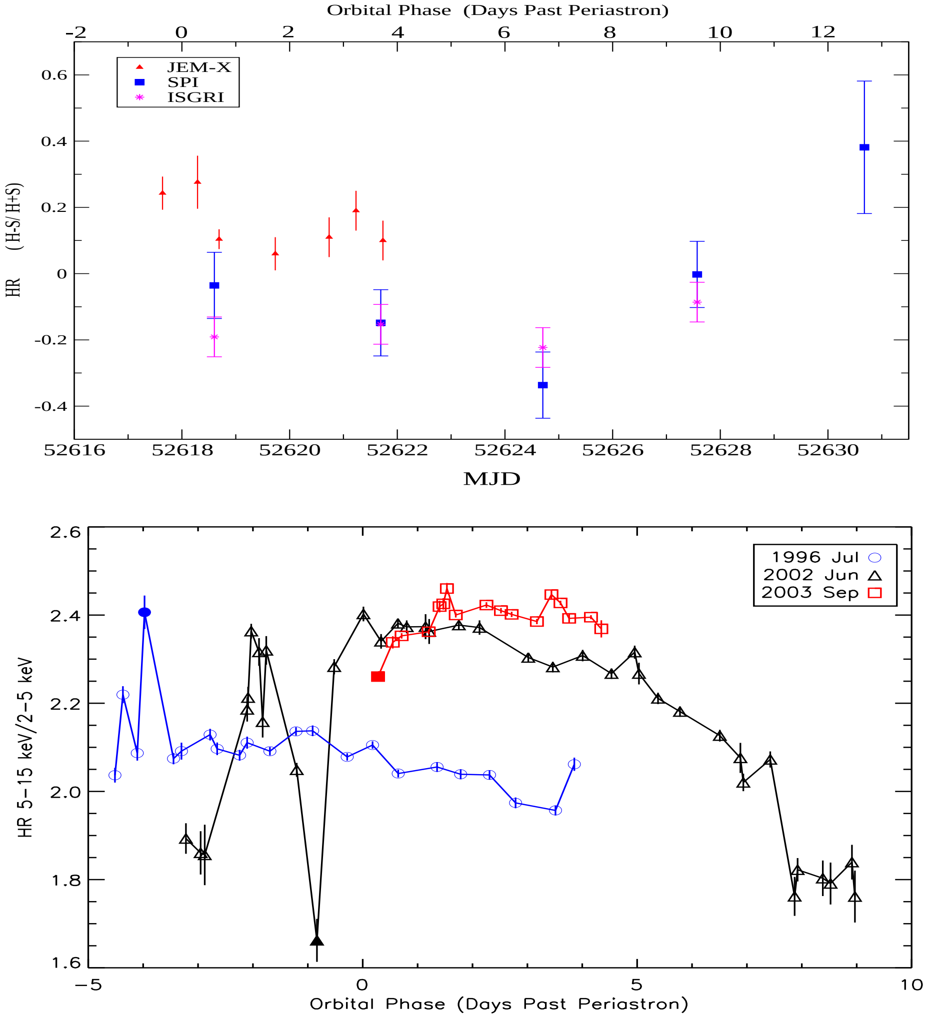

Figure 5.7: Top. Hardness Ratios from JEM-X, ISGRI and SPI during Dec. 2002 outburst (see Table 5.1). At high energies a softening of the spectrum is seen during outburst. *RXTE*/PCA 5-15 keV/2-5 keV hardness ratio vs. orbital phase from three outbursts of EXO 2030+375. Filled symbols denote the hardness ratio for the dip preceding the main outburst.

Table 5.1: Hardness ratios energy bands per instrument.

Instrument	Hard energy band	Soft energy band
RXTE PCA	5–15 keV	2–5 keV
INTEGRAL JEM-X	15–25 keV	5–15 keV
INTEGRAL ISGRI	40–60 keV	20–40 keV
INTEGRAL SPI	40–60 keV	20–40 keV

Figure 5.7 shows JEM-X, ISGRI and SPI HRs during the PV phase outburst. All flux data were computed in Crab units. In spite of the limited statistics, at high energies there seems to exist a softening of the spectrum (ISGRI and SPI data). It should be noted that for JEM-X only part of the outburst is present, due to the observing strategy (see Chapter 2, Sec. 2.3)

Hardness ratios were also generated from *RXTE* PCA data using three energy bands: 2-5, 5-15, and 15-30 keV. Here the hardness ratios were defined as $HR = H/S$. In all three outbursts observed with the *RXTE* PCA, the flux in the 5-15 keV band was larger than that in the other two bands. This differs from where the spectrum peaked in the *INTEGRAL* data, but is likely related to differences in the spectral response of the instruments.

During the main part of all three outbursts, the hardness ratios were roughly constant, as was also observed with *INTEGRAL*. However, the 5-15 keV/2-5 keV ratio, shown in Figure 5.7, exhibited intriguing behavior in the dip preceding the main outburst. In the 1996 outburst, the dip is harder than the main outburst, while in both the 2002 and 2003 outbursts, the dip is softer than the main outburst. Also, this hardness ratio was correlated with intensity in the 2002 outburst, when our observations covered the largest range of orbital phases and intensities.

Spectral analysis

In this section we have characterized the average spectral shape of EXO 2030+375 during the December 2002 outburst. Data from the three high-energy instruments have been combined to achieve a 5-300 keV broad-band average spectrum (Fig. 5.8). This was the first broad-band spectrum of this source obtained. For JEM-X we have extracted an average spectrum in the 5-25 keV energy range by using five Science Windows of revolution 19 (JEM-X 2 data).

Only IBIS/ISGRI spectral data within the fully coded field of view were used for obtaining the 20-100 keV average spectrum. This includes 35 spectra from revolutions 19 and 20. SPI has the largest field of view, hence EXO 2030+375 was detected throughout almost the entire duration of the outburst. In order to improve the signal to noise, data from revolutions 19 to 23 were used for attaining an average spectrum in the 20-300 keV energy range.

We found that the broad-band spectrum can be adequately described by the sum of a disk black body with either a power law model, or a Comptonized component (COMPTT). An absorbed powerlaw with a high energy cut-off was also found compatible. The soft component is interpreted as coming from the accretion disk, the neutron star surface, or an optically thick boundary layer (Barret et al. 2000, and references therein). The harder one is often modeled by simple power laws.

Table 5.2 summarizes the spectral parameters that have been obtained fitting all these models. The soft component has a black body temperature of kT_{BB} ~8 keV, which does not substantially change after applying a power law or a COMPTT model. In addition, we can see that an unbroken power law fits well the hard X-ray component with a $\Gamma=2.04\pm0.11$ keV. We also found that an absorbed power law plus a high energy cut-off is a consistent fit ($\Gamma=1.51$, $E_{cut}=$ 10 keV, $E_{fold}=$ 35 keV).

Moreover, we found compatible fits when a COMPTT model is used with different electron temperatures between $kT_e=30$ keV and $kT_e=60$ keV, although it was not possible to constrain this parameter, hence it was fixed in all the fits. We noticed how the optical depth decreases as

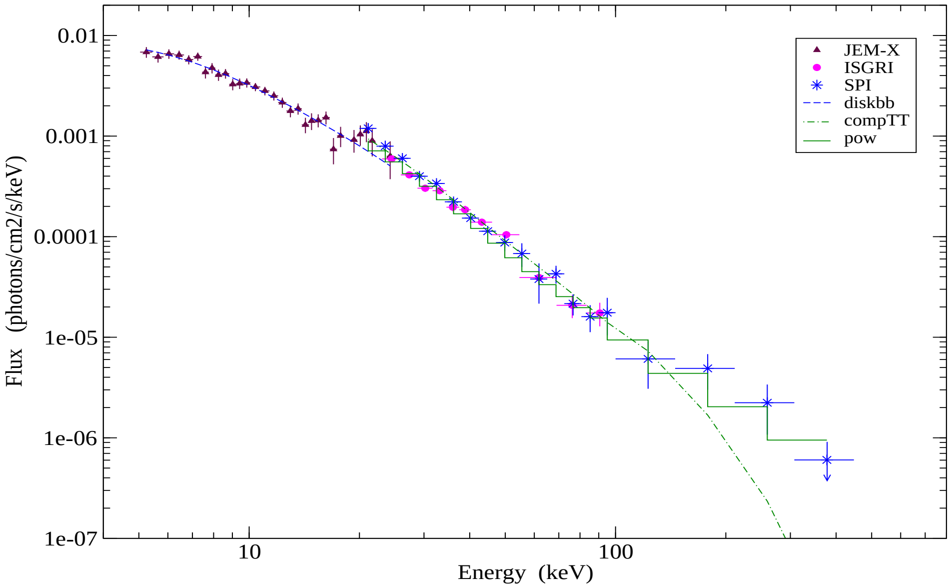

Figure 5.8: Broad-band spectrum obtained combining JEM-X-ISGRI-SPI mean spectra of EXO 2030+375 during the Dec. 2002 outburst. Two models have been fitted to the data: a disk black body plus either a power law (stepped line) or a comptonized component of kT$_e$=30 keV (dashed line).

the temperature increases, while the rest of the parameters are almost constant with temperature. The optical depth seems to scale with the fixed kT$_e$ parameter. For an increment of ΔkT$_e$= 10 keV (range: 20 – 60 keV) the optical depth augments 0.5 each time.

We have applied both spherical and disk geometries yielding to different values for the optical depth of the electron cloud ($\tau_{sphe}/\ \tau_{disk}\sim$2). However, the temperature of the seed photons (kT$_W$), assuming a Wien-type distribution, as well as the black body temperature remained constant.

In any case the addition of an absorption component improved the fits (a wide range of values from 0–5 were used). Nevertheless, it was included as a fixed parameter in the power*highecut model. Neither an iron line

Table 5.2: Broad-band spectral parameters (5-300 keV) with errors estimated in the 90% confidence range. For the comptonized component a spherical geometry was selected.

Model	Parameters	Intercalibration factors (ISGRI/JEM-X) (SPI/JEM-X)
	kT$_{BB}$= $8.2^{+1}_{-0.9}$ keV	$1.0^{+0.2}_{-0.1}$
diskbb	Γ= 2.04±0.11	1.1±0.2
+ pow	χ^2_{red}/dof= 1.07/72	
	Flux*= 1.7 $\times 10^{-9}$	
	kT$_{BB}$= 8±2 keV	$1.2^{+0.3}_{-0.2}$
diskbb	kT$_W$= $1.5^{+0.3}_{-0.4}$ keV	$1.3^{+0.3}_{-0.2}$
+compTT	kT$_e$= 60 keV (fixed)	
	τ= $1.3^{+0.4}_{-0.3}$	
	χ^2_{red}/dof= 1.005/70	
	Flux*= 1.5 $\times 10^{-9}$	
	kT$_{BB}$=7±2 keV	$1.18^{+0.3}_{-0.18}$
diskbb	kT$_W$= $1.5^{+0.3}_{-0.4}$ keV	$1.31^{+0.18}_{-0.2}$
+compTT	kT$_e$= 30 keV (fixed)	
	τ= $2.6^{+0.6}_{-0.5}$	
	χ^2_{red}/dof= 1.03/70	
	Flux*= 1.4$\times 10^{-9}$	
phabs	nH = 2$\times 10^{22}$ cm^{-2} (fixed)	0.965±0.11
+	Γ = $1.51^{+0.2}_{-0.12}$	1.095±0.14
pow*highecut	E$_{cut}$ = 10^{+3}_{-4} keV	
	E$_{fold}$ = 35±7	
	χ^2_{red}/dof= 1.3/86	
	Flux*= 1.4$\times 10^{-9}$	

*(erg cm^{-2}s^{-1})

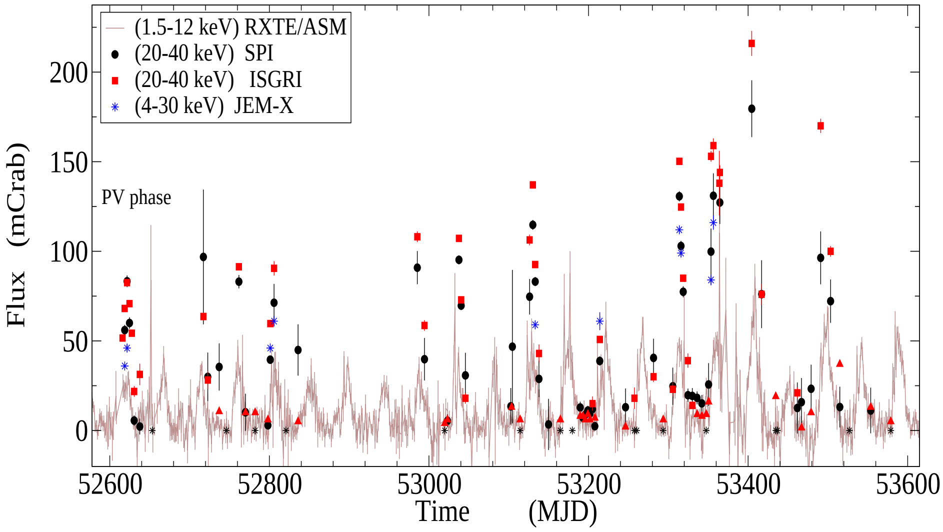

Figure 5.9: *INTEGRAL* (4-30 keV JEM-X, 20-40 keV ISGRI and SPI) light curves from different normal outbursts, and simultaneous data from *RXTE*/ASM (1.5-12 keV).

was detected nor any cyclotron line feature around 36 keV as Reig and Coe (1999) suggested could be observed. No cut-off at 200-300 keV, as seen in black-hole systems (BHs) like Cygnus X-1 (Schönfelder 2001), seems to be present although the data are not conclusive.

5.1.3 Long-term study

Galactic Plane Scans and pointed observations performed by *INTEGRAL* allowed us to partially detect sixteen more normal outbursts of EXO 2030+375. Figure 5.9 shows SPI, ISGRI and JEM-X long-term light curves obtained with all the available data. For comparison *RXTE*/ASM data covering the same period are also plotted.

In all light curves the outbursts show the same trend as previous type-I outbursts: the same duration and shape, and all separated by about 46 days, which corresponds to the orbital period of the system. However, the amplitude of the outbursts varies from one to another. In principle, this can be due to the outbursts not being completely sampled in time during the GPS, since the purpose of some of these observations is to perform saw-tooth-path scans of the Galactic Plane at weekly intervals, where individual exposures are separated by 6° along the scan path.

On the other hand, due to its detector design, data from SPI are highly background dominated. For SPI to achieve a signal to noise ratio of $\sim$10 for a source as bright as EXO 2030+375 an observation of 300 ks would be necessary. Therefore the GPS pointing pattern is not well suited to make a detailed study of point sources.

Another possible explanation is that the pointed observations performed in the Cygnus region were not scheduled for entering EXO 2030+375 in outburst. Hence, the coverage of these outbursts were not completed. However, it is worthy to note that several of these outbursts were observed around their maxima of X-ray luminosity (e.g., rev. 252, 266 or 311, and so on). This allow us to confirm that the outbursts become brighter with time.

Once more, the quality of the data prevent us from performing a detailed long-term spectral analysis. In order to study the spectral variability of EXO 2030+375 we have again carried out a long-term HR analysis of these normal outbursts with *INTEGRAL* . JEM-X 7-10 keV/4-7 keV HR vs. 4-7 keV flux are shown in Fig. 5.10 (Top). At low energy bands, there seems to be a softening of the spectra of EXO 2030+375 as the flux increases. In the bottom of the same Figure we have plotted the ISGRI and SPI long-term HR history computed the same way that in the PV phase outburst. We found identical behavior than at low energies, that is, a softening of the spectra with increasing flux.

5.1.4 Discussion

We have carried out *INTEGRAL* imaging, timing and spectral analysis of the Be/X-ray binary EXO 2030+375 December 2002 outburst. In addition, we have reported sixteen more outbursts detected during *INTEGRAL* GPS surveys and pointing observations around the Cygnus region.

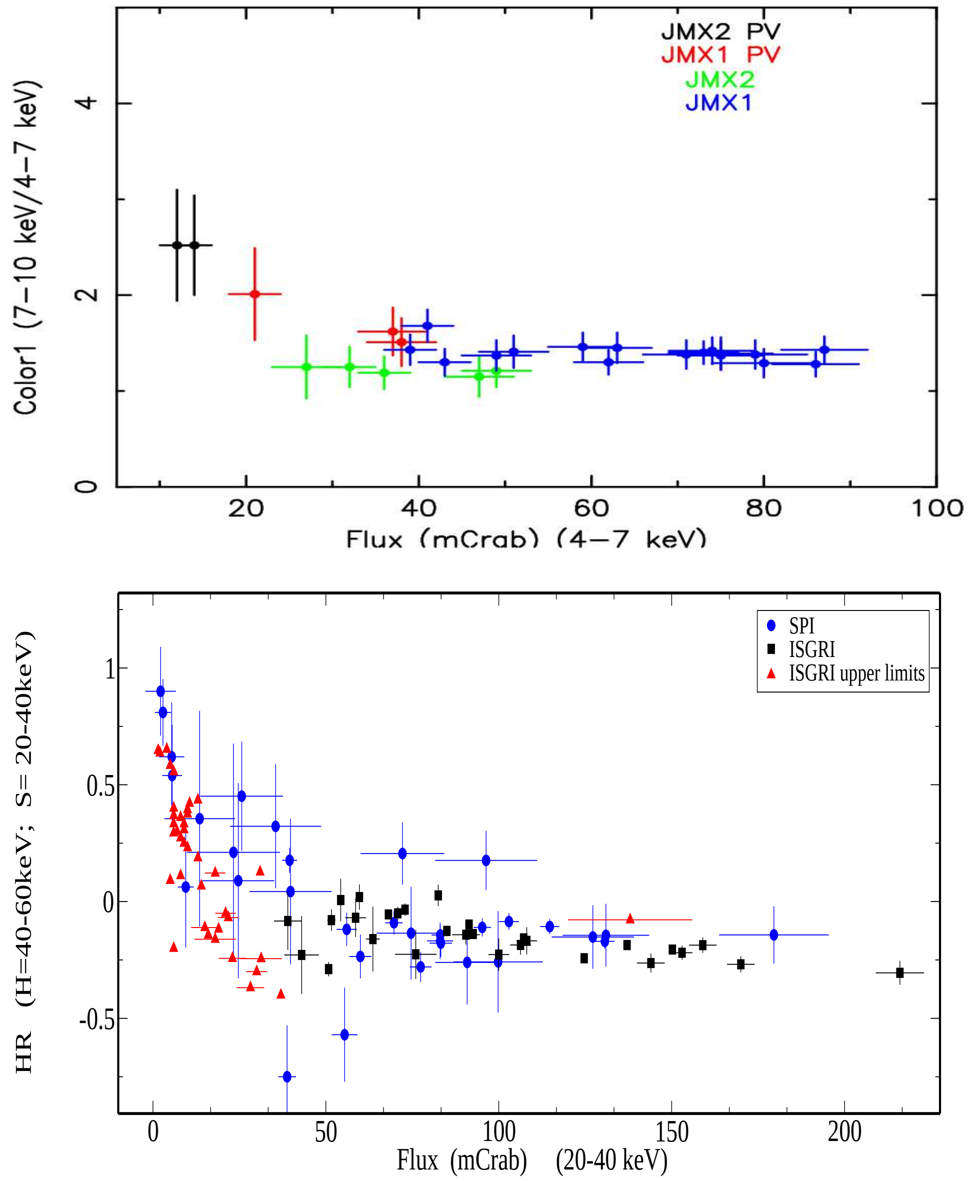

Figure 5.10: Top. JEM-X 7-10 keV/4-7 keV long-term hardness ratio vs. 4-7keV Flux of EXO 2030+375. Bottom. ISGRI and SPI long-term HR analysis vs. 20–40 keV Flux of this source.

Timing

Temporal analysis performed with JEM-X and IBIS/ISGRI observations showed X-ray pulsations. Previous results using *INTEGRAL* data by Kuznetsov et al. (2004) gave a value of 41.6897±0.0001 s. Our best fit period obtained is 41.691798 ± 0.000016 s, in excellent agreement with previous results (Parmar et al. 1989; Reynolds et al. 1993; Reig and Coe 1998; Wilson et al. 2002, 2005).

The global trend in the pulsar spin frequency was spin-down from 1994 through 2002. Based on the 2002 and 2003 outburst observations with *RXTE* PCA, Wilson et al. (2005) observed a change from spin-down to spin-up. They suggested that the pattern of constant spin, followed by spin-up, followed by spin-down, observed with BATSE, is repeating with an approximately $\sim$ 11 yr cycle. Nevertheless, no significant spin-up (or spin-down) was detected during the *INTEGRAL* PV phase outburst.

The X-ray behavior of EXO 2030+375 in the medium term, is characterized by a regular increase of the X-ray flux modulated with the orbital period (type I outbursts). The average X-ray luminosity was 9.7×10^{36} erg s^{-1}, for an assumed distance of 7.1 kpc (Wilson et al. 2002). This luminosity value is of the same order as previous type-I outbursts of this source. We have estimated the L_{1-20}/L_{20-200} ratio for EXO 2030+375, obtaining a value $\sim$1.2. This allows us to locate this source in the so-called X-ray burster box, whereas all black holes are found outside it (Barret et al. 2000).

During the PV phase outburst a four-day delay between the maximum of luminosity and the periastron passage of the neutron star was found. Previous results showed that EXO 2030+375's outbursts abruptly shifted from peaking about 6 days after periastron to peaking before periastron and then gradually shifting to after periastron, depending on a density perturbation precessing in a prograde direction around the Be disk (Wilson et al. 2002). Recent *RXTE* ASM data indicate that the main peak is currently about 12 days after periastron (see Fig. 5.11).

The second feature found in the EXO 2030+375 *INTEGRAL*/SPI light curve is not detected in another outbursts by *RXTE*, and there are not enough ISGRI data covering this period for comparison. When interpret-

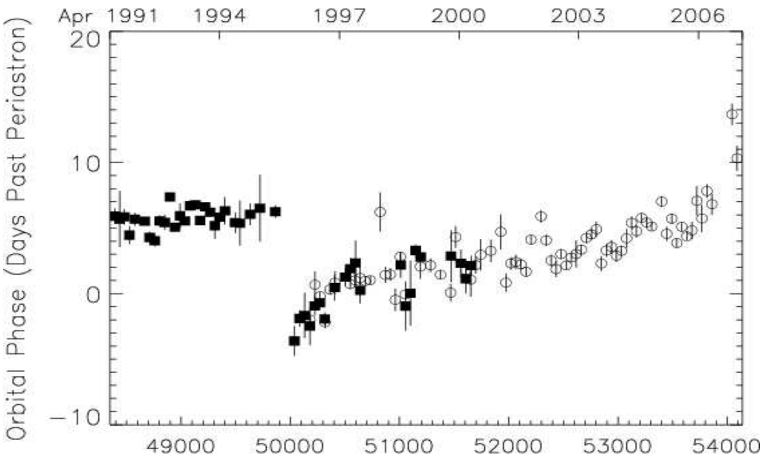

Figure 5.11: Orbital phase of EXO 2030+375 outburst peaks by Colleen Wilson-Hodge (2006b). Filled squares are peaks measured with BATSE. Open circles mark peaks measured with *RXTE* . These are determined by gaussian fits to 46-day intervals of *RXTE* ASM data.

ing SPI timing analysis it is important to take into account the possible influence of a very strong source like Cygnus X-1 in the field of view of this coded mask instrument. To resolve all sources each should have a clear coding pattern from the mask, and if this is incomplete for any of the sources, especially for a weak one, the mask pattern may correlate with parts of the mask pattern of neighboring sources introducing a systematic error in flux values.

This phenomenon of an incomplete detector pattern due to a source outside the FCFOV can also be seen in the two dips at the end of the Cygnus X-1 light curve. The observation detector pattern of the second EXO 2030+375 feature is not completely inside the FCFOV of the instrument, i.e. this feature could have a systematic error due to cross correlation with Cygnus X-1.

In Fig. 5.12 we can see four large flares in the Cygnus X-1 light curve. In principle, if such a kind of correlation is occurring we would expect four unusual features in EXO 2030+375 light curve. However, only the first and last of these correlate to the EXO 2030+375 features, but there is no correlation for the second and third. Therefore, we cannot rule out the possibility that the second peculiarity in the SPI data of EXO 2030+375 is real.

Analysis of *INTEGRAL* and *RXTE* data did not show clear spectral differences between the initial and maximum peaks. If the emission characteristics during the initial peak and the main outburst are different this would indicate two different accretion mechanisms. Interestingly, the RXTE data showed evidence for a spectral difference in the dip between the peaks. However limited statistics did not allow a detailed spectral analysis.

A 0535+26 is another source showing a pre-spike during a normal outburst in 2005 (see Chapter 7, Sec. 7.3 for discussion). In addition, 2S 1845-024, a 94-second pulsar in an eccentric (e=0.88) 242-day orbit, exhibits the same recurrent structure as EXO 2030+375 consisting of an initial peak preceding the maximum and followed by another weaker peak (Finger et al. 1999). In this source, the spikes are interpreted as due to the passage of the pulsar through the Be star's circumstellar envelope in an orbit inclined with respect to the equatorial plane of the Be star, while the main peak was interpreted as due to disk accretion.

Spectral fit

Reig & Coe (1999) studied the continuum spectral shape of EXO 2030+375 in the 2-20 keV energy range, representing it with an exponential cut-off ($\Gamma = 1.00 \pm 0.06$, $E_{cut} \sim 8.85 \pm 0.33$ keV), plus absorption by cold material ($N_H = (2.6 \pm 0.3) \times 10^{22}$ cm^{-2}) and an iron emission line at $\sim$ 6.5 keV. In the Gamma-ray band data are scarce. *CGRO*/BATSE observations in the 20-150 keV energy range did not find significant variations of the spectral parameters over a 134-day period, with a thermal bremsstrahlung as the best-fitting model ($kT = 20.2 \pm 0.3$ keV, Stollberg et al. (1999)).

INTEGRAL observations in the 5-25 keV range by Martínez Núñez et al. (2003) have reported as the best fit an exponential cut-off ($\Gamma = 0.52 \pm 0.12$, $E_{cut} \sim 7.8$ keV), although an iron emission line was not detected. Kuznetsov et al. (2003) fitted the 20-100 keV spectrum using a power law

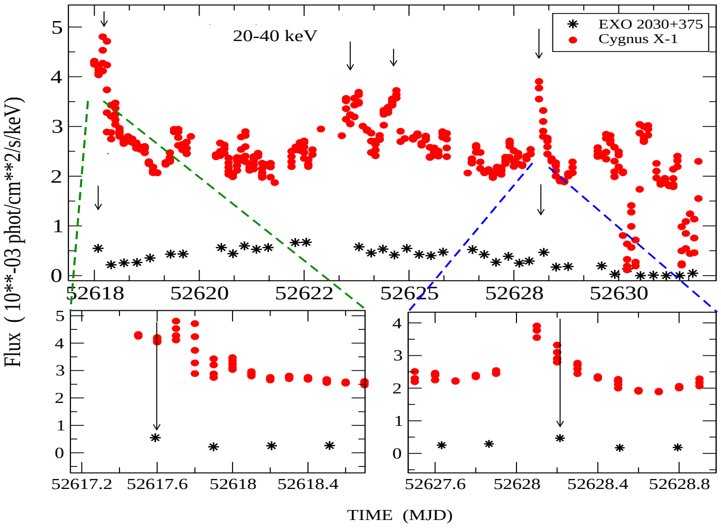

Figure 5.12: Cygnus X-1 and EXO 2030+375 light curves from *INTEGRAL* PV phase data. The four maxima in the Cygnus X-1 light curve and the two EXO 2030+375 spikes are marked with arrows.

plus an exponential cut-off ($\Gamma = 1.5 \pm 0.2$, $E_{cut} \sim 37\,\mathrm{keV}$). Furthermore, in the 20-150 keV energy range Bouchet et al. (2003) found that a single power law ($\Gamma = 2.72 \pm 0.02$) or a bremsstrahlung ($kT = 27.2 \pm 0.1\,\mathrm{keV}$) were compatible fits. Preliminary 10-200 keV broad-band spectrum by Camero Arranz et al. (2004) showed that either an unbroken power law ($\Gamma = 2.54 \pm 0.14$) or a bremsstrahlung ($kT = 34 \pm 0.4\,\mathrm{keV}$) were again good fits.

In the present work the hard component of the 5-300 keV broad-band spectrum, described by a single power law model with a Γ=2.04±0.11 keV, confirms *INTEGRAL* preliminary results. As we said in the previous section, we have used in addition a Comptonization model (COMPTT) for EXO 2030+375. Due to the fact that this is the first time that such a model has been used for this source, we can not compare our results with previous studies. We will compare them with other analysis performed in another neutron stars and black-hole systems. These studies, however, are concentrated on NS in low-mass systems with lower magnetic fields than accreting X-ray binaries.

On average, BH spectra are harder than NS spectra and this has been tentatively explained by the additional cooling provided by the NS surface, which may act as a thermostat capable of limiting the maximum kT_e achievable in these systems (Kluzniak 1993; Sunyaev and Titarchuk 1989). Using the COMPTT model for fitting BH spectra showed that electron temperatures greater than 50 keV seem to be common, while NS temperatures are usually smaller than that value (Barret 2001).

For EXO 2030+375 we have found that electron temperatures between 30 keV and 60 keV are compatible in describing the broad-band spectrum hard X-ray component. The 60 keV temperature value seems to be inconsistent with the general behavior of NSs. However, that criterion is still under debate since a temperature of about 50 keV, derived from the fitting of the hard X-ray spectra with a Comptonization model, was found by Torrejón et al. (2004) for the High Mass X-ray Binary 4U2206+54, as well as some speculative BH candidates for which kT_e is below 50 keV (e. g., IGR J17464-3213 and GRS 1758-258; kT_e ~18 keV and ~33 keV, respectively; Capitanio et al. (2004); Mandrou et al. (1994)). In any case, this is applied when an energy cutoff is observed. But such cutoffs are not always present in NS hard X-ray spectra. EXO 2030+375 does not show a cuttoff in the hard X–ray domain (Γ = 2.04), but at 10 keV (considering the absorbed power law plus a cut-off model; Γ=1.51, E_{fold}= 35 keV).

The same behavior is found in some weekly magnetized NS like 1E 1724-3045 and Aql X-1, revealing a nonattenuated hard power law of $\Gamma = 1.8$ up to 200 keV (Barret et al. 1991) and Γ in the range 2.1-2.6 in the 20-100 keV energy range (Harmon et al. 1996), respectively. Therefore, the indication of a steep hard X-ray ($E \gtrsim 30$ keV) spectrum with $\Gamma \gtrsim 2.5$ cannot alone be used to claim that such a spectrum comes from a NS. Similarly, a hard X-ray power-law spectrum with $\Gamma \lesssim 2.5$ is not unique to BHs (e.g., 4U 0614+091: Γ=2.3; Piraino et al. (1999).

Barret et al. (2000) suggested that there might be two classes of NSs. Members of the first class would display hard X-ray spectra with energy cutoffs, which would result from thermal Comptonization. Members of the second class, where EXO 2030+375 could be included, would have nonattenuated power laws which could be produced by nonthermal Comptonization, similar to the ones observed in the soft state of BHs.

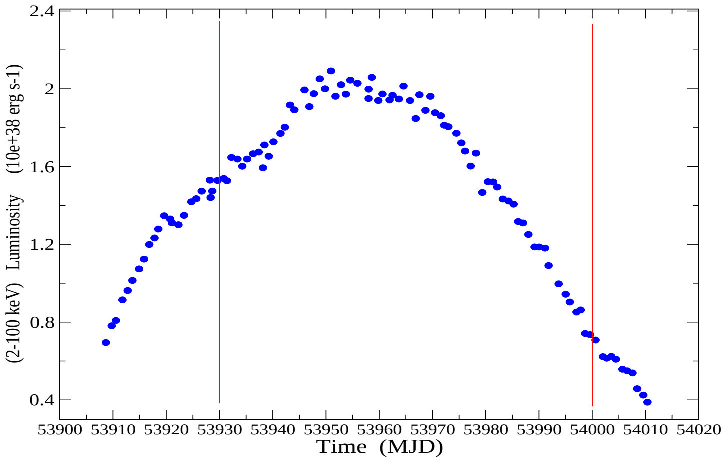

Figure 5.13: 2006 giant outburst light curve obtained with *RXTE* PCA and HEXTE cluster B data for EXO 2030+375. Red vertical lines denote the period in which simultaneous PCA, HEXTE clusters A and B data are available.

5.2 THE GIANT OUTBURST

As we mentioned in the introduction, EXO 2030+375 underwent a giant outburst in 2006 June-October, after approximately 21 years since the discovering giant outburst in 1985. We have seen in previous section that prior to the current giant outburst, the normal outbursts brightened considerably and exhibited dramatic spin-up (see Fig. 5.1). During the 2006 giant outburst, the observed spin-up rate was 1.27×10^{-11} Hz/s (Wilson and Finger 2006), approximately 75% of the 1985 giant outburst (Parmar et al. 1989). Probably this one was brighter than the 2006 giant outburst. The pulse profile evolution exhibited by EXO 2030+375 during the 2006 giant outburst was similar to that in 1985 (Colleen Wilson, private communication).

Many efforts have been made in the past in order to measure the magnetic field of EXO 2030+375 with no success. The most noteworthy signature during the 2006 giant outburst was the detection of a cyclotron absorption feature by Wilson and Finger (2006). The following section is going to focus on the study of the evolution of the spectral parameters during this giant outburst using the *RXTE* PCA and the two HEXTE clusters.

5.2.1 Observations

The 2006 giant outburst from EXO 2030+375 was observed with the *RXTE* PCA using more than 200 daily observations of 1-5 ks in duration beginning on 2006 June 22. In this thesis work, the spectral analysis was performed using the Standard 2 PCA. For HEXTE, we used the science data mode for both clusters A and B. Data analysis was performed using Ftools v6.1.2. Cluster A was not rocking. However, as we described in chapter 4.3.3, thanks to a method developed by Pottschmidt et al. (2006) from the *RXTE* team, an estimation of the HEXTE cluster A background spectrum could be obtained using the `hextebackest` Ftool.

Analysis of *INTEGRAL* and *Swift* observations of EXO 2030+375 during this giant outburst can be found in Klochkov et al. (2007). However, the coverage of this outburst with these instruments is much poorer than with *RXTE* .

5.2.2 Spectral Analysis

For each *RXTE* PCA, and HEXTE cluster A and B observation, we extracted source and background spectra and corrected them for deadtime following the standard procedure described in chapter 4.3.3. Systematic errors of 3% were also added. Unfortunately, no cluster A source spectra could be extracted corresponding to the beginning of this giant outburst (from MJD 53908 to MJD 53930) and to the tail (see Figure 5.13). Therefore, we will show a partial evolution of the spectral behaviour of EXO 2030+375.

The available PCA and HEXTE data were fitted from each observation using `xspec` with an absorbed power-law with a gaussian iron line and a high energy cutoff (PHABS(POWERLAW+GAUSSIAN)HIGHECUT). We then added a gaussian absorption feature to represent a cyclotron line. Figure 5.14 shows the cyclotron line parameters and the significance of the

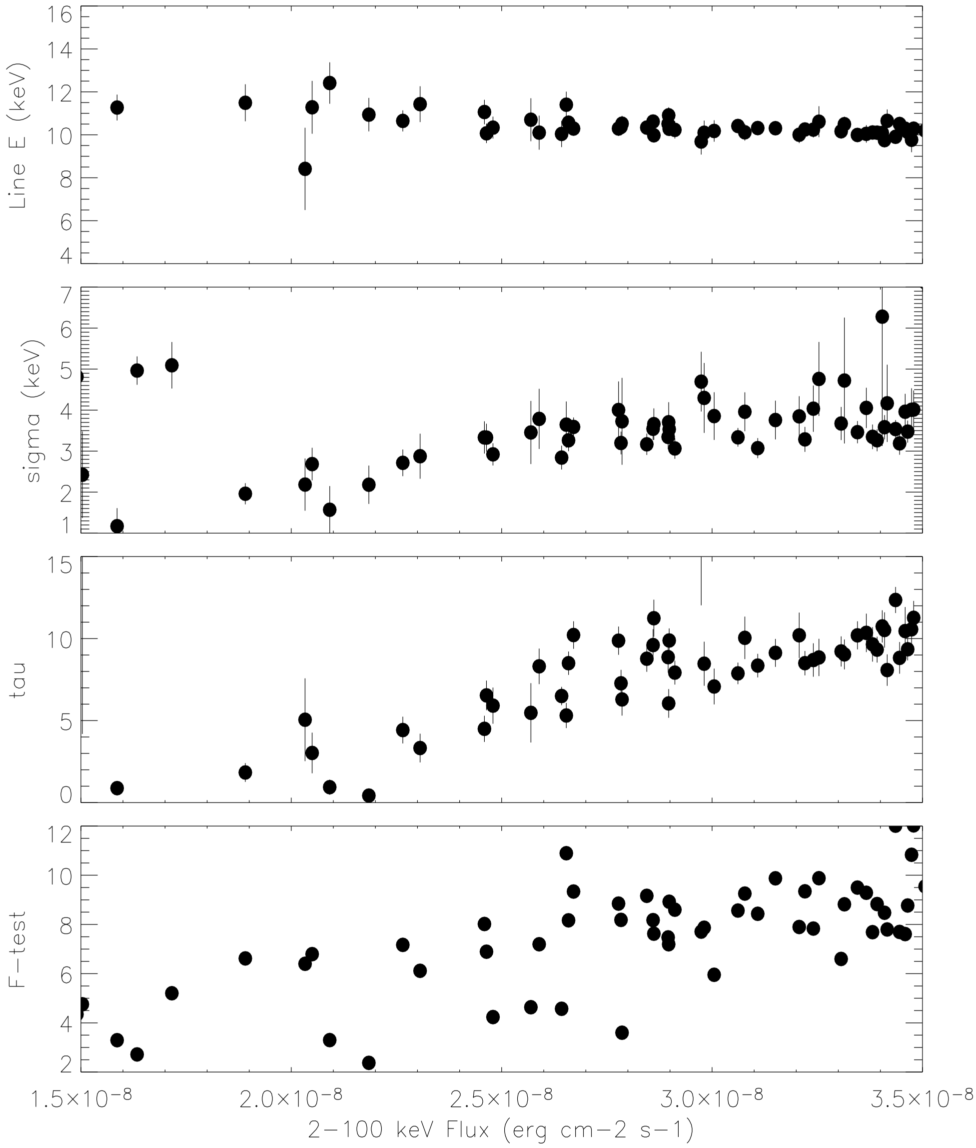

Figure 5.14: Evolution of the gaussian absorption feature modeling the cyclotron line with Flux (2–100keV). The top three panels show the line energy (keV), the width (keV), and the optical depth. The fourth panel shows the significance of this feature measured using an F-test.

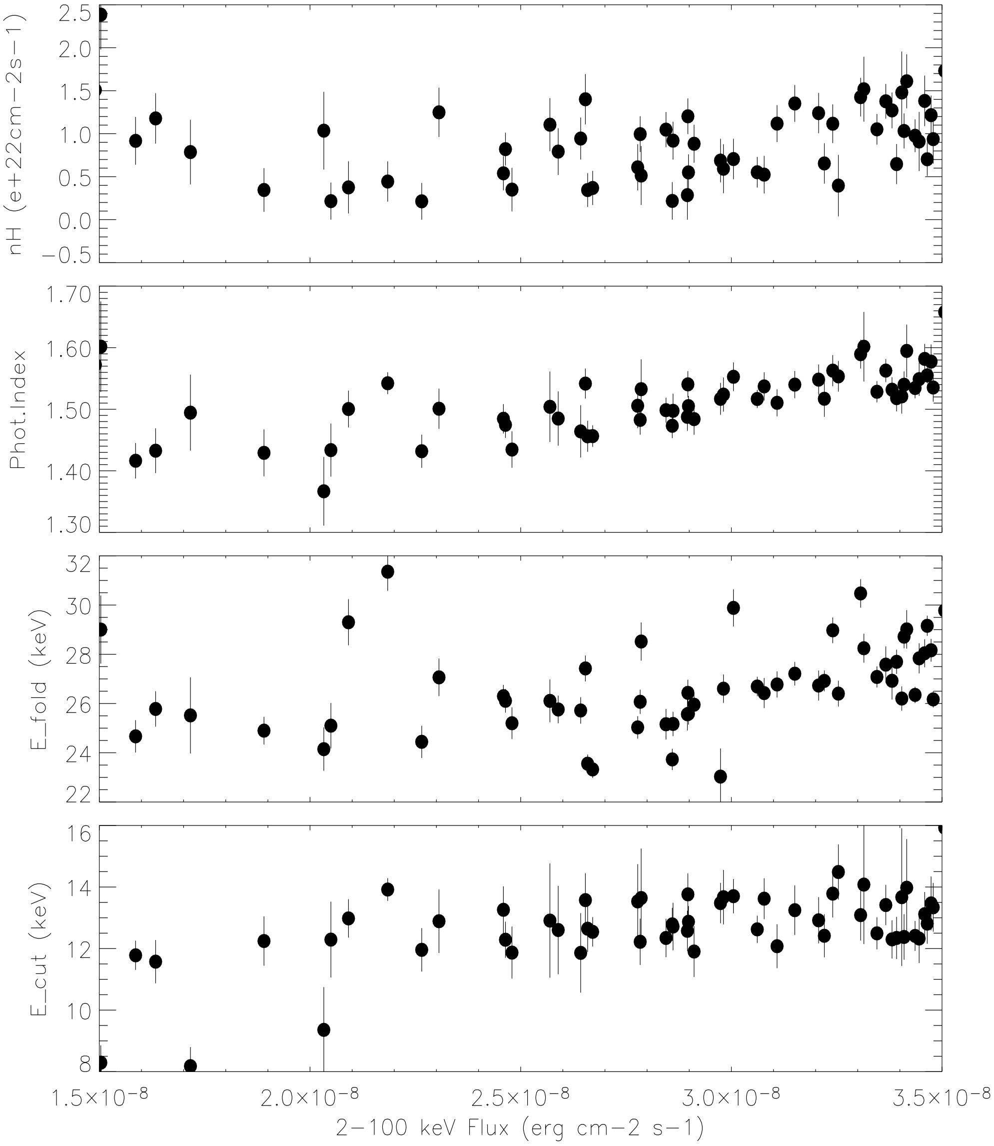

Figure 5.15: Additional parameters of the same model. From top to bottom: the absorption N_H, the Photon Index, cut-off E_{cut}, e-folding energy E_{fold}.

cyclotron feature (computed using an F-test) vs. 2–100 keV Flux. In this study the cyclotron feature was significantly detected during the giant outburst at fluxes larger than 1.7×10^{-8} erg cm^{-2} s^{-1}.

Figure 5.15 shows the behavior of the other spectral parameters from the same model, i.e., the absorption N_H, the photon Index, cut-off E_{cut} and the e-folding energy E_{fold}.

5.2.3 Discussion

From a joint fit to *RXTE* PCA and HEXTE data from August 15, 2006 (MJD 53962), Wilson & Finger (2006) found evidence for a cyclotron scattering feature near 10 keV. The model used was an absorbed power-law with a high-energy cut-off, an iron line, and a gaussian cyclotron absorption line. The power-law had a photon index of 1.53(2), with a cutoff energy at 12.4(4) keV, a folding energy of 27.4(5) keV. The cyclotron energy was 10.1(2) keV, with a gaussian width of 3.3(2) keV and a peak depth of 1.1(1). This feature was significant at a 7.5 sigma level.

We confirm the detection of such a cyclotron line near 10 keV and for X–ray luminosity larger than 9.8×10^{37} erg s^{-1}. The corresponding magnetic field has the value of 8.7×10^{11} G, reported by Wilson and Finger (2006). Klochkov et al. (2007) obtained an estimation of the magnetic field strength $\sim$1–4 $\times10^{12}$ G, which they claimed is consistent with a fundamental cyclotron line in the range $E_{cyc} \sim$ 10–50 keV. Both results seem to be consistent. We neither confirm the presence of cyclotron line at $\sim$36 keV suggested by Reig and Coe (1999).

Following the *INTEGRAL*/*Swift* results from Klochkov et al. (2007), we tried adding either a second gaussian absorption feature around 20 keV (where the line energy was exactly twice that of the other feature) or a broad emission line at $\sim$13-15 keV (a “bump”). F-tests showed that either approaches did not significantly improve the fits. The poor agreement for the second feature at 20 keV may be due to the fact that it is located in the intersection of the PCA/HEXTE responses.

Luminosity (2–100 keV flux) correlations can be seen in Figures 5.14 and 5.15, as well as in Table 5.3. We can see that the 10 keV cyclotron line

Table 5.3: Correlation coefficients of some spectral parameters for the 2006 giant outburst, estimated for luminosity (2-100 keV Flux) states above a given value.

Spectral parameter	F$\gtrsim 1.7 \times 10^{-8*}$	F$\gtrsim 1.4 \times 10^{-8*}$
E_{cyc} (keV)	-0.459	-0.228
Sigma (keV)	0.590	0.448
tau	0.764	0.468
F-test	0.519	0.589
n_H (cm^{-2} s^{-1})	0.517	0.337
Γ	0.770	0.658
E_{fold} (keV)	0.552	0.475
E_{cut} (keV)	0.329	0.473

* erg $cm^{-2}s^{-1}$

energy does not vary as the outburst brightens. However, at lower fluxes it seems to disperse to greater values with maximum around 12 keV.

In Table 5.3 we show different correlation coefficients of some spectral parameters. We estimated those coefficients for 2–100 keV fluxes larger than $\sim 1.7 \times 10^{-8}$erg $cm^{-2}s^{-1}$ and $\sim 1.4 \times 10^{-8}$erg $cm^{-2}s^{-1}$ ($\sim 1.4{\times}10^{38}$ erg s^{-1} and $\sim 8{\times}10^{37}$ erg s^{-1} X–ray luminosities), respectively.

For 2-100 keV fluxes $\gtrsim 1.7 \times 10^{-8}$ erg $cm^{-2}s^{-1}$, the line width, the optical depth parameter, the significance, the Photon Index, the absorption and the e-folding energy (in spite of the scatter) show luminosity dependence. However, there is not cut-off luminosity correlation. Including lower flux values in this study, we notice that only the F-test and the Photon Index parameters remain correlated with luminosity.

Tsygankov et al. (2006) studied the transient X-ray pulsar V 0332+53 cyclotron energy evolution with source luminosity. They found that the line energy increased linearly with decreasing luminosity, as the height of the accretion column. EXO 2030+375 behavior might be explained by the same argumentation.

5.3 CONCLUSIONS

Our main results can be summarized as follows:

- We have obtained the first 5-300 keV broad-band spectrum using *INTEGRAL* observations of the December 2002 EXO 2030+375 outburst. A single power law ($\Gamma = 2.04 \pm 0.11$) or a COMPTT model (kT_e=30 keV) can describe the hard X-ray component, while a disk black body can represent the soft component (kT_{BB} ∼8 keV). No Cyclotron feature was found.

- We have reduced the pulse period uncertainty determinations to ∼20% of previous *INTEGRAL* measurements.

- In the medium-term analysis, two unusual features in the light curve were found, an initial peak before the main outburst and an indication for another weaker one after the maximum (this one only by SPI). The physical mechanisms producing these features are unknown. *RXTE* observations confirm only the existence of the initial spike. Further observations would be needed to find out which physical mechanisms modulate the X-ray flux.

- We confirm the detection of the 10 keV cyclotron line by Wilson and Finger (2006) only during the 2006 giant outburst.

- Neither a second gaussian absorption feature around 20 keV nor a “bump” was detected in the same outburst.

- The 10 keV cyclotron line energy does not significant vary as the giant outburst brightens, but at lower luminosities it seems to increase up to 12 keV.

- The line width, the line depth, the significance, the Photon Index, the absorption and the e-folding energy show luminosity dependence, for X–ray luminosities above $\sim 1.4\times10^{38}$ erg s^{-1}.

Bibliography

Angelini, L., Stella, L., and Parmar, A. N.: 1989, *ApJ* **346**, 906

Barret, D.: 2001, *Advances in Space Research* **28**, 307

Barret, D., Mereghetti, S., Roques, J. P., Mandrou, P., Salotti, L., Lebrun, F., Laurent, P., Ballet, J., Churazov, E., Gifanov, M., Sunyaev, R., Khavenson, N., Chulkov, I., Novikov, B., Kuznetzov, A., and Dyachkov, A.: 1991, *ApJ Lett.* **379**, L21

Barret, D., Olive, J. F., Boirin, L., Done, C., Skinner, G. K., and Grindlay, J. E.: 2000, *ApJ* **533**, 329

Bouchet, L., Jourdain, E., Roques, J. P., Mandrou, P., von Ballmoos, P., Boggs, S., Caraveo, P., Cassé, M., Cordier, B., Diehl, R., Durouchoux, P., von Kienlin, A., Knodlseder, J., Jean, P., Leleux, P., Lichti, G. G., Matteson, J., Sanchez, F., Schanne, S., Schoenfelder, V., Skinner, G., Strong, A., Teegarden, B., Vedrenne, G., and Wunderer, C.: 2003, *A&A* **411**, L377

Camero Arranz, A., Reig, P., Connell, P., Martínez Númez, S., Blay, P., Beckmann, V., and Reglero, V.: 2004, in *Proc. of the 5th INTEGRAL Workshop*

Camero Arranz, A., Wilson, C. A., Connell, P., Martínez Núñez, S., Blay, P., Beckmann, V., and Reglero, V.: 2005, *A&A* **441**, 261

Capitanio, F., Kretschmar, P., Ubertini, P., Barlow, E. J., Bazzano, A., Brandt, S., Bouchet, L., Budtz-Jorgensen, C., Cadolle Bel, M., Castro-Tirado, A., Dean, A. J., De Cesare, G., Del Santo, M., Farinelli, R., Frontera, F., Gehrels, N., Goldoni, P., Goldwurm, A., Huovelin, J., Lund, N., Mirabel, F., Natalucci, L., Piraino, S., Reglero, V., Roques, J. P., Tarana, A., Vilhu, O., Westergaard, N. J., and Zdziarski, A. A.: 2004, in V. Schoenfelder, G. Lichti, and C. Winkler (eds.), *ESA SP-552: 5th INTEGRAL Workshop on the INTEGRAL Universe*, p. 313

Coe, M. J., Payne, B. J., Longmore, A., and Hanson, C. G.: 1988, *MNRAS* **232**, 865

Corbet, R. H. D. and Levine, A. M.: 2006, *The Astronomer's Telegram* **843**, 1

Courvoisier, T. J.-L., Walter, R., Beckmann, V., Dean, A. J., Dubath, P., Hudec, R., Kretschmar, P., Mereghetti, S., Montmerle, T., Mowlavi, N., Paltani, S., Preite Martinez, A., Produit, N., Staubert, R., Strong, A. W., Swings, J.-P., Westergaard, N. J., White, N., Winkler, C., and Zdziarski, A. A.: 2003, *A&A* **411**, L53

Diehl, R., Baby, N., Beckmann, V., Connell, P., Dubath, P., Jean, P., Knödlseder, J., Roques, J.-P., Schanne, S., Shrader, C., Skinner, G., Strong, A., Sturner, S., Teegarden, B., von Kienlin, A., and Weidenspointner, G.: 2003, *A&A* **411**, L117

Finger, M. H., Bildsten, L., Chakrabarty, D., Prince, T. A., Scott, D. M., Wilson, C. A., Wilson, R. B., and Zhang, S. N.: 1999, *ApJ* **517**, 449

Goldwurm, A., David, P., Foschini, L., Gros, A., Laurent, P., Sauvageon, A., Bird, A. J., Lerusse, L., and Produit, N.: 2003, *A&A* **411**, L223

Harmon, B. A., Wilson, C. A., Tavani, M., Zhang, S. N., Rubin, B. C., Paciesas, W. S., Ford, E. C., and Kaaret, P.: 1996, *A&AS* **120**, C197+

Klochkov, D., Horns, D., Santangelo, A., Staubert, R., Segreto, A., Ferrigno, C., Kretschmar, P., Kreykenbohm, I., La Barbera, A., Masetti, N., McCollough, M., Pottschmidt, K., Schönherr, G., and Wilms, J.: 2007, *A&A* **464**, L45

Kluzniak, W.: 1993, *A&AS* **97**, 265

Krimm, H., Barthelmy, S., Gehrels, N., Markwardt, C., Palmer, D., Sanwal, D., and Tueller, J.: 2006, *The Astronomer's Telegram* **861**, 1

Kuznetsov, S., Falanga, M., Blay, P., Goldwurm, A., Goldoni, P., and Reglero, V.: 2003, *A&A* **411**, L437

Kuznetsov, S., Falanga, M., Goldwurm, A., and di Salvo, T.: 2004, in V. Schoenfelder, G. Lichti, and C. Winkler (eds.), *ESA SP-552: 5th INTEGRAL Workshop on the INTEGRAL Universe*, p. 285

Mandrou, P., Roques, J. P., Bouchet, L., Niel, M., Paul, J., Leray, J. P., Lebrun, F., Ballet, J., Churazov, E., Gilfanov, M., Sunyaev, R., Novikov, B., Khavenson, N., Kuleshova, N., Sheikhet, A., and Tserenin, I.: 1994, *ApJS* **92**, 343

Martínez Núñez, S., Reig, P., Blay, P., Kretschmar, P., Lund, N., and Reglero, V.: 2003, *A&A* **411**, L411

Mavromatakis, F.: 1994, *A&A* **285**, 209

McCollough, M. L., Turler, M., Willis, D., and Shaw, S. E.: 2006, *The Astronomer's Telegram* **868**, 1

Motch, C. and Janot-Pacheco, E.: 1987, *A&A* **182**, L55

Parmar, A. N., White, N. E., Stella, L., Izzo, C., and Ferri, P.: 1989, *ApJ* **338**, 359

Piraino, S., Santangelo, A., Ford, E. C., and Kaaret, P.: 1999, *A&A* **349**, L77

Pottschmidt, K., Rothschild, R. E., Gasaway, T., Suchy, S., and Coburn, W.: 2006, in *AAS High Energy Astrophysics Division*, Vol. 9 of *AAS High Energy Astrophysics Division*, p. 18.21

Reig, P. and Coe, M. J.: 1998, *MNRAS* **294**, 118

Reig, P. and Coe, M. J.: 1999, *MNRAS* **302**, 700

Reynolds, A. P., Parmar, A. N., and White, N. E.: 1993, *ApJ* **414**, 302

Schönfelder, V.: 2001, *The Universe in Gamma Rays*, The Universe in Gamma Rays

Stollberg, M. T., Finger, M. H., Wilson, R. B., Scott, D. M., Crary, D. J., and Paciesas, W. S.: 1999, *ApJ* **512**, 313

Sun, X.-J., Kawai, N., Matsuoka, M., Yoshida, A., Yamauchi, S., and Koyama, K.: 1992, in Y. Tanaka and K. Koyama (eds.), *Frontiers Science Series*, p. 95

Sunyaev, R. A. and Titarchuk, L.: 1989, in J. Hunt and B. Battrick (eds.), *ESA SP-296: Two Topics in X-Ray Astronomy, Volume 1: X Ray Binaries. Volume 2: AGN and the X Ray Background*, pp 627–631

Torrejón, J. M., Kreykenbohm, I., Orr, A., Titarchuk, L., and Negueruela, I.: 2004, *A&A* **423**, 301

Tsygankov, S. S., Lutovinov, A. A., Churazov, E. M., and Sunyaev, R. A.: 2006, *MNRAS* **371**, 19

Walter, R., Favre, P., Dubath, P., Domingo, A., Gienger, G., Hermsen, W., Pineiro, J., Kuiper, L., Schmidt, M., Skinner, G., Tuttlebee, M., Ziegler, G., and Courvoisier, T. J.-L.: 2003, *A&A* **411**, L25

Westergaard, N. J., Kretschmar, P., Oxborrow, C. A., Larsson, S., Huovelin, J., Maisala, S., Martínez Núñez, S., Lund, N., Hornstrup, A., Brandt, S., Budtz-Jørgensen, C., and Rasmussen, I. L.: 2003, *A&A* **411**, L257

Wilson, C., Dwyer, M., Finger, M., Camero Arranz, A., Fabregat, J., Steele, I., and Coe, M.: 2006, in *AAS High Energy Astrophysics Division*, Vol. 9 of *AAS High Energy Astrophysics Division*, p. 01.62

Wilson, C. A., Fabregat, J., and Coburn, W.: 2005, *ApJ Lett.* **620**, L99

Wilson, C. A. and Finger, M. H.: 2006, *The Astronomer's Telegram* **877**, 1

Wilson, C. A., Finger, M. H., Coe, M. J., Laycock, S., and Fabregat, J.: 2002, *ApJ* **570**, 287

Chapter 6

SAX J2103.5+4545

SAX J2103.5+4545 was discovered by the *BeppoSAX* satellite (Hulleman et al. 1998). This source is a Be High Mass X-ray Binary pulsar with an orbital period of 12.68 d (the shortest known in Be/X-ray binary systems) and X-ray pulsations of 358 s. The likely optical counterpart is a B0Ve star (V = 14.2) at a distance of 6.5 kpc (Reig et al. 2004). Baykal et al. (2002) found a correlation between spin-up rate and X–ray flux during the 1999 outburst. Moreover, using *XMM-Newton* data a quasi-periodic oscillation at 22.7 s was discovered by İnam et al. (2004). This strongly suggests the formation of an accretion disk during periastron passage of the neutron star.

However, SAX J2103.5+4545 is not a typical Be/X–ray system. For instance, it does not follow the Corbet P_{orb}/P_{spin} correlation found in other accreting pulsar systems. A single and a double peak pulse profiles were found by Baykal et al. (2002) and İnam et al. (2004) respectively, in the soft X–ray range. In the hard X–ray range, Filippova et al. (2004) found a single peak profile. However, Falanga et al. (2005) and Sidoli et al. (2005) found a double peak profile. Previous works of SAX J2103.5+4545 during quiescence by Reig et al. (2005) showed that this is a very interesting case. They found that the source was emitting X–rays even after the complete loss of the circumstellar disk.

As a review, this source has been analyzed previously by Hulleman et al. (*BeppoSAX*, 1998), Baykal et al. & İnam et al. (*RXTE*, *XMM-Newton*, 2000, 2004, 2007), Reig et al. (optical & IR wavelengths, 2004, 2005), Filippova et al. (optical wavelength; *RXTE*, *XMM-Newton*, *INTEGRAL*, 2004), Blay et al., Falanga et al. and Sidoli et al. only with *INTEGRAL* data (2004, 2005, 2005, respectively), Blay (optical/X-ray correlation; *INTEGRAL* 2006) and Camero-Arranz et al. (2006) with *RXTE* & *INTEGRAL* .

We present a long-term pulse profile study, as well as a spectral and pulse-timing analysis of SAX J2103.5+4545 using data from both *INTEGRAL* and *RXTE* missions.

6.1 OBSERVATIONS AND DATA REDUCTION

SAX J2103.5+4545 has been detected by IBIS/ISGRI during the *INTEGRAL* PV phase and the GPS survey from 2002 to 2005 (MJD 52618 - MJD 53356), with a total observing time of ∼860 ks. We obtained a list of good events times per science window in the 20–60 keV band. *INTEGRAL* data reduction was carried out with the Offline Scientific Analysis software, release 5.0.

SAX J2103.5+4545 was also frequently observed with *RXTE* PCA and HEXTE from 1999 to 2004 (MJD 51512.8 - MJD 53047.9), with a total observing time of ∼1900 ks. However, it is important to note that during that period there were two gaps with no observations taken by those instruments (MJD 51900 - MJD 52000 and MJD 52025 - MJD 52430).

For each available observation, we have analyzed PCA Standard 1 data for the light curves and Standard 2 data for spectral analysis using Ftools V6.2. In addition, GoodXenon PCA data were selected for the pulse profile study, and HEXTE binned mode data from clusters A and B for the spectral analysis.

6.2 DATA ANALYSIS AND RESULTS

6.2.1 Pulse Profile

In order to study the long-term pulse profile dependence on luminosity, time and orbital phase, we extracted 548 *RXTE* PCA Standard1 light curves in the 2-60 keV energy range. The background was not subtracted in this first step. As usual, we corrected the times to the barycenter of the solar system, as well as for the orbital motion using the binary orbital parameters by Baykal et al. (2002). We constructed pulse profiles by fitting the data with a harmonic expansion in pulse phase (6 harmonics were used). Typically we use data spanning a ∼4000 s interval (∼11 pulse periods).

We have obtained 2–60 keV *RXTE* PCA pulse shapes varying from only single sinusoidal-like peak (phases 0.9–1), to profiles with two peaks (phases 0.7–0.9), and even occasionally with three (phases 0.5–0.7) and four peaks (0.2–0.5).

Taking consecutive pulse profiles in time during outbursts, and after visual inspection, we found no correlation between the patterns from one outburst to another, and even different rise and fall patterns for a given outburst (see Fig. 6.1, where Relative Flux is the number of counts per second and per PCU relative to the mean rate).

In general, the shapes vary from a strong single sinusoidal-like peak to double. However, three or even four weaker peaks are often found in addition to the main one. This source showed the same random behavior sorting the profiles by orbital phase (see Fig. 6.2). Moreover, we expected to obtain a base profile for a given X–ray luminosity. Nevertheless, we discovered a diversified range of shapes with no clear pattern (see Fig. 6.3).

In addition we have quantified the strength of all peaks. We have defined the strength of one peak of the pulse profile as the ratio (I_{max}-I_{np})/I_{np}, where I_{np} was defined as the non-pulsed flux at the middle point between the two adjacent minima of the peak. We have plotted this magnitude in time as well as versus the orbital phase and luminosity (2–60 keV rms flux) for 548 *RXTE* observations (Figs. 6.5, 6.6 and 6.7).

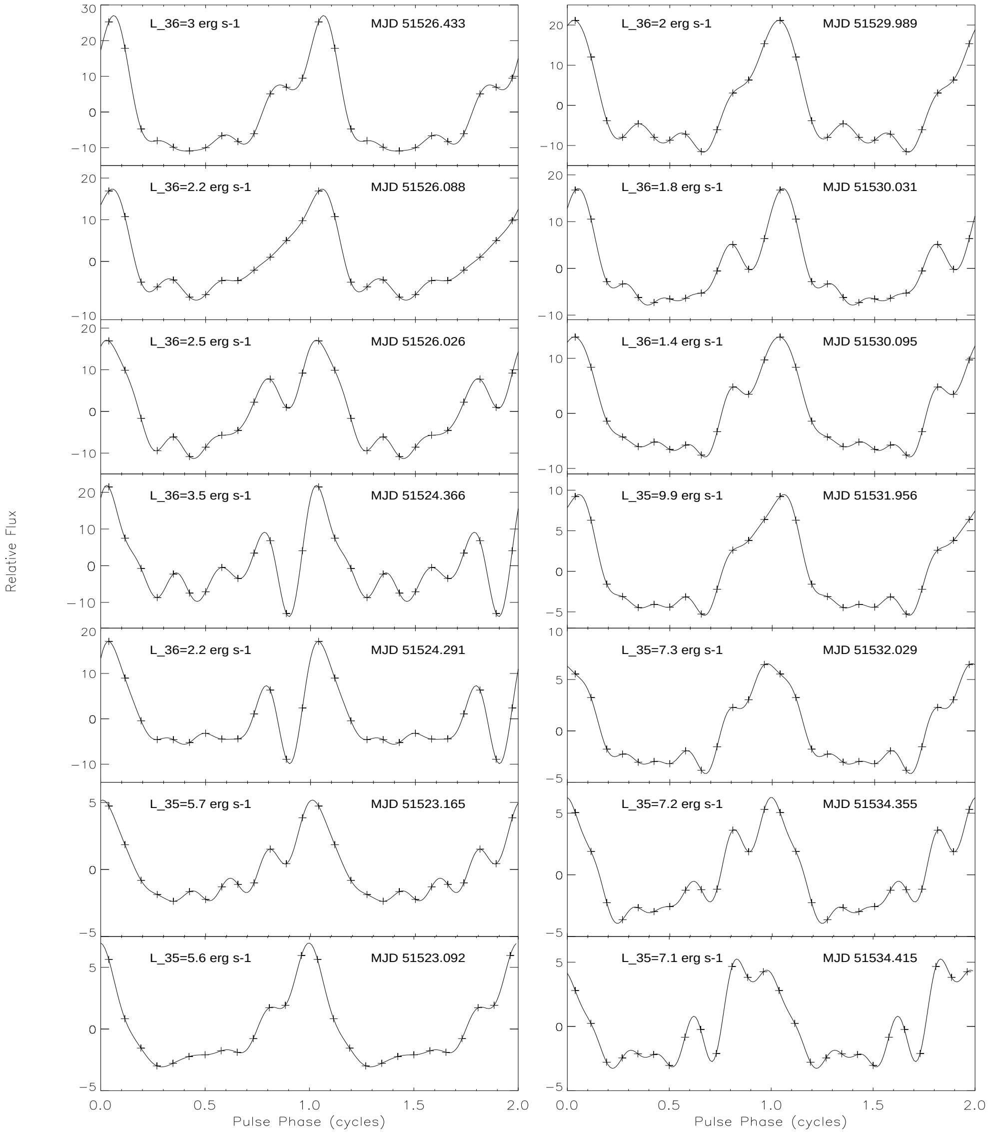

Figure 6.1: *RXTE* PCA (2–60 keV) pulse profiles consecutive in time during one outburst. Two cycles are plotted for clarity. The evolution on intensity of the first part of the outburst is plotted on the left column increasing from bottom to top. The fall is plotted on the right, with intensity decreasing from top to bottom.

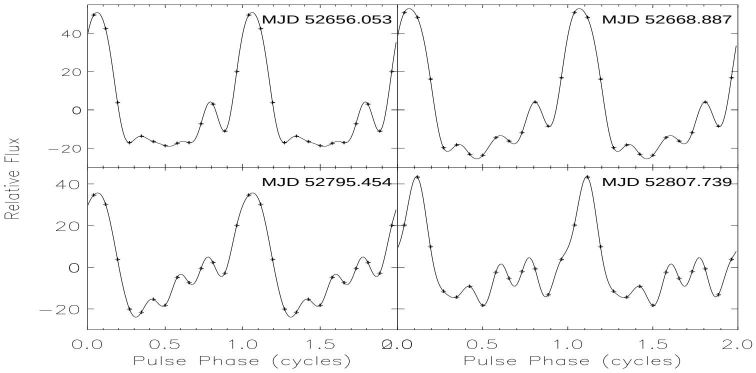

Figure 6.2: PCA (2-60 keV) pulse profiles at the same orbital phase (0.73±0.02 cycles) and at the same luminosity state ($5.62 \pm 0.04 \times 10^{+36}$ erg s^{-1}).

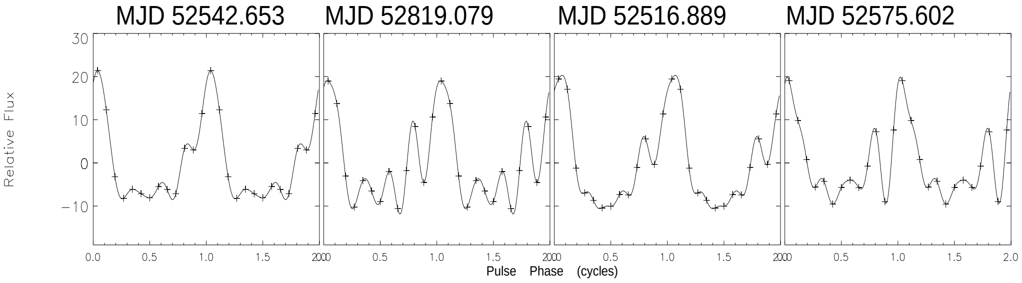

Figure 6.3: *RXTE* PCA 2-60 keV pulse profiles at the same luminosity state (L = $2 \pm 0.6 \times 10^{+36}$ erg s^{-1}; see Fig. 6.4).

In addition we have quantifed the strength of all the peaks. We have defined the strength of one peak of the pulse profile as the ratio (I_{max}-I_{np})/I_{np}, where I_{np} was defined as the non-pulsed flux at the middle point between the two adjacent minima of the peak. We have plotted this magnitude in time as well as vs. the orbital phase and luminosity (2-60 keV rms flux) for 548 *RXTE* observations (see Fig. 6.5, and 6.6). The root-mean-square flux of each observation was estimated as $[\sum_{i=0}^{1} (a_{ih}^2 - a_{iherr}^2)/2]^{1/2}$, where a_{ih} are the harmonics coefficients of the Fourier series for profile i and harmonic h, and a_{iherr} are the errors on those coefficients.

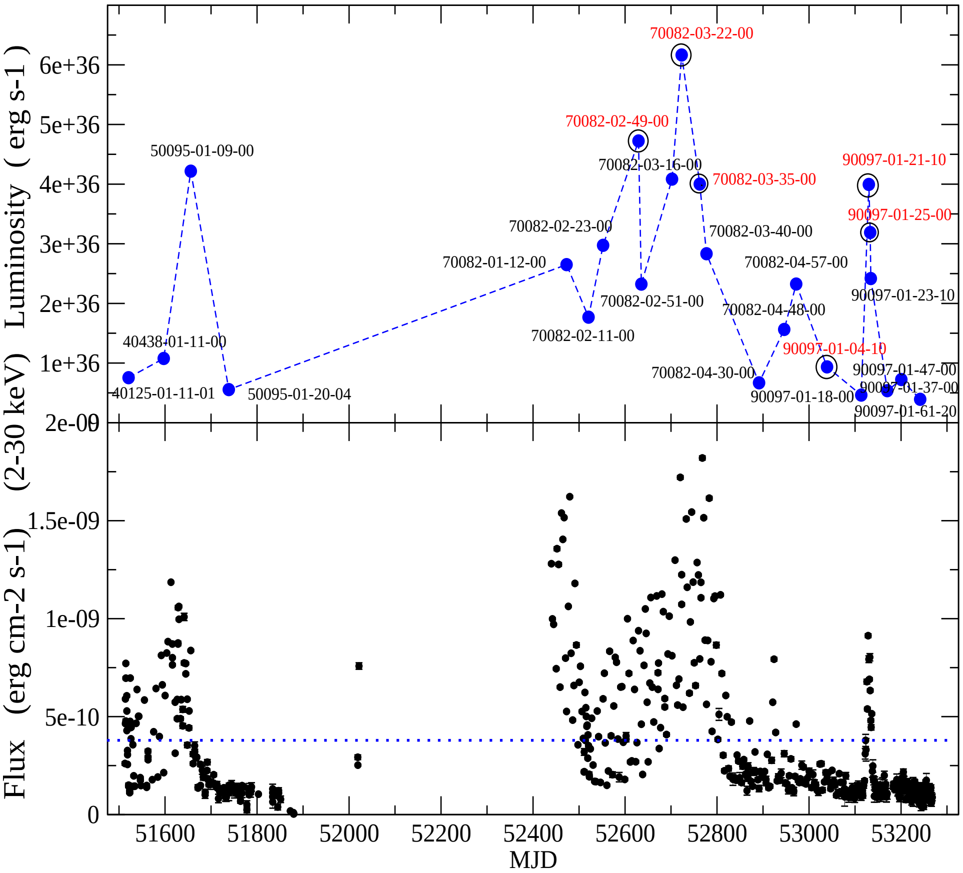

Figure 6.4: Top. Sample of PCA observations selected for the pulse profile intensity analysis. An extra circle indicates the *INTEGRAL* IBIS/ISGRI observation. Bottom. *RXTE* PCA flux in the 2-30 keV energy range. The horizontal dotted line denotes the luminosity level of ~5.6×10^{+36} erg s^{-1}.

Apparently, all four peaks seem to become more pronounced with increasing luminosity (see Fig. 6.8). However, computing the ratio of the main to the second peak of the pulse profile (P1/P2), and to the third (P1/P3) and to the fourth one (P1/P4), we found a wide range of the ratio values for a given luminosity state. This confirms our initial visual inspection, i.e., the pulse shapes vary with no clear pattern.

From Fig. 6.6 it appears that the strength of the four peaks increases with the luminosity. However, the correlation coefficients of the main, second, third and fourth peaks were 0.95, 0.83, 0.30 and 0.56, respectively (with significance values of their deviations from zero being 0, 1×10^{-41}, 0.0002, 2×10^{-14}). This suggests that all but the third are correlated with luminosity. In addition, computing the ratio of the main to the second peak of the pulse profile (P1/P2), and to the third (P1/P3) and to the fourth one (P1/P4), we found a wide range of the ratio values for a given luminosity state (see Fig. 6.8). This confirms our initial visual inspection, i.e., the pulse shapes vary with no clear pattern. On the other hand, we believed it was worthwile to compute also the correlation coefficients of P1/P2, P1/P3, P1/P4. They were all found to be ∼0.44, after rejecting some values with very large uncertainties. When we focused on the lower part of the flux range (rms Flux from 0 to ∼10), there was only a slight improvement on the P1/4 correlation coefficient, with a value of ∼0.50.

Once we confirmed that no evident temporal, orbital or luminosity correlations were found in the original PCA data sample in the 2-60 keV range, we decided to choose only 24 GoodXenon *RXTE* PCA observations for the energy dependence study. The chosen data set follows the long-term light curve behavior and covers MJD 51512.8 to 53047.9 (see Fig. 6.4). The PCA background subtracted light curves were obtained in four energy ranges: 2.06-5.31 keV, 5.31-7.76 keV, 7.76-13.93 keV, 13.93-20.62 keV.

Then, the same procedure was followed to construct the phases and then the profiles, as we described in Chapter 4.3.3 (Sec. 4.3.3). Typically, the duration of a *RXTE* PCA observation is about 3000 s and the profiles contain about 8 pulse cycles. To complete this study, we obtained a list of events in good time intervals for science window (ScW) with IBIS/ISGRI in the 20–60 keV energy band. Table 6.1 shows a summary of the detections and non detections with this instrument, as well as the number

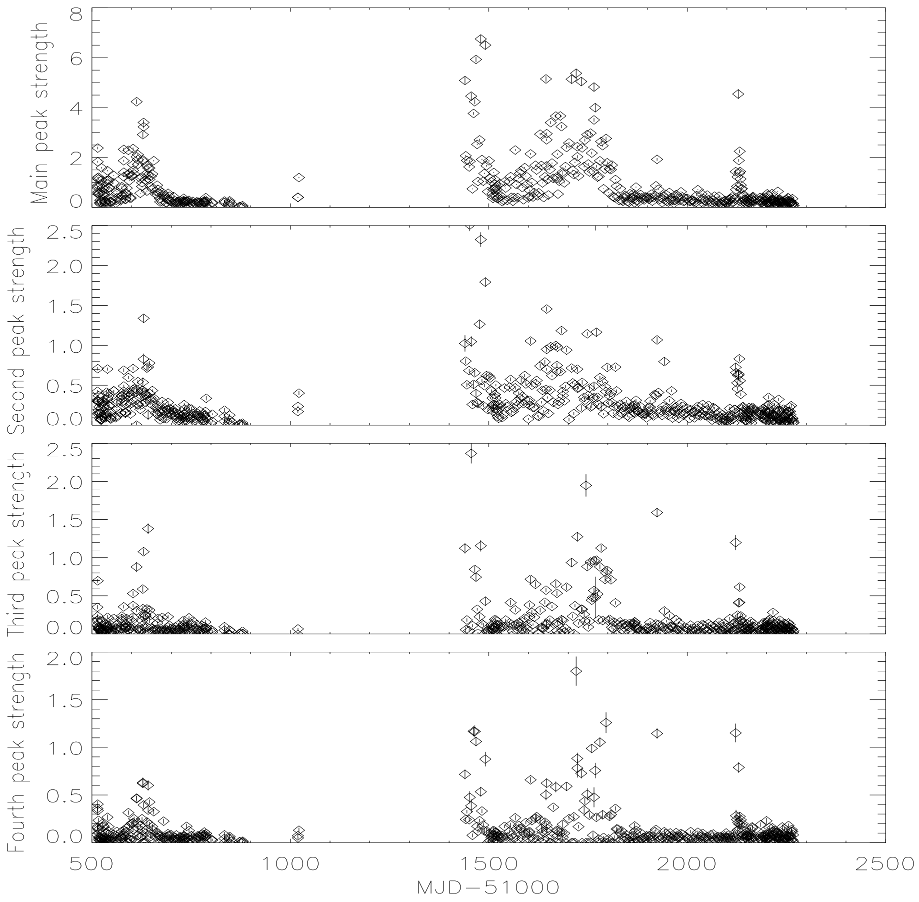

Figure 6.5: From top to bottom, the strength of all the four peaks is plotted vs. time.

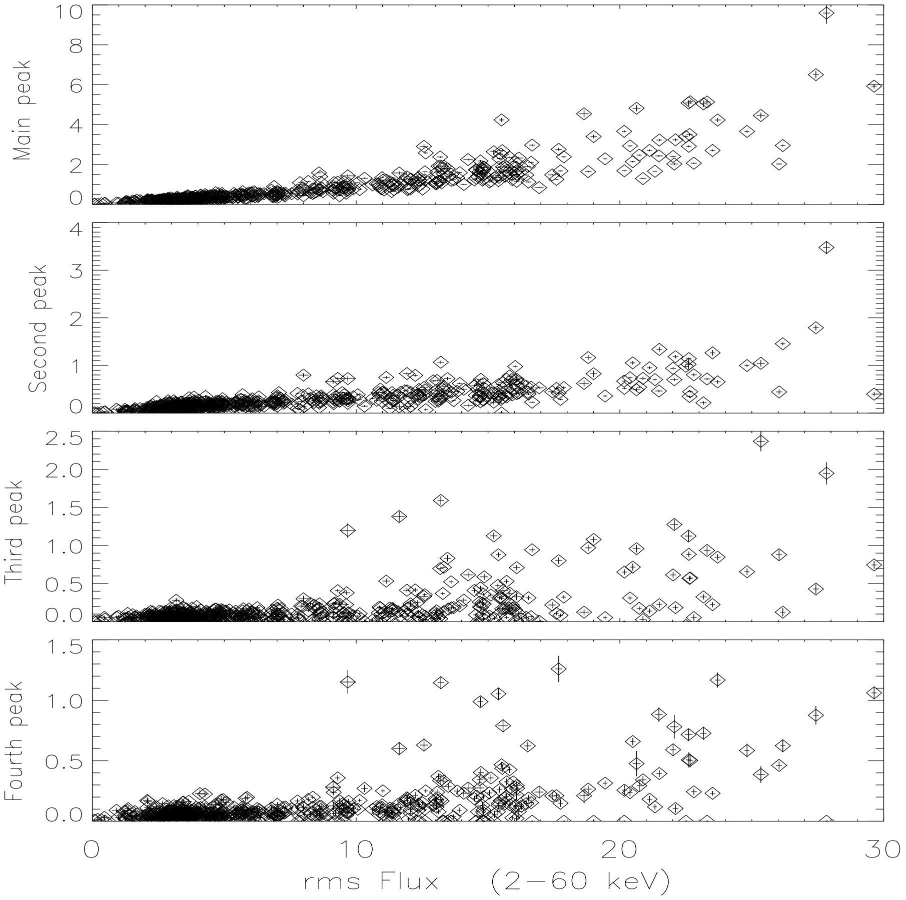

Figure 6.6: From top to bottom, the strength of all four peaks is plotted vs. luminosity (2-60 keV rms Flux).

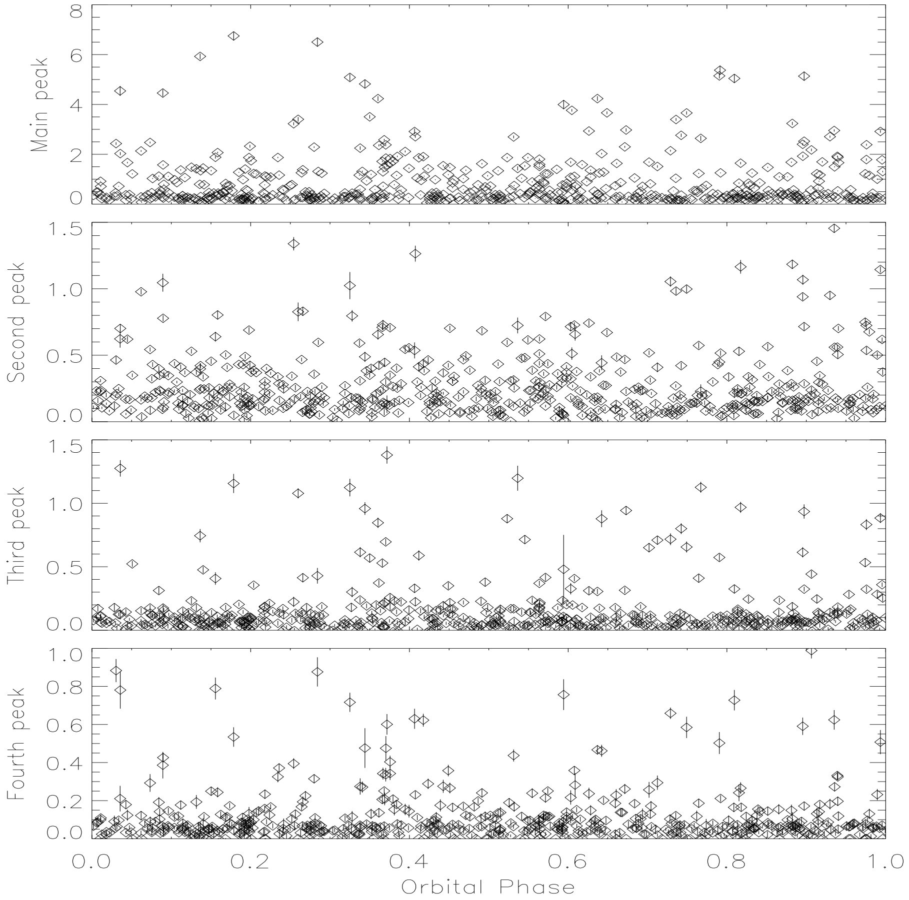

Figure 6.7: From top to bottom, the four peaks intensity is plotted vs. orbital phase.

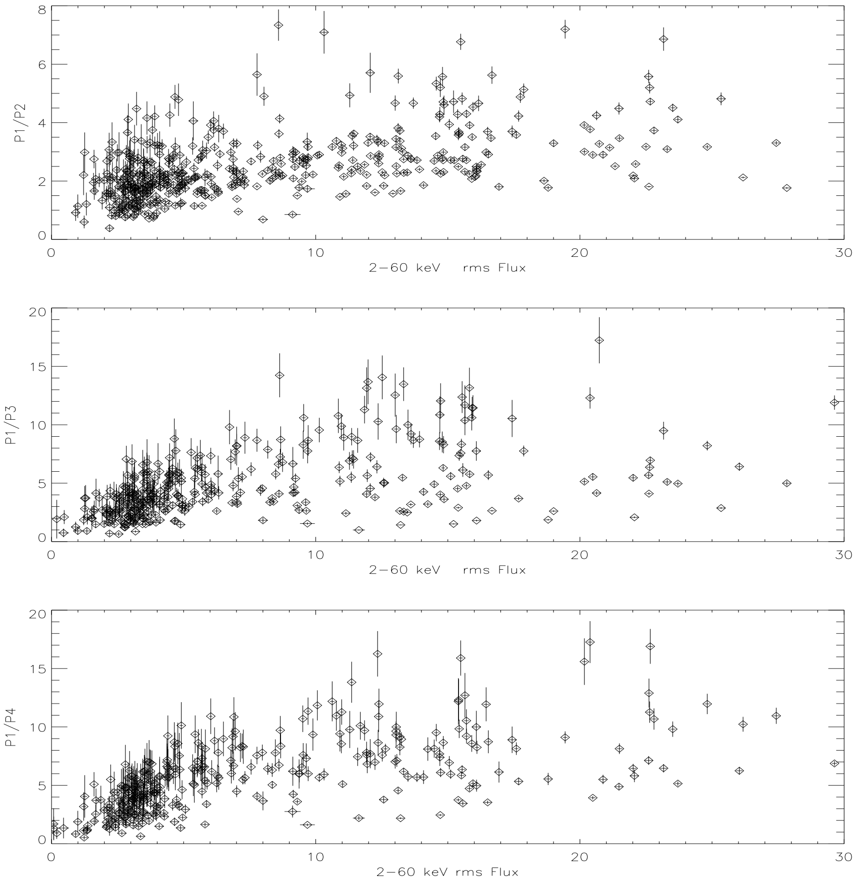

Figure 6.8: From top to bottom, the ratio of the main to the second, the third and the fourth peak plotted vs.luminosity (2–60 keV rms Flux). See text for a definition of each peak. We have rejected a few observations in the faint state with large uncertainties for clarity.

of ScWs used for making profiles. In Fig. 6.4 we marked on red (and an extra circle) those 6 points in which we also have an IBIS/ISGRI positive detection.

Figs. 6.9 and 6.10 show the evolution of some of the PCA profiles in four energy bands (with energy increasing from top to bottom). As we already mentioned, the profiles present a prominent peak among other features. These can vary from one to three peaks in addition to the main one. The general behavior is:

(a). First peak. The right side of the main peak (phases 0.0–0.2) remains quite similar as energy increases.

(b). Fourth peak. The region at phases 0.2–0.5 is not always a peak. But when a peak is present then it tends to strengthen as energy increases.

(c). Third peak. When a peak is present at phases 0.5-0.7, it's strength decreases with energy. This indicates that the third peak has a soften spectrum than the average.

(d). Secondary peak. At phases 0.7 to 0.9 a secondary peak or shoulder is present. It gets smaller with increasing energy.

(e). The dip in the main peak (phase 0.9) becomes deeper as the flux increases. The maximum depth is found in the 7.76–13.93 keV band, and then decreases again with energy. In particular, observations 70082-03-16-00 and 70082-04-57-00 show this notch especially deep and wide, evolving in this last observation to a strong double peak (see Figs. 6.9 and 6.10).

This trend is also seen in the 20-60 keV IBIS/ISGRI profiles (see Fig. 6.11), where the second and the third peaks are almost missing and the fourth one is stronger, but still weaker than the mean peak. It should be noted that in Fig. 6.11, the profile in the upper left is substantially offset from phase 1.0. The reason is that all of these profiles are arbitrary pulse phased and are not phase aligned with one another. The two profiles on the right are rather close in time to each other, so the phases of the main peak are similar while the ones on the left are more widely spaced in time.

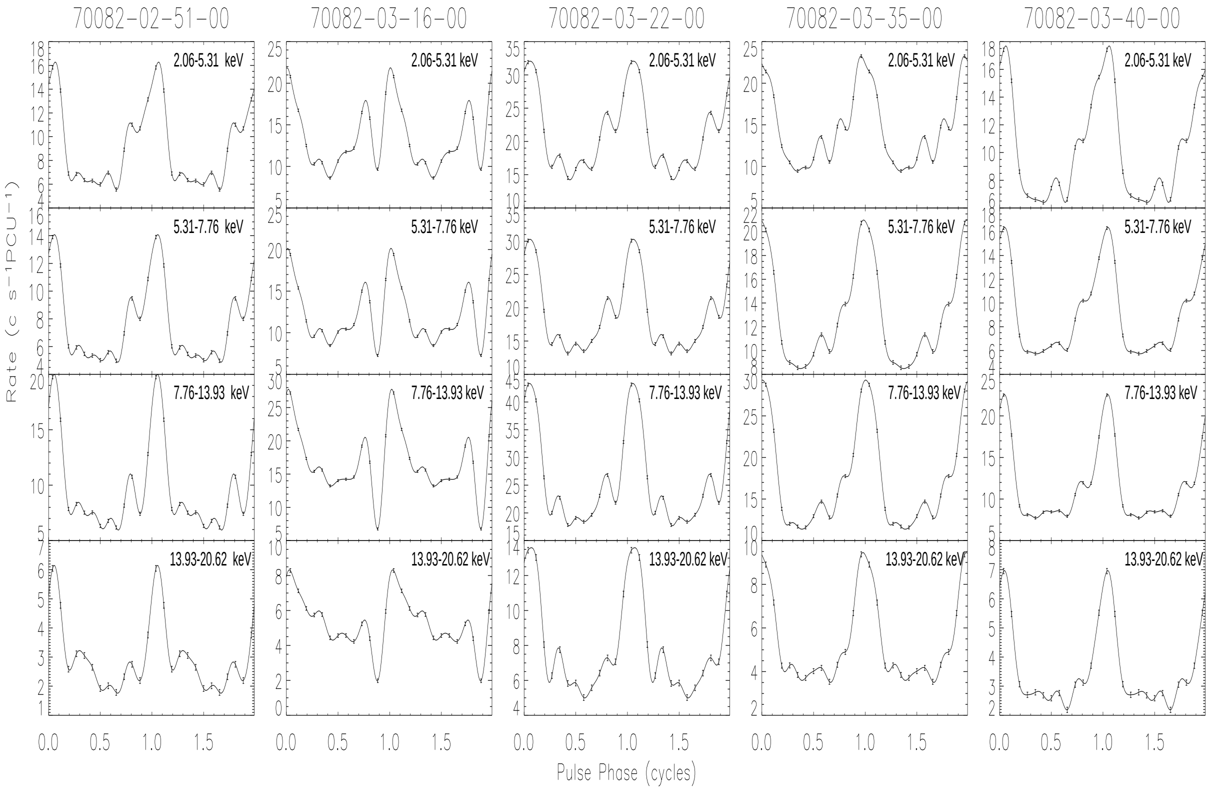

Figure 6.9: Evolution of SAX J2103.5+4545 PCA pulse profile with intensity in 4 energy bands (from top to bottom). They are sorted consecutive in time during the brightest period (MJD 52650-52800) of the source.

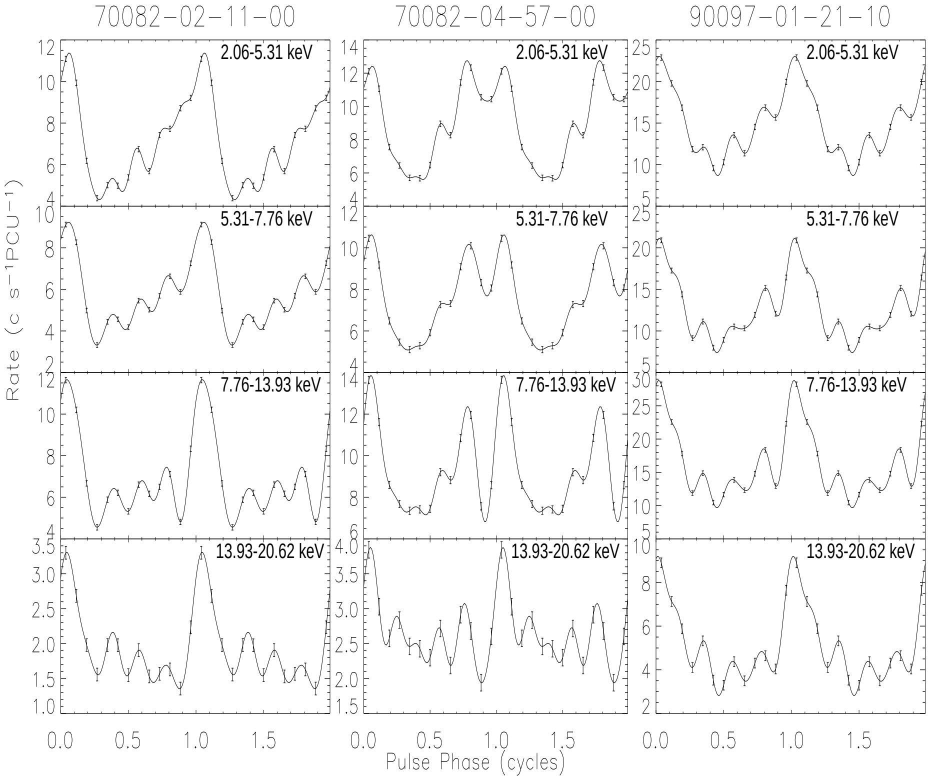

Figure 6.10: Some examples of SAX J2103.5+4545 PCA pulse profiles showing a more complex structure, in the same 4 energy bands.

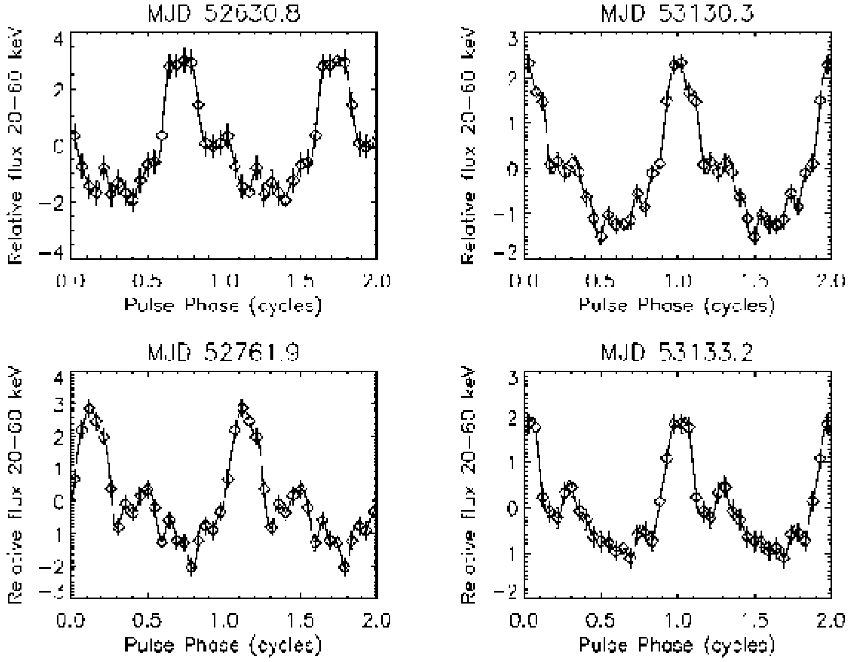

Figure 6.11: ISGRI (20-60 keV) mean pulse profiles of SAX J2103.5+4545 generated by combining profiles from individual *INTEGRAL* ScWs (see Table 6.1). The 20-60 keV band was selected for making profiles in order to increase the statistics.

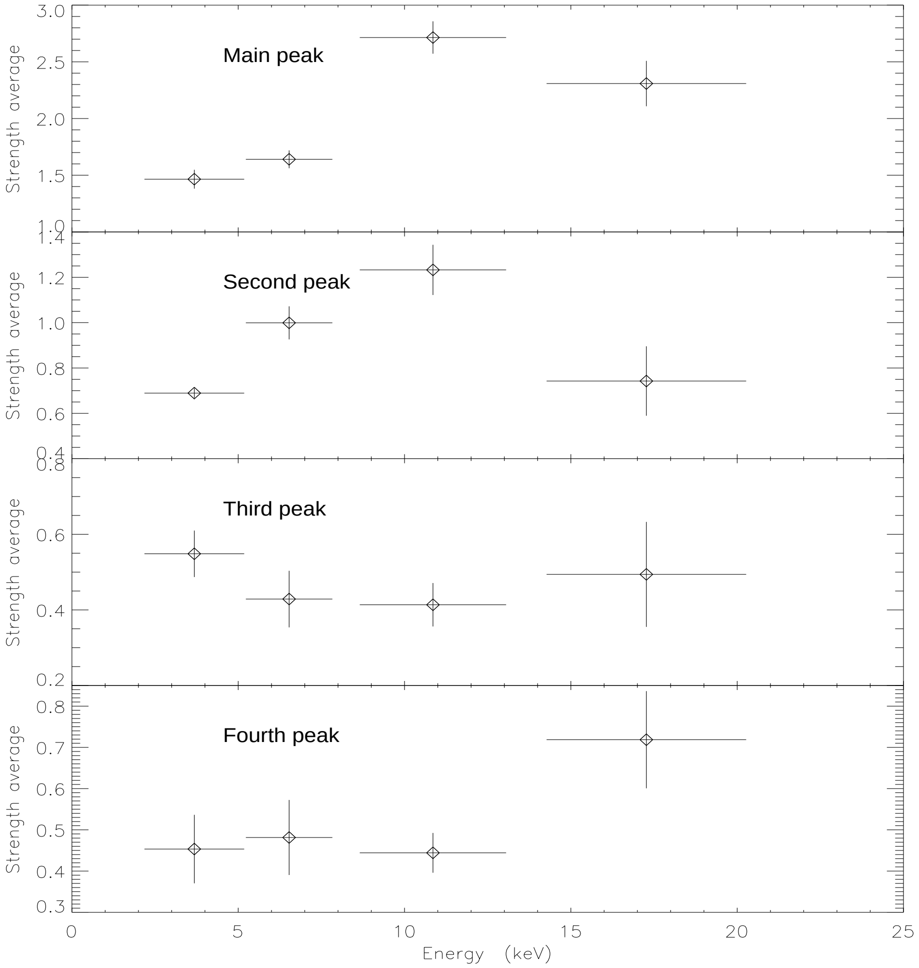

Figure 6.12: Averaged peaks intensity evolution with energy. The behavior displayed here follows the one proposed from points (a) to (e) in the text.

The averaged strength of the main and the rest of the peaks have been plotted vs. energy band in Fig. 6.12. We can see the peaks evolution with energy suggested in points (a) to (e).

6.2.2 Spectral Analysis

We have obtained 548 spectra from 6 years of *RXTE* PCA and HEXTE data (MJD 51512.8 – MJD 53047.9). For each observation, we have selected PCA Standard 2 data and HEXTE binned mode data from clusters A and B. Then, fluxes in all the different energy ranges were obtained by fitting a cut-off power law model plus a photoelectric absorption (phabs×(gauss + cutoffpl)) to each 2.7-70 keV spectrum, fixing the iron line value and its width to 6.43 keV and 0.165, respectively (Baykal et al. 2002). We have included 1% of systematics.

In Fig. 6.14 (bottom) we show the long-term flux history of SAX J2103.5+4545 using *RXTE* and *INTEGRAL* data, which follows very nicely the general trend of the long-term frequency derivatives history obtained after the timing analysis (see next section).

To study the spectral variability of SAX J2103.5+4545 we have computed the long-term hardness ratios (HR) using two energy bands: the soft band was 2-10 keV (S), and the hard band was 10-30 keV (H) (defined as HR = H/S). Fig. 6.13 (top) shows an average of the calculated HR vs. time and intensity, using those energy bands. In the HR vs. intensity plot we took out a few detections corresponding to the faintest state, due to their enormous error bars, which hid the general trend.

The correlation between the HR either with time or intensity is clear. We can see that the source becomes harder when the flux is higher. In the same figure we have included some plots showing the evolution of the absorption, the Photon Index, the cutoff and the reduced χ^2 with intensity. We have also rejected the faintest flux values since the uncertainties obtained in the parameters were very large.

We found variable behavior just in the Photon Index vs. intensity plot. The larger is the flux the lower is the the photon index. This anticorrelation was expected and shows again that in the bright state the

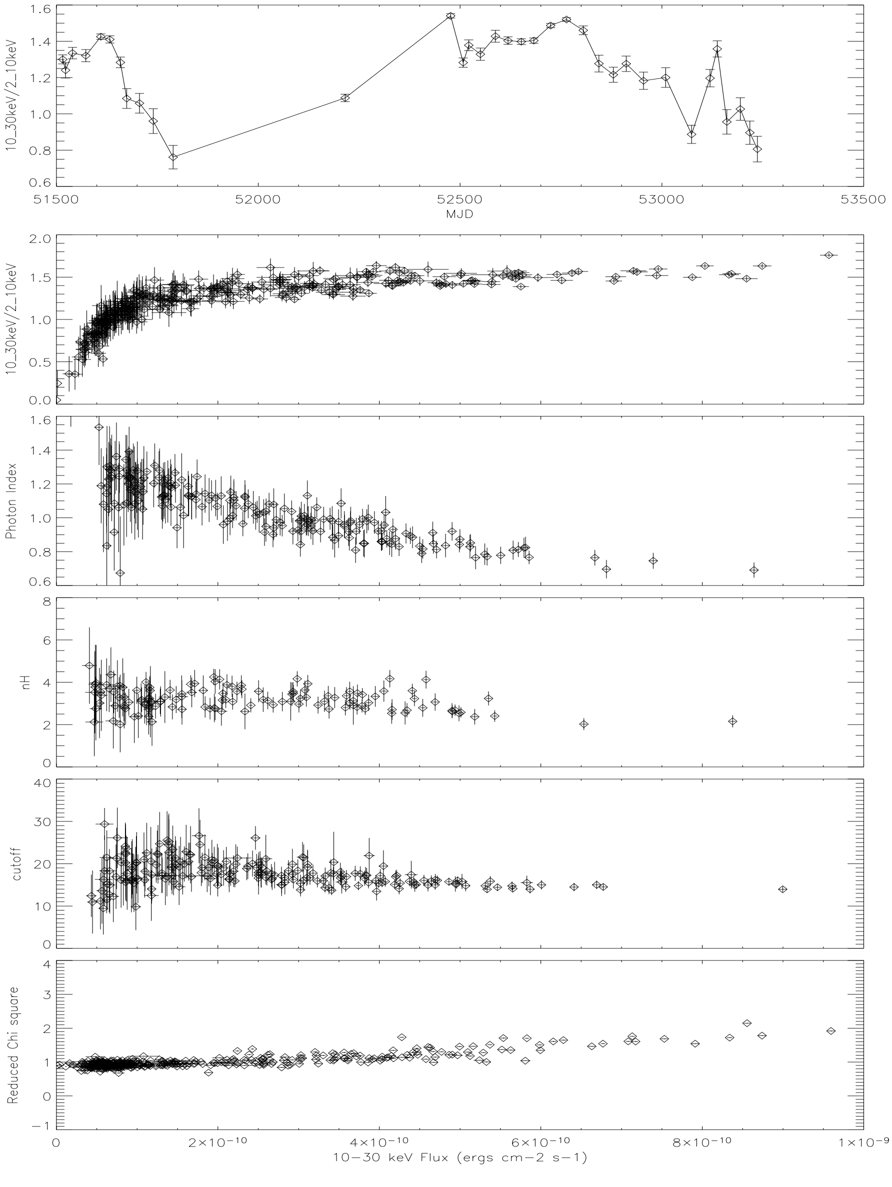

Figure 6.13: Top. Long-term Hardness ratios history. From middle to bottom: HR-intensity diagram and spectral parameters evolution vs. intensity.

spectrum of SAX J2103.5+4545 is harder than in the faint state. It is clear that the fitting model applied is not the perfect one for the bright state, as we can see in the reduced χ^2 vs. intensity figure. Nevertheless, it was found to be the best simple model for all the ~500 spectra analyzed. Baykal et al. (2007) suggested that this type of spectral softening with decreasing flux was found to be mainly a consequence of mass accretion rate change and was not necessary to be related to a significant accretion geometry change.

6.2.3 Timing Analysis

Phasing

We selected again the 548 *RXTE* PCA observations for the long-term timing analysis. We constructed SAX J2103.5+4545 pulse profiles as we described in Chapter 4.3.3 (Sec. 4.3.3), grouped into 12.69 d intervals for the frequency search.

As we stated before, with *INTEGRAL* IBIS/ISGRI data the approach was different, due to the non continuous observational pattern and the sensitivity of the ISGRI detector. A template profile was created from the average profile from the set of ISGRI ScWs (see Table 6.1).

Fig. 6.14 shows the long-term spin-frequency and spin-up rate history obtained after repeating the grid search with the new profiles and phases. For IBIS/ISGRI the spin rates were computed by differencing adjacent frequency measurements and dividing by the corresponding time difference. The PCA spin rates were computed by fitting a quadratic function to the phases, which were divided in 29 time intervals.

We see that the first outburst of SAX J2103.5+4545 started with a spin-up trend (bright state), made a transition to a steady spin rate (faint state), and then begin a spin-down trend. The following available data started with a quick spin-up trend (bright state), and then a transition to a slower spin-up rate (faint state). We have selected the *RXTE* HEXTE 40–60 keV flux for the bottom panel of Fig. 6.14, to avoid possible absorption effects.

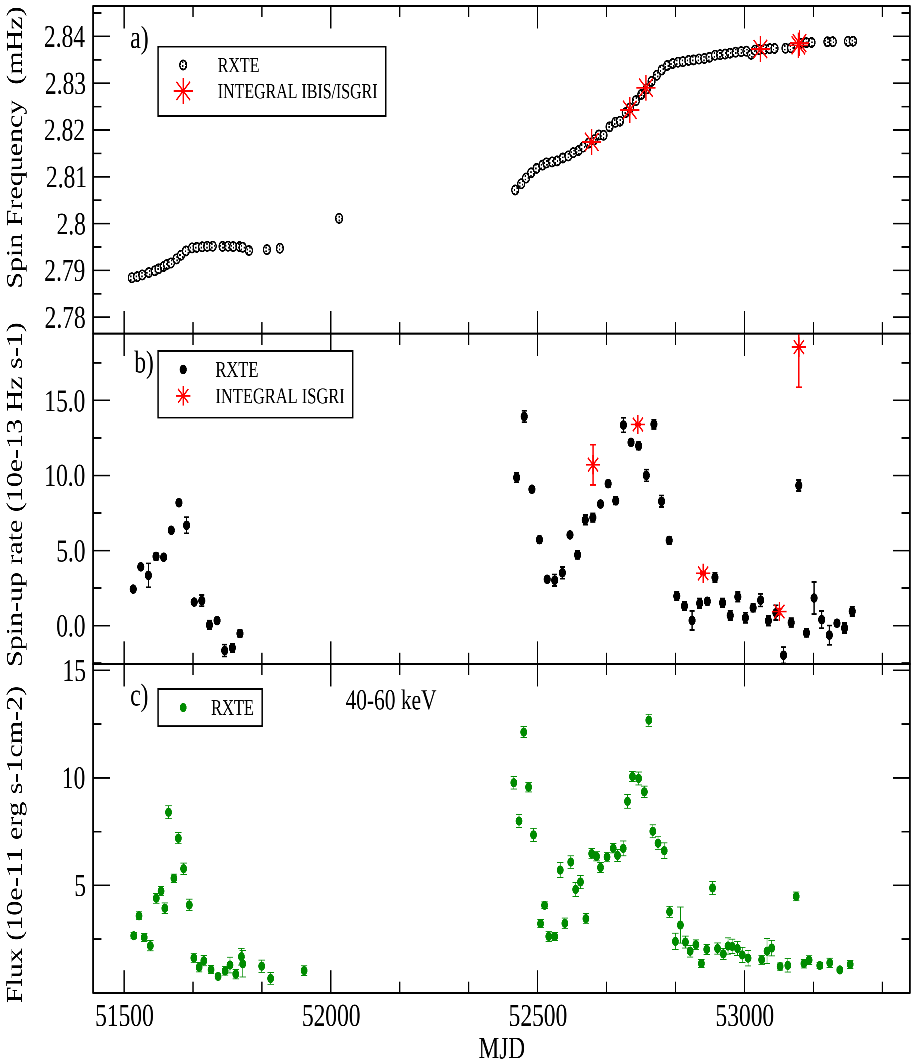

Figure 6.14: Top: Long-term frequency history. Middle: Averaged spin-up rates history. Bottom: 40-60 keV *RXTE* HEXTE averaged fluxes. The strong correlation between spin-up rate and X-ray flux indicates that an accretion disk is present during periastron passage.

Table 6.1: Pulse Period detections of SAX J2103.5+4545 with IBIS/ISGRI. The second column shows the number of ScWs used for the computation in each epoch.

Epoch (MJD)	number of ScWs	Pulse Period (s)
52619.299	6	-
52630.755	49	354.927 ±0.014
52637.303	18	-
52722.884	3	354.072±0.014
52761.947	35	353.478±0.017
52797.040	2	-
52805.978	3	-
52820.945	2	-
53021.331	74	-
53038.548	119	352.446±0.019
53041.996	21	-
53102.514	3	-
53130.288	77	352.350±0.006
53133.176	51	352.29±0.01
53188.993	2	-
53258.517	3	-
53333.056	6	-
53349.280	5	-
53354.965	4	-

Comparing the fluxes obtained in the non averaged long-term light curve (the one composed of around 500 individual flux measurements from the spectra; see bottom of Fig. 6.4), we realized that while SAX J2103.5+4545 was in the faint state (MJD 53100), suddenly it increased dramatically its luminosity for a short time period. This was not the first episode of such a behavior but the strongest one. Therefore, the ISGRI frequency derivative outlier cannot be ruled out since it seems it is related to a significant event.

Orbit fitting

In order to achieve a better characterization of the geometry of this binary system, we have used *RXTE* PCA Standard1 data to obtain a new set of orbital parameters. Following the method described in Chapter 4.3.3 (Sec. 4.3.3), we split the *RXTE* results into 29 intervals (3 orbits) and fit an orbit to the phases in each interval (the orbital Period was fixed).

The final orbital parameters were obtained from a unweighted average of the best fit parameters from just 28 intervals. As we mentioned above, taking a look at the long-term light curve we noticed that around MJD 53100 took place a huge and narrow spike while the source was in the faint state. This surprisingly behavior was also noticed in the orbital fit number 26, obtaining a highly dispersed fit that was finally rejected. The final orbital epoch and period were obtained by making a linear fit to the 28 best fit orbital epochs. The errors in these parameters were estimated from the scatter of the best fit parameters. Table 6.2 lists the final orbital parameters obtained.

Our orbital parameters agree within errors with those obtained by Baykal et al. (2007) with the exception of $a_x \sin i$, where our value is $\sim 7\sigma$ larger. Since both results were obtained from essentially the same data set, the difference must be due to the different approaches taken in the analysis. Baykal et al. analyzed data from 11 intervals of varying size which where fit with a global orbital model, with independent 5th order phase models for each interval. We made local orbital fits for 28 intervals of 3 orbit duration including a second order phase model with each, and then averaged the local orbital parameters to obtain a mean orbit model.

Table 6.2: Orbital solutions for SAX J2103.5+4545.

	Baykal et al. (2002)	İnam et al. (2004)	Sidoli et al. (2005)	Baykal et al. (2007)	Present work
$T_{pi/2}$ (MJD)	51519.3±0.2	52633.90±0.05		52469.336±0.057	52545.411±0.024
P_{orb} (days)	12.68±0.25		12.670±0.005	12.66536±0.00088	12.66528±0.00051
$a_x \sin i$ (lt-s)	72±6			74.07±0.86	80.81±0.67
e	0.4±0.2			0.4055±0.0032	0.401±0.018
ω	240±30			244.3±6.0	241.36±2.18

However, here the torque variations are not random, but are correlated with the flux, which at higher flux levels is correlated with orbital phase. One possibility is that some of the orbital signature is being absorbed into the phase model used for each interval in the Baykal et al. analysis, which contains 4 parameters to describe the intrinsic torque during the each interval. The Baykal et al. analysis used on average 0.55 torque parameters per binary orbit, while our torque models uses 0.33 torque parameter per orbits.

In addition, the shortest intervals in the Baykal analysis, which used up to 1.9 torque parameters per orbit, tended to occur at the highest flux levels, where the data has more weight in the global fit. Out of 28 estimations of $a_x \sin i$ we find only two that have values below the Baykal et al. value.

Spin-up Torque-Flux correlations

We averaged the non absorbed flux every 1.5 and 2.5 pulsar orbits. The 1.5 orbits average is the smallest time interval that allowed us to fit a quadratic function to the phases when the spin rates were computed. The second time interval of 2.5 orbits was chosen as a good representative of the general trend.

Fig. 6.15 shows more clearly the spin-up rate vs. flux correlation. We have fitted both data sets with a single power law (*solid line*). In the same figure, a dashed line denotes our best-fit power law with an index fixed at 6/7, which represents the relationship between spin-up and flux predicted by simple accretion theory (see Eq. 3.10, Chapter 3).

In principle, Fig. 6.15 seems to be nearly identical to Fig. 5 from Baykal et al. (2007), and our results confirm those found by them. However, we believe that an interesting feature should be emphasized. Data averaging over 1.5 orbits scatters more than averaging over 2.5 orbits. It appears that the smaller is the average the bigger is the scattering. This might suggest that, in addition to the disk accretion mechanism, there seems to exist another mechanism producing erratic variations.

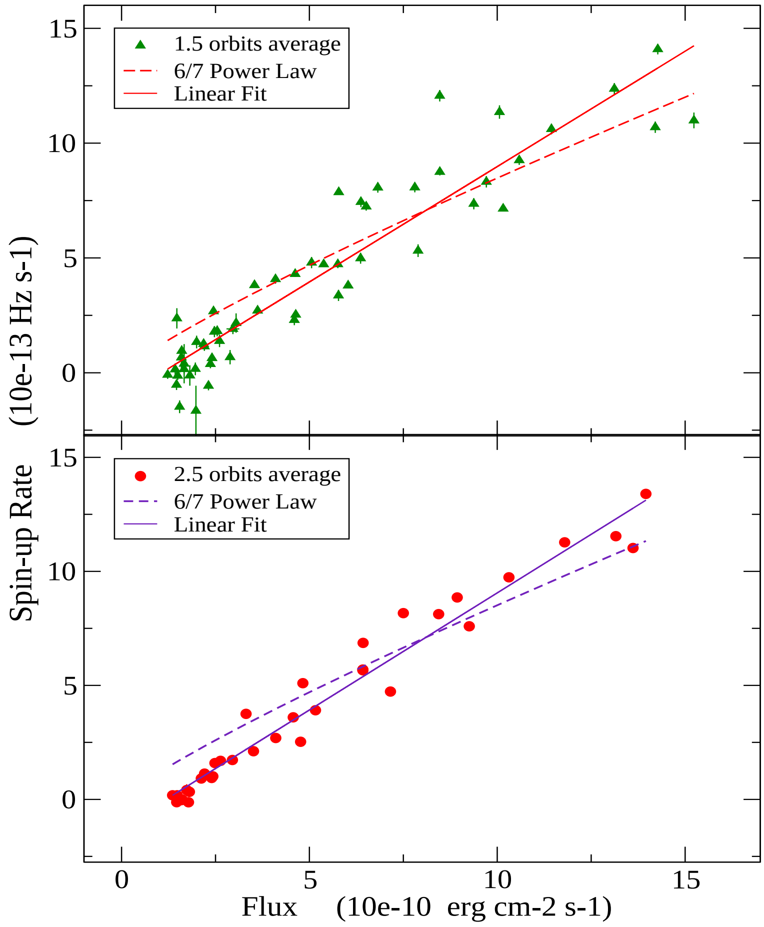

Figure 6.15: Spin-up rates vs. *RXTE* 2-100 keV non absorbed averaged Flux every 1.5 and 2.5 orbits. A linear fit was found the best one.

6.3 DISCUSSION

6.3.1 The Pulse Profile

Some X-ray pulsars, like EXO 2030+375 (Parmar et al. 1989), show a clear pulse shape dependence on source luminosity, most likely controlled by accretion rate. Others show very similar pulse profiles despite large variation in flux (Vela X-1). Differences in X-ray pulse profiles are considered to be due to the differences in the geometrical configuration with respect to the rotational axis of the neutron star, the axis of magnetic dipole moment, and the observer's line of sight (Nagase 1989). The structure of the accretion column determines the basic profile of the pulse pattern.

However, simple geometric models with two pencil beams coming from the magnetic poles or two bright spots on the neutron star surface, cannot explain the non variability observed in some other systems, like Vela X-1. Previous studies by Kreykenbohm et al. (2002) confirmed for that system a very complex pulse profile at low energies (below 6 keV), showing a five peak structure. Above 10 keV the pulse profiles evolved into a simple double peak. They pointed out that a good description of the processes responsible for the complex shape at low energies is still missing.

In the present work, the 2-60 keV SAX J2103.5+4545 pulse profiles obtained with *RXTE* PCA were found to be peculiarly complex and variable either with luminosity, time or orbital phase. The pulse shapes seem to vary randomly from single gaussian peak to profiles with two, tree and even occasionally four peaks, with no evident pattern. For a given energy range, the temporal variability of the pulse profile of SAX J2103.5+4545 was explained by Sidoli et al. (2005) as likely due to a time-dependent emission pattern, or to changes in the opacity of the magnetized plasma where the radiation propagates.

Previous works by Baykal et al. (2002), Falanga et al. and Sidoli et al. (2005) obtained a single peak pulse profile in soft X–ray bands, using *RXTE* and *INTEGRAL* data. However, İnam et al. (2004) found a double peak profile using *XMM-Newton*, but this exception could be compatible with the variability seen in our study for SAX J2103.5+4545.

In the hard X–ray range, we have obtained much simpler double peak profiles 20–40 keV *INTEGRAL* ISGRI profiles, in agreement with previous results by Falanga et al. and Sidoli et al. (2005). Filippova et al. (2004) published a 20–100 keV single peak pulse profile using PV phase *INTEGRAL* data. Taking into account the uncertainties in their results, this could be compatible with our PV phase results (see Fig. 6.11, MJD 52630 pulse profile).

In addition, our study allowed us to confirm an energy dependence pattern for SAX J2103.5+4545. İnam et al. (2004) found practically no variation in the energy dependence of the 0.9–11 keV pulse profiles, which is not in agreement with our results. Falanga et al. (2005) obtained an energy dependent secondary peak around phase 0.2, which became more evident at energies above 20 keV. This peak might be compatible with the evolution of our peak at phase 0.7. They also claimed that at phase 0.6 some very short variation features (hicc-ups) were present, in agreement with those observed by İnam et al. (2004) using *XMM-Newton* data. These "hicc-ups" were only visible at high energies (40–80 keV). Again, these features might be compatible with our dip at phase 0.9.

It is generally accepted that in order to explain the energy-dependent changes seen in the pulse profile, the anisotropic radiation transfer must be taken into account (Nagase 1989). Previous studies by Kraus et al. (2003) found that energy-dependent peaks in medium luminosity binary X–ray pulsars, are mainly due to energy-dependent relative importance of the halo (which forms around the accretion funnel where the neutron star surface is irradiated) and the column contributions to the observed flux Sidoli et al. (2004).

For SAX J2103.5+4545, Falanga et al. (2005) found that changes in the morphology of the pulse profile as a function of energy were consistent with variations in the spectral components visible in their pulse phase resolved spectra analysis. Their study also showed that differences in the double-peak can be modeled by a different scattering fraction between the radiation from the two magnetic poles.

6.3.2 Nature of the Source

First studies of SAX J2103.5+4545 by Baykal et al. (2002) showed a transition from spin-up to spin-down in the *RXTE* observations from an outburst in November 1999, suggesting the presence of an accretion disk. The detection of a quasi-periodic oscillation at 22.7 s discovered by İnam et al. in 2004, provided further evidence for its existence. The spin-up rate and X-ray flux correlation is also observed in the present work, confirming that an accretion disk is present during periastron passage. Previous results by İnam et al. (2004) and Baykal et al. (2002, 2007) are in good agreement with our results. In general, neither the pulse period estimations from Sidoli et al. (2005) nor those from Blay (2006) are in good agreement with our results.

An accretion disk will form if the specific angular momentum of the accreted material ℓ (see Eq. 3.7, Chapter 3) is comparable to the Keplerian specific angular momentum at the magnetospheric radius ℓ_m (see Eq. 3.9, Chapter 3). To estimate ℓ for SAX J2103.5+4545, we assumed typical pulsar parameters, and typical values of $\dot{\nu} \simeq 7 \times 10^{-13}$ Hz s^{-1}, $F \simeq 7 \times 10^{-10}$ erg cm^{-2} s^{-1} (see Fig. 6.15). The distance of the source from optical observations is 6.5±0.9 kpc (Reig et al. 2004, 2005). Several authors have discussed a possible value for the magnetic field. Recently, Baykal et al. (2007) obtained a value of 16.5×10^{12} Gauss. But this implied a distance of 4.5 kpc. In order to explain the spin-up rate observed, and assuming that the distance of 6.5 kpc is correct, Sidoli et al. (2005) obtained a magnetic field of $\sim 1.6\times10^{12}$ Gauss. No cyclotron lines have been observed from this source. One explanation could be a high magnetic field as proposed by Baykal et al. (2007) which would imply a fundamental line at ~200 keV.

We have summarized in Tab. 6.3 the different values obtained for ℓ, using the two magnetic field measurements discussed above, assuming two distance values of 6.5 kpc and 4.5 kpc, and for $k = 0.91$ (simple spherical accretion model) and 0.47 (Ghosh and Lamb (1979) model). As expected, all cases confirm that a disk is likely to be present. Only those cases with lower ℓ/ℓ_m ratio might indicate that alternating periods of wind accretion and disk accretion could also take place in this system.

It is generally accepted that the propeller effect is likely connected to quiescence states. Reig et al. (2005, and references therein) stated as possible values for the threshold X–ray luminosity $\sim 10^{32}$–10^{33}erg s^{-1}. Unusually, from photometric and spectroscopic observations performed in 2004 (Reig et al. 2005) and during the faint state of this source, SAX J2103.5+4545 continued emitting X–rays even after having completely lost the disk.

To determine whether or not centrifugal inhibition of accretion is operating, we estimated the flux at the onset of this effect by equating the magnetospheric radius to the corotation radius. For SAX J2103.5+4545 the threshold flux for the onset of centrifugal inhibition of accretion, i.e.,

$$F_{min} \simeq 2 \times 10^{-12} erg\ cm^{-2} s^{-1} \times k^{7/2} \mu_{30}^{2} M_{1.4}^{-2/3} R_{6}^{-1} P_{354.9s}^{-7/3} d_{kpc}^{-2} \qquad (6.1)$$

where μ_{30}, $M_{1.4}$, R_6, and $P_{354.9}$ are the pulsar's magnetic moment in units of 10^{30} G cm^3, mass in units of $1.4M_{\odot}$, radius in units of 10^6 cm, and spin period in units of 354.9 s, respectively. Tab. 3 shows our measured F$_{min}$ using equation 6.1. Our observed upper limit fluxes are in the range $\simeq$ (5–0.9)$\times 10^{-12}$ erg cm^{-2} s^{-1}, consistent with SAX J2103.5+4545 entering the centrifugal inhibition of accretion regime only for $B = 16.5\times10^{12}$ G (see Tab. 6.3).

In principle, as Reig et al. (2005, and references therein) pointed out, it is still possible to produce X–rays when the propeller effect is working (e.g. through accretion onto the magnetosphere as opposed to onto the neutron star surface or through leakage through the magnetosphere). However, due to the fact that SAX J2103.5+4545 is located in the region of wind-fed supergiant binaries in the P$_{spin}$–P$_{orb}$ diagram, accretion from the stellar wind of the B0 companion might be the origin of the observed luminosity. Reig et al. (2005) closed their work saying that the relatively narrow orbit of SAX J2103.5+4545 implies that the wind, at the position of the neutron star, does not reach its terminal velocity, but varies in the range $\sim$[0.7–0.9].

Table 6.3: Comparison of the specific angular momentum of the accreted material to the Keplerian specific angular momentum at the magnetospheric radius. An estimation of the flux for the onset of centrifugal inhibition of accretion is also shown.

	B= 16.5×10^{12} G (4.5 - 6.5) kpc	B= 1.65×10^{12} G (4.5 - 6.5) kpc
k=0.91	ℓ= (0.61 - 0.33)ℓ_m	ℓ= (1.19 - 0.63)ℓ_m
	F$_{min}$*= (20.4 - 9.8)	F$_{min}$*= (0.2 - 0.097)
k=0.47	ℓ= (0.85 - 0.45) ℓ_m	ℓ= (1.65- 0.88) ℓ_m
	F$_{min}$*= (2.02 - 0.97)	F$_{min}$*= (0.02 - 0.0097)

* ×10^{-12} erg cm^{-2}s^{-1}

6.3.3 Transient vs. Persistent

Up to now, SAX J2103.5+4545 has been classified as a transient Be/X–ray binary system. However, as we stated above, this source is a very interesting case. Maybe, its location in the wind-fed supergiant region might also be the origin of its complex pulse profile behavior. It should be noted that a large population of persistent, likely wind-accreting supergiants are being discovered by the *INTEGRAL* mission.

In the present work SAX J2103.5+4545 was detected clearly in all our observations, hence there is no well-defined limit dividing outbursting vs. quiescence. Defining a threshold for the observed flux at 5×10^{-12} erg cm^{-2}s^{-1}, we can identify 5 outbursts from Fig. 6.4 (bottom). Ignoring the fact that the luminosity never exceeds 10^{37} erg cm^{-2}s^{-1}, the first three might qualify as type II outbursts because: a) they last for multiple orbits, b) there is only moderate orbital modulation (see Fig. 6.16), c) there is a flux-spin up correlation. The last two outbursts are short and could be considered as type I. In the "quiescence" state where the luminosity is ~10^{35} erg cm^{-2}s^{-1}, we see a gradual flux decline after the third "type II" outburst, yet the frequency continues to increase. This is again not typical, but it has been seen in other wind-fed systems (Bildsten et al. 1997).

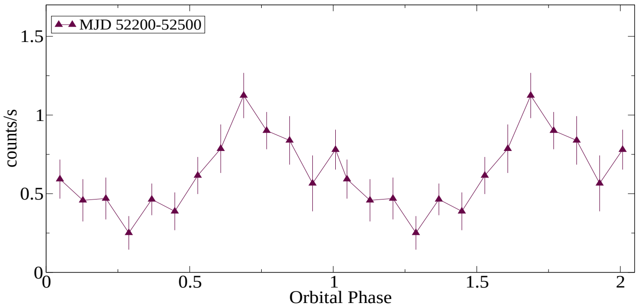

Figure 6.16: *RXTE* ASM orbital light curve of SAX J2103.5+4545 from MJD 52200-52500.

Overall, the behavior of the source does not fit well with the standard picture of Be/X–ray transients. We also believe that this peculiar Be/X–ray system with the narrowest of orbits, may be classified as a Persistent (but highly variable) source.

Bibliography

Baykal, A., Inam, S. Ç., Stark, M. J., Heffner, C. M., Erkoca, A. E., and Swank, J. H.: 2007, *MNRAS* **374**, 1108

Baykal, A., Stark, M. J., and Swank, J. H.: 2002, *ApJ* **569**, 903

Bildsten, L., Chakrabarty, D., Chiu, J., Finger, M. H., Koh, D. T., Nelson, R. W., Prince, T. A., Rubin, B. C., Scott, D. M., Stollberg, M., Vaughan, B. A., Wilson, C. A., and Wilson, R. B.: 1997, *ApJS* **113**, 367

Blay, P.: 2006, *PhD Thesis University of Valencia*

Camero-Arranz, A., Wilson, C. A., and Finger, M. H.: 2006, in *AAS/High Energy Astrophysics Division*, Vol. 9 of *AAS/High Energy Astrophysics Division*, p. 01.85

Falanga, M., di Salvo, T., Burderi, L., Bonnet-Bidaud, J. M., Goldoni, P., Goldwurm, A., Lavagetto, G., Iaria, R., and Robba, N. R.: 2005, *A&A* **436**, 313

Filippova, E. V., Lutovinov, A. A., Shtykovsky, P. E., Revnivtsev, M. G., Burenin, R. A., Arefiev, V. A., Pavlinsky, M. N., and Sunyaev, R. A.: 2004, *Astronomy Letters* **30**, 824

Ghosh, P. and Lamb, F. K.: 1979, *ApJ* **234**, 296

Hulleman, F., in 't Zand, J. J. M., and Heise, J.: 1998, *A&A* **337**, L25

İnam, S. Ç., Baykal, A., Swank, J., and Stark, M. J.: 2004, *ApJ* **616**, 463

Kraus, U., Zahn, C., Weth, C., and Ruder, H.: 2003, *ApJ* **590**, 424

Kreykenbohm, I., Coburn, W., Wilms, J., Kretschmar, P., Staubert, R., Heindl, W. A., and Rothschild, R. E.: 2002, *A&A* **395**, 129

Nagase, F.: 1989, *PASJ* **41**, 1

Parmar, A. N., White, N. E., Stella, L., Izzo, C., and Ferri, P.: 1989, *ApJ* **338**, 359

Reig, P., Negueruela, I., Fabregat, J., Chato, R., Blay, P., and Mavromatakis, F.: 2004, *A&A* **421**, 673

Reig, P., Negueruela, I., Papamastorakis, G., Manousakis, A., and Kougentakis, T.: 2005, *A&A* **440**, 637

Sidoli, L., Mereghetti, S., Larsson, S., Chernyakova, M., Kreykenbohm, I., Kretschmar, P., Paizis, A., Santangelo, A., and Ferrigno, C.: 2004, in V. Schoenfelder, G. Lichti, and C. Winkler (eds.), *ESA Special Publication*, Vol. 552 of *ESA Special Publication*, p. 475

Sidoli, L., Mereghetti, S., Larsson, S., Chernyakova, M., Kreykenbohm, I., Kretschmar, P., Paizis, A., Santangelo, A., Ferrigno, C., and Falanga, M.: 2005, *A&A* **440**, 1033

Chapter 7

A 0535+26

A 0535+26 is a transient Be/X–ray binary pulsar, discovered by *Ariel V* during a giant outburst in 1975 (Rosenberg et al. 1975a). The orbital period is 111.10(3) days Finger et al. (2007, in preparation) , and the pulse period is ~103 s in a eccentric orbit (e ~0.47, Finger et al. (1994a)). The optical counterpart is the O9.7 IIe star HDE 245770 (Liller and Eachus 1975).

The X–ray intensity of A 0535+26 varies by almost three orders of magnitude with three basic intensity states: quiescence with flux levels below 10 mCrab, normal outbursts (10 mCrab – 1 Crab), and very large ("giant") outbursts. Since the last giant outburst in 1994 and two subsequent weaker outbursts spaced at the orbital period (Finger et al., 1996), the source had gone into quiescence for 11 years. Figure 7.1 displays three long-term light curves of A 0535+26 from 1975 to 2005, obtained from different missions.

In May 2005 (MJD 53500) a new giant outburst occurred, and was followed by two normal outbursts in August-September 2005 and December 2005-January 2006 (MJD 53613–53740). Each of these outbursts began approximately a week before the periastron passage in A 0535+26's 111 day orbit. Unfortunately the giant outburst was poorly observed due to the closeness of the Sun to the source. There are only a handful of *RXTE* ASM dwells and serendipitous Swift/BAT observations near the outburst peak. In addition a pointed *RHESSI* observation (Smith et al. 2005) has

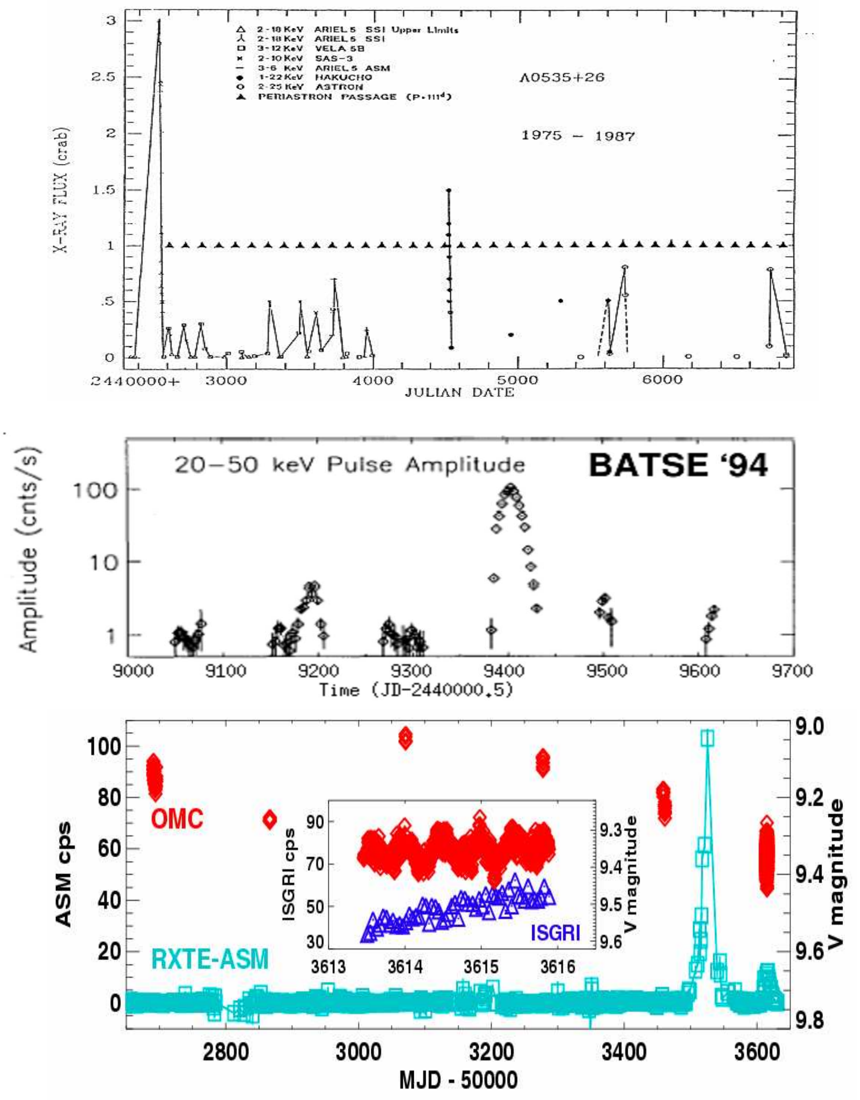

Figure 7.1: Long-term light curve history for A 0535+26. Top. Detections from various missions from 1975 to 1987 (Giovannelli and Graziati 1992). Middle. BATSE detections during 1994 by Finger et al. (1994a). Bottom. *RXTE* ASM and *INTEGRAL* OMC measurements. The inset shows the OMC and ISGRI light curves during the *INTEGRAL* TOO observations in 2005 (Kretschmar et al. 2005).

been reported. It will take special effort to analyze as *RHESSI* is designed to study the sun and not astronomical sources (Kretschmar, private communication). The following normal outbursts were well observed with both *RXTE* and *INTEGRAL*. Finger et al. (1996) detected a broad QPO component from 27 to 72 mHz during the giant outburst observed by BATSE (*CGRO*) in 1994. This confirmed the presence of an accretion disk.

In the March/April 1989 giant outburst, two cyclotron resonance scattering features were detected at ∼45 keV and ∼100 keV (Kendziorra et al. 1994). In the February 1994 outburst, the ∼45 keV feature was not detected (Grove et al. 1995). However, it was firmly confirmed by *INTEGRAL* (Kretschmar et al. 2005), *RXTE* (Wilson and Finger 2005) and *Suzaku* (Inoue et al. 2005) missions. Recent studies with both *INTEGRAL* and *RXTE* data (Caballero et al. 2007) reported on the detection of those two cyclotron features during the August/September 2005 outburst.

Figure 7.2 shows the long-term spin frequency history of A 0535+26 obtained by several authors since 1975 to 2006. Among them: Rosenberg et al. (1975b), Fishman and Watts (1977), Bradt et al. (1976), Li et al. (1979), Hameury et al. (1983), Frontera et al. (1985), Nagase et al. (1982), Sembay et al. (1990), Motch et al. (1991), Coe et al. (1990), Makino (1989), Sunyaev and Titarchuk (1989), Cusumano et al. (1992), Finger et al. (1994b), Caballero et al. (2007), and recently Finger et al. (2007; in preparation) with Swift/BAT 15–50 keV data.

In the same Figure, A 0535+26 shows a spin-down period (MJD 42000–44000) followed by a overall spin-up trend (MJD 44000–49500), and ending with a spin-down trend. Although between MJD 50000 to MJD 53500, apparently this source did not show any X–ray activity (see Fig. 7.1), Coe et al. (2006) detected a 110±0.5 d orbital modulation pattern during the quiescent X–ray state, as well as Hill et al. (2007) in a short observation by *INTEGRAL* in 2003. Then, suddenly the 2005 giant outburst took place followed by two normal outbursts. Nevertheless, Figure 7.2 indicates that a transition to spin-down happened between the last two giant outbursts.

In 2004, Finger et al. determined the orbital parameters of A 0535+26 from pulse timing using BATSE observations of three normal outbursts which occurred in 1993. However, they realized that, using these orbital

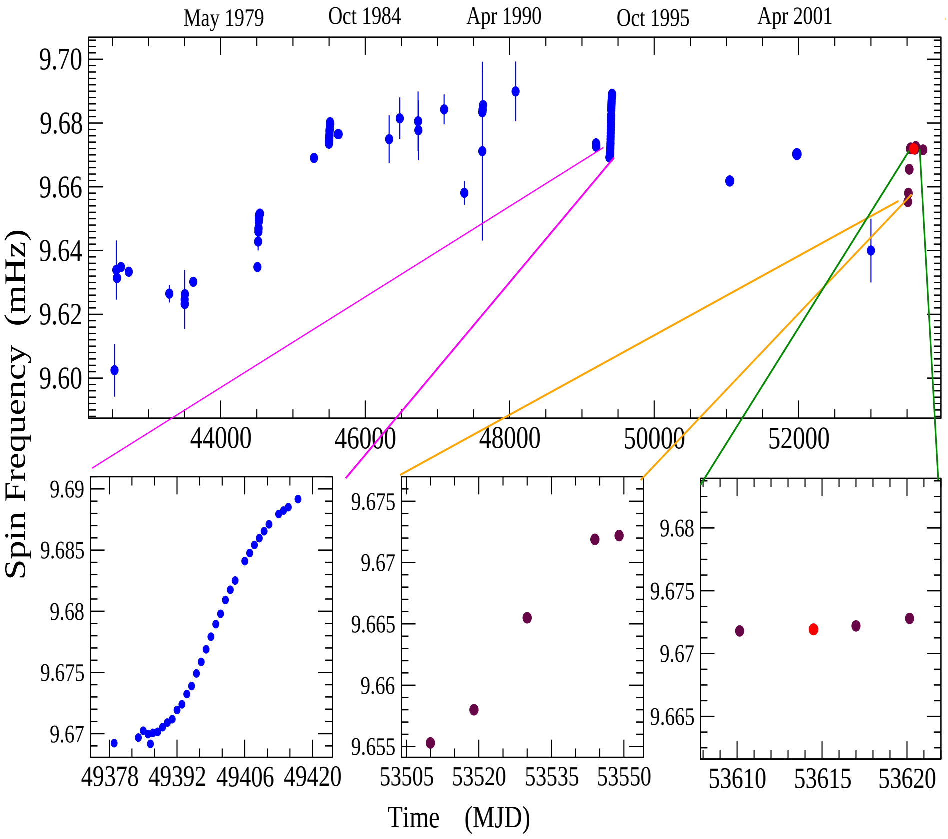

Figure 7.2: Top. Long-term spin frequency history of A 0535+26. We can clearly see several spin-up rate periods. Bottom. Zoom of the of the 21 μHz spin-up seen the 1994 outburst (left), and of the 17 μHz spin-up seen in the 2005 giant outburst (middle) plus the following normal outbursts (right). Dark points are recent *Swift* results from Finger et al. (in preparation), and the red one is from *INTEGRAL* (Caballero et al. 2007).

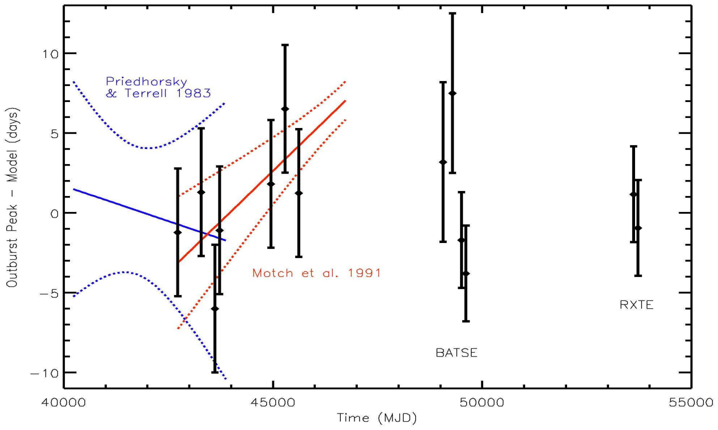

Figure 7.3: The data points show the difference of the measured outburst peak times from Finger et al. best fit ephemeris. The differences between previous ephemeris and from Finger et al. (2007) are also shown. The new orbital solution is: P_{orb}= 111.10(3) d and $T_{periastron}$ = 53613.0(13) MJD.

elements, predictions of recent periastron passage epochs have errors of several weeks, due mainly to the error on the orbital period. To obtain an improved orbital period Finger et al. (2007) updated the outburst ephemeris presented by Motch et al. (1991). They obtained their outburst ephemeris by fitting the outburst peak times of to a model of the form $T_{peak} = \mathrm{T}_0 + \mathrm{N}\times\mathrm{P}_{orbit}$, were N is the orbital cycle number. Only outbursts with flux less then 0.5 Crab were used, since the giant outbursts were know to peak far from periastron passage.

To the data given by Motch et al., Finger et al. (2007) added peak times for four normal outbursts observed by *BATSE*, and peak times for the two normal outbursts observed with *RXTE*. The best fit ephemeris obtained is T_{peak} = MJD 48095.9(10) + N×111.10(3). The residuals of the fit are shown in Figure 7.3. Also shown is the difference between the Priedhorsky and Terrell (1984) ephemeris (from Fourier analysis of Vela B data) and Finger et al. (2007) ephemeris, as well as the difference between the Motch et al. ephemeris and Finger et al. ephemeris. Using this period and the Finger et al. (1996) periastron epoch, the estimated periastron passage for the first normal outburst is at MJD 53613.0(13).

Normal Outburst Light Curves

Figure 7.4 shows the PCA light curves for the two normal outbursts from Finger et al. (2007), and the ASM one day average light curves for the same normal outbursts. The highest flux in the first normal outburst was reached during a short spike prior to periastron passage, followed by a more gradual rise to a peak and then an exponential tail. This pre–periastron spike was also evident in the *RXTE* ASM and the Swift/BAT data (see Fig.7.5).

Similar pre–periastron spikes have been seen in other Be/X–ray binaries such as 2S 1845-024 and EXO 2030+375 (see Chapter 5). A possible explanation is that when the neutron star first approaches the Be star disk, it has a burst of wind-like accretion from capture of low angular momentum material, while the higher angular momentum material forms an accretion disk, which feed the main part of the outburst (M. Finger, private communication). There was no evidence for a spike in the second normal outburst.

7.1 OBSERVATIONS AND DATA REDUCTION

The tail of the May 2005 giant outburst (MJD 53500) as well as the following two normal outbursts in August–September 2005 and December 2005-January 2006 (MJD 53613–53740) were observed with *RXTE* PCA and HEXTE, with a total of 58 observations. For the pulse profile study and for each available observation, we have analyzed either GoodXenon or event mode PCA data (time bin size 125μs, 64M energy channels), and HEXTE science event data from clusters A and B (8μs time bin, 256 channels) using Ftools V6.0.5.

INTEGRAL also observed A 0535+26 near the maximum of the September 2005 normal outburst (MJD 53613–5361.89), with a total exposure

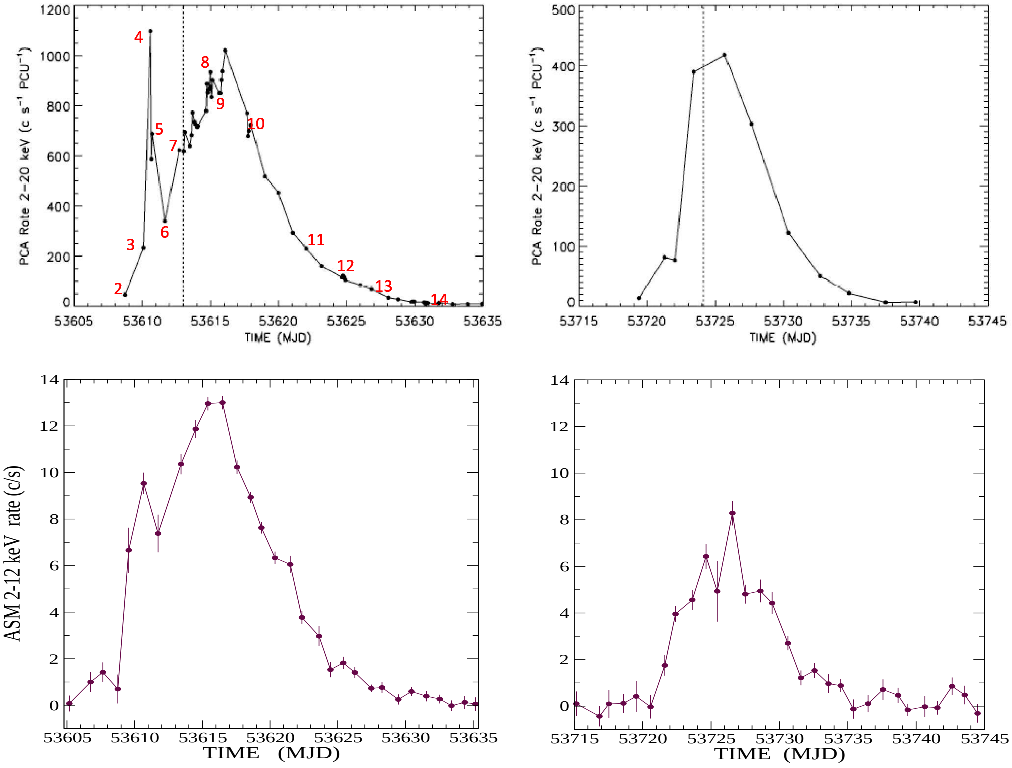

Figure 7.4: Top: *RXTE* PCA light curves in the 2–20 keV for the two normal outbursts of A 0535+26 (MJD 53613-53740) from Finger et al. (2007). The dotted line gives the time of periastron passage. Bottom: *RXTE* ASM one day average light curve for the same period.

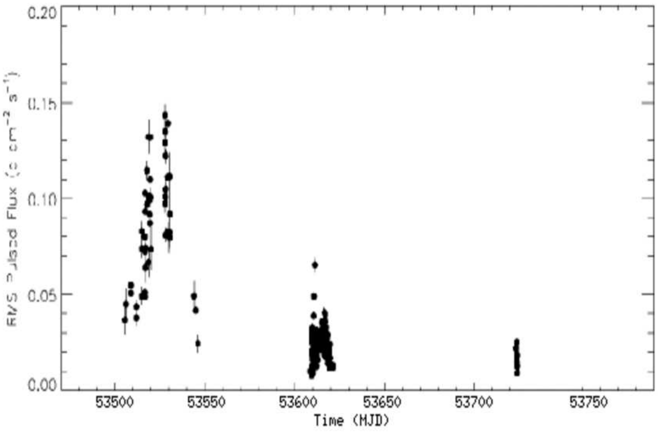

Figure 7.5: *Swift* 15–50 keV light curve of A 0535+26 during the 2005 giant outburst and the two followed normal outbursts. It is clearly visible the spike detected in the first normal outburst (Finger et al. 2007).

time of 198.4 ks. *OSA v5.1* has been used for the reduction process. To generate light curves from *IBIS* ISGRI alternative software provided by the IASF Palermo has been used (see Chapter 4).

7.2 DATA ANALYSIS AND RESULTS

We followed the same procedure described in Chapter 4 in order to make pulse profiles from the 58 *RXTE* observations. Almost all these observations were split into different orbits, finally obtaining 81 PCA and 78 HEXTE light curves. We corrected the times to the barycenter of the solar system, as well as for the orbital motion using the binary orbital parameters by Finger et al. (2007). We then constructed pulse profiles by fitting the data with a harmonic expansion in pulse phase (12 harmonics were used). The background was subtracted. Typically we use data spanning about 4000 s interval (∼36 pulse periods).

We found that A 0535+26 pulse shape varies from 1 to 4 (sometimes even 5) peak components. At low energies the pulse shapes obtained are

Table 7.1: Mean flux-luminosity conversions for A 0535+26.

Flux (c/s/PCU)	$L_{3-15keV}$ (10^{36} erg s−1)
500	3
200	1.5
100	0.5
50	0.2
20	0.06

in general more complex. These four peaks were labeled depending on the different phase intervals covered (see Fig. 7.6):

– The first main peak cover phases 0–0.2.

– The second peak span from phases 0.2–0.5.

– The third peak can be found at phases 0.5–0.7. This peak a few times splits into two peaks, at about phases 0.5–0.62 and 0.62–0.72.

– The fourth peak is present at around phases 0.7–0.9.

In the next section we will discuss the presence of pulse profile luminosity or energy correlations. Table 7.1 shows some flux-luminosity conversions, which will be used throughout the chapter.

7.2.1 Pulse profile evolution with Luminosity

We have selected 14 pulse profiles in Figure 7.6 during the first normal outburst, to show the evolution of their components with luminosity (2.06–5.31 keV Flux). Fig 7.4 displays the times where the selected observations where taken. It was found a general trend (that is confirmed in the second normal outburst) :

– At low luminosities ($\leq$10 c/s/PCU; panel 1) the pulse shape is a single sinusoidal-like peak. As the luminosity increases the pulse shape becomes double peak, each one covering about half the pulse phase.

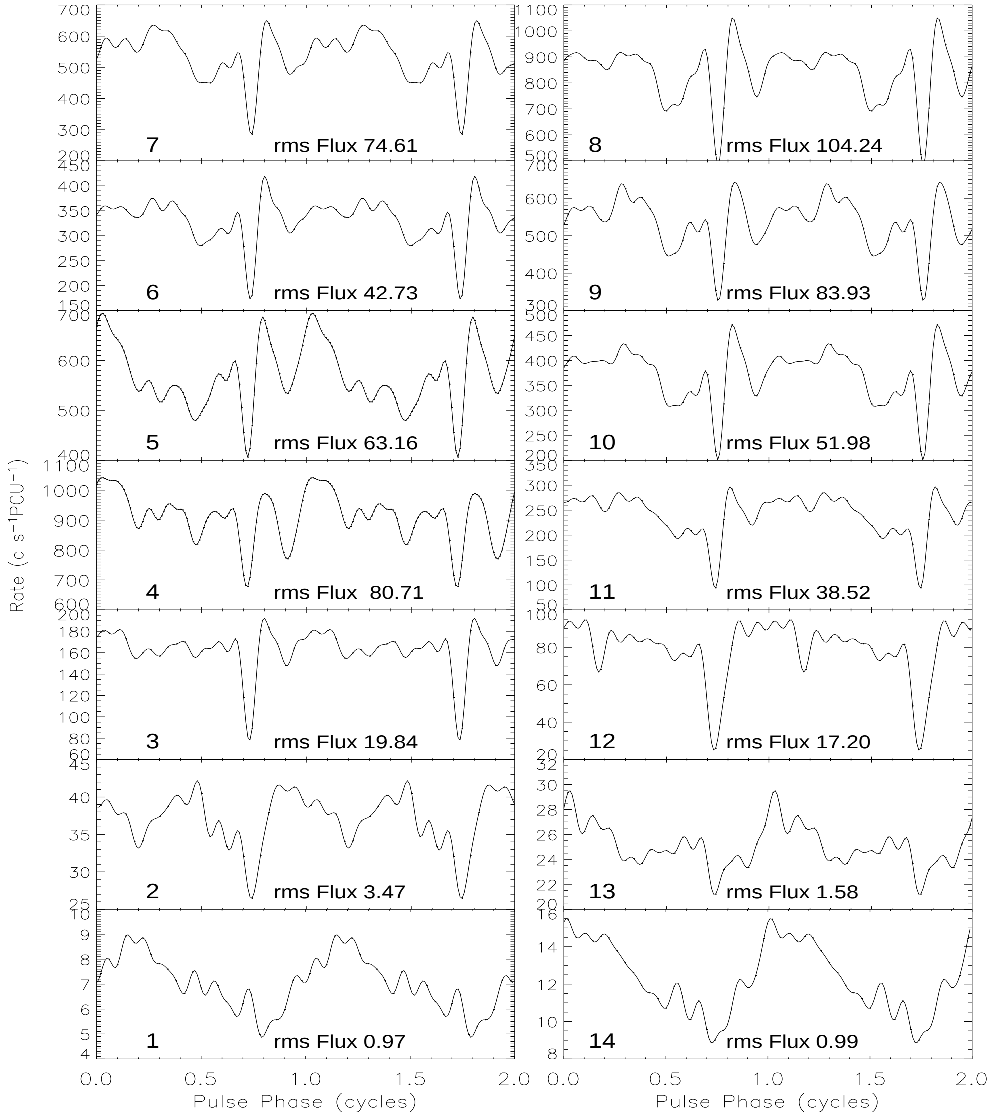

Figure 7.6: Left: PCA 2.06–5.31 keV pulse profiles evolution during the first normal outburst, with increasing luminosity from bottom to top. Right: profiles with luminosity decreasing from top to bottom. Panels number 4 and 5 correspond to the initial spike and number 8 to the maximum. In Fig. 7.4, red numbers locate each of these observations in the PCA light curve.

Table 7.2: A 0535+26 dips/notch variations with luminosity (2.06-5.31 keV range). We only consider as notch the feature at phase 0.7, the rest are designed as dips.

Dip & Notch phase	Evolution with luminosity
0.2	It gets deeper up to intermediate luminosities, and then it almost disappears at high luminosities (excepting during the spike).
0.5	Appears at medium–high luminosities (∼200 c/s/PCU).
0.7	Increases and narrows with increasing luminosity.
0.9	It only appears at medium–high luminosities, and increases with increasing luminosity.

– As the luminosity grows (∼50 c/s/PCU; panel 2 of that Figure), the secondary peak increases, becoming as large as the first main peak and showing a weak feature at phases (0.5–0.7).

– The third feature is broad and asymmetric, made of two merged peaks (at phases 0.5–0.6 and 0.6–0.7), which becomes more prominent at higher luminosities (specially the asymmetric part between phases 0.6–0.7). Only in a few observations these two peaks are seen clearly separated.

– At intermediate luminosities (∼100 c/s/PCU; panel 12) the pulse shape is no longer sinusoidal, in fact it is pretty flat almost like top-hat twins.

– For larger luminosities (≥100 c/s/PCU; panels 3 to 8) a fourth peak begins to appear in the profiles, the strength of which increases with increasing luminosity. This yields to a shortening of the first main peak.

– We found a special pulse shape behavior at the spike (panels 4 and 5). The four components are present, as usual for higher luminosities, but the first main peak is much stronger than in the rest of the observations during the outburst, and the fourth component also becomes much wider. However, the third component decreases.

Other interesting features are the notch and dips present in the profiles. In Table 7.2 we show a description of their evolution with luminosity. It is worthy to note that comparing some observations from the rise and the fall of the outburst at the same luminosity level (below medium–low luminosities, $\lesssim$100 c/s/PCU), some shapes are not completely the same. This also happens in the second normal outburst.

7.2.2 Pulse profile evolution vs. Energy

We have selected 17 energy bands for the *RXTE* pulse shape energy correlation study. For PCA the ranges were: 2.06–5.31 keV, 5.31–7.76 keV, 7.76–13.93 keV and 13.93–20.62 keV. HEXTE energy bands varied from 15 to 40 keV, divided in 5 keV intervals, then from 40 to 61 keV the intervals were 3 keV wide to check possible changes around the cyclotron line, and finally from 61 to 190 keV the intervals were back to 5 keV wide. Figures 7.7 and 7.9 show examples of PCA and HEXTE pulse profiles during the first normal outburst. We can see that each peak evolves in a different way.

Main peak (phases 0–0.2) evolution with energy:

(a) for medium-low L_X ($\leq$100 c/s/PCU) it decreases with increasing energy up to 20 keV (see Fig. 7.7, column 2 –from left to right–). For the lower luminosity values the single-peak profile shows the same trend (same Figure, column 1). For energy ranging above 20 keV, the profiles are very noisy and therefore we cannot conclude any trend.

(b) for med-high L_X ($\geq$100 c/s/PCU and $\leq$400 c/s/PCU) it increases with increasing energy (Fig. 7.7, columns 2 and 3) up to $\sim$25 keV. Above that value it decreases with increasing energy, becoming an asymmetric almost flat single-peak (see Fig. 7.9). We point out that this flatness do not happen always in the same energy band, but at energies around the cyclotron line, that is, from 35 to 55 keV. Finally, as long as the statistics

Table 7.3: A 0535+26 dips and notch evolution with energy.

Dip & Notch phase	Evolution with energy
0.2	-For $L_X \lesssim 200$ c/s/PCU: decreases with increasing energy (poor statistics at energies larger than ∼50 keV) -For $L_X \gtrsim 200$ c/s/PCU: increases with energy (maximum at ∼20 keV) and then decreases again (except for the spike).
0.5	Disappears with energy. It shifts to phase 0.62
0.62	Decreases with energy, and merges with the second main peak with increasing energy.
0.72	Decreases and broad with increasing energy
0.92	Dissolved with increasing energy

are still good enough, we can see that it increases again (while the second peak decreases).

(c) for high L_X (Fig. 7.7, column 4) it slightly decreases with increasing energy, and it tends to melt with peak at phases 0.8–0.9 (except for the spike; see Fig. 7.8). Above ∼25 the evolution is the same as in med-high L_X.

Second peak (phases 0.2–0.5) evolution:

(a) for medium-low L_X it decreases with increasing energy, either been melted with the first main peak forming one single broad peak or just vanishing. For the lower luminosity values the single-peak profile shows the same trend (see e.g. Fig. 7.7, column 1). The statistics are not good at high energy bands, therefore we cannot conclude any trend.

(b) for med-high L_X it decreases with energy and becomes as broader as the first main peak (Fig. 7.7, columns 2 and 3). Then, the evolution is that exposed before for the first peak.

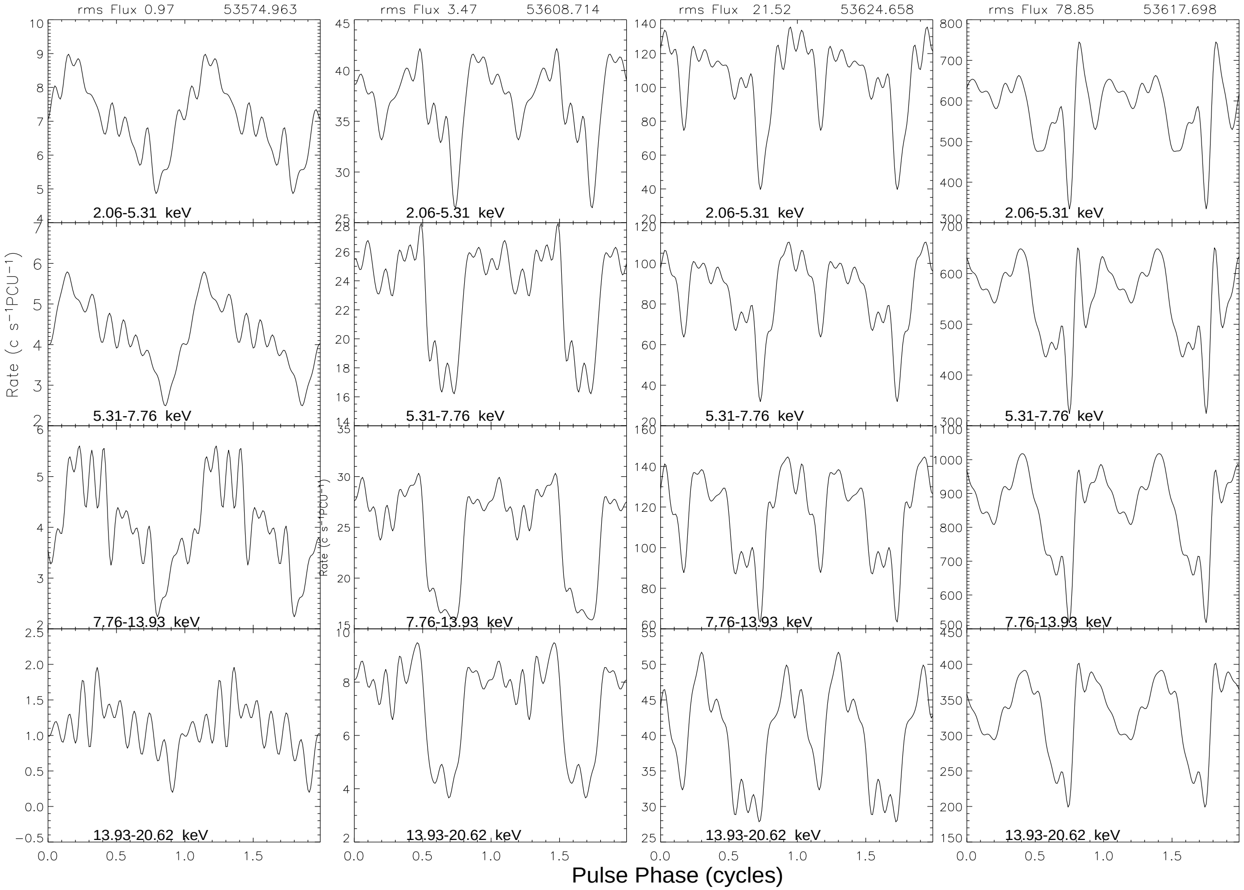

Figure 7.7: PCA pulse profiles in four energy bands sorted with the luminosity increasing from left to right. The observation times are in MJD.

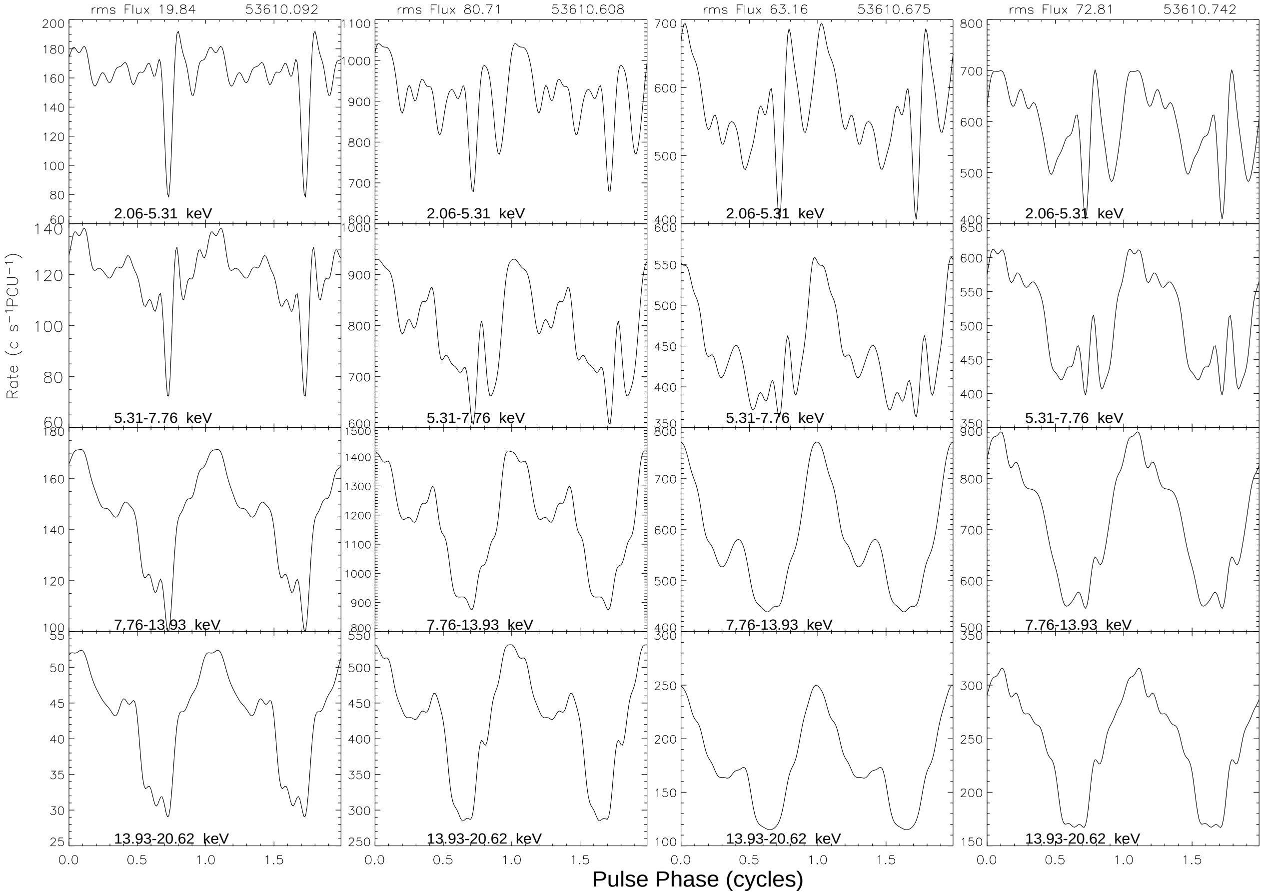

Figure 7.8: Temporal *RXTE* PCA pulse profiles evolution during the spike, in four energy bands. The observation times are also in MJD. After the spike the pulse profile is similar to the pre-spike shape.

(c) for high L_X it increases with energy (maximum at 15–20 keV) and then decreases again (except for the spike) (Fig. 7.7, columns 3 and 4; see also Figs. 7.8 and 7.9).

As we stated before, the third and fourth components are found to be present at low energies. In particular, the third peak (phases 0.5–0.7) decreases with energy, and disappears having merged with the second main peak. (Fig. 7.7, columns 3 and 4).

The fourth peak (phases 0.7–0.9) decreases with energy, and almost dissolves at high energies (Fig. 7.7, column 4; see also Fig. 7.8).

Figure 7.10 shows *INTEGRAL* JEM–X and ISGRI pulse profiles, and the ones obtained with *RXTE* PCA and HEXTE data (all extracted by folding the data according to A 0535+26 pulse period), during an observation near the maximum of the outburst (MJD 52614.007). We can see that pulse shapes at the same energy band are quite similar for all the instruments.

The narrow notch at phases 0.7–0.9 is a very interesting feature. It is present in the lower energy bands until except in the faintest end of the outburst tail. As the flux decreases from the peak, the notch widens at high energies with the leading edge moving earlier in phase. This widening also progresses from higher to lower energy bands. The trailing edge of the notch is generally close in phase for all energy bands. Table 7.3 shows a general description of the notch evolution with energy. The initial spike is also a special case, because at high energies the pulse shape is not flat. It is s the only case at high luminosities, when it looks like a sinusoidal peak (accompanied with a weaker peak, but not always).

7.3 DISCUSSION

Frontera et al. (1985) found that the time-averaged pulse profile near the peak of the October 1980 outburst, at hard X–ray energies (< 27 keV), exhibited a different structure from those measured during different outbursts or epochs or both. The common features that all the compared profiles showed was a main peak following a narrow dip. Since they found

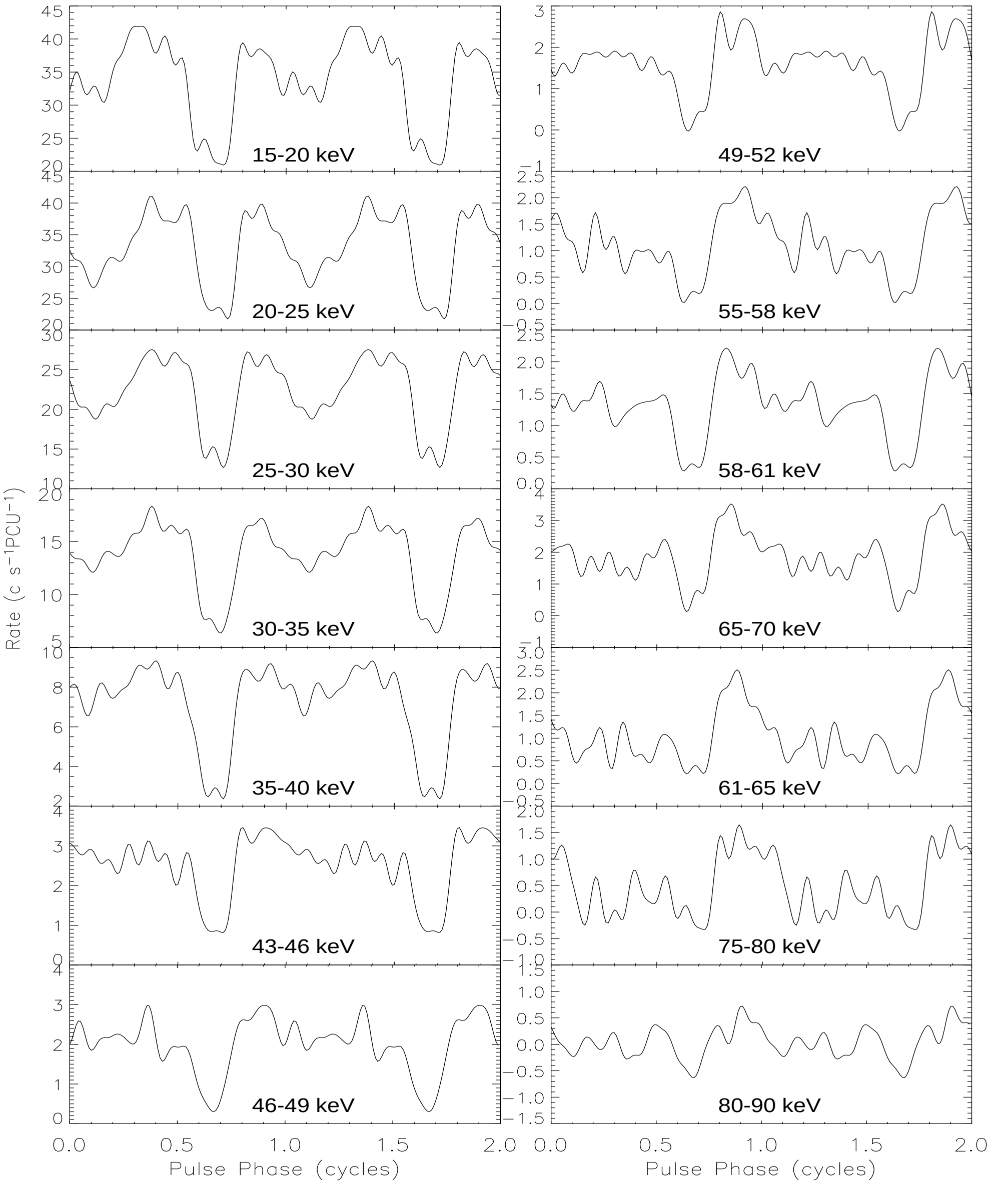

Figure 7.9: Evolution with energy of HEXTE pulses profiles of one observation near the maximum (MJD 53614.747).

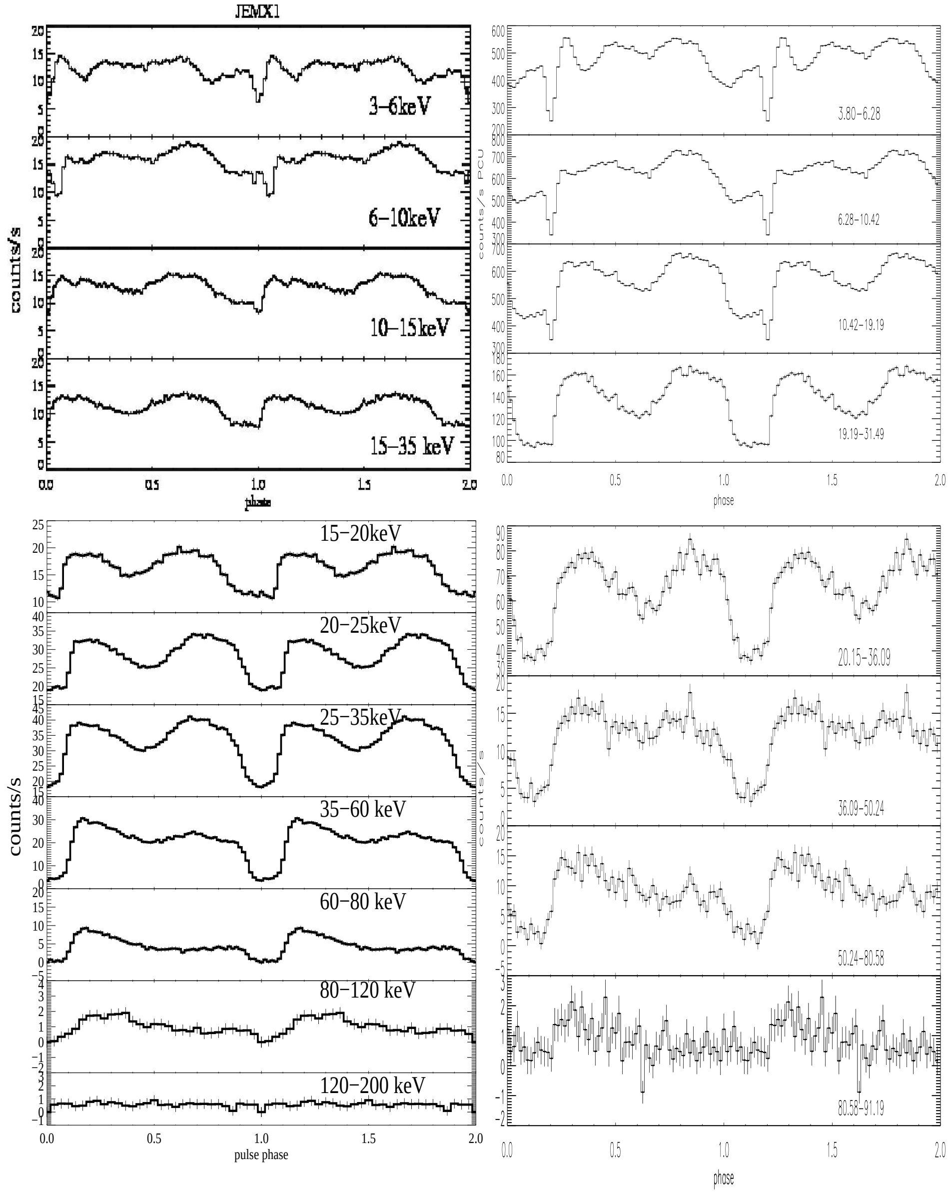

Figure 7.10: Left panels: *INTEGRAL* JEMX–1 (top) and ISGRI (bottom) profiles evolution with energy, near the maximum of the first normal outburst (MJD 53614.007). Right: *RXTE* PCA (top) and HEXTE (bottom) profiles evolution with energy of the same observation. Pulse shapes are identical from both missions.

that the luminosity changed about a factor of 6, the relatively small decrease of the accretion rate likely affected the pulse profile (Giovannelli and Graziati 1992, and references therein).

They also found a significant variability in pulse shape on time scales of 1000 s, as well as, on shorter time scales (around 10 s). They detected a random spiky variability distributed uniformly in pulse phase. They concluded that two mechanisms could explain the complex variability of A 0535+26: (i) a first mechanism triggers the shots and, being uncorrelated with pulse phase, was probably inherent to the accretion process; (ii) a second mechanism changes the pulse shape, and it is related to variations of the intrinsic beaming pattern.

Using OSSE data Maisack et al. (1996) obtained pulse profiles of A 0535+26 in 4 energy bands (from 35 to 100 keV) during the first and the second half of the 1994 giant outburst. They saw that the increase between the first and the second half of the observation was most pronounced at lower energies, indicating that the spectrum become softer as the overall intensity rose. This was also evident from their phase-averaged spectral analysis. The pulse shape was similar to that reported from the previous giant outburst in 1989 with HEXTE (Kendziorra et al. 1994), showing a strong asymmetric primary peak and a smaller secondary. The secondary peak became narrower with increasing energy, indicating that the spectral shape differed across that pulse. In all energy bands, the main intensity increase between the early and late parts of the observation data set was strongest in the primary peak and in the dip between the secondary and the primary peak. This dip was deeper that the dip between the primary and the secondary at the beginning of the observation, but become shallower as the overall intensity increased.

Kretschmar et al. (1996) presented pulse-phase-resolved spectral analysis of A 0535+26, using TTM/HEXE observations from 1989. They found that the pulse profiles exhibited a double peaked structure with a clearly asymmetric "main" peak and a more symmetric "secondary" pulse. Despite strong pulse to pulse variations, the average pulse profile was remarkably constant over time. Due to instrumental limitations, they could not comment on the complex pulse profile structure observed by Bradt et al. (1976) at energies below ∼8 keV.

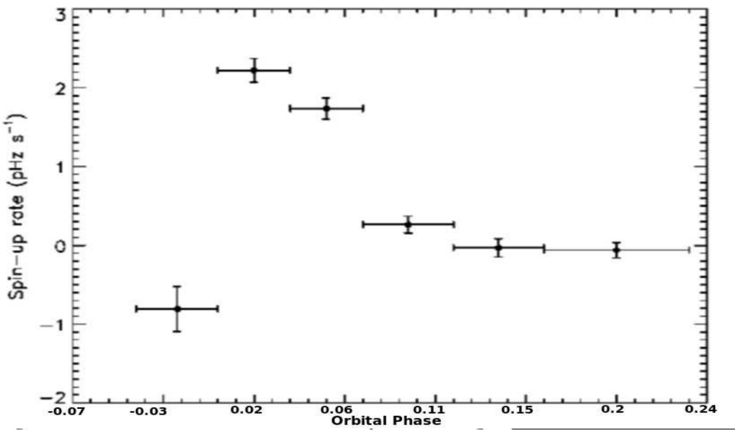

Figure 7.11: PCA spin-up rates during the first normal outburst, estimated using a quadratic spine fit to pulse phases Finger et al. (2007, in preparation) . A large spin-up rate happened in A 0535+26 after the first spike (orbital phase ~ 0) .

Bildsten et al. (1997) presented a pulse profile evolution study with luminosity and energy (20–70 keV range), during the 1994 giant outburst of A 0535+26. They found a double peak profile for X–ray luminosities $\geq 1.6\times10^{3}6$ erg s^{-1}. Below this luminosity value a broad single sinusoidal-like peak was reported. As the energy increases the second peak decreases becoming more prominent the first peak. This is in agreement with our results from the normal outbursts. At low luminosities, Bildsten et al. found that the single peak was no longer sinusoidal but more like a top-hat, as the energy increased. The present work at medium-low luminosities presents poor statistics at energies above 20 keV, preventing us from carrying out any comparison. We note we are comparing a giant vs. normal outbursts.

Lately Kretschmar et al. (2005), Finger et al. (2007) and Caballero et al. (2007) carried out a broad-band pulse profile study. They all found that, similar to other accreting pulsars like SAX 2103.5+4545 (see Chapter 6), the source displayed a complex profile shape in the soft X–ray range and a simple two-peaked profile, with very different spectral shape of the pulses, at higher energies. The pulse profiles were similar to that seen in previous outbursts but differed significantly in various details, suggesting at a variable accretion geometry.

Our study at energies above 20 keV revealed that, at high luminosities, the secondary peak at phases 0.2–0.5 evolved in a particular way, increasing with energy up to the 15–20 keV range and decreasing again up to 90 keV (except for the spike). In addition, Fig. 7.9 shows that the secondary peak evolved in a complex flickering way, likely because we selected narrow energy bands. The dip narrow notch at phases 0.7–0.9 found at lower energies and which broaden and become shallower at higher energies (disappearing at low fluxes), could be due to most of the emission being from the sides of the accretion column at higher luminosity, with less projected area of these sides being visible when our viewing direction is close to the magnetic pole.

We have also found as Bradt et al. (1976), a 4 (few times even 5 peaks) pulse shape structure at low energies for med-high luminosity states of A 0535+26. However, in the present study, those peaks were found to evolve slowly with energy, becoming smooth in a more simple structure at energies above ∼20 keV (instead at 8 keV).

An intriguing case was the pulse shape behavior during the spike never reported before. The physical mechanisms producing this pre-spike are still under debate. A possible general explanation was given by Okazaki et al. (2007) for EXO 2030+375. He claimed that a similar feature was found in his SPH simulations. He believes that this was due to the strong phase dependence of the specific angular momentum of the material transferred from the Be disk: it is lowest at periastron and rapidly increases with the orbital phase. Thus, the material transferred later takes more time to accrete and causes the separate main peak.

Figure 7.11 shows spin-up rates during the first normal outburst, estimated by fitting the PCA pulse phases to a spline model Finger et al. (2007, in preparation). In the first place, this Figure clearly shows a torque-flux correlation, suggesting disk accretion. The peak spin-up rate was near 2 pHz s-1, comparable to the 1994 giant outburst peak spin-up rate of 12.5 pHz s-1 (scaled by the peak flux ratio).

Although the most interesting feature is that the spin-up rate started after the pre-spike (orbital phase ∼0, periastron passage). This is in good agreement with Okazaki's explanation. An on going study by Caballero et al. (in preparation), has revealed the change of the cyclotron line value to ∼50 keV during the spike. This also contributes to suggest that a different physical mechanism occurs during the first spike, and that a more stable accretion disk around the neutron star seems to be formed later.

7.4 CONCLUSIONS

- Luminosity and energy correlations were found in the pulse profile study. At low X–ray luminosities the pulse shapes are single-peaked. As luminosity increases two, three and four (in a few cases even five) components become prominent features.
- An energy dependence pattern was also found. As the luminosity increases, low energy profiles are more complex, exhibiting multiple components. High energy profiles evolve from double to single peaks.
- The pre-spike in the 2005 normal outburst shows a different pulse shape, corresponding to a spin-up rate.
- There seem to be changes in the pulse shape at energies around the 45 keV cyclotron line.

Bibliography

Bildsten, L., Chakrabarty, D., Chiu, J., Finger, M. H., Koh, D. T., Nelson, R. W., Prince, T. A., Rubin, B. C., Scott, D. M., Stollberg, M., Vaughan, B. A., Wilson, C. A., and Wilson, R. B.: 1997, *ApJS* **113**, 367

Bradt, H., Mayer, W., Buff, J., Clark, G. W., Doxsey, R., Hearn, D., Jernigan, G., Joss, P. C., Laufer, B., Lewin, W., Li, F., Matilsky, T., McClintock, J., Primini, F., Rappaport, S., and Schnopper, H.: 1976, *ApJ Lett.* **204**, L67

Caballero, I., Kretschmar, P., Santangelo, A., Staubert, R., Klochkov, D., Camero, A., Ferrigno, C., Finger, M. H., Kreykenbohm, I., McBride, V. A., Pottschmidt, K., Rothschild, R. E., Schönherr, G., Segreto, A., Suchy, S., Wilms, J., and Wilson, C. A.: 2007, *A&A* **465**, L21

Coe, M. J., Carstairs, I. R., Court, A. J., Davies, S. R., Dean, A. J., Dipper, N. A., Lewis, R. A., Perotti, F., Quadrini, E., Bazzano, A., Ubertini, P., and Stephen, J. B.: 1990, *MNRAS* **243**, 475

Coe, M. J., Reig, P., McBride, V. A., Galache, J. L., and Fabregat, J.: 2006, *MNRAS* **368**, 447

Cusumano, G., Mineo, T., Sacco, B., Scarsi, L., Gerardi, G., Agrinier, B., Barouch, E., Comte, R., Parlier, B., Masnou, J. L., Massaro, E., Matt, G., Costa, E., Salvati, M., Mandrou, P., Niel, M., and Olive, J. F.: 1992, *ApJ Lett.* **398**, L103

Finger, M. H., Cominsky, L. R., Wilson, R. B., Harmon, B. A., and Fishman, G. J.: 1994a, in S. Holt and C. S. Day (eds.), *The Evolution of X-ray Binaries*, Vol. 308 of *American Institute of Physics Conference Series*, p. 459

Finger, M. H., Wilson, R. B., and Hagedon, K. S.: 1994b, *iaucirc* **5931**, 1

Fishman, G. J. and Watts, Jr., J. W.: 1977, *ApJ* **212**, 211

Frontera, F., dal Fiume, D., Morelli, E., and Spada, G.: 1985, *ApJ* **298**, 585

Giovannelli, F. and Graziati, L. S.: 1992, *Space Science Reviews* **59**, 1

Grove, J. E., Strickman, M. S., Johnson, W. N., Kurfess, J. D., Kinzer, R. L., Starr, C. H., Jung, G. V., Kendziorra, E., Kretschmar, P., Maisack, M., and Staubert, R.: 1995, *ApJ Lett.* **438**, L25

Hameury, J. M., Boclet, D., Durouchoux, P., Cline, T. L., Teegarden, B. J., Tueller, J., Paciesas, W. S., and Haymes, R. C.: 1983, *ApJ* **270**, 144

Hill, A. B., Bird, A. J., Dean, A. J., McBride, V. A., Sguera, V., Clark, D. J., Molina, M., Scaringi, S., and Shaw, S. E.: 2007, *ArXiv e-prints* 708

Inoue, H., Kunieda, H., White, N., Kelley, R., Mihara, T., Terada, Y., Takahashi, H., Kokubun, M., Makishima, K., and The Suzaku Team: 2005, *The Astronomer's Telegram* **613**, 1

Kendziorra, E., Kretschmar, P., Pan, H. C., Kunz, M., Maisack, M., Staubert, R., Pietsch, W., Truemper, J., Efremov, V., and Sunyaev, R.: 1994, *A&A* **291**, L31

Kretschmar, P., Kreykenbohm, I., Pottschmidt, K., Wilms, J., Coburn, W., Boggs, S., Staubert, R., Santangelo, A., Kendziorra, E., Segreto, A., Orlandini, M., Bildsten, L., and Araya-Gochez, R.: 2005, *The Astronomer's Telegram* **601**, 1

Kretschmar, P., Pan, H. C., Kendziorra, E., Kunz, M., Maisack, M., Staubert, R., Pietsch, W., Truemper, J., Efremov, V., and Sunyaev, R.: 1996, *A&AS* **120**, C175+

Li, F., Clark, G. W., Jernigan, J. G., and Rappaport, S.: 1979, *ApJ* **228**, 893

Liller, W. and Eachus, L. J.: 1975, *iaucirc* **2892**, 2

Maisack, M., Grove, J. E., Johnson, W. N., Jung, G. V., Kendziorra, E., Kinzer, R. L., Kretschmar, P., Kurfess, J. D., Starr, C. H., Staubert, R., and Strickman, M. S.: 1996, *A&AS* **120**, C179+

Makino, F.: 1989, *iaucirc* **4768**, 2

Motch, C., Stella, L., Janot-Pacheco, E., and Mouchet, M.: 1991, *ApJ* **369**, 490

Nagase, F., Hayakawa, S., Kunieda, H., Makino, F., Masai, K., Tawara, Y., Inoue, H., Kawai, N., Koyama, K., Makishima, K., Matsuoka, M., Murakami, T., Oda, M., Ogawara, Y., Ohashi, T., Shibazaki, N., Tanaka, Y., Miyamoto, S., Tsunemi, H., Yamashita, K., and Kondo, I.: 1982, *ApJ* **263**, 814

Okazaki, A. T., Owocki, S. P., and Stefl, S. (eds.): 2007, *Active OB-Stars: Laboratories for Stellare and Circumstellar Physics*, Vol. 361 of *Astronomical Society of the Pacific Conference Series*

Priedhorsky, W. C. and Terrell, J.: 1984, *Nat* **307**, 390

Rosenberg, F. D., Eyles, C. J., Skinner, G. K., and Willmore, A. P.: 1975a, *Nat* **256**, 628

Rosenberg, F. D., Eyles, C. J., Skinner, G. K., and Willmore, A. P.: 1975b, *Nat* **256**, 628

Sembay, S., Schwartz, R. A., Orwig, L. E., Dennis, B. R., and Davies, S. R.: 1990, *ApJ* **351**, 675

Smith, D. M., Hazelton, B., Coburn, W., Boggs, S. E., Fivian, M., Hurford, G. J., Hudson, H. S., Grefenstette, B., and Gilmore, R.: 2005, *The Astronomer's Telegram* **557**, 1

Sunyaev, R. A. and Titarchuk, L.: 1989, in J. Hunt and B. Battrick (eds.), *ESA SP-296: Two Topics in X-Ray Astronomy, Volume 1: X Ray Binaries. Volume 2: AGN and the X Ray Background*, pp 627–631

Wilson, C. A. and Finger, M. H.: 2005, *The Astronomer's Telegram* **605**, 1

Figure 7.12: The Scutum constellation. Credits: Till Credner y Sven Kohle (2004).

Chapter 8

THE SCUTUM SURVEY

Intense star formation is known to take place in rich molecular clouds. Important populations of high mass X–ray binaries should be associated with these dense molecular clouds with on-going stellar formation, yet such an association has not been detected so far. The large optical depth of massive molecular clouds produce a high photo-absorption in the optical, UV and X–ray wavelengths.

These energy regions constitute the classical observing windows where most known HMXRB have been discovered, and their counterparts identified. The only suitable windows to search for high energy sources in the innermost regions of the massive molecular clouds are the IR and γ–ray regions, where photo-absorption is significantly lower.

A proof of the existence of such a population of highly absorbed X–ray binaries is, e.g., the discovery by *INTEGRAL* of the object IGR J16318-4848 (Courvoisier et al. 2003). With a photo-absorption of NH> 4×10^{23} cm^{-2} it is virtually unobservable below 4 keV (Revnivtsev 2003), and it has remained undetected with X–ray missions before *INTEGRAL* .

The region of the galactic plane around l=30° has a conspicuous intensity emission in infrared, radio, CO molecular line and γ ray (Hayakawa et al. 1979). It corresponds to the so-called Scutum or 5–kpc galactic arm (see Fig. 8.1). The distribution of the K-band brightness derived from

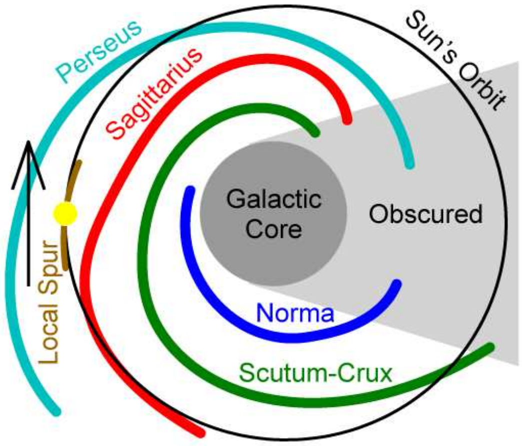

Figure 8.1: Observed structure of the Milky Way's spiral arms. Credits: Wikipedia®.

discrete sources and its correlation with the 2.6 mm line emission of CO and the 115–192 far infrared brightness strongly suggest the presence of an active star formation in this area (Ananth and Nagaraja (1982), Hammersley et al. (1994)).

The 5-kpc arm has been proposed to be the site of a dynamic formation of X–ray pulsars. Koyama et al. (1990) reported on the discovery by Ginga, in the 2–37 keV band, of seven X–ray pulsars. All but one are strongly absorbed sources, with $N_H \approx 10^{23}$ cm^{-2} or higher, and located at a distance of the order of the galactic scale of about 10 kpc. Only the less absorbed source, GS 1843+00, with $N_H < 10^{22}$ cm^{-2} and located in the northern border of the 5-kpc arm region, has been identified in archival *ROSAT* observations, and has a known optical-IR counterpart (Israel et al. 2001).

Since then, a few other sources have been detected in the Scutum region with X–ray observatories, but all of them have lower absorption values, and are closer than the main region of star formation. An example is AX 1845.0-0433, with $N_H = 4{\times}10^{22}$ cm^{-2} and a distance lower than 4 kpc (Coe et al. 1996).

The picture that emerges is that only the nearest sources in the direction of the Scutum arm have been discovered, and the bulk of X–ray pulsars, most likely situated at 10 kpc in a region of strong absorption, still remain undetected. As a consequence, our knowledge of the distribution of X–ray pulsars in the Scutum arm, and by extension in most of the regions of active star formation in the galaxy, is very limited. Figure 1.1 (Chapter 1) shows the galactic distribution of the latest 1652 sources of the 27th *INTEGRAL* catalog.

The *INTEGRAL* observatory is specially well suited to address this problem. At the energy range of the IBIS instrument the interstellar absorption is much lower than in the X–ray band, allowing the detection of the highly absorbed X–ray pulsars which are likely to exist in the densest regions of the 5-kpc arm.

The IBIS imaging capabilities should provide small error boxes for the discovered γ-ray sources, which would allow the subsequent identification of the IR counterpart. In this Chapter we will present preliminary imaging results of the Scutum survey, the GPS and the GCDE performed by the three high-energy instruments on board *INTEGRAL*.

8.1 OBSERVATIONS AND DATA REDUCTION

The imager IBIS is the prime instrument in these observations, because of its large collecting area and the ability to detect heavily absorbed objects as demonstrated by the discovery of new sources. Nevertheless, JEM–X and SPI were also used in order to cover low energies and to compare ISGRI results in the same energy band (20–40 keV).

A list of 3044 pointings was selected for ISGRI and SPI for covering completely this galactic arm, including the Scutum survey, GPS and GCDE observations (total exposure time 67.64×10^3 ks). The spectrometer SPI is able to work in imaging mode, but there are software and instrumental limitations which imply it is not the best instrument for searching new sources (see Chapters 2 and 4).

For ISGRI we first run the standard OSA5.1 pipeline for all the available data in three different energy bands: 15–20 keV, 20–40keV and 40–60 keV. The search was done using the last version (number 27) of the ISDC general catalog and the catalog of mosaic results. (see Tab. B.1).

In this study we have used preliminary imaging ISGRI software recently developed by A. Segreto (see Chapter 4). Therefore, the OSA5.1 analysis presented in this Chapter has been complemented by the use of this software for the same data set.

Other OSA5.1 limitation is that JEM–X cannot make a mosaic skymap from more than 999 ScWs. Hence, we divided into three regions the initial data set and we excluded pointings around the Galactic Center. Only pointings with galactic longitude less than 33° were finally selected. The first monitor JEM–X 1 provided a total exposure time of 2.36×10^3 ks of available data and the second monitor JEM–X 2 1.29×10^3 ks (see Chapter 4 for a description of the software used for this instrument).

8.2 IMAGING RESULTS

8.2.1 Known sources

Only 9 known sources were identified by the standard OSA5.1 software in the final mosaic. We used the SExtractor (see Chapter 4) to localize more objects in the mosaic. In the 20–40keV OSA5.1 image (see Figure 8.11) a total of 55 known sources were localized with a detection level above 7 (they are marked in *red* in Table B.1). The 9 initially detected by OSA5.1 were also identified. The detection level is the signal to noise ratio measured directly on the map, therefore it is not normalized to the local background standard deviation.

In Table B.1 the column named "ScW NUM" specifies the number of ScWs a source was detected by OSA5.1, and the "OG. BAND" column (**O**bservation **G**roup band) tells us if a given source was located in the final mosaic. We can see that almost all the 50 sources initially not detected in the mosaic, were nevertheless clearly detected in a certain number of ScWs by the standard software. Most likely they are transient sources. Only one source (marked with a *sex*) was identified in the 20-40 keV mosaic image by SExtactor but not by the OSA software.

In addition, Figure 8.13 shows the 20–40 keV mosaic image obtained using Segreto's imaging software. A total of 59 known sources were clearly detected in this energy range, with a sigma detection greater than 5, which is considered by this software as the lower limit (see Table B.1). Comparing results coming out from the OSA5.1 final mosaic catalog and the Segreto's software catalog, in the 20–40 keV band, we point out that 5 over 59 sources is a considerable difference. Only after spending a large effort either on visual inspection or/and using alternative software (SExtactor), the number of sources detected by the OSA5.1 release and Segreto's imaging software become similar.

SPI known sources detected in the 20–40 keV band are also shown in Table B.1. In this case, 46 objects were identified with a sigma greater than 3, although to be a reliable detection this value is expected to be greater than 5. Figure 8.15 shows the obtained SPI image. The number of objects detected by SPI is less than IBIS/ISGRI mainly due to the fact that the spectrometer was optimized for narrow line emission and not for broad-band studies (see Chapter 4.3.3).

Table B.1 shows also the list of detections with both JEM–X monitors. Figures 8.16 and 8.17 shows two mosaics in the 4–10 keV band obtained by JEM–X 1, almost covering the Scutum region.

8.2.2 New candidates

The detection level of a source depends on the skymap variance. For an ideal instrument and mosaic map reconstruction method, the skymap variance should be 1σ, but for a real, and hence not perfect instrument (and software), as ISGRI, the skymap variance is larger than 1, mainly because the detector background is projected into the mosaic map of the sky. Consequently, the detection level must be scaled and its threshold determined from the background fluctuations in the mosaic map.

Our method (see Chapter 4.3.3) performed a local source flux and background estimation on the initial OSA5.1 reconstruction mosaic images in 3 energy bands, as well as for combined images in the 15–60 keV range, obtained using software developed at the University of Valencia. With

Table 8.1: Statistical results of the output OSA5.1 ISGRI maps after applying our method.

Energy band (keV)	Mean image sigma level	Standard deviation
15-20	-0.0080	1.93311
15-40	-0.0095	1.67555
15-60	-0.0087	1.58655
20-40	-0.0065	1.10360
20-60	-0.0059	1.10453
40-60	-0.0028	0.98513

the background removed the output is a group of source significance maps for different sigma detection thresholds (0,3,4 and 5 sigma). We present results from the maps with a 5 sigma significance level (see Fig. 8.18).

Table 8.1 contains the image residue statistics after applying our method, which shows the mean sigma level and its standard deviation in each output sigma map for the different energy combinations. The standard deviation of some images was greater that 1 sigma. Therefore, they were rejected for this study.

Figure 8.2 (left) shows ISGRI histograms in the 20–40 keV and 20–60 keV bands, after the background subtraction procedure. We see that for both bands a new candidate may be believed as real for a sigma greater than ~3 sigma. From the histogram of the original ISGRI map, the detection threshold for claiming a source candidate was about 30 sigma.

Table 8.2 shows some of the resulting new ISGRI candidates in the 20–40 keV and 20–60 keV ranges. Furthermore, Table B.4 contains new candidates detected in the Segreto mosaic (20–40 keV) by visual inspection. The detection level of all the sources was between 5–8 sigma. In the Tables we marked in *blue* possible matches in the 20–40 keV range and

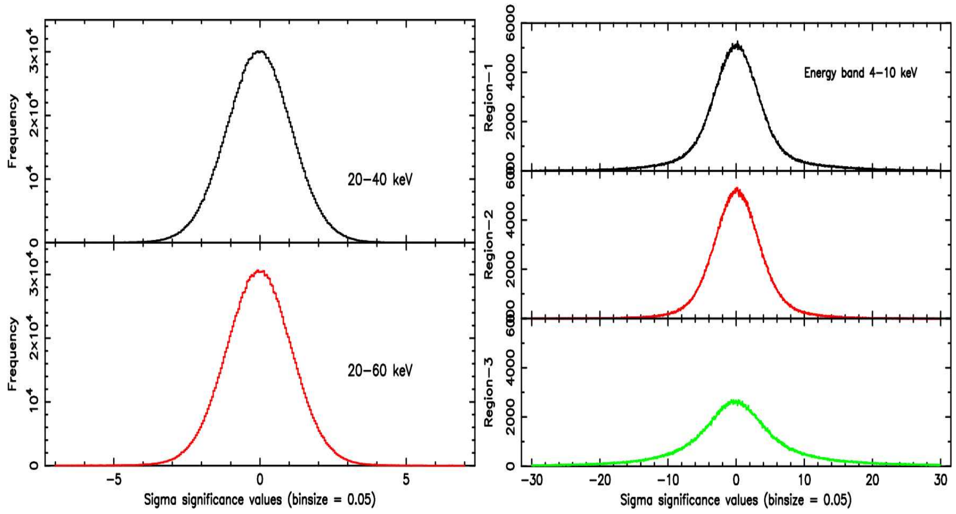

Figure 8.2: Histograms of the 20–40 keV and 20–60 keV skymaps from the OSA5.1 ISGRI mosaic (left) after background subtraction, and from three of the original JEM–X (right) mosaics in the 4–10 keV band.

magenta in the 40–60 keV range. The source number one of Table 8.2 coincides with the first one found by SExtractor. Table B.2 shows all our ISGRI candidates for new sources. In addition, Figures 8.3 and 8.4 show a cut profile for the first and the second sources from Table B.2. We have selected the source significance map for sigma detection threshold 0. Although, it is the most background contaminated, the sources showed up very clearly.

In the right panel of Figure 8.2 we can see 3 histograms corresponding to the 3 different JEM–X mosaic skymaps covering the Scutum region, in the 4–10 keV energy band. From these maps it can be seen that the detection threshold for claiming a source candidate varies from 16 to 30 (or more) sigma, depending on the region analyzed.

Tables B.5 and B.6 show possible new source candidates detected by JEM–X (*green*)(in the 4–10 keV, 10–15 keV and 15–35 keV bands), and SPI (20–40 keV). We found particularly interesting new candidates detected in 2 or 3 bands by JEM–X, but further study is needed to confirm

Table 8.2: Some of the most reliable new source candidates found by ISGRI using our method.

Energy band (keV)	Coordinates (degrees)	sigma level
20–40 keV	(283.621,9.031)	7.3
	(287.392,1.130)	5.3
	(287.543,10.60)	6.7
20–60 keV	(289.16,9.46)	5.7
	(277.736,-10.092)	5.4
	(298.148,2.487)	6.3

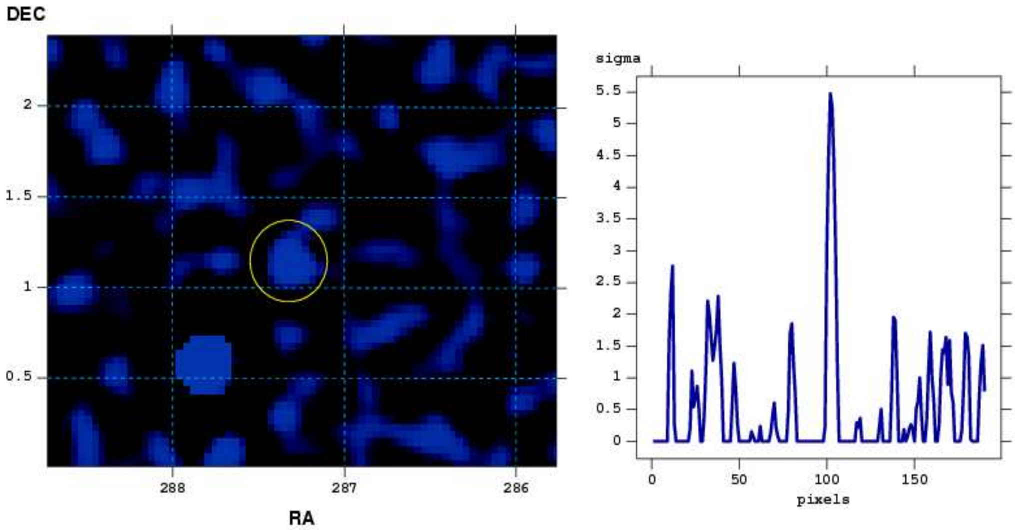

Figure 8.3: Cut profile view of the source candidate number 1 in the 20–40 keV energy range (right) and a zoom of the region (left).

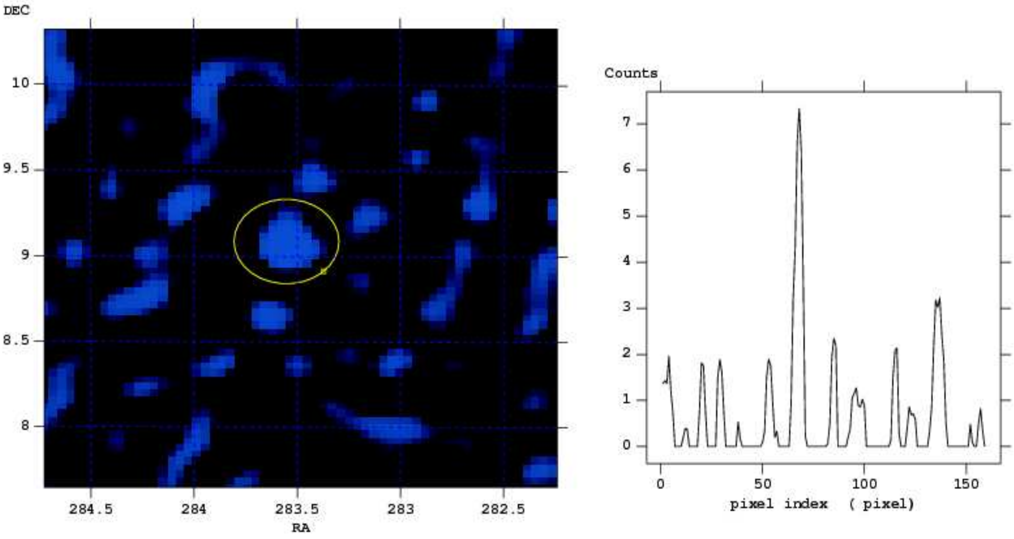

Figure 8.4: Cut profile view of the new source candidate number 2 in the 20-40 keV energy range (right) and a zoom of the region (left).

them. Also we have no confirmation from analysis of SPI observations.

8.3 DISCUSSION AND CONCLUSIONS

In the first 4 years of observing the sky, ISGRI has detected ∼500 sources, around half of which are new or unknown. The number of sources from each of the major classes detected by ISGRI are listed in Figure 8.7 for new (≡ IGRs) and previously known sources (Bodaghee et al. 2007). 'Miscellaneous' sources are Galactic objects that are not X–ray binaries, and 'Uncl.' refers to the group of sources that have not been classified yet.

Figures 8.5 and 8.6 show the distribution of all these sources. ISGRI has detected similar numbers of X–ray Binaries and Active Galactic Nuclei (AGN), and the number of detected HMXRB is greater than the number of LMXRB. We also noticed that the Scutum region is one of the most populated.

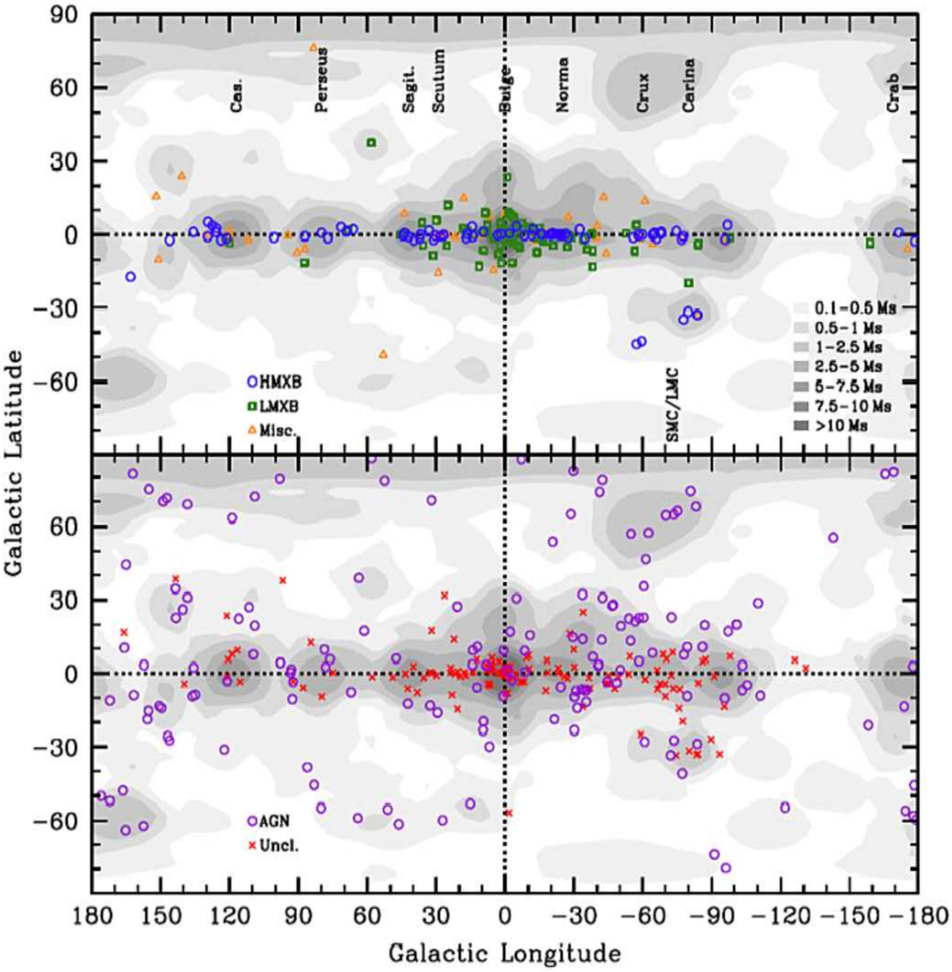

Figure 8.5: Right. Spatial distribution in Galactic coordinates of sources detected so far by ISGRI (Bodaghee et al. 2007).

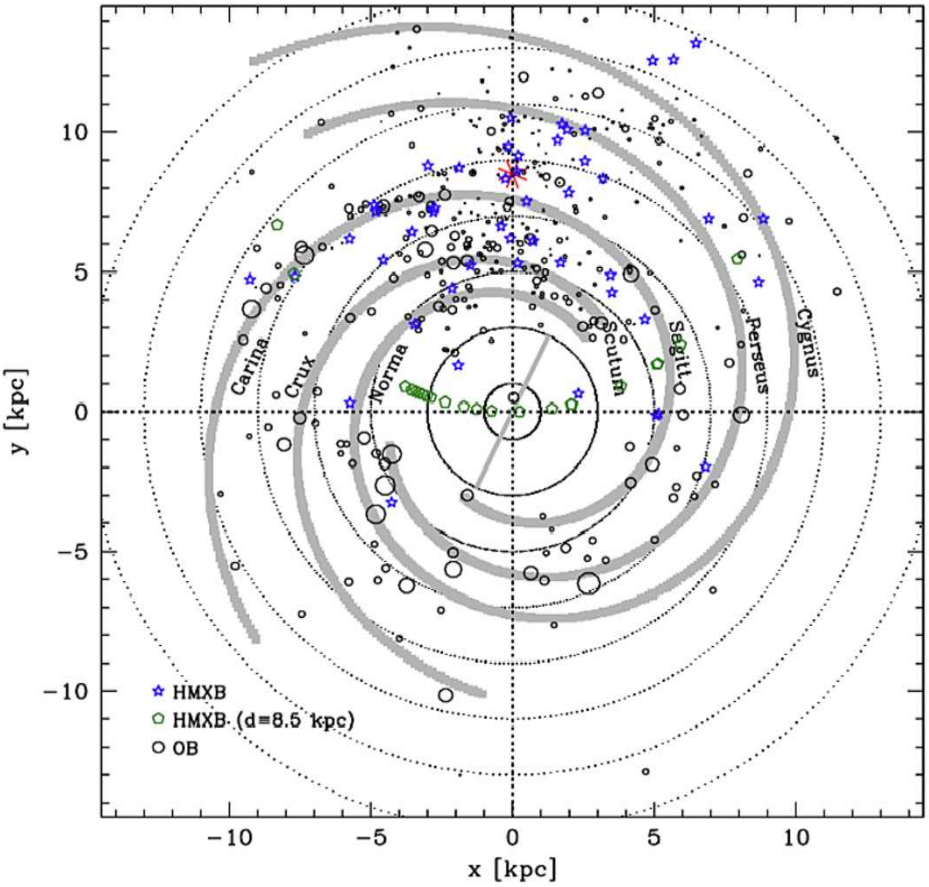

Figure 8.6: Galactic distribution of HMXBs whose distance are known (49, star symbols) and the locations of star-forming complexes (464, circles). HMXBs with unknown distances have been placed at 8.5 kpc (23,pentagons)(Bodaghee et al. 2007).

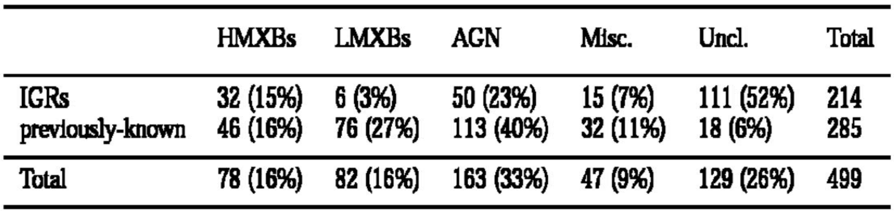

	HMXBs	LMXBs	AGN	Misc.	Uncl.	Total
IGRs	32 (15%)	6 (3%)	50 (23%)	15 (7%)	111 (52%)	214
previously-known	46 (16%)	76 (27%)	113 (40%)	32 (11%)	18 (6%)	285
Total	78 (16%)	82 (16%)	163 (33%)	47 (9%)	129 (26%)	499

Figure 8.7: Number of sources from each of the major classes detected by ISGRI from Bodaghee et al. (2007).

A. Segreto has crosschecked our results using his newly developed software for source detection in noisy skymaps, and applied this to ISGRI mosaic maps in the 20–40 keV energy range.

In Fig. 8.8 we can see the histogram of the OSA5.1 skymap before and after its renormalization to mean 0.0 and standard deviation 1.0 using Segreto's software. In the renormalized skymap this software identified 54 known sources plus the following two new sources (in degrees): (1) (283.53, 9.076) and (2) (287.32, 1.149)

These sources are coincident with the two found by using our method. Figures 8.9 show skymap zooms and relative local histograms for source number 1, both in the original OSA skymap and in the renormalized skymap.

In conclusion, we propose these 2 candidates as possible real new sources. We also found interesting the source located at (287.279,10.58) since it has been detected by JEMX (in all the energy bands), and by our software and SExtractor, in the 20–40 keV OSA5.1 ISGRI mosaic map. However, it does not present an uniform pixel distribution but elongated.

In a first approach, we searched for known Be type stars in the Simbad data base. Those sources containing Be stars will be our primary targets for the IR study. Unfortunately, no Be stars were found at any of the new source candidate positions, within an error radius of 12 arcmin.

The identification of optical/IR counterparts will allow multiwavelength studies, necessary to the modeling of these complex systems.

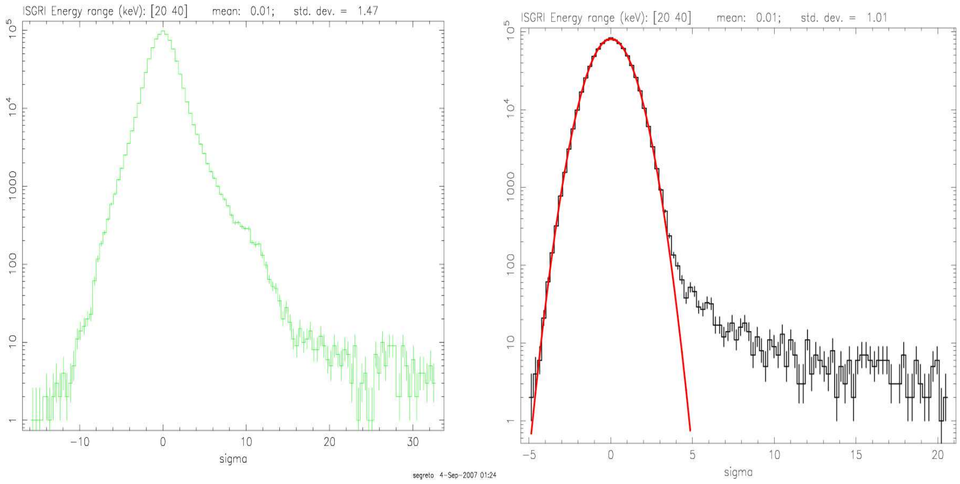

Figure 8.8: Histograms by A. Segreto from the 20–40 keV OSA5.1 mosaic skymap (left) before the background subtraction and (right) after the subtraction.

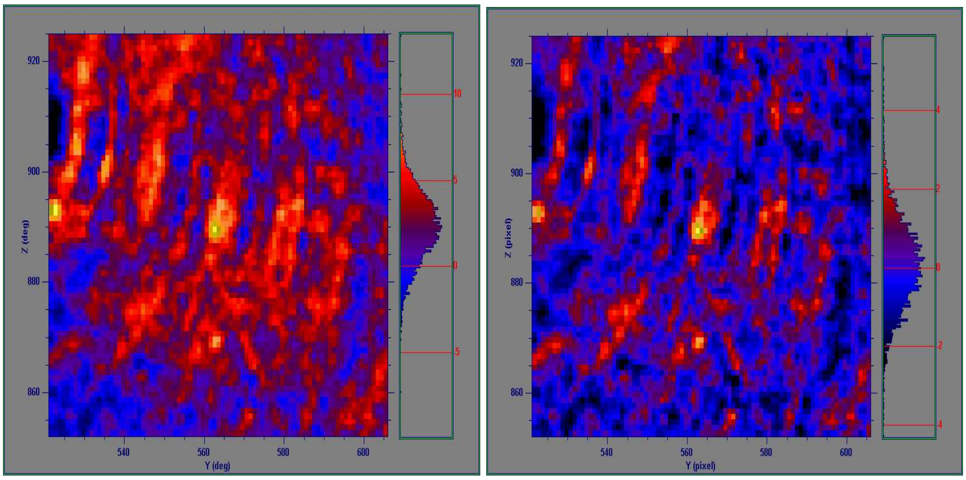

Figure 8.9: Zoom images by A. Segreto for the first source candidate, before the image renormalization (left) and after (right).

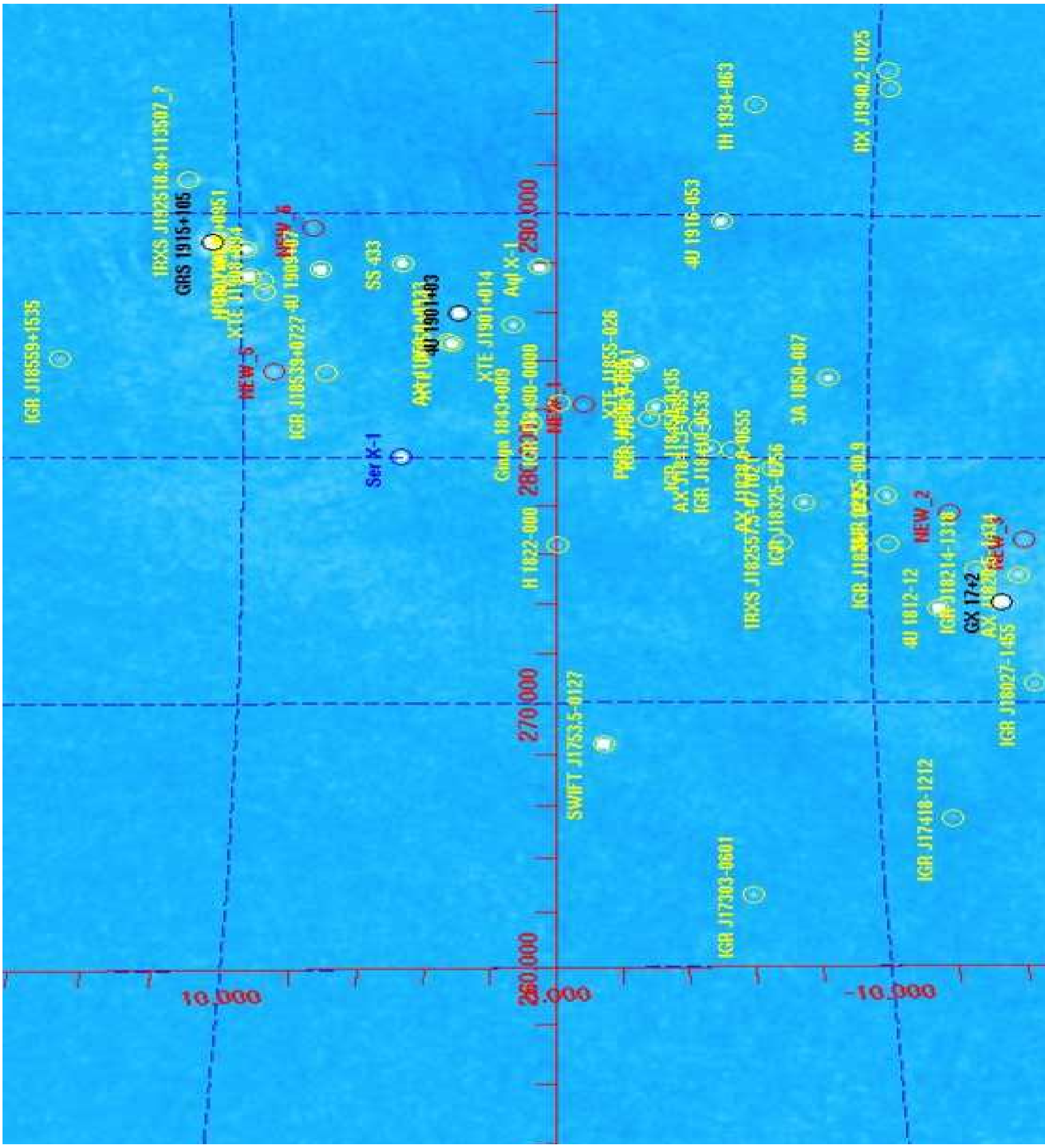
IGR J18559+1535
1RXS J192518.9+113507_?
GRS 1915+105
XTE J1908+094
NEW_5
NEW_6
4U 1909+07
IGR J18539+0727
Ser X-1
SS 433
4U 1901+03
XTE J1901+014
Ginga 1843+009
Aql X-1
H 1822-000
IGR J18490-0000
NEW_1
260.000
270.000
280.000
290.000
10.000
0.000
-10.000
SWIFT J1753.5-0127
XTE J1855-026
IGR J18450-0435
AX J1841.3-0455
IGR J18410-0535
IGR J17303-0601
4U 1916-053
1H 1934-063
1RXS J182557.5-071021
IGR J18325-0756
3A 1850-087
RX J1940.2-1025
4U 1812-12
NEW_2
IGR J17418-1212
IGR J18214-1318
GX 17+2
NEW_3
IGR J18027-1455

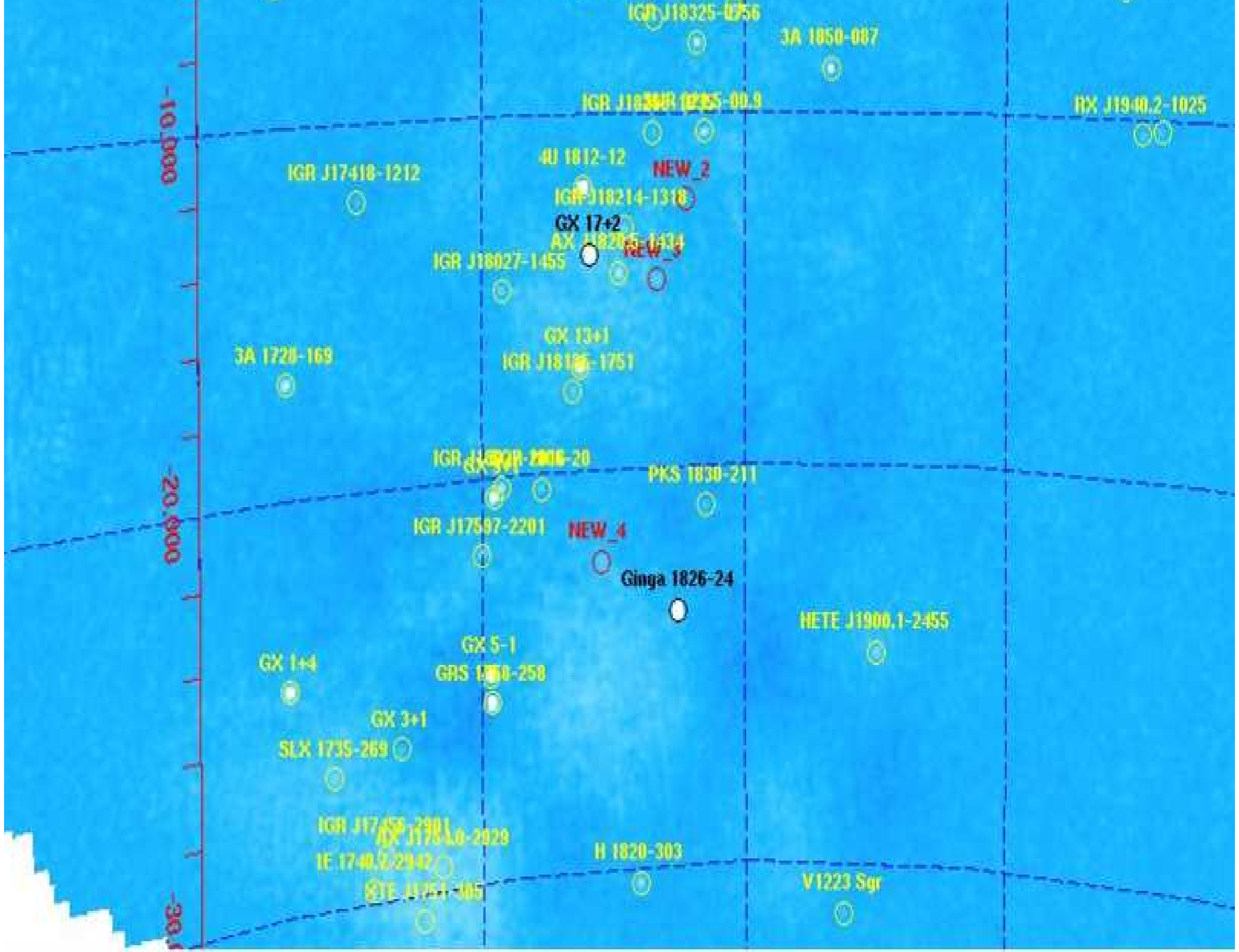

Figure 8.11: Mosaic of the Scutum region by ISGRI using the OSA5.1 release software, in the 20-40 keV band in equatorial coordinates.

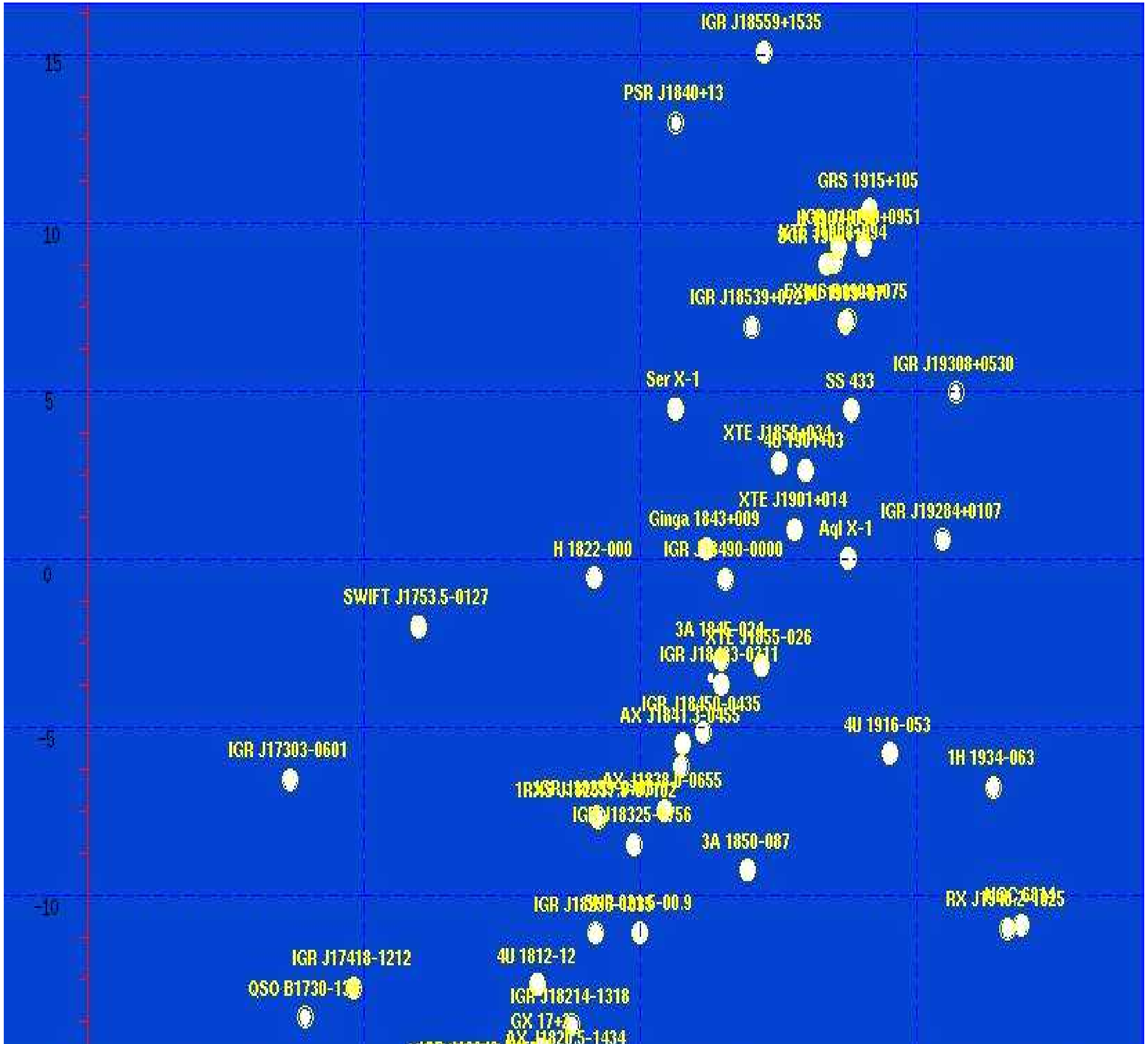
15
10
5
0
-5
-10
IGR J18559+1535
PSR J1840+13
GRS 1915+105
IGR J18539+0727
IGR J19308+0530
Ser X-1
SS 433
XTE J1901+014
Ginga 1843+009
IGR J19284+0107
Aql X-1
H 1822-000
SWIFT J1753.5-0127
3A 1845-024
XTE J1855-026
IGR J18450-0435
AX J1841.3-0455
4U 1916-053
IGR J17303-0601
1H 1934-063
IGR J18325-0756
3A 1850-087
IGR J17418-1212
4U 1812-12
QSO B1730-130
IGR J18214-1318
GX 17+2
AX J18205-1434

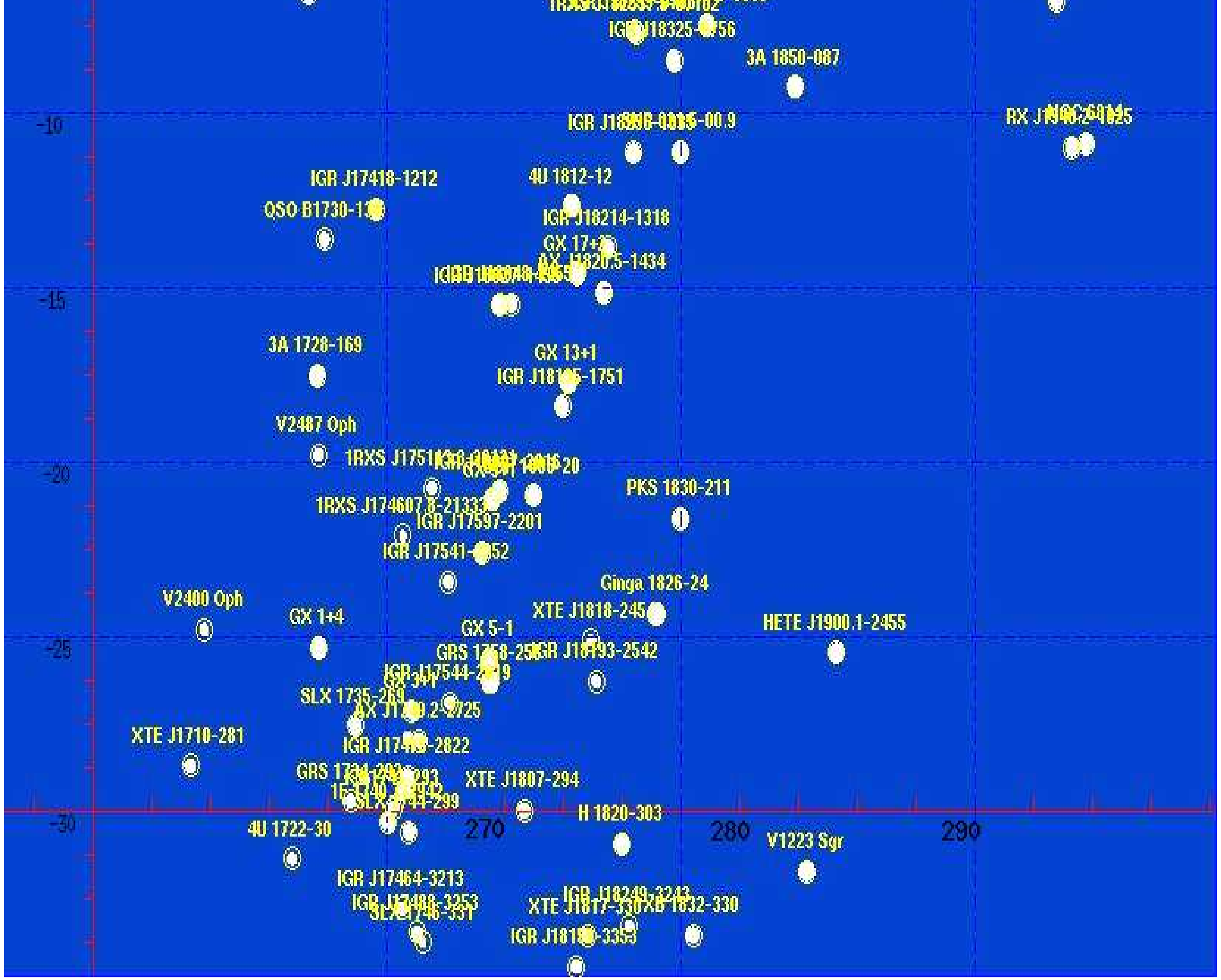

Figure 8.13: Mosaic of the Scutum region by ISGRI using the alternative software by A. Segreto, also in the 20-40 keV band and in equatorial coordinates.

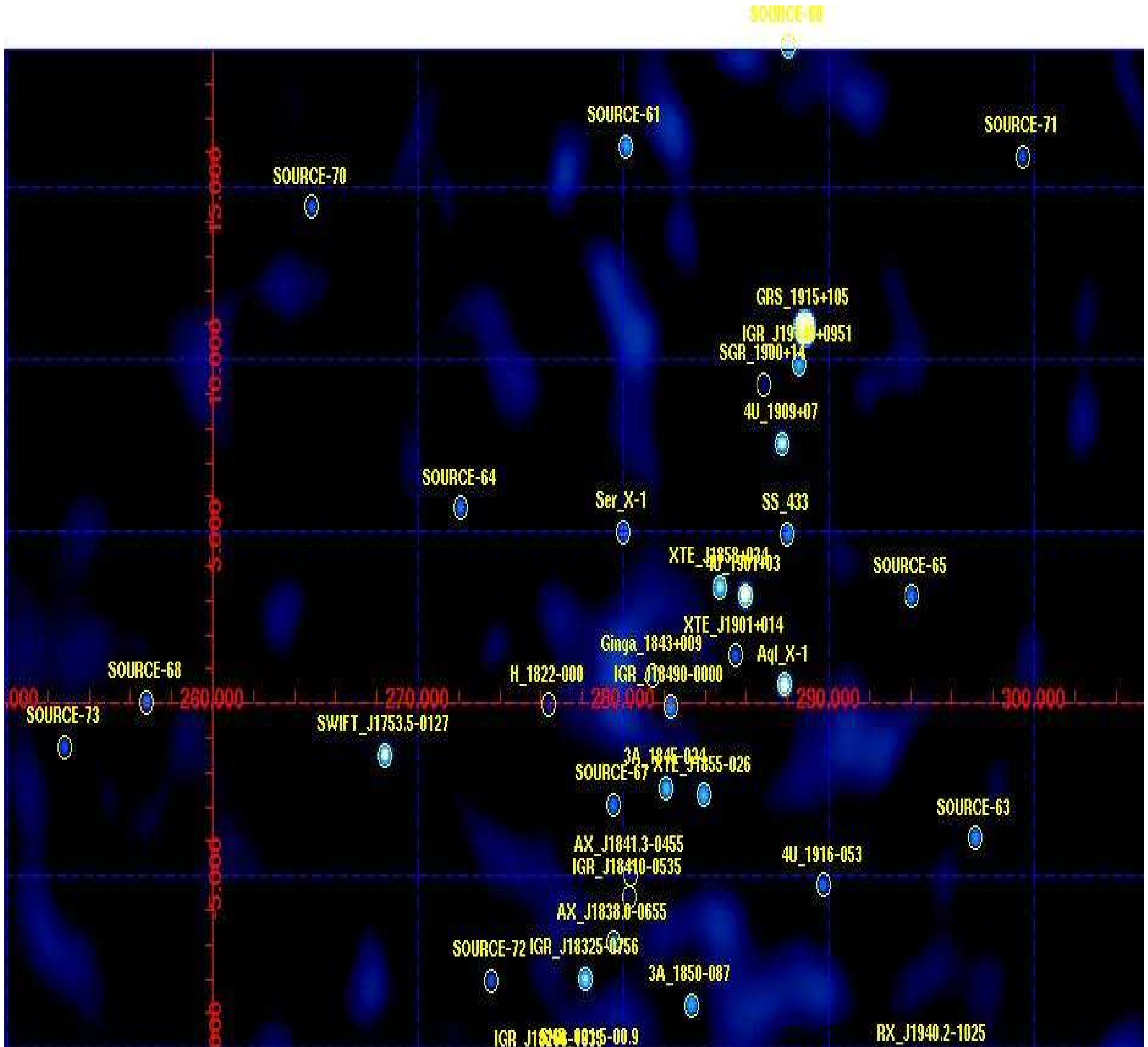
SOURCE-60
SOURCE-61
SOURCE-71
SOURCE-70
GRS_1915+105
IGR_J19140+0951
SGR_1900+14
4U_1909+07
SOURCE-64
Ser_X-1
SS_433
XTE_J1858+034
4U_1901+03
SOURCE-65
XTE_J1901+014
Ginga_1843+009
Aql_X-1
SOURCE-68
H_1822-000
IGR_J18490-0000
SOURCE-73
SWIFT_J1753.5-0127
3A_1845-024
XTE_J1855-026
SOURCE-67
SOURCE-63
AX_J1841.3-0455
IGR_J18410-0535
4U_1916-053
AX_J1838.0-0655
SOURCE-72
IGR_J18325-0756
3A_1850-087
RX_J1940.2-1025
260.000
270.000
280.000
290.000
300.000
15.000
10.000
5.000
-5.000

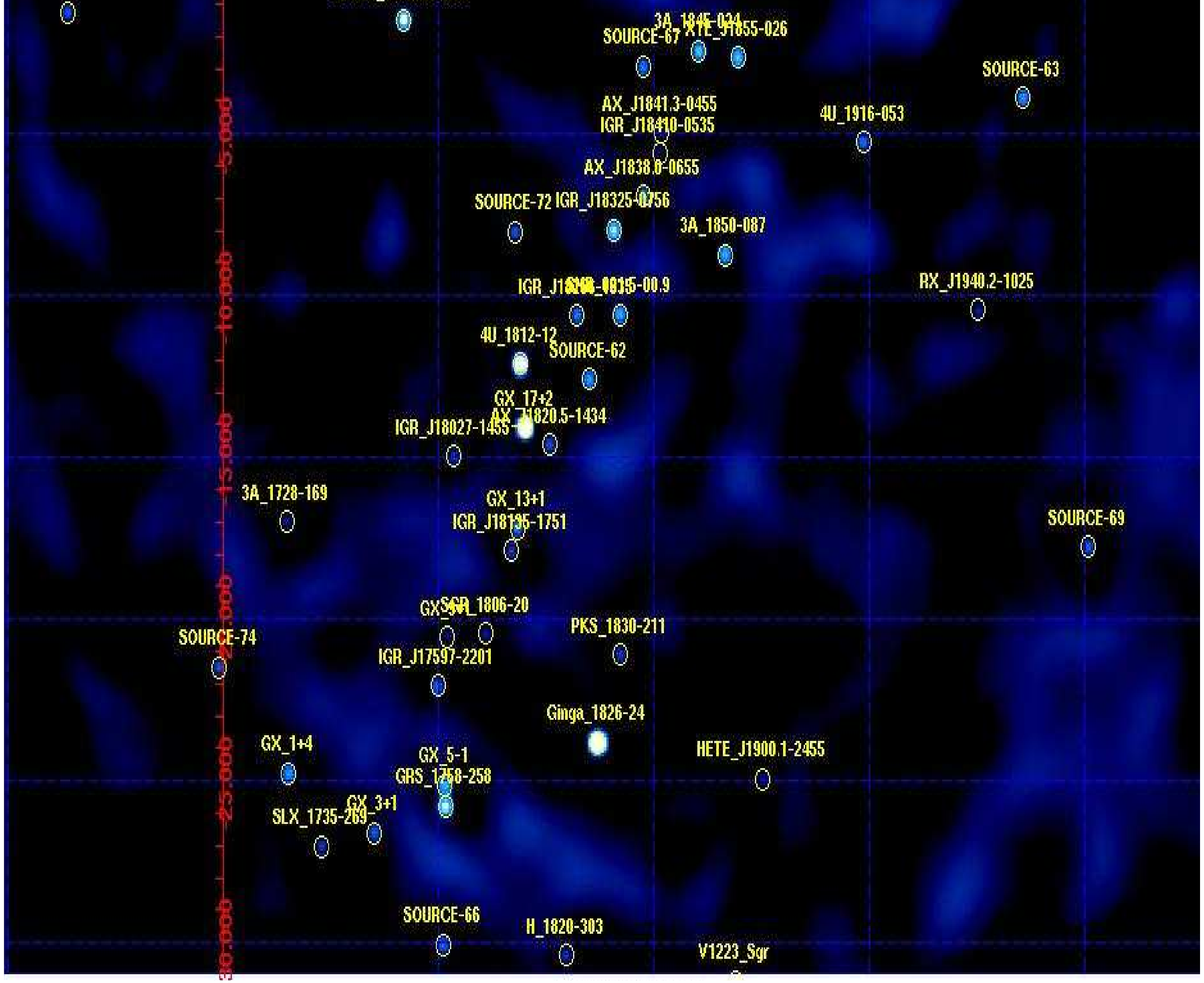

Figure 8.15: A 20-40 keV image of the Scutum region by SPI in equatorial coordinates.

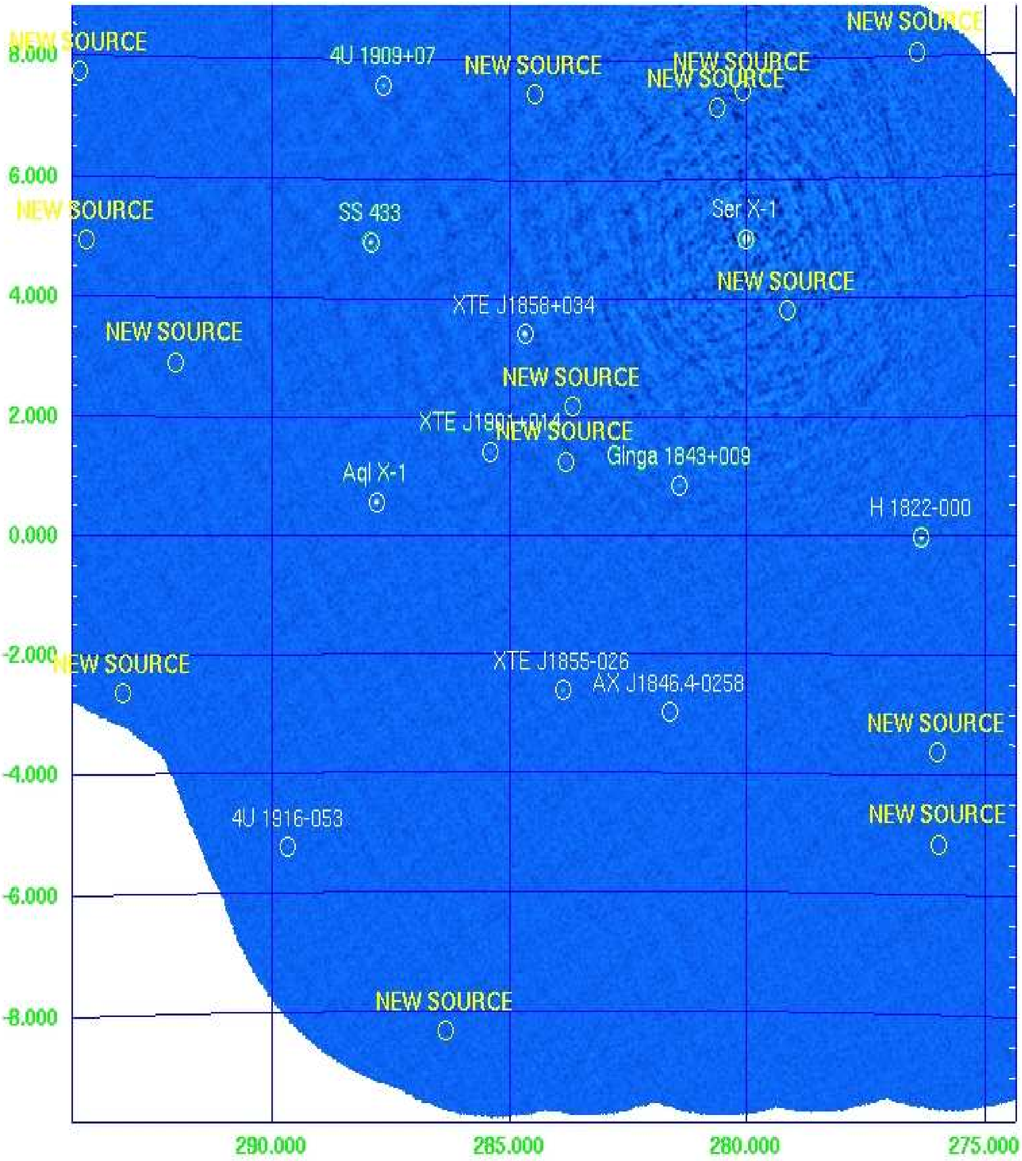

Figure 8.16: Mosaic of part of the Scutum region by JEM-X in the 4-10 keV band.

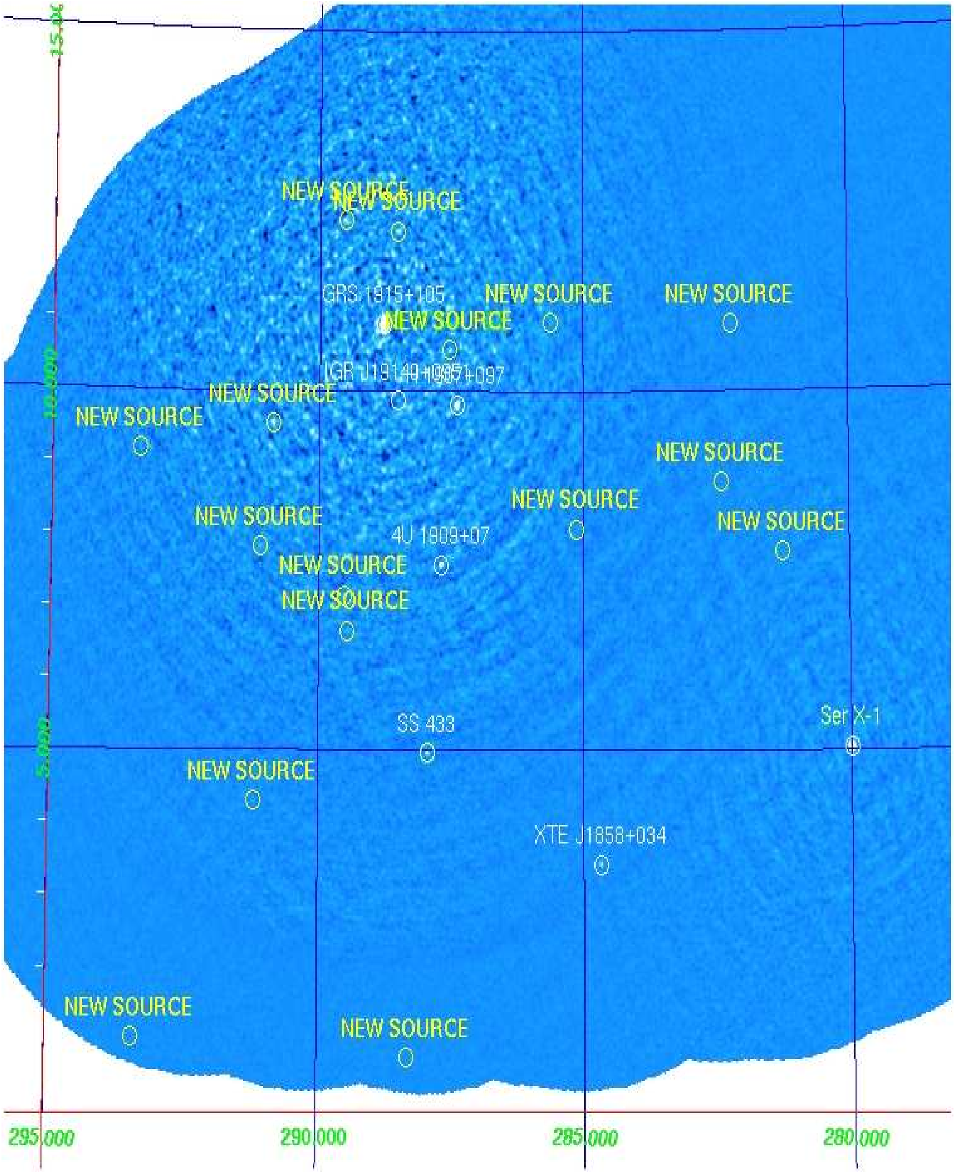

Figure 8.17: Another JEM-X mosaic covering the rest of the Scutum region, in the same 4–10 keV band.

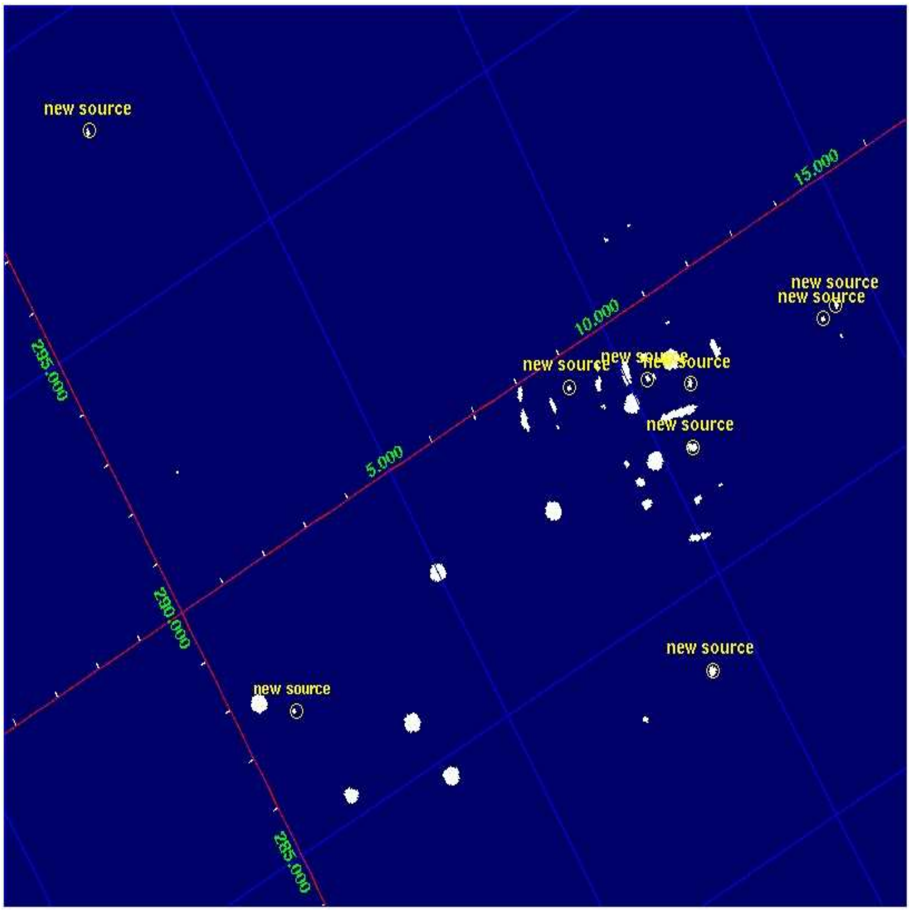

Figure 8.18: New source candidates in the in the 20–40keV band detected following our method.

Bibliography

Ananth, A. G. and Nagaraja, B. V.: 1982, *ApJ* **259**, 664

Bodaghee, A., Courvoisier, T. J.-L., Rodriguez, J., Beckmann, V., Produit, N., Hannikainen, D., Kuulkers, E., Willis, D. R., and Wendt, G.: 2007, *A&A* **467**, 585

Coe, M. J., Fabregat, J., Negueruela, I., Roche, P., and Steele, I. A.: 1996, *MNRAS* **281**, 333

Courvoisier, T. J.-L., Walter, R., Beckmann, V., Dean, A. J., Dubath, P., Hudec, R., Kretschmar, P., Mereghetti, S., Montmerle, T., Mowlavi, N., Paltani, S., Preite Martinez, A., Produit, N., Staubert, R., Strong, A. W., Swings, J.-P., Westergaard, N. J., White, N., Winkler, C., and Zdziarski, A. A.: 2003, *A&A* **411**, L53

Hammersley, P. L., Garzon, F., Mahoney, T., and Calbet, X.: 1994, *MNRAS* **269**, 753

Hayakawa, S., Matsumoto, T., Murakami, H., Uyama, K., Yamagami, T., and Thomas, J. A.: 1979, *Nat* **279**, 510

Israel, G. L., Negueruela, I., Campana, S., Covino, S., Di Paola, A., Maxwell, D. H., Norton, A. J., Speziali, R., Verrecchia, F., and Stella, L.: 2001, *A&A* **371**, 1018

Koyama, K., Kawada, M., Kunieda, H., Tawara, Y., and Takeuchi, Y.: 1990, *Nat* **343**, 148

Revnivtsev, M. G.: 2003, *Astronomy Letters* **29**, 644

Chapter 9

Conclusions

The study of the HMXRBs along the Galactic Plane mentioned above, along with the Scutum region, allowed us to obtain several results of scientific interest:

- The HMXRB system EXO 2030+375 (as A 0535+26) showed an unusual feature (pre–spike) in the medium-term light curve before the maximum. Another possible spike was maybe detected in addition. The physical mechanisms producing these features remain still unknown. For EXO 2030+375, our spectral analysis during a normal outburst in the 5–300 keV did not show any cyclotron feature. Only during a giant outburst we can confirm the detection of the 10 keV cyclotron line.

- This first long-term pulse profile analysis of the X-ray pulsar SAX J2103.5+4545 revealed single, double, triple or even quadruple peaks pulse profile structure. The pulse shape was complex and highly variable either with time, orbital phase or luminosity. However, the strength of all the peaks increases with luminosity. We could confirm that SAX J2103.5+4545 becomes harder when the flux is higher. A new orbital solution was also obtained.

- A medium–term pulse profile analysis was carried out for A 0535+26. We found luminosity and also energy correlations in the pulse profile. This is the first time that a pulse profile study during the pre–spike was done, confirming that during that short time period a change in the pulse shape was evident. In addition, the pulse profile energy study revealed pulse to pulse variations.

- Our study of the Scutum region discovered possible new X–ray source candidates, to be analyzed in more detail. The IR study will allow us to distinguish the likely HMXRB systems among them.

9.1 Future work

We are still handling *RXTE* EXO 2030+375 data from the 2006 giant outburst. We plan to perform a detailed pulse profile study, to obtain the cyclotron line variations with energy and luminosity and a pre–spike pulse profile analysis. SAX J2103.5+4545 is a puzzling system. Pulse phase resolved spectral analysis might resolve some issues. This is also worthwhile to be done for A 0535+26, as well as to obtain the cyclotron line variations with energy and luminosity. In a further step, we plan to build a model which would explain some of the pulse shape variety found for SAX J2103.5+4545 and A 0535+26.

Our group is running a long-term multiwavelength monitoring program of a sample of X-ray pulsars, which includes IR photometry and spectroscopy. Currently we perform regular observing runs to obtain infrared photometry at the 1.5m. Carlos Sanchez Telescope in Tenerife (Spain), and also obtaining IR spectroscopy in the 3.6m Galileo Telescope in La Palma (Spain). Once a new γ ray source will be detected by *INTEGRAL*, our IR imaging photometry will allow the identification of counterpart candidates as highly reddened objects inside the X/γ–ray error circle. IR spectroscopy will indicate which of the candidates are B supergiants or Be stars, the most common companions to X–ray pulsars. After this, we will carry out a spectral and temporal study, as it has been presented in previous chapters of this dissertation.

Appendix A

INTEGRAL Observations of EXO 2030+375

Table A.1: Journal of Observations.

Instrument	Rev	Obs.Time ks	Mean MJD	Mean Flux mCrab
JEM-X	19	5.4	52618.70	36±1
(4-30 keV)	20	3.6	52621.67	46±2
	80	7.2	52801.12	46±1
	82	2.2	52805.92	61±3
	191	7.2	53133.19	59±2
	218	1.8	53214.13	61±5
	251	9.0	53313.79	112±2
	252	9.0	53315.92	99±2
	265	2.2	53353.51	84±3
	266	2.2	53356.50	116±4
IBIS/ISGRI	18	87.5	52615.97	51.6±1.2
(20-40 keV)	19	230	52618.70	68.1±0.6
	20	281.9	52621.66	82.5±0.8
	21	171.8	52624.68	70.8±0.8
	22	13	52627.60	54.3±0.6
	23	13	52630.63	21.8±3*

Continued...

Table A.1: Continued.

Instrument	Rev	Obs.Time ks	Mean MJD	Mean Flux mCrab
	25	2.2	52637.59	31.29±6*
	31	0	52653.33	–
	52	4.4	52717.31	63.6±2
	54	2.2	52722.83	28.18±5*
	59	6.6	52737.12	10.6*
	62	0	52746.19	–
	67	79.2	52761.80	91.37±1.1
	70	8.8	52770.11	10*
	74	5.4	52782.15	10*
	79	75.6	52798.22	6*
	80	83.6	52801.12	59.65±0.7
	82	11	52805.92	90.5±4
	87	0	52820.87	–
	92	2.2	52835.98	5*
	142	8.8	52985.39	108.11±3
	145	8.8	52994.38	58.6 ±3
	153	41.4	53019.70	4*
	154	36	53023.19	6*
	159	129.6	53037.59	107.2 ±0.7
	160	162.8	53040.44	72.9±0.7
	162	6.6	53045.66	18±3*
	181	6.6	53103.59	13 *
	185	6.6	53114.26	6*
	189	11	53126.15	106.33±3
	190	127.8	53130.19	137.05±0.74
	191	136.8	53133.19	92.6 ±0.7
	193	2.2	53137.94	43±5
	197	0	53149.94	–
	202	4.4	53164.73	6*
	207	0	53179.71	–
	210	48.6	53189.58	8*
	211	27	53193.05	8*
	212	27	53195.98	6*

Continued...

Table A.1: Continued.

Instrument	Rev	Obs.Time ks	Mean MJD	Mean Flux mCrab
	213	14.4	53199.21	9*
	214	18	53201.88	6*
	215	1.8	53204.98	15±4
	216	16.2	53207.93	7*
	218	48.6	53214.13	50.8±0.9
	229	4.4	53246.42	2*
	233	11	53257.55	18±6*
	234	0	53260.47	–
	241	11	53281.48	30±3*
	245	4.4	53293.62	6*
	249	8.8	53305.58	23±4*
	251	55.8	53313.79	150.2±0.8
	252	102.6	53315.92	124.7 ±0.6
	253	64.8	53318.68	85±1
	255	3.6	53324.55	39 ±4
	257	28.8	53330.05	14±0.5*
	259	14.4	53336.11	9*
	261	5.4	53342.04	8*
	263	6.6	53347.54	9*
	264	11	53350.53	16*
	265	8.8	53353.51	153±3
	266	11	53356.50	159±4
	268	3.6	53363.94	138±18*
	269	11	53364.63	144±4
	282	6.6	53404.55	216±7
	286	4.4	53416.92	76±6
	292	2.2	53434.65	19*
	301	6.6	53461.69	21±3*
	303	4.4	53466.91	1.5*
	307	6.6	53478.97	10*
	311	8.8	53491.03	170±4
	315	8.8	53503.43	100±3
	319	2.2	53514.95	37*

Continued...

Table A.1: Continued.

Instrument	Rev	Obs.Time ks	Mean MJD	Mean Flux mCrab
	323	0	53526.95	–
	332	8.8	53553.69	13*
	340	2.2	53578.87	5*
	384	2.2	53709.64	31*
SPI (20-40 keV)	19	180	52618.70	56±3
	20	169.2	52621.66	83±3
	21	135	52624.68	60±3
	22	99	52627.60	55±4
	23	158.4	52630.63	6±3
	25	79.2	52637.59	2±4
	31	6.6	52653.33	–
	52	4.4	52717.31	97±38
	54	11	52722.83	30±14
	59	8.8	52737.12	35±13
	62	11	52746.19	–
	67	64.8	52761.80	83±4
	70	11	52770.11	10±10
	74	13.2	52782.15	–
	79	113.4	52798.22	3±2
	80	117	52801.12	40±2
	82	11	52805.92	71±10
	87	15.4	52820.87	–
	92	6.6	52835.98	45±14
	142	13.2	52985.39	91±9
	145	8.8	52994.38	40±12
	153	90	53019.70	–
	154	70.2	53023.19	5±4
	159	131.4	53037.59	95±3
	160	138.6	53040.44	70±3
	162	8.8	53045.66	31±13
	181	11	53102.58	13±10
	185	11	53114.26	–

Continued...

Table A.1: Continued.

Instrument	Rev	Obs.Time ks	Mean MJD	Mean Flux mCrab
	189	13.2	53126.15	75±10
	190	127.8	53130.19	115±3
	191	136.8	53133.19	83±3
	193	13.2	53137.94	29±10
	197	8.8	53149.94	3±14
	202	13.2	53164.73	–
	207	4.4	53179.71	–
	210	54	53189.58	13±3
	211	106.2	53193.05	7±2
	212	106.2	53195.98	9±2
	213	88.2	53199.21	11±3
	214	99	53201.88	9±2
	215	86.4	53204.98	12±3
	216	108	53207.93	2±2
	218	99	53214.13	39±3
	229	13.2	53246.42	13±10
	233	15.4	53257.55	–
	234	2.2	53260.47	–
	241	13.2	53281.48	41±11
	245	11	53293.62	–
	249	13.2	53305.58	25±10
	251	86.4	53313.79	131±3
	252	82.8	53315.92	103±3
	253	99	53318.68	77±3
	255	66.6	53324.55	20±4
	257	84.6	53330.05	19±4
	259	61.2	53336.11	18±4
	261	61.2	53342.04	15±5
	263	11	53347.54	–
	264	11	53350.53	26±12
	265	8.8	53353.51	100±13
	266	11	53356.50	131±13
	269	19.8	53364.63	127±12

Continued...

Table A.1: Continued.

Instrument	Rev	Obs.Time ks	Mean MJD	Mean Flux mCrab
	282	6.6	53404.55	180±16
	286	4.4	53416.92	76±19
	292	4.4	53436.73	–
	301	8.8	53461.69	13±14
	303	8.8	53466.91	16±13
	307	11	53478.97	23±13
	311	8.8	53491.03	96±15
	315	8.8	53503.43	72±12
	319	8.8	53514.95	13±11
	323	8.8	53526.95	–
	332	8.8	53553.69	11±13
	340	6.6	53578.87	–
	384	4.4	53709.64	57*

* upper limits only

Appendix B

Detections in the Scutum region

Table B.1: Known sources detected using the 3-high energy instruments on board *INTEGRAL*. The IBIS and SPI results in this Table are in the 20–40 keV band, and JEM—X results in the 4–10 keV energy range.

NAME OSAA5.1	DET. LEV	ScW NUM	OG BAND*	SIG Det. Segreto Mosaic	SPI SIG Det	JEM–X SIG	E. band mosaic**	JEM–X2 ScW det	JEM–X1 ScW det
$GRS1915+105$	1337.96	1707	1,2,3	2326.7	300.3	1.541	1,2,3	152	376
$GX17+2$	563.11	1449	1,2	493.5	48.82	1.5307	1,2,3	84	165
$ScoX-1$	267.84	31	1,2	246.9	12.41				
$Ginga1826-24$	250.96	606	2,3	270.1	61.39				
$4U1901+03$	159.06	2337	1,2	332.9	30.33	-	-	245	-
$SerX-1$	144.86	2327	1	102.5	10.16	1.6070	1,2,3	41	267
$SWIFTJ1753.5-0127$	130.5	1268	3	144.6	22.18	-	-	-	4
$4U1812-12$	94.98	1588	3	200.9	33.43	1.5008	1,2,3	-	3
$GRS1758-258$	73.29	422	3	119.9	18.58				
$H1907+097$	160.07	1814	-	142.2	-	1.6004	1,2,3	21	36
$4U1909+07$	155.85	1977	-	128.7	19.21	1.5179	1,2,3	6	22
$GX5-1$	145.97	481	-	108.5	13.44				
$XTEJ1858+034$	144.06	2380	-	85.0	19	1.2891	1,2,3	-	78
$AqlX-1$	126.49	2388	-	124.4	24.53	1.4867	1,2,3	86	44
$GX13+1$	115.8	1199	-	77.4	8.76	1.5449	1,2,3	35	60
$XTEJ1855-026$	111.36	2788	-	113.8	14.45	1.3323	1,2,3	4	9
$GX9+1$	108.86	855	-	57.4	2.88				
$SS433$	95.66	2119	-	92.1	11.25	1.459	1,2,3	22	18
$IGRJ19140+0951$	82.86	1791	-	69.9	14.2	1.3780	3	5	3
$4U1916-053$	70.49	2101	-	73.2	8.65	1.2513	1	38	-
$GX1+4$	66.24	272	-	53.9	11.0				
$3A1728-169$	52.16	548	-	30.6	4.34				
$Ginga1843+009$	47.65	2687	-	43.9	5.58	1.4396	1,2,3	-	6
$IGRJ18483-0311$	47.07	2845	-	48.1					
$3A1850-087$	43.35	2227	-	46.8	13.0	1.4403	1,2	-	-
$AXJ1820.5-1434$	32.5	1451	-	23.3	6.36				

Continued...

Table B.1: Continued.

NAME OSAA5.1	DET. LEV	ScW NUM	OG BAND*	SIG Det. Segreto Mosaic	SPI SIG Det	JEM–X det. level	E. band mosaic**	JEM–X2 ScW det	JEM–X1 ScW det
$AXJ1859.0+0333$	31.64	2363	-						
$IGRJ18325-0756$	31.44	2288	-	34.6	17.13				
$XTEJ1901+014$	30.71	2484	-	29.4	7.51	1.3203	1,2	-	-
$AXJ1754.0-2929$	29.73	127	-						
$H1820-303$	28.6	95	-	22.9	5.39				
$H1822-000$	27.38	2526	-	16.5	4.99	1.47	1,2	22	26
AX J1755.2-3017	27.11	78	-						
$SNR021.5-00.9$	26.73	2017	-	25.6	12.47	1.4768	1	-	-
SAX J1750.8-2900	26.65	137	-						
$1E1740.7-2942$	26.46	87	-	8.6					
$IGRJ18027-2016$	25.97	874	-	23.5					
AX J1754.5-2927	25.95	127	-						
PSR B1841-04	25.88	2776	-						
$AXJ1841.3-0455$	25.88	2776	-	23.4	3.71				
1A 1742-294	24.95	105	-						
AX J1748.6-2957	24.81	86	-						
1E 1743.1-2852	24.1	132	-						
IGR J17507-2856	24	146	-						
1E 1743.1-2843	23.63	147	-						
IGR J17475-2822	22.81	163	-						
1E 1742.8-2853	22.69	132	-						
$XTEJ1751-305$	22.4	62	-						
AX J1747.0-2828	21.58	162	-						
$IGRJ17456-2901$	21.38	125	-						
AX J1745.6-2900	21.38	124	-						
1A 1742-289	21.38	123	-						
SWIFT J174540.2-2900	21.38	125	-						
KS 1741-293	21.34	106	-						
RX J1745.7-2904	21.3	122	-						

Continued...

Table B.1: Continued.

NAME OSAA5.1	DET. LEV	ScW NUM	OG BAND*	SIG Det. Segreto Mosaic	SPI SIG Det	JEM–X det. level	E. band mosaic**	JEM–X2 ScW det	JEM–X1 ScW det
1E 1742.7-2902	21.3	123	-						
SAX J1744.7-2916	21.19	107	-						
AX J1747.0-2837	21.12	156	-						
1E 1742.2-2857	20.93	126	-						
IGR J17461-2853	20.8	133	-						
1E 1742.9-2852	20.8	133	-						
SLX 1744-299	20.5	82	-	4.1					
SLX 1744-300	20.5	80	-						
GRO J1744-28	20.45	138	-						
IGR J18173-2509	20.18	483	-						
$SLX1735-269$	20.06	206	-	6.2	5.8				
IGR J17487-3124	19.79	28	-						
XTE J1748-288	19.63	165	-						
$IGRJ18214-1318$	19.53	1577	-	6.6					
1E 1742.9-2849	19.52	135	-						
IGR J18193-2542	19.44	430	-						
AX J1748.3-2854	19.31	135	-						
GC X-4	18.37	103	-						
GX 1.1-1.0	18.3	181	-						
$HETEJ1900.1-2455$	17.91	429	-	12.7	4.04				
$AXJ1838.0-0655$	17.53	2500	-	19.9	9.74				
GRS 1741.9-2853	17.36	125	-						
Ginga 1741.2-2859	17.25	120	-						
1E 1742.5-2859	17.25	121	-						
SAX J1818.6-1703	17.2	1232	-						
2CG 013+00	16.81	1219	-						
GRS 1739-278	16.36	184	-						
GRS 1747-312	16.31	36	-						
SAX J1810.8-2609	15.99	390	-						

Continued...

Table B.1: Continued.

NAME OSAA5.1	DET. LEV	ScW NUM	OG BAND*	SIG Det. Segreto Mosaic	SPI SIG Det	JEM–X det. level	E. band mosaic**	JEM–X2 ScW det	JEM–X1 ScW det
XTE J1818-245	15.97	542	-						
$IGRJ17597-2201$	15.78	716	-	13.9	7.9				
1E 1742.5-2845	15.77	137	-						
IGR J17407-2808	15.73	151	-						
XTE J1739-285	15.57	127	-						
GX 359+2	15.54	120	-						
IGR J17497-2821	15.47	177	-						
$IGRJ18027-1455$	15.44	1257	-	11.1	5.71				
2CG 359-00	15.43	52	-						
$SGR1900+14$	15.42	1855	-	7.6	3.66				
AX J1742.5-2845	15.21	129	-						
AX J1743.9-2846	15.11	132	-						
1A 1743-288	15.06	134	-						
$IGRJ18135-1751$	14.88	1141	-	7.8	5.94				
$PSRJ1846-0258$	14.77	2858	-						
IGR J18246-1425	14.75	1490	-						
IGR J18134-1636	14.66	1236	-						
AX J1738.4-2902	14.52	92	-						
AX J1747.1-2809	14.52	181	-						
$IGRJ18539+0727$	14.45	2070	-	4.3					
SLX 1737-282	14.41	141	-						
AX J1739.4-2656	14.32	218	-						
$IGRJ17303-0601$	14.17	713	-	13.5					
AX J1818.8-1527	14.08	1373	-						
$NGC6814$	14.05	766	-	12.0					
AX J1742.6-2901	13.92	113	-						
IGR J17419-2802	13.87	166	-						
AX J1739.5-2730	13.85	187	-						
$GX3+1$	13.71	290	-	9.2					

Continued...

Table B.1: Continued.

NAME OSAA5.1	DET. LEV	ScW NUM	OG BAND*	SIG Det. Segreto Mosaic	SPI SIG Det	JEM–X det. level	E. band mosaic**	JEM–X2 ScW det	JEM–X1 ScW det
AX J1819.2-1601	13.67	1328	-						
SAX J1819.3-2525	13.65	459	-						
1RXS J182129.0-13164	13.47	1580	-						
AX J1758.0-2818	13.14	209	-						
AX J1739.3-2923	13.14	83	-						
HESS J1825-137	13.07	1552	-			-	-	-	1
AX J1818.8-1559	12.99	1325	-						
AX J1747.3-2809	12.88	181	-						
*RXJ*1940.2 − 1025	12.82	830	-	10.4	7.43				
IGR J18048-1455	12.78	1278	-						
*RXJ*1826.2 − 1450	12.49	1458	-						
AX J1821.0-1420	12.46	1474	-						
I*GRJ*18450 − 0435	12.35	2786	-	14.9		1.1986	1	-	1
AX J1742.6-3022	12.33	51	-						
IGR J17445-2747	12.2	193	-						
*XTEJ*1908 + 094	11.76	1845	-	6.4					
AX J1755.7-2818	11.75	198	-						
KS 1732-273	11.49	162	-						
*IGRJ*18559 + 1535	11.46	1324	-	10.7					
IGR J17364-2711	11.44	177	-						
IGR J18308-1232	11.33	1755	-						
2EG J1811-2339	11.22	643	-						
AX J1754.2-2754	11.18	221	-						
SAX J1752.3-3138	10.95	27	-						
AX J1740.2-2848	10.72	113	-						
EXS 1737.9-2952	10.62	66	-						
AX J1819.2-1548	10.4	1350	-						
*SGR*1806 − 20	10.29	890	-	13.6	4.51				
AX J1739.5-2910	10.27	97	-						

Continued...

Table B.1: Continued.

NAME OSAA5.1	DET. LEV	ScW NUM	OG BAND*	SIG Det. Segreto Mosaic	SPI SIG Det	JEM–X det. level	E. band mosaic**	JEM–X2 ScW det	JEM–X1 ScW det
AX J1824.7-1253	10.23	1644	-						
$IGRJ18410-0535$	10.2	2694	-	12.2	3.16				
PSR J1811-1926	10.03	995	-						
AX J1740.5-2937	9.98	82	-						
$IGRJ18490-0000$	9.78	2729	-	9.3	11.01				
AX J1740.2-2903	9.77	101	-						
RX J1744.7-2713	9.64	231	-						
KS 1739-304	9.51	48	-						
PDS 456	9.45	543	-						
3A 1845-024	9.3	2857	-	12.0					
AX J1825.1-1253	9.29	1650	-						
IGR J17472+0701	9.08	613	-						
AX J1830.6-1002	9.01	2028	-						
$PKS1830-211$	8.77	863	-		11.1				
AX J1817.0-1607	8.75	1301	-						
AX J1740.4-2856	8.73	104	-						
AX J1736.4-2910	8.71	80	-						
2EG J1825-1307	8.63	1579	-						
IGR J19267+1325	8.47	1496	-						
GRS 1736-297	8.43	74	-						
AX J1822.2-1425	8.27	1477	-						
2EG J1813-1229	8.22	1482	-						
2EGS J1736-2904	8.03	88	-						
KS 1731-260	7.81	220	-						
PSR J1840+13	7.78	1487	-						
GRS 1734-292	7.72	88	-						
IGR J18259-0706	7.64	2247	-	4.2					
1RXS J182557.5-07102	7.6	2242	-						
GRO J1719-24	7.33	131	-						

Continued...

Table B.1: Continued.

NAME OSAA5.1	DET. LEV	ScW NUM	OG BAND*	SIG Det. Segreto Mosaic	SPI SIG Det	JEM–X det. level	E. band mosaic**	JEM–X2 ScW det	JEM–X1 ScW det
AX J1734.5-2915	7.31	66	-						
IGR J17476-2253	7.19	558	-						
AX J1740.5-3014	6.94	53	-						
3EG J1824-1514	6.92	1421	-						
3EG J1800-0146	6.91	1568	-						
AX J1810.5-1917	6.89	1008	-						
IGR J18256-1035	6.87	1892	-	8.1					
AX J1846.0-0231	6.82	2865	-			-	-	-	1
AX J1832.5-0916	6.76	2139	-						
PSR J1844-0258	6.75	2864	-						
AX J1753.5-2745	6.68	232	-						
EQ J1906+09	6.67	1890	-						
AX J1751.1-2748	6.67	222	-						
AX J1910.7+0917	6.59	1842	-						
IGR J19378-0617	6.56	1355	-						
1H 1934-063	6.56	1359	-	6.2					
3EG J1646-0704	6.55	77	-						
AX J1825.6-1214	6.45	1716	-						
4U 1651-06	6.37	148	-						
AX J1824.5-1311	6.3	1608	-						
2EGS J1708-0927	6.27	280	-						
AX J1749.2-2725	6.26	249	-						
AX J1844.7-0305	6.12	2865	-						
IGR J17314-2854	6.04	62	-						
AX J1812.1-1835	6.01	1073	-						
AX J1825.5-1144	5.98	1761	-						
IGR J17464-3213	5.95	9	-						
IGR J17418-1212	5.95	930	-	7.5					
AX J1811.2-1828	5.94	1082	-						

Continued...

Table B.1: Continued.

NAME OSAA5.1	DET. LEV	ScW NUM	OG BAND*	SIG Det. Segreto Mosaic	SPI SIG Det	JEM–X det. level	E. band mosaic**	JEM–X2 ScW det	JEM–X1 ScW det
IGR J18485-0047	5.92	2773	-						
QSO B1730-130	5.91	689	-						
Ginga 1855-02	5.9	2767	-						
XTE J1856+053	5.8	2244	-						
XB 1940-04	5.79	1434	-						
AX J1808.2-2021	5.71	900	-						
IGR J17541-2252	5.6	619	-						
AX J1832.3-0840	5.59	2212	-						
Briggs Source	5.46	58	-						
V1223 SgrV	5.46	58	-	8.2					
AX J1846.4-0258	-	-	-	-	-	1.4639	1		
BriggsSource^{sex}	6.33	-	-	-	-	-	-	-	-

* IBIS/ISGRI mosaic detection energy band 1: 15–20 keV ; energy band 2: 20–40 keV ; energy band 3: 40–60 keV

*∗ JEM–X mosaic energy band 1: 4-10 keV ; energy band 2: 10-15 keV ; energy band 3: 15-35 keV

On *red* ISGRI known sources detected in the OSA5.1 mosaic but not included in the mosaic results catalog.

^{sex} detected only by SExtractor in the OSA5.1 ISGRI mosaic.

Table B.2: New ISGRI source candidates detected using our method in the 20–40 keV (in blue)and 20–60 keV (in magenta) energy bands.

OSA5.1 RA FIN	ISGRI map Dec FIN	DET SIG
287.392	1.130	5.5
283.621	9.031	7.4
287.889	13.88	5.5
287.959	14.24	6.0
289.478	8.887	5.3
287.279	10.58*	6.7
286.42	10.21	6.0
288.281	11.05	6.0
288.818	10.34	6.6
289.171	10.44	7.2
289.47	11.146	5.6
289.556	9.556	5.7
277.736	−10.092	5.3
278.23	−9.24	5.5
274.658	−17.105	5.8
267.87	−20.23	5.4
298.148	2.487	6.3

* detected by JEMX.

Table B.3: New source candidates detected by SExtractor in the ISGRI OSA5.1 original map in the 20–40 keV range.

OSA5.1 RA FIN	ISGRI map Dec FIN	DET SIG
283.51	9.11	13.01
285.76	9.96	9.50
286.39	10.27	9.64

Continued...

Table B.3: Continued.

OSA5.1 RA FIN	ISGRI Dec FIN	DET SIG
287.83	10.73	11.62
288.54	11.84	9.82
289.10	10.015	9.90
289.16	9.46	7.99

Table B.4: New source candidates located by visual inspection in the Segreto's mosaic (20–40 keV range). The sigma detection of all the sources are between ∼5–8.

RA FIN	Dec FIN
274.483	-22.371
276.521	-14.722
285.896	10.903
287.658	9.248
288.190	1.540
291.295	10.765
298.028	2.488
299.110	17.861

Table B.5: Probably new source candidates detected by JEM-X.

RA OBJ	DEC OBJ	SIGMA	EN. BAND
271.251	-12.69	1.68	2
272.368	-17.53	1.69	3
275.244	-17.92	1.87	1
277.170	-3.79	1.69	1
277.658	−10.85	1.48	3

Continued...

Table B.5: Continued.

RA OBJ	DEC OBJ	SIGMA	EN. BAND
281.913	-15.04	1.76	1
283.681	2.20	1.88	1
283.811	-2.64	1.25	1,2
283.820	1.28	1.90	1
284.477	7.45	8.95	2
287.543	10.60	1.48	1,2,3
288.542	12.24	1.78	2
289.533	12.39	1.71	2
290.879	9.56	1.93	2
291.114	7.85	1.68	1

* JEM–X mosaic:
energy band 1: 4–10 keV;
energy band 2: 10–15 keV;
energy band 3: 15–35 keV

Table B.6: New source candidates detected by SPI in the 20-40 keV range.

	SPI RA FIN	Dec FIN	ERR radius	DET SIG
SOURCE-60	288.013	19.151	0.144	20.9
SOURCE-61	280.108	16.226	0.237	12.6
SOURCE-62	276.973	-12.567	0.256	11.7
SOURCE-63	297.130	-3.859	0.278	10.8
SOURCE-64	272.050	5.719	0.325	9.2
SOURCE-65	293.991	3.147	0.300	10.0
SOURCE-66	270.196	-30.025	0.359	8.4
SOURCE-67	279.477	-2.899	0.320	9.4
SOURCE-68	256.773	0.103	0.321	9.3
SOURCE-69	300.150	-17.731	0.394	7.6
SOURCE-70	264.809	14.453	0.391	7.7
SOURCE-71	299.416	15.931	0.398	7.5
SOURCE-72	273.520	-8.001	0.397	7.6
SOURCE-73	252.768	-1.224	0.421	7.1
SOURCE-74	259.785	-21.459	0.412	7.3

Appendix C

Resumen en castellano

C.1 INTRODUCCIÓN

Los objetivos principales de esta tesis han sido el estudio de binarias de rayos–X a altas energías, para determinar sus propiedades espectrales y temporales, claves así mismo para derminar su naturaleza. Podríamos dividir en dos fases la metodología desarrollada: (a) análisis temporal y/o espectral de determinadas binarias de rayos–X situadas a lo largo del plano galáctico: EXO 2030+375, SAX J2103.5+4545, A 0535+262, (b) identificación, para una futura posterior clasificación espectral y temporal de las fuentes detectadas dentro de la región del brazo galáctico de Scutum.

Para ello se ha procedido a la reducción de datos en rayos–X, obtenidos principalmente con las misiones INTEGRAL y RXTE. Con ésto se pretende cubrir simultaneamente desde los rayos–X blyos (con RXTE) hasta rayos–X duros (con INTEGRAL).

Este Apéndice constituye un resumen en castellano de los contenidos de esta tesis doctoral. No se trata de una traducción, sino de una breve descripción de la tesis. No se incluyen figuras ni tablas, refiriéndonos siempre a las ya incluídas en el cuerpo central del trabajo.

C.2 MISIONES DE RAYOS–X

C.2.1 La misión INTEGRAL

INTEGRAL es un misión de la ESA (Agencia Espacial Europea) de altas energías lanzada con éxito el 17 de octubre del 2002. Sus principales objetivos son la obtención de espectros e imágenes de alta resolución en el rango de energía 15 keV – 10 MeV, así como el seguimiento simultáneo de la emisión en rayos–X y en el óptico de fuentes de rayos γ.

El satélite está formado por dos principales instrumentos: un espectrómetro (SPI) y una cámara de imágenes (IBIS). Completan el satélite dos monitores, uno de rayos–X (JEM-X) y otro en la bya óptica (OMC), coalineados con los instrumentos principales.

Los principales objetivos científicos de INTEGRAL son: objetos compactos, astronomía galáctica, nucleosíntesis estelar, el plano de nuestra galaxia y estructura central, los procesos de aceleración de partículas, la identificación de fuentes de alta energía y el descubrimiento de nuevas fuentes inesperadas.

Los tres instrumentos de alta energía son telescopios de máscaras codificadas. Estos telescopios estan formados por una máscara codificada, i.e, una matriz de elementos opacos y transparentes organizados siguiendo un patrón regular, situada entre las fuentes y un detector sensible a la posición (ver Fig. 2.1). Conociendo el patrón regular de la máscara y la imagen producida en el plano detector, se puede reconstruir la imagen del cielo por medio de métodos de deconvolución (Caroli et al. 1987).

Los instrumentos

- SPI es un espectrómetro diseñado para la obtención de espectros de alta resolución en la bya de energía 18 keV – 8 MeV con una resolución energética de 2.5 keV a 1.1 MeV y una resolución angular de 2.5°. El instrumento está formado por 19 detectores de Ge puro y una máscara codificada situada a 1.7 m del plano detector.

- IBIS está diseñado para la obtención de imágenes de alta resolución (12') en el rango de energía 15 keV – 10 MeV. Está formado por dos planos detectores: ISGRI y PCsIT, más una máscara codificada situada a 3.4 m de ISGRI.

  ISGRI contiene 16384 detectores de CdTe. Está optimizado para obtener imágenes, alcanzado una resolución energética de $\sim$ 8% a 60 keV. PCsIT consiste en 4096 detectores de centelleo de CsTi(Tl) y está optimizado para operar en el rango de energía 175 keV – 20.4 MeV con una resolución energética de 18.4 % a 511 keV.

- JEM-X está diseñado para la obtención de imágenes con resolución angular de 3.35' y espectros con una resolución energética de 2 keV a 22 keV en el rango de energía 4 – 35 keV. Está formado por dos telescopios de máscaras codificadas, formados por una unidad detectora y una máscara codificada situada a 3.4 m del plano detector. Los dos telescopios son idénticos, excepto que sus máscaras estan rotadas 180° una respecto a la otra.

- OMC proporciona observaciones fotométricas de larga duración en la bya óptica simultáneas con las observaciones en rayos–X y γ. La cámara se basa en una óptica refractiva con una apertura de 50 mm y una CCD con una sensibilidad en V de 18.

C.2.2 La misión RXTE

RXTE es una misión de la NASA que fue lanzada en Diciembre de 1995. Su duración ha superado con mucho las expectativas iniciales, siguiendo en funcionamiento en la actualidad. Las principales características de esta misión son su gran resolución temporal en combinación con una moderada resolución espectral que ha permitido y permite explorar el amplio rango de variabilidad de muchas fuentes de rayos–X. Escalas de tiempo desde microsegundos hasta meses son cubiertas por *RXTE* en un rango espectral desde 2 a 250 keV.

RXTE lleva a bordo 3 instrumentos. “PCA” fue diseñado para realizar análisis temporal y espectral de fuentes de rayos–X muy brillantes dentro del rango energético de 2–60 keV. El instrumento HEXTE extiende la sensibilidad hasta 200 keV. Y por último el monitor ASM escanea todo el cielo cada 1.5 horas en la bya 2–10 keV.

Los instrumentos

- El monitor ASM consiste en 3 cámaras escáner de sombra montadas en un sitema de rotación motorizado. Cada escáner lleva un contador proporcional sensible a la posición. La máscara está compuesta por láminas de aluminio. El campo de visión es de $6^\circ \times 90^\circ$ de anchura a media altura (FWHM).
- PCA consiste en 5 unidades de contadores propocionales de gran área. Cada uno tiene una área colectora de $\sim$1600 cm^2. Los detectores consisten en un colimador mecánico de FWHM $\sim 1^\circ$, una ventana aluminizada Mylar, un volúmen de veto rellenado con propano y un contador principal relleno de Xenon.
- HEXTE está compuesto de dos bloques, cada uno de ellos contiene 4 detectores de centelleado. Cada bloque puede moverse de forma limitada en direcciones mutuamente ortogonales, lo cual conlleva medidas del fondo o ruido del cielo desde 1.5 a 3○. alejados de la fuente de rayos–X cada 16 ó 128 s.

C.3 PULSARES ACRETORES

El descubrimiento de la primera binaria de rayos–X en la década de los 60, Sco X–1, por Giacconi et al. (1962), constituyó el principio de la astronomía en rayos–X. En la época de su descubrimiento, se desconocían los procesos físicos que podían dar lugar a dicha emisión. Después de la identificación de la contrapartida óptica de Sco X–1 por Syage et al (1966), se sugirió la transferencia de masa en sistemas binarios cercanos como posible mecanismo productor de rayos–X.

Un sistema binario de rayos–X está formado por un objeto compacto y una estrella acompañante, donante que orbita alrededor del centro de masas conjunto. El objeto compacto puede ser o bien una enana blanca (Variables cataclísmicas), una estrella de neutrones o un agujero negro. Por otro lado, la estrella compañera puede tener o bien baja masa o alta masa, clasificándolas entonces como sistemas de dos tipos: Sistemas Binarios de Baja Masa o Sistemas Binarios de Alta Masa.

Tanto la luminosidad, como el comportamiento temporal y espectral de una binaria de rayos–X depende principalmente: de la masa de la contrapartida óptica, del ritmo de acreción, de la geometría de dicho proceso de acreción desde la compañera y del tipo de objeto compacto. Si el objeto compacto es una estrella de neutrones, entonces la fuerza gravitatoria y la topología del campo magnético juegan un papel determinante en la emisión de rayos–X. En el caso de agujeros negros el campo gravitatorio domina todo el proceso.

Los procesos de acreción, es decir, los de transferencia de masa desde la estrella compañera hasta el objeto compacto, pueden deberse a los siguientes mecanismos:

- Desbordamiento del lóbulo de Roche: durante el proceso evolutivo de la estrella donante, su tamaño puede sufrir cambios en varias ocasiones, adquiriendo e incluso superyo el tamaño del lóbulo de Roche propiciyo el desbordamiento de materia.
- Acreción por viento estelar: el viento procedente de la estrella donante es atrapado por el potencial gravitacional de la estrella compacta. Estos sistemas se llaman de "alimentación por viento" (tipos O y B).
- Corriente ecuatorial de masa, por ejemplo, acreción procedente del disco circumestelar de una estrella de tipo Be: cuyo la estrella de neutrones pasa a través del disco circumestelar de la estrella Be, parte de masa es transferida desde aquí hacia el objeto compacto.

Dentro del grupo de las binarias de rayos–X existe un subgrupo denominado "binarias pulsantes de rayos–X". Estos sistemas están formados por una estrella de neutrones y una estrella poco evolucionada, y emiten radiación pulsante en rayos–X de forma periódica. Se ha encontrado un amplio rango de períodos de pulso, oscilyo entre unos pocos milisegundos a miles de segundos. Así mismo, se han detectado cambios diversos a distintas escalas temporales.

C.4 TÉCNICAS DE ANALISIS

La reducción que las misiones *INTEGRAL* y *RXTE* proporcionaron se han reducido hasta la obtención de imágenes, espectros y curvas de luz o listas de eventos, usyo el software oficial estándar que está a disposición de cualquier usuario a través de sus respectivas páginas web.

Dichos productos finales de ambas misiones han sido analizados usyo las herramientas del paquete FTOOLs. Además, los productos resultantes del análisis temporal han sido tratados usyo un software específico inicialmente desarrollado en en centro NASA MSFC. Esto tiene por objetivo calcular de forma muy precisa los parámetros orbitales de dichos sistemas. Por último los espectros han sido analizados ajustyo modelos canónicos y/o físicos con el paquete XSPEC. Así mismo se ha utilizado sotfware preliminar para la obtención de imágenes y listas de eventos creado por Segreto y Ferrigno de la Universidad de Palermo.

C.5 EXO 2030+375

C.5.1 Introducción

EXO 2030+375 es una binaria de alta masa con una compañera óptica de tipo Be, descubierta en 1985 por *EXOSAT* durante un estallido gigante de rayos–X (Parmar et al. 1989). Con un período orbital $P_{\rm orb}$=46.0214±0.0005 dias y una excentricidad de e=0.419±0.002 (Wilson et al. 2002), EXO

2030+375 presenta variabilidad a todas las escalas. En la región de rayos–X la estrella de neutrones presenta pulsaciones de 41.7 s y períodos de actividad e inactividad relacionados principalmente con su paso por el periastro. El período de pulsación presenta aumentos y disminuciones a lo largo de su historia.

Desde su descubrimiento la fuente ha mostrado sólo estallidos de tipo I (o normal): *EXOSAT* (28 Octubre - 3 Noviembre 1985, Parmar et al. 1989), *Ginga* (29-31 Octubre 1989 y 24 Octubre 1991, Sun et al. 1992), *ROSAT*(Noviembre 1990, Mavromatakis 1994), *CGRO*/BATSE y *RXTE* satélites (desde Abril 1991 los estallidos han sido detectados casi en cada paso por el periastro y continuan siendo detectados con el monitor ASM, Wilson et al. (2002, 2005), y *INTEGRAL* (6-18 Diciembre 2002, y continúan siendo detectados durante los escáners del plano galáctico y otras observaciones puntuales).

Estos estallidos de tipo I tienen una luminosidad $L_x < 10^{37}$ erg s^{-1}. La intensidad de estos estallidos y el ritmo de incremento del período del pulso parecen estar atados a la variación de la intensidad de la estrella Be en la banda K (Wilson et al. 2005).

En el 2006 la fuente presentó un estallido gigante, el segundo detectado hasta la fecha, mostrando por primera vez evidencias de la presencia de una linea ciclotrón alrededor de 10 keV con *RXTE* (Wilson and Finger 2006), y otra posible línea a 20 keV solo detectada por *INTEGRAL* (Klochkov et al. 2007).

En este capítulo hemos realizado un análisis temporal y espectral de estallidos de tipo I de la fuente detectados con *INTEGRAL* y *RXTE* (primera parte) . En un segundo bloque, presentamos los resultados espectrales preliminares del estallido gigante del 2006 con *RXTE* , mostrándose una evolución de los parámetros espectrales durante el desarrollo del mismo.

C.5.2 Los estallidos normales

Observaciones y análisis de los datos

Los datos analizados en esta sección fueron obtenidos de las misiones *INTEGRAL* y *RXTE* en períodos distintos. Con *INTEGRAL* hemos analizado todos los datos disponibles desde la fase de calibración y verificación científica de los instrumentos (Nov-Dic 2002) hasta finales del 2005.

Durante este período *INTEGRAL* detectó 17 estallidos de tipo I, de ellos tan sólo uno ha sido cubierto en su totalidad por *INTEGRAL* . Por consiguiente este estudio se centrará en una primera etapa en el estudio de este estallido completo, y en segundo lugar se presentará un estudio de la cobertura parcial del resto de los estallidos normales. El diario de observaciones se muestra en la Tabla B.1.

Respecto a la misión *RXTE* se han analizado datos correspondientes a 3 estallidos normales detectados en 3 períodos: Julio del 1996, Junio del 2002 y Septiembre del 2003. Para los estallidos de 1996 y 2002 tenemos una cobertura global.

Hemos realizado un análisis detallado de estos datos obteniendo con *INTEGRAL* imágenes de la región de EXO 2030+375, extrayendo curvas de luz, listados de eventos y espectros para cada uno de los instrumentos. Los principales objetivos de este análisis han sido:

- Localización de la fuente mediante la obtención de imágenes en diferentes bandas de energía (ver Fig. 5.3) para el estallido de Dic-2002.
- Análisis temporal a corta y media escala del mismo estallido . Los objetivos han sido: (a) la determinación de forma muy precisa del período y la forma del pulso (ver Fig. 5.4), tanto en rayos–X blyos (JEM–X) como en la parte dura (ISGRI), (b) caracterizar la forma de la curva de luz del estallido completo de Dic-2002.
- Estudio de la variabilidad espectral de la fuente mediante la obtención de diagramas de color-tiempo para el estallido de dic-2002,

y diagramas color-flujo para todos los estallidos normales detectados.

- Análisis espectral: caracterización del espectro medio del estallido de Dic-2002 desde 5–300 keV. Es la primera vez que se obtiene este tipo de caracterización.

En el caso de *RXTE* se han obtenido curvas de luz y se ha estudiado la variabilidad espectral durante los tres estallidos normales, siendo los principales objetivos de este análisis:

- Análisis temporal a media escala de los 3 estallidos normales (ver Fig. 5.6), para caracterizar la forma de sus curvas de luz.
- Estudio de la variabilidad espectral de la fuente mediante la obtención de diagramas de color-fase orbital.

Resultados obtenidos

El análisis de las imágenes revela en las cercanías de EXO 2030+375 la presencia de otras fuentes, como Cygnus X–3, Cygnus X–1 o SAX J2103.5+4545.

La capacidad de obtención de imágenes y la buena resolución angular de los instrumentos de INTEGRAL, aseguran que la radiación detectada procedente de nuestra fuente no está contaminada por la presencia de otras fuentes en el campo de visión. La fuente es detectada significativamente por los tres instrumentos y hemos podido reducir el círculo de error de localización de la misma.

Los datos de *INTEGRAL* del estallido de Dic–2002 nos han permitido estimar con la mayor precisión hasta la fecha el período de pulsación de la fuente siendo el valor obtenido 41.691798 ± 0.000016 s.

Las curvas de luz del estallido de Dic-2002 presentan dos peculiaridades no detectadas con anterioridad, un prepico inicial antes del máximo y un posible pico secundario tras el máximo. Las curvas de luz obtenidas con *RXTE* confirman la presencia del prepico pero no muestran evidencias del segundo.

Comparando los colores de los diferentes estallidos normales detectados, hemos obtenido una variabilidad espectral acusada, la fuente se hace más blanda conforme el flujo aumenta.

El espectro medio del estallido de Dic-2002 con *INTEGRAL* se puede caracterizar bien ajustando un modelo canónico estándard (disco de cuerpo negro + ley de potencias) o un modelo de disco de cuerpo negro más una comptonización. No se detectaron líneas de emisión del hierro ni líneas ciclotrón.

C.5.3 El estallido gigante de 2006

Observaciones y análisis de los datos

El segundo estallido de tipo II (o gigante) detectado en la historia de esta fuente, fue observado en su totalidad por *RXTE* . Para su análisis espectral se han usado datos de PCA de tipo estardard 2, y datos en modo ciencia de ambas estructuras de bloques A y B que componen HEXTE.

En principio el bloque A de HEXTE perdió su movilidad por esas fechas, con lo cual en principio no había posibilidad de extraer espectros del ruido de fondo para dicho elemento A. Sin embargo, recientemente el equipo de HEXTE de la Universidad de California San Diego ha desarrollado una herramienta para poder estimar dicho ruido de fondo a través de datos de dicho ruido tomados por el bloque B.

Resultados obtenidos

Los resultados obtenidos en el análisis espectral confirman la presencia de una línea ciclotrón a 10 keV y de la línea de emisión del hierro a ∼6.5

keV. Para ello se ha ajustado un modelo canónico estándard con el paquete xspec, compuesto de una ley de potencias más una absorción, una línea gausiana del hierro y un decaimiento exponencial a altas energías. Después añadimos a este modelo una linea gausiana de absorción para representar la linea ciclotrón a 10 keV.

La Fig. 5.14 muestra los resultados de la evolución de los parámetros que representan la línea ciclotrón con la luminosidad (flujo en el rango 2–100 keV) de la fuente durante este estallido gigante.

En general la línea ciclotrón ha sido detectada de forma significante para flujos mayores a 1.7×10^{-8} erg cm-2 s^{-1}. La Fig. 5.15 muestra la evolución de otro parámetros espectrales del mismo modelo.

C.5.4 Discusión y conclusiones

- Hemos obtenido el primer espectro de banda ancha cubriendo desde 5–300 keV utilizando datos de la misión *INTEGRAL* correspondientes al estallido de Diciembre de 2002. Dicho espectro se ha podido ajustar bien usando una ley de potencias no atenuada ($\Gamma = 2.04 \pm 0.11$) o un modelo de contonización (kT$_e$=30 keV) describiendo la parte más dura del espectro, mientras que un disco de cuerpo negro ajusta la parte más blanda (kT$_{BB}$ ∼8 keV). No se encontraró ninguna línea ciclotrón.

- El error en la determinación del período del pulso se ha reducido un ∼20% sobre medidas anteriores con *INTEGRAL* .

- En el estudio a media escala temporal se encontraron dos características inusuales en la forma de la curva de luz del estallido de Dic–2002. En concreto, un prepico de gran intensidad antes de llegar al máximo y otro posible pico de menor intensidad después del máximo. Los datos de *RXTE* de los otros 3 estallidos normales confirman solo la presencia del primer prepico. Los mecanismos físicos que producirían estos dos picos todavía son desconocidos.

- Nuestro estudio espectral del estallido gigante del 2006 confirma la presencia de una línea ciclotrón a 10 keV detectada por Wilson and Finger (2006). Sin embargo no hemos detectado la presencia de otra línea a 20 keV publicada por Klochkov et al. (2007) con datos de *INTEGRAL* . Creemos interesante mencionar la línea a 10 keV con nuestros datos de *RXTE* evoluciona a valores de 12 keV a medida que el flujo disminuye.

- La anchura de la línea, la significancia, el índice de la ley de potencias, la absorción y el decaimiento exponecial de la energía en la parte dura del espectro presentan cierto grado de dependencia con la luminosidad.

C.6 SAX J2103.5+4545

C.6.1 Introducción

SAX J2103.5+4545 es una binaria de rayos–X de alta masa con una compañera óptica de tipo Be. Su período orbital es el más corto de los conocidos para este tipo de sistemas, 12.68 dias. Fue descubierta por el satélite *BeppoSAX* (Hulleman et al. 1998).

La contrapartida óptica más probable es una estrella de tipo B0Ve a una distancia de 6.5 kpc (Reig et al. 2004). En un estudio por Baykal et al. (2002) encontraron una correlación del flujo emitido por este sistema en rayos–X y el ritmo en el incremento del período del pulso. Esto es una indicación de que muy probablemente la estrella de neutrones crea a cada paso por el periastro un disco de acrección de materia.

Pero SAX J2103.5+4545 no es un sistema binario de alta masa, con estrella compañera de tipo Be, estándard. Por ejemplo, no se la localiza dentro de la región reservada para este tipo de sistemas en el diagrama P_{orb}/P_{pulso}.

Estudios publicados por distintos autores obtienen resultados diferentes en cuanto a la forma del perfil del pulso (Falanga et al. (2005);Sidoli et al. (2005)), con su forma variando entre un solo pico y un pico principal más otro secundario. Reig et al. (2005) en su estudio sobre esta fuente en estado de inactividad encontró que aún así se podía detectar emisión en rayos–X. Esto es algo que aún hoy en día no se entiende.

En nuestro estudio presentamos un análisis de la evolución del perfil del pulso de esta fuente a escala temporal larga. También presentamos un estudio espectral, temporal y obtuvimos los parámetros orbitales de este sistema.

C.6.2 Observaciones y análisis de los datos

Para este estudio a larga escala temporal hemos analizado datos públicos de *RXTE* PCA desde 1999 hasta 2004, y datos también públicos de *INTEGRAL* IBIS/ISGRI desde el 2002 hasta el 2004. En concreto a la hora de estudiar la dependencia de la forma del perfil del pulso bien con la luminosidad, el tiempo y/o la energía, hemos procedido a la obtención de 548 curvas de luz en el rango de 2–60 keV con datos de *RXTE* PCA, y de un número de 24 en distintas bandas energéticas para el estudio de la dependencia con la energía (ver Fig. 6.4).

Para el análisis espectral hemos utilizado sólo datos de *RXTE* PCA y HEXTE, con una mejor cobertura temporal que *INTEGRAL* . Es importante mencionar que existe un hueco sin datos durante el 2001.

C.6.3 Resultados obtenidos

Estudio del Perfil del Pulso

- Hemos obtenido perfiles cuya forma varía entre la aparición de un solo pico principal, hasta pulsos con 2, 3 y 4 picos más, hecho nunca antes descubierto.
- No se ha encontrado correlación de la forma del perfil del pulso con la fase orbital (ver Fig. 6.2) ni con el tiempo (ver Fig. 6.1).

En cuanto a la dependencia con la luminosidad se da un aspecto curioso. No se ha encontrado dependencia de la forma del perfil con respecto a su estado luminoso, sin embargo existe una clara correlación entre la intensidad de cada uno de los picos del pulso y dicha magnitud, aumentando a medida que aumenta su estado luminoso (ver Fig. 6.6).

- Del estudio energético del perfil del pulso encontramos una clara correlación. A bajas energías el perfil es más complejo pudiendo mostrar hasta cuatro picos. A energías más altas el perfil se hace más sencillo, presentando un pico principal más otro secundario más débil (ver Figs. 6.9 y 6.11).
- En la Fig. 6.12 mostramos la evolución de la intensidad media de cada pico en cada banda energética. Vemos que el máximo de la intensidad media cada pico está localizado en una banda energética distinta.

Estudio espectral

Hemos obtenido 548 espectros con datos de *RXTE* PCA y de los dos elementos (o bloques) A y B de HEXTE. El espectro conjunto ha sido ajustado con xspec, aplicando un modelo canónico estándard, es decir, una ley de potencias más una absorción a bajas energías, una línea de hierro a ∼6.5 keV, y un decaimiento exponencial en la parte más dura.

- Del estudio de la variabilidad espectral de esta fuente, hemos visto que su espectro se vuelve más blando a medida que la luminosidad decrece (ver Fig. 6.13).
- Hay una clara desviación de la calidad del ajuste del modelo utilizado, permitiéndonos distinguir claramente entre los dos estados de luminosidad principales que presenta esta fuente, el alto y el bajo.
- También encontramos las correlaciones esperadas entre algunos parámetros espectrales y la luminosidad. El hecho más relevante

es que la ley de potencias disminuye a medida que la luminosidad aumenta, hecho que confirma el primer punto descrito más arriba.

Estudio temporal y obtención de una nueva solución orbital

Hemos obtenido las diferentes medidas del período del pulso y del ritmo de variación del mismo a lo largo de los 6 años de datos procesados. Así mismo ésto nos ha permitido obtener una nueva solución orbital del sistema binario.

- Del estudio se desprende que la estrella de neutrones ha variado su período de rotación a lo largo del tiempo, incrementando su frecuencia de giro en una primera etapa para luego permanecer casi estable. Después del hueco generado por la falta de datos encontramos que la fuente de nuevo está en fase de incremento de su frecuencia de giro de una forma mucho más rápida respecto a la primera etapa. Entrando ya en el año 2004 aproximadamente, dicha frecuencia aunque sigue en aumento lo hace de forma mucho más lenta (ver Fig. 6.14, panel superior).
- Todas estas fases en la variación de la frecuencia de giro hemoscomprobado se encuentran relacionadas con el estado luminoso del objeto compacto (ver Fig. 6.14, paneles medio e inferior). Si la fuente presenta una emisión más fuerte en rayos–X entonces el ritmo de la frequencia de giro es fuerte y aumenta. Si por el contrario la emisión en rayos–X es más débil entonces o bien el ritmo de cambio de la frecuencia se ralentiza o bien tiende a estabilizarse.
- Este comportamiento es una indicación bastante probable de la presencia de un disco accretor de materia, cuyo tamaño va variando en consonancia con la fuente entrando en sus dos estados principales alto y bajo (ver Fig. 6.15).
- En la Tabla 6.2 se muestra la nueva solución orbital obtenida, así como su comparación con todas las previamente publicadas hasta la fecha de hoy.

C.6.4 Discusión y conclusiones

- La composición del perfil del pulso varía entre un solo pico principal hasta el principal más subpicos secundarios. Este resultado es bastante peculiar, ya que normalmente la forma de los perfiles del pulso en otros sitemas binarios con compañera Be son más sencillos, por ejemplo EXO 2030+375 (Parmar et al. 1989). No obstante existen otros sitemas binarios de alta masa que nos son de acreción por disco sino por viento estelar, como Vela X–1, que también presentan un perfil complejo a bajas energías (**?**). Se nos plantea la duda de que SAX J2103.5+4545 sea un híbrido entre púlsar acretor por disco y un púlsar acretor por viento estelar. Hasta la fecha no se ha podido dar con una explicación para este comportamiento.

- Al no haber encontrado ninguna correlación de la forma del pulso con el tiempo, con la fase orbital, o con el estado luminoso de la fuente, podemos explicarnos ahora la variación de formas encontrada con anterioridad por otros autores (Baykal et al. (2002);İnam et al. (2004);Falanga et al. (2005);Sidoli et al. (2005)).

- Respecto a la correlación encontrada entre la forma del pulso y la energía, comparando con resultados anteriores de varios autores vemos que están de acuerdo con la tendencia para los perfiles de forma más sencilla (ya que como dijimos antes, hasta ahora no se había obtenido un pulso tan complejo). Para nuestra fuente (y para energías superiores a 20 keV) Falanga et al. (2005) encontraron que los cambios en la morfología del perfil del pulso en función de la energía eran consistentes con variaciones espectrales visibles en su análisis espectral resuelto en fase. Este estudio así mismo mostró que las diferencias entre los dos picos encontrados podían ser modelados aplicando una fracción de desviación por choques distinta entre la radiación proveniente de los dos polos magnéticos.

- La naturaleza de esta fuente sigue siendo objeto de controversia, ya que por ejemplo, según nuestros cáculos se requiere de un gran campo magnético del orden de B= 16.5×10^{12} G (see Tab. 6.3) para que esta fuente entre en un estado de inhibición de la acrección por la fuerza centrífuga (efecto centrífugo). Hecho que no se ha podido constatar ya que no se ha detectado línea ciclotrón alguna en su espectro.

- Además, Reig et al. (2005) hizo notar en un trabajo anterior que es aún posible producir rayos–X cuando el efecto centrífugo está operando. Sin embargo el hecho de que SAX J2103.5+4545 esté localizado enla región de las binarias supergigantes alimentadas por viento en el diagrama P_{pulso}–P_{orb}, hace pensar que la acreción por viento estelar de su compañera de tipo B0 pueda ser el origen de la radiación X detectada durante el período de inactividad.

- Por todo lo anterior, en el presente estudio proponemos que SAX J2103.5+4545 sea reclasificada como una fuente PERSISTENTE y no de carácter TRANSITORIO.

C.7 A 0535+262

C.7.1 Introducción

A 0535+262 es un púlsar dentro de un sistema binario transitorio de alta masa, descubierto por el satélite Ariel V durante un outburst gigante en 1975 (Rosenberg et al. 1975b). El período orbital de esta fuente es de 111.10 días, y su período de pulso es is ∼103 s en una órbita excéntrica con e∼0.47 (Finger et al. 1994b). Su contrapartida óptica es una estrella de tipo espectral O9.7 IIe cuyo nombre más común es el de HDE 245770 (Liller and Eachus 1975).

La intensidad en rayos–X de A 0535+262 varía casi en 3 órdenes de magnitud con 3 estados básicos: inactividad (con niveles de flujo inferiores a 10 mCrab, estallidos normales (10 mCrab – 1 Crab), y estallidos gigantes. Desde el último estallido gigante ocurrido en 1994 y lo dos estallidos normales que le siguieron, la fuente ha permanecido en estado de inactividad durante 11 años (Finger et al. 1996b).

La Fig. 7.1 muestra la curva de luz de *RXTE* ASM durante parte del período de inactividad, el nuevo estallido gigante de 2005, y los otros dos estallidos normales que se dieron a continuación. El hecho más destacable es la aparición de un prepico antes del máximo en el primer estallido normal.

Finger et al. (1996) detectó por primera vez una oscilación quasiperíodica desde los 27 hasta los 72 mHz, durante el outburst gigante de 1994, confirmándose la presencia de un disco de acreción. En el estallido gigante de 1999 dos líneas ciclotrón fueran detectadas en el espectro de esta fuente, la primera a ∼45 keV y la segunda a ∼100 keV (Kendziorra et al. 1994).

Observaciones recientes con *RXTE* e *INTEGRAL* (Caballero et al. 2007) confirman la detección de las dos líneas ciclotrón durante el estallido de Agosto/Septiembre de 2005. En la Fig. 7.2 podemos observar la evolución temporal del valor del período de pulsación de A 0535+262 a lo largo de la historia.

C.7.2 Observaciones y análisis de los datos

En el presente trabajo hemos analizado datos de la missión *RXTE* PCA y HEXTE, correspondiente a la parte final del decaimiento del estallido gigante (Agosto–Septiembre 2005) y los dos estallidos normales siguientes (Dic–2005/Enero–2006), con un total de 58 observaciones. Para el estudio energético del perfil del pulso de cada una de las observaciones, hemos analizado datos PCA bien de tipo GoodXenon o de tipo evento. Para HEXTE se han seleccionado eventos científicos de los dos elementos (o bloques) A y B.

En el caso de *INTEGRAL* , solamente se realizaron observaciones de esta fuente durante un breve período de tiempo, en concreto situado cerca del máximo del primer estallido normal acaecido en Septiembre de 2005.

C.7.3 Resultados obtenidos

- La forma del perfil del pulso de esta fuente presenta de 1 a 4 (o incluso 5) picos. A bajas energías se obtienen perfiles más complejos que a altas energías.
- La evolución del perfil del pulso con la luminosidad es en resúmen la siguiente: (a) a bajas luminosidades el pulso es un sólo pico de forma sinusoidal, que se divide en dos picos a medida que la luminosidad crece, (b) para luminosidades intermedias nos encontramos con que los dos picos se igualan en tamaño, aplanándose en su forma general,(c) Aparece una tercera componente de forma ancha y asimétrica, pareciendo compuesta de dos subpicos que se vuelve más prominente a medida que crece la luminosidad (d) un cuarto pico aparece a más altas luminosidades, cuya intensidad crece con la luminosidad (ver Fig. 7.6).
- La evolución de cada una de las componentes del perfil del pulso con la energía es la siguiente (ver Fig. 7.7): (a) el pico principal (fases 0–0.2) , para luminosidades bajas, decrece con la energía aumentando, pero para luminosidades medias aumenta con la energía, y finalmente decrece muy sutílmente a medida que la energía crece (excepto para el prepico – ver Fig. 7.8 –); (b) el pico secundario (fases 0.2–0.5): decrece a medida que la luminosidad crece, para luminosidades bajas y medio-altas, y para luminosidades altas, aumenta con la energía hasta el rango de 15–20 keV (máximo) decreciendo a continuación a medida que la energía aumenta., (c) el tercer y cuarto picos decrecen con la energía aumentando.

C.7.4 Discusión y conclusiones

A bajas energías nuestro trabajo coincide parcialmente con lo encontrado por Bradt et al. (1976). Encontramos sus mismas componentes del perfil del pulso hasta aproximadamente 20 keV. Sin embargo, Bradt et al. (1976) solo encuentran ese tipo de perfil tan complejo hasta por debajo de 8 keV. Esto puede deberse a la mejoría en las nuevas técnicas empleadas en este tipo de estudios. De hecho estudios más recientes por Kretschmar et al.

(2005) y Caballero et al. (2007) han revelado perfiles igual de complejos que los nuestros. Aunque la gran novedad es la gran covertura temporal que aporta el presente estudio, nunca realizado con anterioridad, que nos ha permitido observar variaciones más finas a muchos niveles.

A altas energías nuestros perfiles se vuelven en general más sencillos, pudiendose comparar con los resultados ya publicados por muchos autores, como Bildsten et al. (1997). No obstante encontramos que a energías mayores de 20 keV, el comportamiento del pico secundario es más compejo de lo que hasta ahora se creía (ver Fig. 7.9).

Un aspecto a destacar es que ésta ha sido la primera vez que se ha detallado la evolución temporal, energética y luminosa del perfil del pulso durante un prepico precediendo al máximo de un estallido normal. Esto nos permitiría estudiar los mecanismos físicos que originan este tipo de hechos.

C.8 El brazo galáctico de Scutum

C.8.1 Introducción

Se sospecha de que la existencia de binarias de rayos–X es mayor que la que se conoce en la actualidad. La razón sería el obscurecimiento de este tipo de fuentes al estar inmersas dentro de densas nubes moleculares localizadas en el plano galáctico, como por ejemplo en el brazo galáctico de Scutum.

Estudios detallados de estos campos a más altas energías donde la materia se hace transparente (E $>$ 30keV) deberían dar pie al descubrimiento de una población de binarias de rayos–X más realista, y por otro lado, fundamental para para la reconstrucción de la "historia química " de la galaxia. Muchos objetos están siendo descubiertos por la misión *INTEGRAL* , como por ejemplo la fuente IGR J16318-4848 (Courvoisier et al. 2003).

C.8.2 Observaciones, análisis y resultados

Gracias a que *INTEGRAL* es una misión con una capacidad sin precedentes para realizar imágenes de gran precisión de rayos–X a gamma, en este capítulo se han obtenido imágenes en distintos rangos energéticos de los 3 instrumentos de altas energías a bordo de dicha misión para este brazo galáctico.

En las Figs. 8.16, 8.17, 8.11, 8.13 y 8.15 mostramos las imágenes obtenidas en distintos rangos enegéticos dependiendo del instrumento, así como resultados paralelos para ISGRI aplicando el software standard OSA5.1 y el alternativo por Alberto Segreto (ver sección C.4). En la Tabla B.1 exponemos todas las fuentes conocidas detectadas en nuestro estudio.

Por otro lado, todos los resultados preliminares (ver Tablas B.1, B.2, B.3, B.6, B.4 y B.5) indican la existencia de candidatas a nuevas fuentes, localizadas en regiones donde se ha comprobado ya la existencia de estrellas de tipo espectral B. Estos primeros esperanzadores resultados serán seguidos por una campaña de fotometría y espectroscopía infraroja para poder identificar a las posibles contrapartidas ópticas.

C.9 CONCLUSIONES

Como ya hemos expuesto con anterioridad, los objetivos principales de esta tesis han sido el estudio de púlsares acretores dentro de sistemas binarios de rayos–X con compañera masiva a altas energías. Hemos determinado en unos casos sus propiedades espectrales y temporales, y en otros casos hemos dado un paso más firme a la hora de confirmar la existencia de posibles nuevos sistemas de este tipo que se encontraban ocultos dentro del brazo galáctico de Scutum.

La primera parte del estudio ha revelado que nuevos mecanismos físicos operan dentro del escenario clásico, por otro lado aún hoy díficil éste de ser entendido, debido a la aparición de componentes inesperadas tanto en el estudio temporal como en el espectral. Pareciera como si una mayor profundidad de estudio nos haya llevado a descubrir escenarios más complejos. Esperamos que trabajos futuros abran más ventanas al entedimiento de lo que está ocurriendo en estos sistemas binarios.

C.9.1 Trabajo futuro

Gracias a los estudios realizados en la presente tesis, hemos entendido que hay que seguir aunando esfuerzos a la hora de mejorar las herramientas de análisis observacional, ya que hemos visto que es esencial para desentrañar el comportamiento intrínseco de este tipo de fuentes. Por otro lado, se hace necesario que nuevas teorías puedan explicar los resultados aquí obtenidos.

Los primeros resultados esperanzadores en el brazo galáctico de Scutum, nos hacen creer que un buen número de nuevas sistemas binarios de alta masa serán resueltos. Para ello, se realizarán senads campañas de fotometría y espectroscopía infrarroja para poder identificar a las posibles contrapartidas ópticas. A éste estudio en la zona Infarroja, se pretende seguir con otro que ahonde en las características espectrales y temporales a altas energías, aplicando nuestras nuevas técnicas de anális de datos.

List of Figures

List of Tables